Topological Defects in Anisotropic Multicomponent Superconductors

Alex Millar Barnes Wormald

University of Leeds
School of Mathematics

Submitted in accordance with the requirements for the degree of
Doctor of Philosophy

October 30, 2021

The candidate confirms that the work submitted is their own, except where work which has formed part of jointly authored publications has been included. The contribution of the candidate and the other authors to this work has been explicitly indicated below. The candidate confirms that appropriate credit has been given within the thesis where reference has been made to the work of others.

Chapter 2 includes work from [1] and [2], whilst Chapter 3 includes work from [2].

All authors contributed equally to each paper but in both cases I mainly performed numerical simulations and analysis. The major roles of my co-authors were analysis and interpretation.

Dedicated to Mum and Dad.

Acknowledgements

First I should like to thank my main supervisors, Martin Speight and Tom Winyard. Thank you both for your help and support. It was with your help that my transition from physics to maths went more smoothly. Martin thank you for your clarity, support and direction: I could not have completed this process without you. Tom, thank you for your help and support especially at the start of the PhD when you were not my supervisor as well as your help with matters numerical and our productive weekly meetings. Furthermore, I would especially like to thank Derek Harland for our discussions during the summers as well as his willingness to answer my emails and help me whenever. Finally, I would like to thank the KTH PhD students: Mats specifically for his help with a graphing problem on Matlab and to both him and Andrea for their work on the collaboration paper.

I am grateful for my EPSRC research studentship that made this PhD possible. Additionally, much of the numerical work of my thesis was done using the code library Soliton Solver, developed by Thomas Winyard, and was undertaken on ARC4, part of the High Performance Computing facilities at the University of Leeds. I am appreciative of the use of both which greatly sped up and enabled my research.

I would especially like to thank my family, the biggest supporters I have. Thank you for your time and love. You have mine back. Thank you to my dad for our grounding chats and discussions and my mum our long walks and support. I am also grateful that my sister is the wonderful and kind person that she is. I would also like to thank Lizzie for bringing joy to my life and being instrumental in getting me to the end of this PhD. You helped me through the twin challenges of the COVID-19 lockdown and writing up. My friends from home, Thom, Simon and Luke, should also be mentioned: always willing to talk and hang out when near.

I have benefited from many discussions and help with colleagues in the department and I wanted to mention but a few; Chris Halcrow, Joe Driscoll, Amit Shah and Richard Matthews. I would finally like to mention my friends on the PhD; Oscar, Muyang, Joseph, Amira, Tom B, Richard, Christina, Laya, and Lilly as well as the members of the wider PhD Whatsapp group chat. Having like minded people around me was key in staying on the path to the conclusion of this PhD. I include my friends on the ultimate frisbee pick-up game group. Having this sport as a way to de-stress was an invaluable antidote to working inside for most of the day.

Abstract

Ginzburg-Landau (GL) theory provides a phenomenological description of superconductors. We study one and two-dimensional topological solitons in unconventional superconductors that can be described by anisotropic multicomponent GL theory. The conventional ansatz, used for isotropic superconductors, fixes the direction of the (internal) magnetic field. However, anisotropy breaks rotational symmetry thus this ansatz is inconsistent with the three-dimensional GL equations. We consider a consistent ansatz that allows the direction of the magnetic field to freely change throughout the superconductor. This introduces novel magnetic phenomena such as magnetic field twisting which we study in $p + ip$, $s + is$ and $s + id$ superconductors.

For domain walls, anisotropy means that changing the orientation of this one-dimensional topological soliton (within a three-dimensional sample) affects its physical properties. Spontaneous magnetic fields occur that can vanish and even change direction (or twist) away from the domain wall for some orientations, providing a way to distinguish between types of superconductors. For $s+is$ and $s+id$ superconductors we find novel types of domain walls that are not degenerate in energy. By linearising the GL equations we are able to predict and observe the oscillatory decay of solutions of the full nonlinear theory. Additionally, we are able to predict magnetic field twisting from the linearisation. This also occurs in the Meissner state but now, due to anisotropy, depends on the direction of the applied magnetic field.

Using the consistent ansatz we study vortices in anisotropic superconductors. We consider the orientation dependence of field configurations which we classify. Magnetic field twisting also occurs for some orientations. Finally, we study vortex lattices in an external magnetic field, allowing us to determine the upper and lower critical fields as well as finding the unit cell shape that minimises energy for a given value of the external magnetic field.

Contents

Nomenclature

Roman symbols

H_{C1}	Lower Critical Field for a Type II Superconductor
H_{C2}	Upper Critical Field for a Type II Superconductor
T	Temperature
T_C	Critical Temperature
A	$U(1)$ Gauge Field or Vector Potential
B	Internal Magnetic Field
H	External Magnetic Field

Greek Symbols

ψ_α	Superconducting Order Parameter or Condensate
θ_α	Phase of the Superconducting Order Parameter or Condensate
θ_{12}	Phase difference between the ψ_1 and ψ_2 Condensates
$\lvert\psi_\alpha\rvert$ or ρ_α	Magnitude of the Superconducting Order Parameter or Condensate

Abbreviations

BTRS	Broken Time Reversal Symmetry

Basis Labels

$(\hat{x}, \hat{y}, \hat{z})$	Basal Plane or Crystalline Orthonormal Basis
$(\hat{x}_1, \hat{x}_2, \hat{x}_3)$	Excitation Plane Orthonormal Basis
(x, y, z)	Basal Plane or Crystalline Coordinates
(x_1, x_2, x_3)	Excitation Plane Coordinates

List of Figures

List of Tables

Chapter 1

Introduction

1.1 Historical Review of Superconductivity

In 1911, when the Dutch Physicist Heike Kamerlingh Onnes ([3],[4],[5]) cooled down a sample of Mercury to 4K it exhibited no electrical resistance when an electric current was passed through it. This discovery led to the phenomenon which was later called superconductivity and earned Onnes a Nobel prize in 1913. Superconductors have one further property, in addition to zero electrical resistance. When cooled below what is known as their critical temperature, T_C, they exhibit the Meissner effect. In 1933 Walther Meissner and Robert Ochsenfeld [6] discovered that a superconducting material will expel an applied magnetic field (up to a certain field strength) which is known as the Meissner effect. Note that the superconductor must have a temperature, $T < T_C$, and an external magnetic field, $H < H_C$, where T_C and H_C are the so called critical values of temperature and external magnetic field above which it has neither zero electrical resistance nor does it expel a magnetic field in the Meissner effect. A superconductor with $T > T_C$ or $H > H_C$ is referred to being in its normal state.

Although superconductors are ubiquitous in modern technology, being used in very sensitive magnometers and in maglev trains or NMR machines, the low temperature required for superconductivity makes their use in the everyday impractical. Thus discovering superconductors that are functional at higher and higher temperatures is still a goal for today and could potentially provide great technological improvements, for example in the national electricity grid.

A phenomenological approach for describing the Meissner effect was taken by the London brothers in 1935 [7] which is known as the London theory and was able to predict that an external magnetic field will penetrate the surface of a superconductor that is exhibiting the Meissner effect before decaying to zero, this is known as the penetration depth. This was later built upon in 1950 when Vitaly Ginzburg and Lev Landau [8] introduced the so called Ginzburg-Landau equations which successfully predicted the macroscopic properties of superconductors and very importantly the description of type I and II superconductors, more on this topic later.

Then in 1957 the first fully microscopic (non-phenomenological) theory to describe low temperature (close to absolute zero) superconductivity for simple materials was published by Bardeen, Cooper, Schrieffer ([9], [10]) and was called the BCS theory. In superconductors a current flows without dissipation, which is known as the supercurrent, j_s, and gives the superconductor its ability to expel magnetic flux and have zero electrical resistance. The BCS theory described how, in simple low temperature superconductors, the supercurrent is composed of pairs of electrons, that are the charge carries for the supercurrent, called Cooper

pairs. A quasi-classical explanation goes as follows: as electrons move through a superconducting lattice they attract positive ions forming regions of positive charge. The ion, being heavier than the electron, takes longer to return to its original position than that of an electron thus the region of positive charge remains after an electron has moved away. This region of positive charge, over certain length scales, can overcome the electrical repulsion between electrons and form coupled pairs of electrons known as Cooper pairs. The BCS theory can be difficult to perform calculations with, so the need for a simpler, effective theory is apparent.
Today much of the work on superconductivity involves the study of so called unconventional superconductors, which have high critical temperatures $T_C > 50K$, such as FFLO [[11],[12]] or multicomponent [[13],[14],[15],[16]] superconductors. Recently discovered iron based superconductors, [17], could possibly be explained by multicomponent superconductivity. Currently, a microscopic theory on the mechanism for these superconductors is not available but their macroscopic properties can be studied through Ginzburg-Landau theory as we discuss in this thesis.
The Meissner effect can be used to experimentally distinguish superconductors from normal conducting materials. Defining, B, as the internal magnetic field of the superconductor and H the externally applied magnetic field, consider Figure 1.1. We start with both an electrical conductor and a superconductor at a temperature, $T > T_C$, where T_C is the (critical) temperature below which the superconductor becomes superconducting. As we cool both materials to $T < T_C$ we see that the superconductor expels the magnetic field so that $B = 0$ in the centre of the superconductor, whereas $B = H$ at the centre of the conductor. We further note that, as well as critical temperature, there is a critical external magnetic field strength, H_C, above which the superconductor does not exhibit the Meissner effect nor have zero electrical resistance. It is in the normal state. We note that H_C is a function of temperature, see Figure 1.2a, and is defined for $T = 0K$. So temperature and external magnetic field are interrelated quantities that both affect superconductivity. This type of superconductivity is referred to as type I and is marked by a rapid transition from the homogenous superconducting state, which is where the superconductor exhibits the Meissner effect and has zero electrical resistance, to the normal state where the superconductor is no longer superconducting. If we introduce the scalar magnetic flux per unit area, $\Phi = \frac{\int_{\mathbb{R}^2} B \cdot d^2x}{\int_{\mathbb{R}^2} d^2x}$, then Figure 1.2a plots Φ versus H for constant T. We see that when $B = 0$ then $\Phi = 0$ and we are in the superconducting state. For the normal state, $B = H$ and $\Phi = H$. It should be noted that at the boundaries of the superconductor there is some penetration by the external magnetic field. The amount of penetration is known as the penetration depth. However, deep in the centre of the superconductor, which is also referred to as the bulk, these boundary effects can be ignored.

Additionally, a new type of superconductivity, type II, was identified in 1936 by Lev Schubnikow [19]. It still exhibits the Meissner effect, similarly to a type I superconductor, however the behaviour is now governed by two critical external magnetic fields. The lower critical field, H_{C1}, is the value of the external field, at $T = 0$, above which the external field starts to penetrate the superconductor at finite points known as vortices, see Figure 1.3. An external field above the upper critical field, H_{C2}, for $T = 0$ completely suppresses superconductivity in a superconductor and as shown in Figure 1.2b is dependent on temperature as is H_{C1}. The interesting features of a type II superconductor arise when $H_{C1} < H < H_{C2}$. Instead of a jump from the superconducting to the normal state the superconductor is penetrated by H at finite points. Again this is shown in Figure 1.3. The points where the external magnetic field penetrates the superconductor are called vortices. In three dimensions, a vortex can be considered a cylinder or tube of magnetic flux, $\Phi_0 = \int_{\mathbb{R}^3} B \cdot d^3x$, through which the external magnetic field penetrates. The magnetic flux through a single vortex is quantised in units of

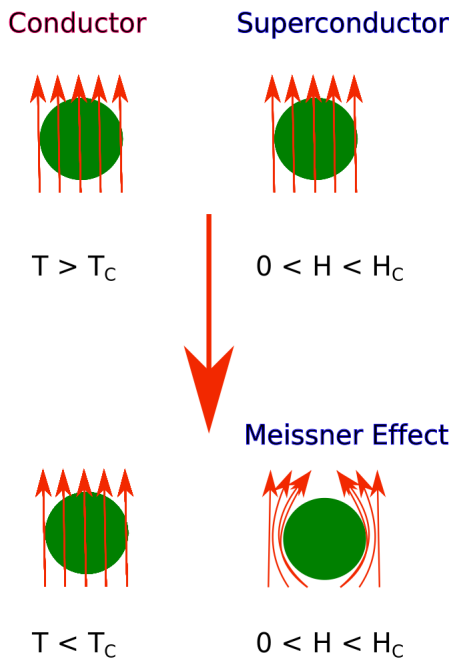

Figure 1.1: *Diagram of the field cooling experiment to distinguish between a conductor and a superconductor. We see that a superconductor will expel an external magnetic field, $H < H_C$, when the temperature, $T < T_C$. The conductor, however, is unaffected by the change of temperature.*
T_C and H_C are the critical values of the temperature and external magnetic field above either of which superconductivity does not occur.

2π. The centre of the vortex, also called the zero, is where the Meissner effect is broken and an external magnetic field fully penetrates the superconductor. Each vortex is arranged in a regular lattice such that the total energy of the system is minimised. This arrangement is known as an Abrikosov lattice. If we consider Figure 1.2b we see how the region $H_{C1} < H < H_{C2}$ provides a smooth transition from the superconducting state to the normal state unlike that in Figure 1.2a. The key point to note is that type I and II are distinguished by their responses to an applied magnetic field, H, rather than the changing of the temperature, T.

1.2 London Theory

The phenomenological London theory was one of the first successful theories to describe the Meissner effect. It follows a quasi-classical approach where we assume quantum particles, electrons, obey Newton's laws [20]. The London brothers assumed that a superconductor had de-localised electrons that moved, without resistance, due to an applied electric field which is known as the supercurrent. It was not known then that the charge carriers were pairs of bound electrons, Cooper pairs. Using Newton's 2nd law we have $m_e \frac{dv}{dt} = -eE$ where m_e is the mass of an electron, v its velocity, e its charge and E the applied electric field which causes the motion. Then, defining the rate of flow of the supercurrent to be $\frac{dj_s}{dt} = -n_s e \frac{dv}{dt}$, where n_s is the number density of the carriers of the supercurrent. The equation derives from the classical idea that the change in current is equal to the density of charge carriers times the volume flow rate. Combining these two equations we produce the first London equation,

$$\frac{dj_s}{dt} = \frac{e^2 n_s}{m_e} E \ . \tag{1.1}$$

Type I

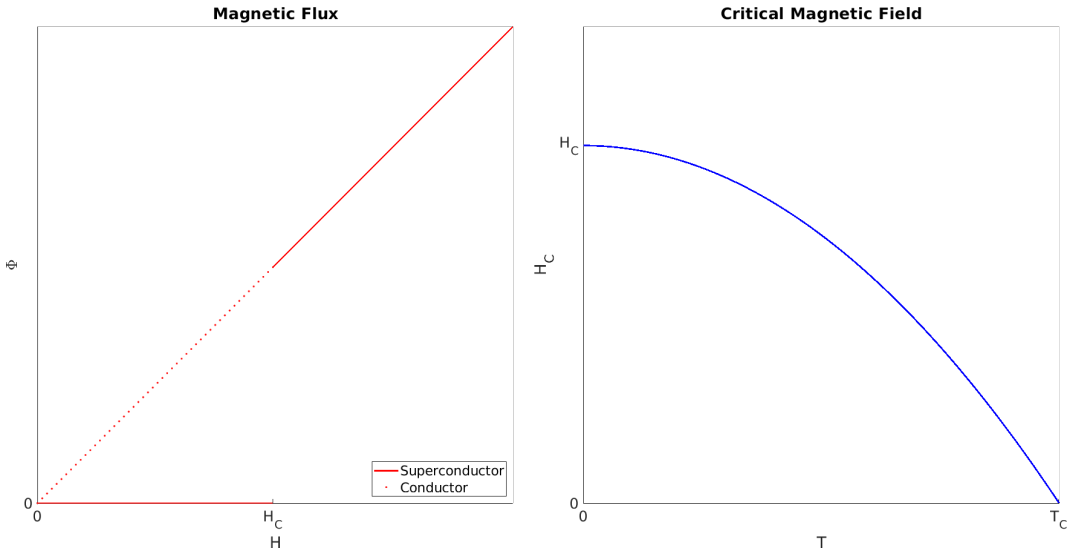

(a) *Diagram of the total magnetic flux per unit area,* $\Phi = \frac{\int_{\mathbb{R}^2} B \cdot d^2x}{\int_{\mathbb{R}^2} d^2x}$*, versus the external magnetic field,* H*, for a type I superconductor at a constant temperature,* $T < T_C$*. While* $H < H_C$ *the material exhibits the Meissner effect so* $\Phi = 0$ *and for* $H > H_C$ *the material becomes conducting, so* $\Phi = H$*.*
The second plot is of H_C *versus* T *showing that when* $T = T_C$ *,* $H_C = 0$*, and past this point* $H_C = 0$ *meaning the material is in the normal state.*

Type II

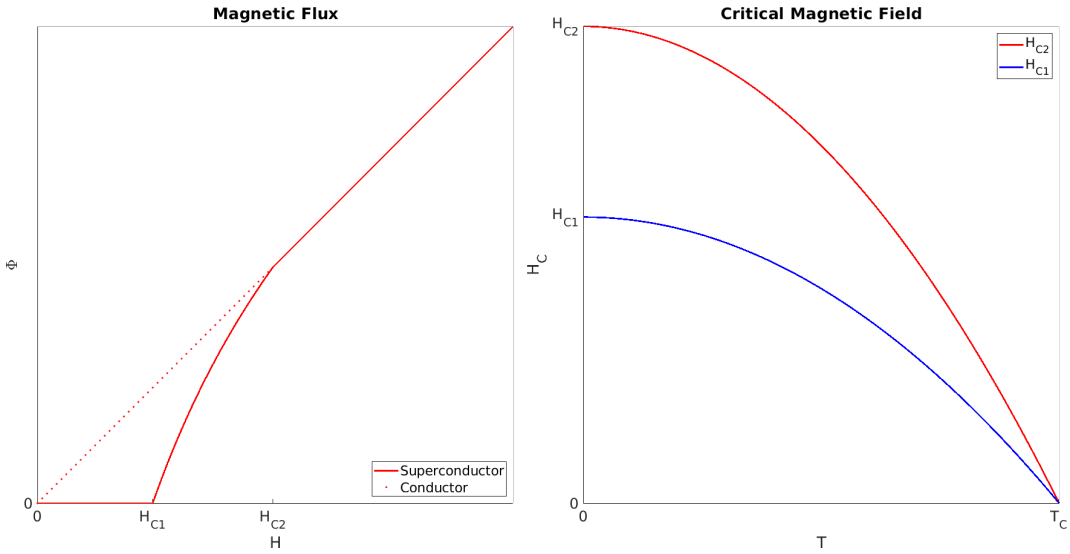

(b) *Diagram of the magnetic flux per unit area,* $\Phi = \frac{\int_{\mathbb{R}^2} B \cdot d^2x}{\int_{\mathbb{R}^2} d^2x}$*, versus the external magnetic field,* H*, for a type II superconductor at a constant temperature,* $T < T_C$*. While* $H < H_{C1}$ *the material exhibits the Meissner effect so* $\Phi = 0$ *and for* $H > H_{C2}$ *the material becomes conducting thus* $\Phi = H$*. However, for* $H_{C1} < H < H_{C2}$ *the superconductor forms an Abrikosov lattice of vortices ([18]), as* H *increase the vortices become closer together so* Φ *increases until we reach the normal state.*
The second plot is of H_{C1} *and* H_{C2} *versus* T *showing for all* $T < T_C$*,* $H_{C2} > H_{C1}$ *which means vortex lattices can form.*

Figure 1.2: *Diagrams showing the external magnetic field,* H *and temperature dependence for a type I and II superconductor.*

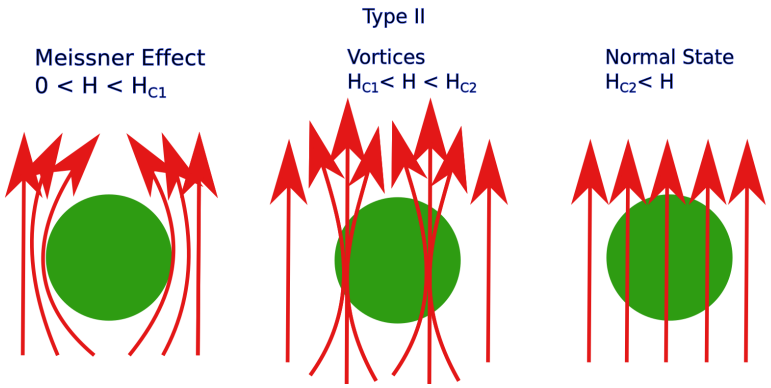

Figure 1.3: *Diagram of the Meissner effect and the vortex state for a type II superconductor where $T < T_C$. The red arrows denote the lines of magnetic field and we see in the case of vortices these field lines penetrate at finite points whilst the surrounding material still exhibits the Meissner effect. Finally, we see the normal state where the superconductor is no longer superconducting and is fully penetrated by an external magnetic field.*

The second London equation comes from applying one of Maxwell's equations of electromagnetism, $\nabla \times E = -\frac{dB}{dt}$, which describes how a time varying magnetic field will generate a spatially varying electric field (and vice versa). We apply this to Equation 1.1, giving $\frac{d}{dt}\left(\nabla \times j_s + \frac{e^2 n_s}{m_e} B\right) = 0$, where B is the magnetic field inside the superconductor. Integrating gives,

$$\nabla \times j_s = -\frac{e^2 n_s}{m_e} B + C_1 \tag{1.2}$$

$$\nabla \times j_s = -\frac{e^2 n_s}{m_e} B \ . \tag{1.3}$$

We set $C_1 = 0$, which is required in order to describe the Meissner effect, and so the justification is phenomenological. We take the curl of Equation 1.3 and used the following two Maxwell's equations of electromagnetism, $\nabla \times B = \mu_0 j_s$ and $\nabla \cdot B = 0$, to simplify. These two equations describe how a magnetic field can induce a current and how magnetic monopoles do not exist,

$$\nabla^2 B = \frac{\mu_0 e^2 n_s}{m_e} B \ . \tag{1.4}$$

Equation 1.4 describes the decay of the internal magnetic field. The coordinates (x, y, z) and the corresponding orthonormal basis $(\hat{x}, \hat{y}, \hat{z})$ are used.
Consider a superconductor that has a boundary with an insulator at $x = 0$ such that the superconductor is in the positive half plane, $x \geq 0$, and the insulator is in $x < 0$. An (electrical) insulator does not conduct electricity. The simplest example would be air. The region, $x \geq 0$, is known as the Meissner state. This is expanded upon in Section 1.4. We can apply an external magnetic field, $H = H_0 \hat{z}$, in the $\hat{z}$ direction such that $B = H_0$ at $x = 0$. This allows us to consider the dependence of B on x for $x \geq 0$, where $\hat{x}$ is the direction normal to the boundary between the superconductor and insulator. Thus we assume that $B \mapsto (0, 0, B_z(x))$ where we have assumed that B points only in the $\hat{z}$ direction, the direction of the external magnetic field. Equation 1.4 then reduces to,

$$\partial_x^2 B_z(x) = \frac{\mu_0 e^2 n_s}{m_e} B_z(x) \ . \tag{1.5}$$

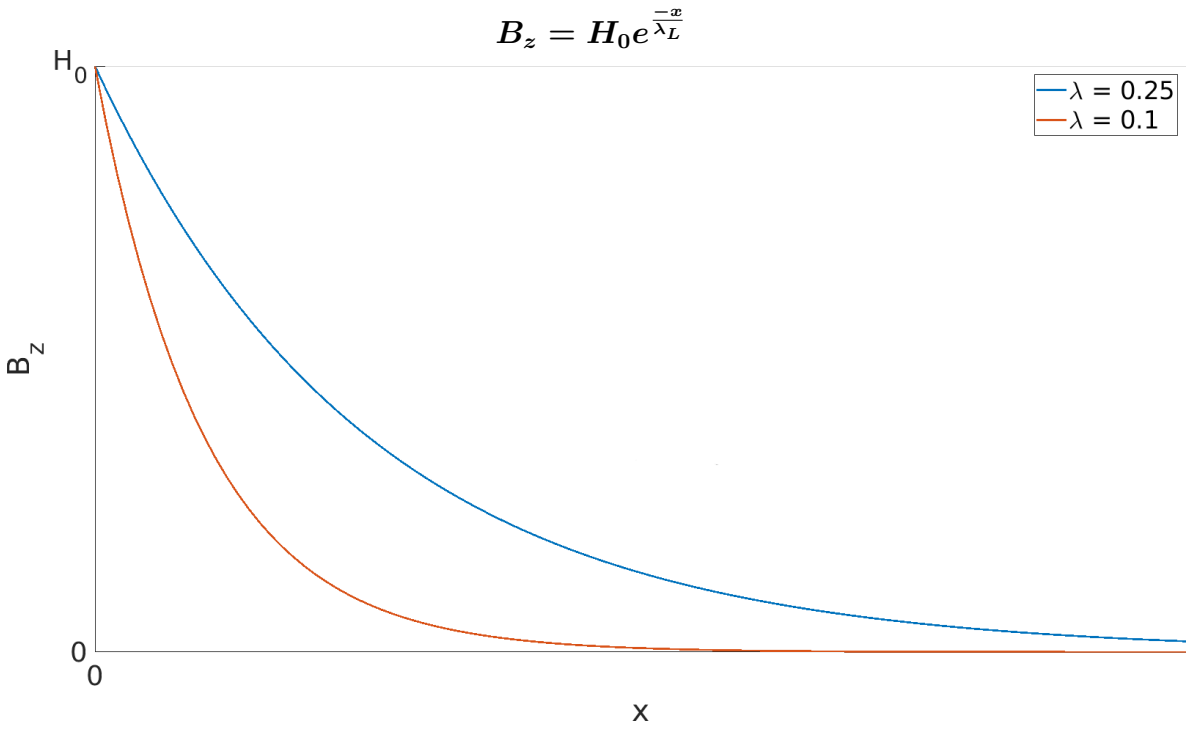

Figure 1.4: *Diagram of the magnetic field penetration as predicted by the London model in one dimension, where $x = 0$ is the boundary between an insulator and a superconductor. The external magnetic field, $H = H_0\hat{z}$, points in the z direction. For $x \geq 0$ we are inside the superconductor and we use the boundary condition $B(x = 0) = H_0\hat{z}$. Note that for $x < 0$ we have $B = H$. We can see that decreasing the value of the London penetration length scale, λ_L, causes B_z to decay faster.*

For the half plane, $x \geq 0$, we have a solution of,

$$B_z = H_0 e^{\frac{-x}{\lambda_L}} \ , \tag{1.6}$$

where we keep only terms that decay to zero as $x \to \infty$ and require that $B_z(x = 0) = H_0$. We see that the magnetic field will penetrate the surface of the superconductor by an amount related to,

$$\frac{1}{\lambda_L^2} = \frac{\mu_0 e^2 n_s}{m_e} \ , \tag{1.7}$$

where λ_L is known as the London penetration length scale or London penetration depth. Figure 1.4 shows how B_z changes with λ_L.

1.3 Ginzburg-Landau Theory

Ginzburg-Landau theory seeks to model the temperature dependence of a superconductor as well as to provide insight into the two types of superconductivity. Consider increasing the temperature of a type I superconductor so that it changes from the superconducting state to the normal state. This change is known as a phase transition and can be physically observed by studying how the internal magnetic field, B, and the electrical resistance both become non zero when in the normal state. This phase transition can be characterised by a complex, spatially varying, order parameter, ψ, which is dependent on the number density of the charge carriers of the supercurrent, n_s. If the order parameter, $|\psi|$ vanishes everywhere then

the material is in the normal state which corresponds to an absence of charge carriers, $n_s = 0$. If, however, $|\psi|$ is constant and non zero everywhere then the material is in the homogenous superconducting state, with $n_s \neq 0$, which characterises a type I superconductor. However, ψ can vary spatially allowing it to model a type II superconductor where, considering the vortex state, we would expect, $n_s = 0$ and therefore $|\psi| = 0$, at the centre of a vortex and, $n_s \neq 0$ and $|\psi| \neq 0$, away from the centre. This is because the magnetic field penetrates a superconductor at the centre of the vortex which breaks the Meissner effect at that point.
The free energy of the superconductor near to the phase transition is given by,

$$F = \int_{\mathbb{R}^3} \left(\frac{1}{2}|\nabla\psi|^2 + \alpha(T)|\psi|^2 + \frac{\beta}{2}|\psi|^4 \right) d^3x \ , \tag{1.8}$$

where $|\psi|^2 = (\psi)^*\psi$ and $|\psi|, |\nabla\psi|$ are assumed to be small near to this phase transition. The expression comes from expanding around small $\psi, (\psi)^*$ and $\nabla\psi, (\nabla\psi)^*$ noting that as we require a real free energy only even powers are kept. This expansion is only mathematically valid for small $|\psi|$ but it turns out that with the correct parametrisation, the free energy is a good approximation for many physical systems. Note that $\alpha(T)$ and β are real parameters of the model and the temperature dependence is introduced through the parameter $\alpha(T)$. Ginzburg-Landau theory truncates this expansion at second order for the gradient term, $|\nabla\psi|$, and fourth order for the potential,

$$F_p(|\psi|) = \alpha|\psi|^2 + \frac{\beta}{2}|\psi|^4 \ . \tag{1.9}$$

Due to the requirement that the free energy must be real the potential must also be hence it is only a function of $|\psi|$. Additionally, $|\psi| = u$, minimises the potential which gives the vacuum value,

$$\psi^{vac} = ue^{i\chi} \ . \tag{1.10}$$

Note that ψ^{vac} minimises F_p for any choice of constant, $\chi \in [0, 2\pi]$. There are two homogenous states:

- $\psi = u$, $u \neq 0$, everywhere. This is called the homogenous superconducting state and it is where the superconductor exhibits the Meissner effect and has zero electric resistance.
- $\psi = 0$ everywhere. This is called the normal state where the material is no longer superconducting and is fully penetrated by an external magnetic field H such that $B = H$.

Figure 1.5 plots the potential for $\alpha = -1$ and $\alpha = 1$, where we see that the sign of α affects the global minimum (or vacuum) of the potential. If $\alpha > 0$ then we are in the normal state where $u = 0$ but for $\alpha < 0$ we are in the homogenous superconducting state where $u = \sqrt{\frac{|\alpha|}{\beta}}$. The temperature dependence of α is introduced to the free energy by writing $\alpha = \alpha_0(T - T_C)$ where we note that for $T > T_C$ $\alpha > 0$ and thus $u = 0$ so we are in the normal state and for $T < T_C$, $\alpha < 0$ and we are in the homogenous superconducting state.

1.3.1 Inhomogeneous Solutions

For the Ginzburg-Landau theory we use the coordinate basis, $(\hat{x}, \hat{y}, \hat{z})$, which we call the basal plane or crystalline basis. Each direction denotes a symmetry axis of the superconductor. A symmetry, for example, could be the reflection in the x, y plane represented by the transformation, $z \mapsto -z$.

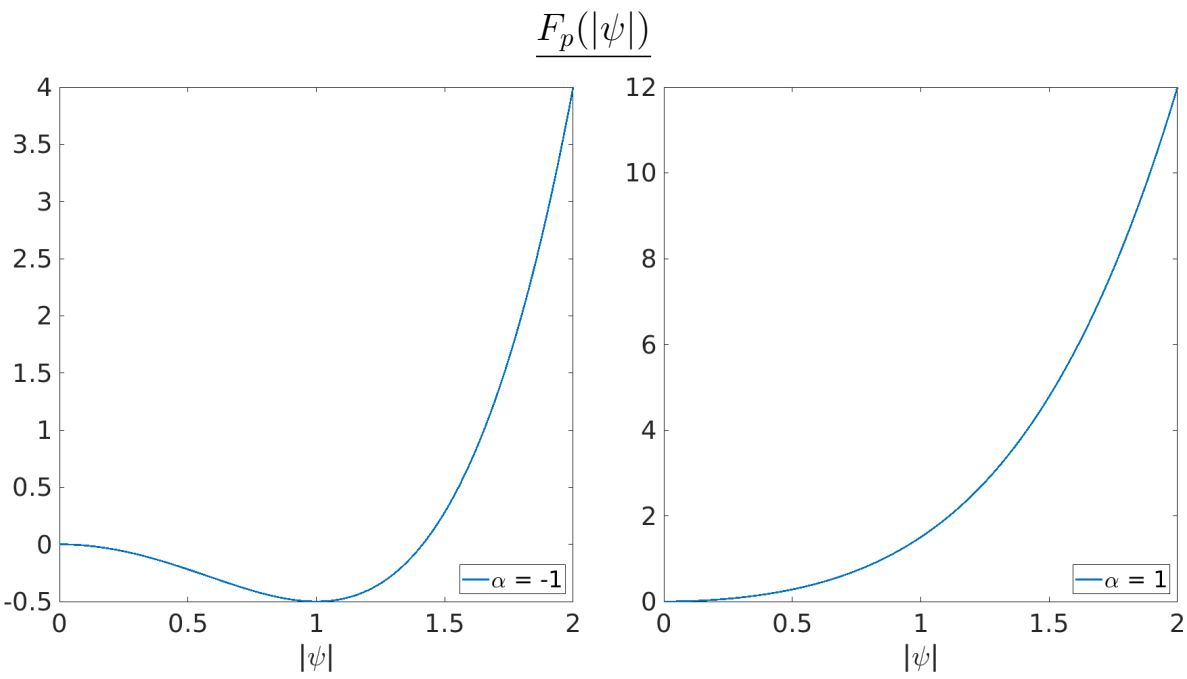

Figure 1.5: *Plots of the stationary points of the potential,* $F_p(|\psi|) = \alpha|\psi|^2 + \frac{1}{2}|\psi|^4$*, in the superconducting,* $\alpha < 0$*, and normal state,* $\alpha > 0$*. We set* $\beta = 1$ *and consider* $|\psi| \in \mathbb{R}$ *as a variable not a field.*
For $\alpha = -1$ *we see that the global minimum of the potential has* $|\psi| \neq 0$ *but for* $\alpha = 1$ *the global minimum is in fact* $|\psi| = 0$*.*

To obtain inhomogeneous solutions of Equation 1.8, we must consider small variations of $\psi = \psi_R + i\psi_I$ given by,

$$\varphi(x, y, z) = \psi_R + \epsilon\eta_R + i(\psi_I + \epsilon\eta_I) \ , \tag{1.11}$$

where $\epsilon << 1$, and $\psi_R, \psi_I, \eta_R, \eta_I$ are scalar fields on $\mathbb{R}^3$ and both η_R and η_I vanish on the boundaries of our domain, ∂C. This fixes $\varphi = \psi$ on ∂C. We now consider the expansion of $f(\varphi, \nabla\varphi)$ in terms of ψ_R and ψ_I,

$$f(\varphi, \nabla\varphi) = f(\psi, \nabla\psi) + \epsilon\left(\eta_R \frac{\partial f}{\partial \psi_R} + \sum_{i=1}^{3} \nabla\eta_R \frac{\partial f}{\partial \nabla_i \psi_R}\right) + i\epsilon\left(\eta_I \frac{\partial f}{\partial \psi_I} + \sum_{i=1}^{3} \nabla\eta_I \frac{\partial f}{\partial \nabla_i \psi}\right) + \mathcal{O}(\epsilon^2) \ . \tag{1.12}$$

We then consider,

$$F[\varphi] = \int_{\mathbb{R}^3} f(\varphi, \nabla\varphi) d^3x \tag{1.13}$$

$$= \int_{\mathbb{R}^3} f(\psi, \nabla\psi) + \epsilon\ \delta F + \mathcal{O}(\epsilon^2) \ , \tag{1.14}$$

where δF is called the first variation. To find extrema of, F, we require that $\delta F = 0$. Performing integration by parts on δF yields,

$$\begin{aligned} \delta F = &\int_{\mathbb{R}^3} \eta_R \left(\frac{\partial f}{\partial \psi_R} - \nabla_i \frac{\partial f}{\partial \nabla_i \psi_R}\right) d^3x + \eta_R \frac{\partial f}{\partial \nabla_i \psi_R}\bigg|_{\partial C} \\ &+ i \int_{\mathbb{R}^3} \eta_I \left(\frac{\partial f}{\partial \psi_I} - \nabla_i \frac{\partial f}{\partial \nabla_i \psi_I}\right) d^3x + i\ \eta_I \frac{\partial f}{\partial \nabla_i \psi_I}\bigg|_{\partial C} \ . \end{aligned} \tag{1.15}$$

The terms evaluated on ∂C vanish as η_R, η_I also vanish on the boundary. Then via the Fundamental Lemma of the Calculus of Variations the integrand of the first term must vanish giving the Ginzburg Landau equation in term of ψ,

$$\alpha\psi + \beta\psi|\psi|^2 - \frac{1}{2}\nabla^2\psi = 0 \ . \tag{1.16}$$

We can see that the trivial, homogenous, solution, $\psi = ue^{i\chi}$ satisfies Equation 1.16. However, with an appropriate choice of boundary conditions, inhomogeneous solutions will also satisfy Equation 1.16. Note that $\delta F = 0$ only ensures that ψ **extremises** Equation 1.8.

1.3.2 Gauged Ginzburg-Landau Theory

Our supercurrent consists of moving electrically charged particles, the motion of which produces a magnetic field. Therefore we need to introduce a coupling between ψ and the magnetic field B. The magnetic field can be written in terms of a vector potential, or gauge field, $A = A_x\hat{x} + A_y\hat{y} + A_z\hat{z}$ where $B = \nabla \times A$. The free energy is now given by,

$$F = \int_{\mathbb{R}^3} f \ d^3x = \int_{\mathbb{R}^3} \left(\frac{1}{2}|D\psi|^2 + \frac{B^2}{2} + \left(\alpha|\psi|^2 + \frac{\beta}{2}|\psi|^4 \right) \right) d^3x \ , \tag{1.17}$$

where f is the free energy density. The covariant derivative, $D = \nabla - iA$, introduces this coupling. We emphasise that the potential, F_p, retains the same form as in Equation 1.8 this means that the condensate vacuum is still $\psi^{vac} = ue^{i\chi}$. Finite energy requires that $|D\psi| = 0$ for the vacuum, this can be achieved by choosing $A^{vac} = 0$ and $\nabla\psi^{vac} = 0$. Furthermore, the introduction of the covariant derivative means that the so called gauge transformations,

$$\psi \mapsto e^{i\chi}\psi \tag{1.18}$$

$$A \mapsto A + \nabla\chi \ , \tag{1.19}$$

leave the free energy unchanged, where χ is a real smooth spatially varying function. By this we mean, $F(e^{i\chi}\psi, A + \nabla\chi) \equiv F(\psi, A)$.
To understand the gauge transformation for Equation 1.17 we must first distinguish between the fields ψ and A which are gauge dependent, that is they change when we make a gauge transformation, and gauge invariant quantities such as,

$$F \ , |\psi| \ , B \ , j_s \ , \tag{1.20}$$

which are unaffected by a gauge transformation: we expect physical (or gauge invariant) quantities, such as the magnetic field, to be real therefore they should not change with our choice of χ. We give an example of a gauge transformation where the gauge, $\chi = -\arg\psi$, and we assume $\psi \neq 0$ so that χ is well defined everywhere,

$$\psi \mapsto |\psi| \tag{1.21}$$

$$A \mapsto A - \nabla \arg\psi \ , \tag{1.22}$$

this transforms the condensate to be purely real. This is useful for numerics as it means there is one less field to solve for as, $\operatorname{Im}\psi = 0$. This can help decrease run times.
There are two types of gauge transformations:

- A global gauge transformation has a constant χ such that $\nabla\chi = 0$ and is given by,

$$\psi \mapsto e^{i\chi}\psi \tag{1.23}$$

$$A \mapsto A \ . \tag{1.24}$$

- A local gauge transformation has a spatially varying χ and is given by Equations 1.18 and 1.19.

The Ginzburg-Landau equations are derived by varying Equation 1.17 with respect to $\bar{\psi}$ and A and are given below,

$$\alpha\psi + \beta\psi|\psi|^2 - \frac{1}{2}D \cdot D\psi = 0 \tag{1.25}$$

$$\frac{i}{2}(\psi^* D\psi - \psi(D\psi)^*) - \nabla \times B = 0 \ . \tag{1.26}$$

We see that Equation 1.25 is simply Equation 1.16 where $\nabla \mapsto D$.

By recognising Equation 1.26 as Ampere's Law, $(\nabla \times B) = j_s$, we can define our supercurrent as,

$$j_s = \frac{i}{2}(\psi^* D\psi - \psi(D\psi)^*) \ , \tag{1.27}$$

for our Ginzburg-Landau free energy.

1.3.3 Linearisation of the Ginzburg-Landau Equations

If we consider solutions of Equations 1.25 and 1.26 for the positive half plane, $x \geq 0$, there are two fundamental length scales that govern their decay at long range, $x \to \infty$. The coherence, ξ_{GL}, and penetration, λ_{GL}, length scales describe the decay of the order parameter and magnetic field respectively. At long range, that is far away from any boundaries or defects, the order parameter is close to its vacuum value such that,

$$\hat{\psi} = |\psi| - u \ , \tag{1.28}$$

is a small quantity. We are interested in the spatial dependence of both ψ and B at long range, for $x \geq 0$, hence we require that $\psi \mapsto \psi(x)$ and $A \mapsto A(x)$. Furthermore, without loss of generality, we can fix our magnetic field to point in the $\hat{z}$ direction such that $B = B_z\hat{z} = \partial_x A_y \hat{z}$. This is achieved by setting $A_z = 0$. We will expand upon the choice of ansatz in Section 2.2.1, where we will show that setting $A_z = 0$ is a consistent choice for this isotropic superconductor. The length scales can be derived by linearising Equations 1.25 and 1.26, for the above conditions, giving,

$$\hat{\psi} - \frac{1}{4|\alpha|}\partial_x\partial_x\hat{\psi} = 0 \tag{1.29}$$

$$\frac{|\alpha|}{\beta}A_x = 0 \tag{1.30}$$

$$\frac{|\alpha|}{\beta}A_z = 0 \tag{1.31}$$

$$\frac{|\alpha|}{\beta}A_y - \partial_x B_z = 0 \ . \tag{1.32}$$

Equation 1.29 gives us a matter equation for the spatial variations of the order parameter. Equations 1.30 and 1.31 set the values of A_x and A_z required for $B = B_z\hat{z}$. Whilst Equation 1.32 can be rewritten as,

$$\frac{|\alpha|}{\beta}B_z - \partial_x^2 B_z = 0 \ , \tag{1.33}$$

by differentiating with respect to x. This is the London Equation, Equation 1.5 , written in terms of the Ginzburg-Landau parameters. Therefore, the coherence and penetration length scales in Ginzburg-Landau theory are,

$$\xi_{GL}^2 = \frac{1}{4|\alpha|} \tag{1.34}$$

$$\lambda_{GL}^2 = \frac{\beta}{|\alpha|} \ , \tag{1.35}$$

respectively and the behaviour of the fields at long range, is given by,

$$\hat{\psi} = \psi_0 e^{-\frac{x}{\xi_{GL}}} \tag{1.36}$$

$$B_z = B_0 e^{-\frac{x}{\lambda_{GL}}} \ , \tag{1.37}$$

where ψ_0 and B_0 are arbitrary constants to be determined by the boundary conditions. Note that we can now define long range, with respect to the length scales, as $\frac{x}{\xi_{GL}} >> 1$, $\frac{x}{\lambda_{GL}} >> 1$ for the condensate and magnetic field respectively.

1.3.4 Ginzburg Landau Parameter, κ

We define the Ginzburg-Landau parameter,

$$\kappa = \frac{\lambda_{GL}}{\xi_{GL}} = \sqrt{\frac{\beta}{4}} \ , \tag{1.38}$$

the value of which can be used to determine the type of superconductor from the Ginzburg-Landau parameters, α and β. This ability to predict the two types of superconductivity is one of the most significant achievements of Ginzburg-Landau theory.
To make sense of this parameter, first consider the normalised potential for $T < T_C$,

$$\hat{F_p} = F_p - F_p(u) = \frac{\alpha^2}{2\beta} - |\alpha||\psi|^2 + \frac{\beta}{2}|\psi|^4 \ , \tag{1.39}$$

which can be rewritten as,

$$\hat{F_p} = \frac{\beta}{2}\left(u^2 - |\psi|^2\right)^2 \tag{1.40}$$

$$= 2\kappa^2\left(u^2 - |\psi|^2\right)^2 \ . \tag{1.41}$$

From [21] (p.197), we see that the critical coupling occurs when $4\kappa^2 = \frac{1}{4}$ which gives the critical value of $\kappa = \frac{1}{4}$. Note that we can rewrite the potential as,

$$\hat{F_p} = \frac{\lambda}{8}\left(u^2 - |\psi|^2\right)^2 \ , \tag{1.42}$$

where, $\lambda = 16\kappa^2 = 4\beta$, and a value of $\lambda = 1$ is equivalent to $\kappa = \frac{1}{4}$ so the critical coupling now occurs at unity. We will now use λ going forwards.
It was recognised at the time that the critical value marked the boundary between the two types of superconductivity.

- If $0 < \lambda < 1$ then our superconductor is type I which means it only forms the homogenous superconducting state or the normal state, see Figure 1.2a.
- If $\lambda > 1$ then our superconductor is type II can form a Abrikosov vortex lattice state, see Section 1.6 for more details, in addition to the homogenous superconducting state or the normal state. See Figure 1.2b.

1.3.5 Magnetising a Superconductor

Magnetising refers to applying an external magnetic field, H, to a sample. Previously we have considered the energy of our superconductor, Equation 1.17, in the absence of an applied external magnetic field. We have seen from Section 1.1 that the properties of a superconductor are sensitive to both temperature, T, as well as H. We saw in Section 1.3 that the temperature dependence can be introduced through the sign of the potential parameter,

$$\alpha = \alpha_0 \left(T - T_C\right) \ . \tag{1.43}$$

We now look to introduce H dependence. Applying an external magnetic field to a superconductor will change its energy and so we need a new formulation of the energy that includes the energy due to H. This is known as the Gibbs free energy,

$$G = \int_{\mathbb{R}^3} \left(\frac{1}{2}|D\psi|^2 + \frac{(B-H)^2}{2} + F_p \right) d^3x \tag{1.44}$$

$$G = F - \int_{\mathbb{R}^3} B \cdot H \ d^3x + \int_{\mathbb{R}^3} \frac{H^2}{2} \ d^3x \ , \tag{1.45}$$

note that when $H = 0$ then $G = F$. If we consider applying a constant, $H = H_0\hat{z}$, external magnetic field in the $\hat{z}$ direction then the superconducting state ($\psi = u, \ B = 0$) has a Gibbs free energy per unit volume, $\frac{G}{\mathbb{V}} = \frac{H_0^2}{2} + F_p(u)$, where $\mathbb{V} = \int_{\mathbb{R}^3} \ d^3x$. The normal state ($\psi = 0, \ B = H$) has $\frac{G}{\mathbb{V}} = 0$ hence it is normalised with respect to the normal state. Alternatively we can normalise with respect to the superconducting state,

$$\hat{G} = (F - F_p(u)) - \int_{\mathbb{R}^3} B \cdot H \ d^3x \ , \tag{1.46}$$

which can be more useful when we want to consider the transition from vortex state to normal state in a type II superconductor.

As a further example of the uses of Ginzburg-Landau theory: we can use the Gibbs free energy to calculate the thermodynamic critical field, H_C, in terms of the Ginzburg-Landau parameters. Consider Equation 1.45 with a type I superconductor in the homogenous superconducting state, $|\psi| = u, B = 0$. Apply an external field $H = H_0\hat{z}$ and when the Gibbs free energy for the superconducting state, G_s, is equal to the Gibbs free energy of the normal state, $G_n = 0$, then $H_0 = H_C$.

$$G_s = G_n \tag{1.47}$$

$$\frac{H_C^2}{2} + F_p(u) = 0 \tag{1.48}$$

$$H_C = \sqrt{\frac{\alpha^2}{\beta}} \tag{1.49}$$

$$= \frac{\sqrt{\lambda}}{2} u^2 \ . \tag{1.50}$$

1.4 Meissner State

In Section 1.3 we found two length scales that describe the decay of the magnetic field and condensate in the linearised theory. However, this was only valid at long range, $x \to \infty$,

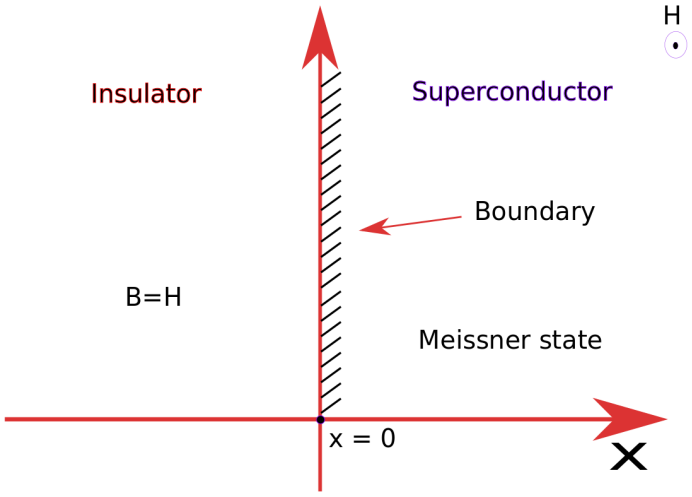

Figure 1.6: *Diagram of the Meissner State. For $x < 0$ we have an electrical insulator and for $x > 0$ we have a superconductor that for $x >> 0$ it is in the homogenous superconducting state and thus exhibits the Meissner effect. The Meissner state is the region $x \geq 0$, we note that $H = H_0\hat{z}$ in the insulator.*

so using the full, nonlinear theory we can accurately determine the behaviour of the fields near the boundary, $x = 0$. Consider Figure 1.6, in the region $x \geq 0$ we have an infinite superconductor and for $x < 0$ we have an insulator, $\hat{x}$ is the direction of the inward pointing normal of the superconductor. We apply a constant external magnetic field, $H = H_0\hat{z}$, in the $\hat{z}$ direction. The superconductor is in the Meissner state which, as $x \to \infty$, approaches the homogenous superconducting state. We note that for $H_0 > H_C$ the superconductor moves to the normal state where the Meissner effect does not occur.

We consider the ansatz,

$$\psi \mapsto \psi(x) \tag{1.51}$$

$$(A_x, A_y, A_z) \mapsto (0, A_y(x), 0) \ , \tag{1.52}$$

for the region $x \geq 0$. This is equivalent to assuming translational invariance in the $\hat{y}$ and $\hat{z}$ directions which means we dimensionally reduce the three-dimensional Ginzburg-Landau free energy to one dimension. The ansatz sets $B = B_z\hat{z}$ and for isotropic superconductors the magnetic field will point only in the direction of $H = H_0\hat{z}$ hence this ansatz is valid. We now consider the associated Gibbs free energy per unit area (normalised with respect to the homogenous superconducting state),

$$\hat{G} = \int_{\mathbb{R}} \hat{g} \ dx = \int_{\mathbb{R}} \left(\frac{1}{2} \left(|\psi'|^2 + |A_y\psi|^2 \right) + \frac{((A_y)')^2}{2} + \frac{\lambda}{8}(u^2 - |\psi|^2)^2 \right) dx - H_0 \int_{\mathbb{R}} (A_y)' dx \ , \tag{1.53}$$

where, $\psi' = \frac{d\psi}{dx}$ and $(A_y)' = \frac{dA_y}{dx}$.
Expanding on Section 1.3.1, we write $\phi_a = (\psi_R, \psi_I, A_y)$ then we consider the variation of the Gibbs free energy,

$$\delta\hat{G} = \int_{\mathbb{R}} \left(\frac{\partial \hat{g}}{\partial \phi_a} - \frac{d}{dx}\frac{\partial \hat{g}}{\partial (\phi_a)'} \right) \delta\phi_a + \int_{\partial C} \frac{\partial \hat{g}}{\partial (\phi_a)'} \delta\phi_a dx \ , \tag{1.54}$$

where $\delta\phi_a$ is the variation of ϕ_a, where for Equation 1.11 the variation would be $\epsilon(\eta_R + i\eta_I)$, and we denote ∂C as the boundary of our domain. The boundary term must vanish in order for $\delta\hat{G} = 0$ this can happen in two ways:

- Setting $\delta\phi_a|_{\partial C} = 0$ fixes the value of ϕ_a on the boundary. This is called a fixed boundary condition.
- Setting $\left.\frac{\partial \hat{g}}{\partial(\phi_a)'}\right|_{\partial C} = 0$ allows ϕ_a to vary on the boundary. This is called a natural boundary condition.

For the Meissner state we use natural boundary conditions at $x = 0$, this allows the values of the fields to vary and they are as follows,

$$(\psi_R)'|_{x=0} = 0 \tag{1.55}$$
$$(\psi_I)'|_{x=0} = 0 \tag{1.56}$$
$$(A_y)'|_{x=0} = H_0 \ , \tag{1.57}$$

where we note that $(A_y)' = B_z$. The right hand boundary, $x \to \infty$, is far away from the $x = 0$ boundary so the superconductor is in the homogenous superconducting state thus the fields can be fixed to their vacuum values,

$$\lim_{x\to\infty} \psi = ue^{i\chi} \tag{1.58}$$
$$\lim_{x\to\infty} (A_y)' = 0 \ . \tag{1.59}$$

For simplicity we choose $\chi = 0$.
We seek field configurations, with the above boundary conditions, that are locally minimising solutions to Equation 1.53. We start with an initial configuration for the fields, ψ, A_y, satisfying the above boundary conditions and flow towards a local minimum use a gradient descent algorithm. Figure 1.7 shows such a solution. We see that $B_z = H_0$ at $x = 0$ and then decays to $B = 0$ as $x \to \infty$ whilst $|\psi| \neq u$ on the boundary and then approaches u as $x \to \infty$. This shows us that the superconductor will exhibit the Meissner effect away from the boundary at $x = 0$.

1.5 Topological Solitons

In this section we define topological solitons, which are studied throughout this thesis, and then demonstrate some general behaviour using simple soliton solutions. Topological solitons are solutions, with a spatially localised energy, to a set of partial differential equations. A topological soliton is stable due to the topology of the system and cannot be removed via continuous deformations of the solution. For topological solitons in superconductors we consider solutions to the Ginzburg-Landau equations.
As an example we consider the one-dimensional static Sine-Gordon model [22] with energy,

$$E = \int_{-\infty}^{\infty} \left(\frac{1}{2} \left(\frac{d\phi}{dx} \right)^2 + 2 \sin \left(\frac{\phi}{2} \right)^2 \right) \ dx \ , \tag{1.60}$$

where ϕ is a real scalar field on $\mathbb{R}$. The vacua of the potential, $F_p = 2 \sin \left(\frac{\phi}{2} \right)^2$, are given by,

$$\phi^{vac} = 2\pi N \ , \tag{1.61}$$

with, $N \in \mathbb{Z}$. The value of N can be fixed by specifying the value of ϕ on the left and right boundaries, such that

$$N = \frac{\phi(\infty) - \phi(-\infty)}{2\pi} \ , \tag{1.62}$$

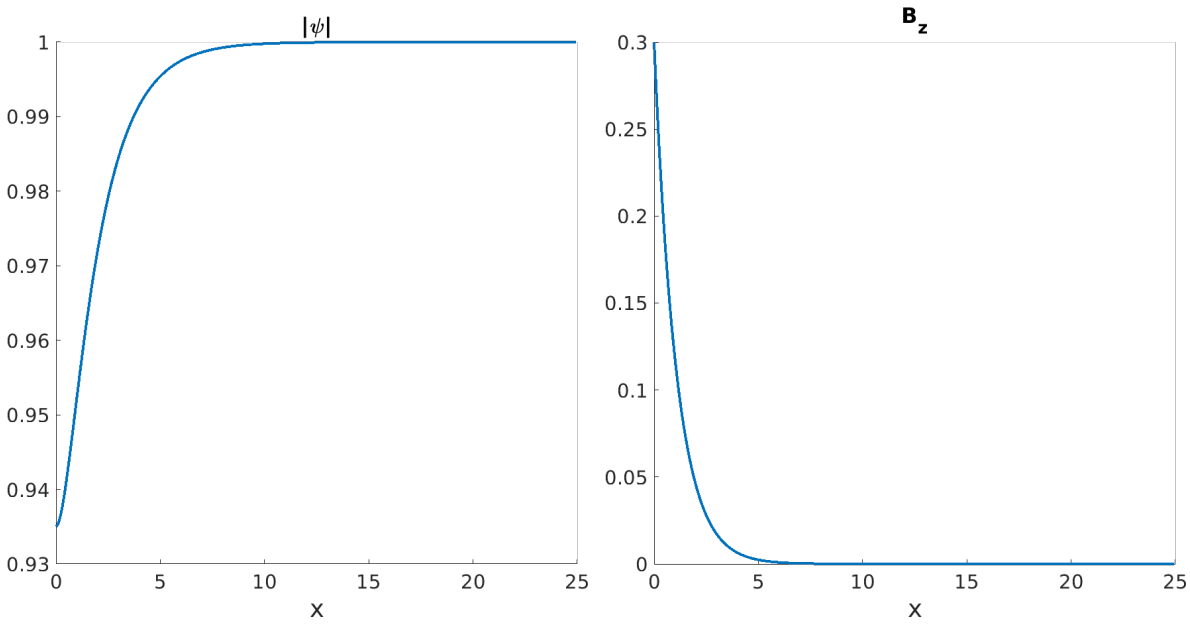

Figure 1.7: *Meissner state solution for* $\lambda = 0.75, u = 1$ *and* $H_0 = 0.3$*, note that* $\lambda < 1$ *and* $H_0 < H_C$ *where* $H_C = \frac{\sqrt{3}}{4}$*, so this type I superconductor will exhibit the Meissner state for our value of* H_0*. We see that the superconductor approaches the homogenous superconducting state as* $x \to \infty$*,* $B_z \to 0$ *and* $\psi \to u$*.*

where $\phi(-\infty)$ and $\phi(\infty)$ are the field values on the left and right boundaries of our domain respectively.
If we consider the variation of E with respect to ϕ, we arrive at the one-dimensional static Sine-Gordon equation,

$$-\frac{d^2\phi}{dx^2} + \sin(\phi) = 0 \ . \tag{1.63}$$

The Sine-Gordon model can be solved analytically, with the boundary conditions,

$$\phi(-\infty) = 0 \tag{1.64}$$
$$\phi(\infty) = 2\pi N \ . \tag{1.65}$$

We first rewrite Equation 1.60 by completing the square, which we relabel as E_N,

$$E_N = \int_{-\infty}^{\infty} \frac{1}{2}\left(\frac{d\phi}{dx} - 2\sin\left(\frac{\phi}{2}\right)\right)^2 dx + 2\int_{-\infty}^{\infty} \frac{d\phi}{dx}\sin\left(\frac{\phi}{2}\right) dx \tag{1.66}$$
$$E_N = \int_{-\infty}^{\infty} \frac{1}{2}\left(\frac{d\phi}{dx} - 2\sin\left(\frac{\phi}{2}\right)\right)^2 dx + 2\int_{0}^{2\pi N} \left|\sin\left(\frac{\phi}{2}\right)\right| d\phi \tag{1.67}$$
$$E_N = \int_{-\infty}^{\infty} \frac{1}{2}\left(\frac{d\phi}{dx} - 2\sin\left(\frac{\phi}{2}\right)\right)^2 dx + 8|N| \ , \tag{1.68}$$

where the last line uses the fact that the integrand is periodic on 2π which gives us a lower bound for the energy, $E_N \geq 8|N|$. The globally minimum solution, for the given boundary conditions, has $E_N = 8|N|$. This occurs when the integrand vanishes, giving us a first order equation,

$$\left(\frac{d\phi}{dx} - 2\sin\left(\frac{\phi}{2}\right)\right) = 0 \ . \tag{1.69}$$

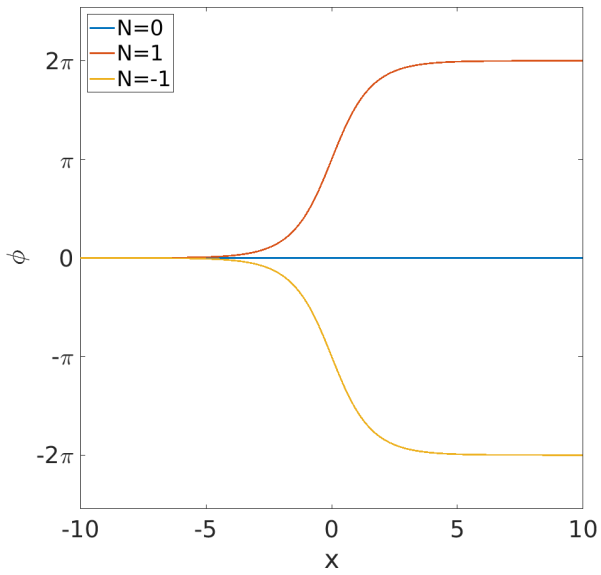

Figure 1.8: *Static kink and anti-kink solutions of the Sine-Gordon model in one dimension, we note that there are no $|N|>1$ static solutions.*
$\phi = 4\arctan\left(e^{x-x_0}\right)$ *where* $x_0 = 0$.

This equation can be solved to produce an exact solution,

$$\phi = 4\arctan\left(e^{x-x_0}\right) , \tag{1.70}$$

known as a kink, were x_0 is a free parameter that translates the kink solution. We note that there are no static $|N|>1$ solutions and we call the $N=-1$ solution an anti-kink. The possible static solutions can then be plotted as seen in Figure 1.8.

1.6 Vortices

A vortex in a superconductor is a solution to the Ginzburg-Landau equations where at the centre, or zero of the vortex, $\psi = 0$ and the magnetic field fully penetrates the superconductor. Both the condensate, ψ, and the vector potential, A, wind around the centre of the vortex. Vortices are two-dimensional topological solitons hence we consider the below two-dimensional Ginzburg-Landau free energy (per unit length),

$$\hat{F} = \int_{\mathbb{R}^2} \left(\frac{1}{2}|D_x\psi|^2 + \frac{1}{2}|D_y\psi|^2 + \frac{(\partial_x A_y - \partial_y A_x)^2}{2} + \frac{\lambda}{8}(u^2 - |\psi|^2)^2 \right) d^2x , \tag{1.71}$$

which comes from applying the ansatz,

$$\psi \mapsto \psi(x,y) \tag{1.72}$$
$$A \mapsto (A_x(x,y), A_y(x,y), 0) , \tag{1.73}$$

to Equation 1.17. The potential is normalised with respect to the superconducting state, $|\psi| = u$, and it is of the same form as Equation 1.17 with $\alpha = \frac{u^2\lambda}{4}, \beta = \frac{\lambda}{4}$, [21]. Note that $D_x = \partial_x - iA_x$, $D_y = \partial_y - iA_y$. For this model λ determines the type, with $\lambda > 1$ giving a type II superconductor. Finally, our choice of ansatz fixes B to be perpendicular to the xy plane, $B = (0, 0, B_z)$.
Vortices are rotationally symmetric about their centre, so the problem simplifies if we consider

the free energy in polar coordinates, $x = r\cos\theta, y = r\sin\theta$,

$$\hat{F} = \int_0^{\infty}\int_0^{2\pi}\left(\frac{1}{2}|D_r\psi|^2+\frac{1}{2r^2}|D_\theta\psi|^2+\frac{(\partial_r A_\theta - \partial_\theta A_r)^2}{2r^2} + \frac{\lambda}{8}(u^2-|\psi|^2)^2\right) r dr d\theta \ , \tag{1.74}$$

with $A_r = A_x\cos\theta + A_y\sin\theta$, $A_\theta = r\left(-A_x\sin\theta + A_y\cos\theta\right)$ and $D_r = \partial_r - iA_r$, $D_\theta = \partial_\theta - iA_\theta$. To proceed with our analysis, we first choose the gauge transformation that sets $A_r = 0$. For polar coordinates a gauge transformation is given by,

$$\psi \mapsto \psi e^{i\chi(r,\theta)} \tag{1.75}$$

$$A_r \mapsto A_r + \partial_r\chi(r,\theta) \tag{1.76}$$

$$A_\theta \mapsto A_\theta + \frac{1}{r}\partial_\theta\chi(r,\theta) \ , \tag{1.77}$$

where we have transformed Equations 1.18 and 1.19 which are written in the crystalline or Cartesian coordinates. If we choose

$$\chi(r,\theta) = -\int_0^r A_r(r',\theta)\ dr' \ , \tag{1.78}$$

then $A_r \to 0$, note that χ is smooth if A_r is a smooth function. The free energy then reduces to,

$$\hat{F} = \int_0^{\infty}\int_0^{2\pi}\left(\frac{1}{2}|\partial_r\psi|^2+\frac{1}{2r^2}|D_\theta\psi|^2+\frac{(\partial_r A_\theta)^2}{2r^2} + \frac{\lambda}{8}(u^2-|\psi|^2)^2\right) r dr d\theta \ . \tag{1.79}$$

We will now use ψ^∞ and A_θ^∞ to denote the value of ψ and A_θ on the boundary of our two-dimensional domain. We seek to find the boundary conditions by considering the limit $r \to \infty$. In order for the energy to be finite, on this boundary, we require $|\psi| \to u$ and $\partial_r\psi \to 0$. We note that $\psi^\infty = ue^{i\chi^\infty(\theta)}$ is the set of field values that satisfies this such that,

$$\psi^\infty : S_1^\infty \to S^1 \tag{1.80}$$

where S_1^∞ is the unit circle at infinity and the map is characterised by an integer winding number, N. This is because the first homotopy group of circles, $\pi_1(S^1)$, is the integers.
We also require that $\partial_r A_\theta \to 0$ and $D_\theta\psi \to 0$. This implies that A_θ^∞ becomes constant with respect to r which we denote $A_\theta^\infty(\theta)$ and that $A_\theta^\infty(\theta) = \partial_\theta\chi^\infty(\theta)$.
We now define a vortex as a field solution that (at least) locally minimises Equation 1.79 with the general boundary conditions,

$$\psi^\infty = ue^{i\chi^\infty} \tag{1.81}$$

$$A_\theta^\infty(\theta) = \partial_\theta\chi^\infty(\theta) \tag{1.82}$$

$$A_r^\infty = 0 \ . \tag{1.83}$$

The centre of the vortex is the point where $\psi = 0$, and this is the point around which the fields wind where the winding number is determined by the map in Equation 1.80.
By applying a gradient descent algorithm to initial configurations of the fields with the below fixed boundary conditions,

$$\psi^\infty = ue^{iN\theta} \tag{1.84}$$

$$A_\theta^\infty(\theta) = N \tag{1.85}$$

$$A_r^\infty = 0 \ , \tag{1.86}$$

we can generate vortex solutions to Equation 1.79. Figure 1.9a plots the dependence of $|\psi|$ and $B_z = \partial_r A_\theta$ on the radial coordinate, r. As expected we see both quantities approach their vacuum values as r increases and $|\psi|$ vanishes at the centre of the vortex, $r = 0$. Figure 1.9b shows the same data but as heat plots which are useful when depicting solutions that are not rotationally symmetric. These heat plots are used extensively in Chapters 4 and 5.

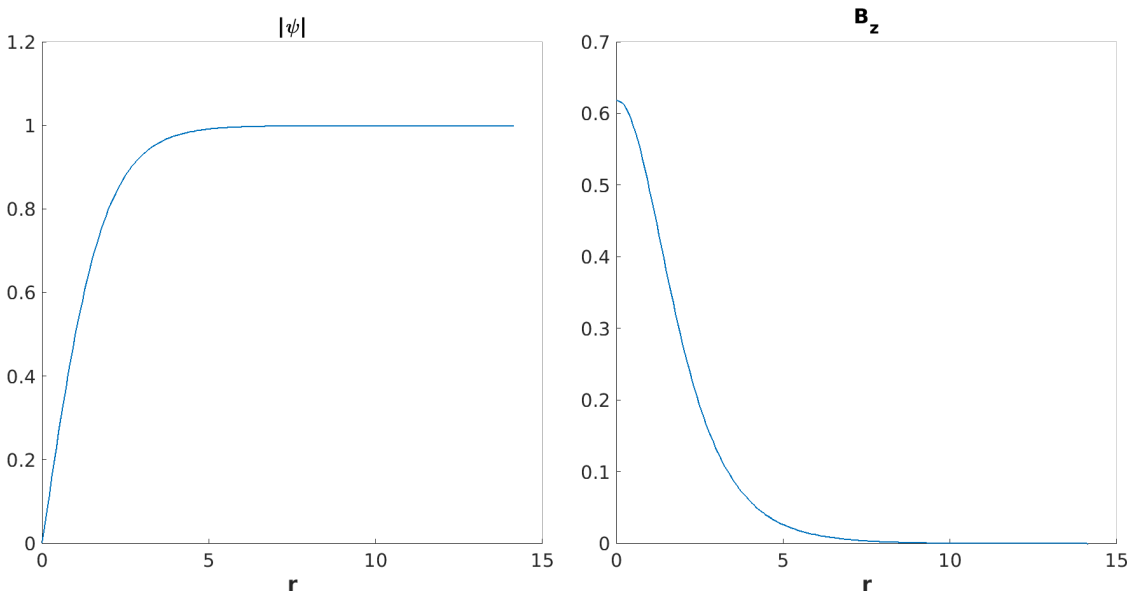

(a) *Plots of the modulus of the order parameter, $|\psi|$, and the z component of the magnetic field, B_z as functions of the radius, r.*

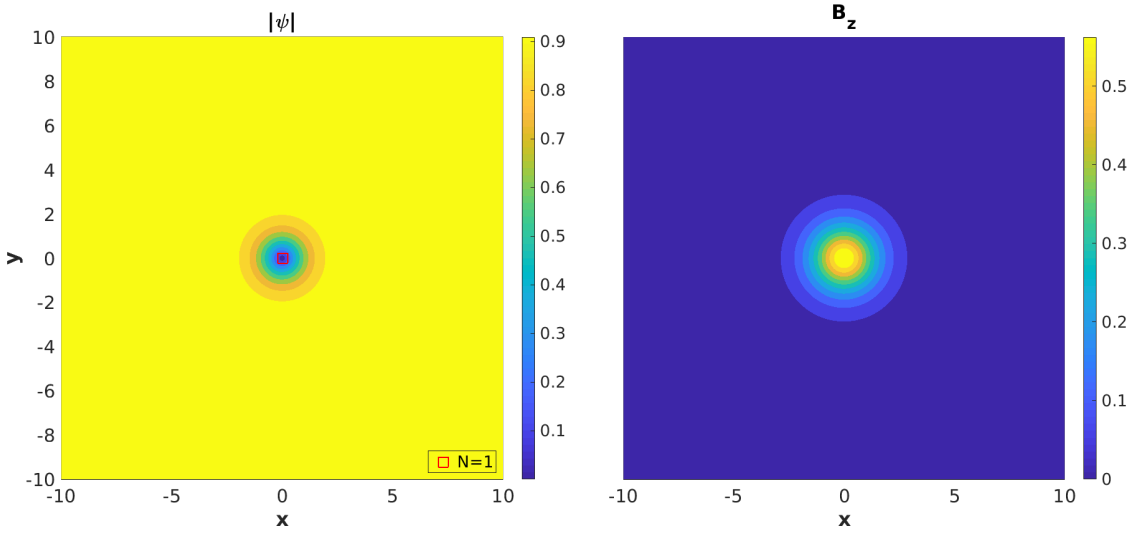

(b) *Heat plots for $|\psi|$ and B_z . The □ marks the centre of the vortex with the winding number, N.*

Figure 1.9: *Plots of an $N = 1$ vortex solution in an isotropic superconductor. As expected we see both quantities approach their vacuum values as r increases and $|\psi|$ vanishes at the centre of the vortex, $r = 0$.*
Parameters: $\lambda = 2, u = 1, N = 1$.

1.6.1 Topological Charge

The winding number, N, of the map ψ^∞ is given by,

$$N = \frac{1}{2\pi}\int_0^{2\pi} \partial_\theta \chi^\infty d\theta = \frac{1}{2\pi}\left(\chi^\infty(2\pi) - \chi^\infty(0)\right) \tag{1.87}$$

and is a topological invariant. We see that like the Sine-Gordon kinks, see Section 1.5, the choice of boundary conditions determines the topological degree, N.
Making use of the fact that, for a finite energy solution, $A_\theta^\infty(\theta) = \partial_\theta \chi^\infty(\theta)$ we can write N in terms of the magnetic field,

$$N = \frac{1}{2\pi}\int_0^{2\pi} A_\theta^\infty d\theta \tag{1.88}$$

$$= \frac{1}{2\pi}\int_{\mathbb{R}^2} B\ d^2x\ , \tag{1.89}$$

where Stokes' theorem has been used to write the integral in terms of the magnetic field. We see that the total magnetic flux through the system, $\Phi = \int_{\mathbb{R}^2} B\ d^2x$, is quantised in units of 2π.
For $|N|> 1$, there can exist vortex solutions which have multiple points on the plane where $\psi = 0$, that is multiple vortices. If we label each vortex as $a, b, c, ...$ then each vortex will have an associated winding number which we label $n_a, n_b, n_c, ...$. The topological degree,

$$N = n_a + n_b + n_c + ...\ , \tag{1.90}$$

is the sum of the winding numbers of each individual vortex. In other words, N counts the number of vortices, up to multiplicity, in the system. This is especially useful for unconventional superconductors that form vortex solutions with multiple zeros and is explored in Chapters 4 and 5.

1.6.2 Vortex Lattices

Consider a large type II superconductor with an applied magnetic field, $H_{C1} < H_0 < H_{C2}$ which ensures that the vortex state can occur. The vortices form a repeating pattern known as an Abrikosov lattice. The smallest element of that pattern is known as the unit cell. The shape of the unit cell is such that it minimises its Gibbs free energy per unit area. Figure 1.10 gives the Abrikosov lattice for a given N, λ, u and external magnetic field, $H = H_0\hat{z}$. We see that the unit cell is hexagonal, that is the smallest internal angle, $\alpha = \frac{\pi}{3}$, and the sides are of the same length. As expected the point where $|\psi|$ vanishes in a given unit cell corresponds to the maximum value of the magnetic field.

1.7 Multicomponent Ginzburg-Landau Theory

The first extension of Ginzburg-Landau theory is increasing the number of condensates. This can be required when the phenomenological properties of a superconductor cannot be fully described by a single condensate. A multicomponent superconductor would be among the simplest of unconventional superconductors. Focussing on a two component superconductor, the free energy is given by,

$$F = \int_{\mathbb{R}^3} f\ d^3x = \int_{\mathbb{R}^3} \left(\sum_{\alpha=1}^{2} |(D\psi_\alpha)|^2 + \frac{B^2}{2} + \sum_{\alpha=1}^{2} \left(\alpha_\alpha |\psi_\alpha|^2 + \frac{\beta_\alpha}{2}|\psi_\alpha|^4 \right) \right) d^3x\ , \tag{1.91}$$

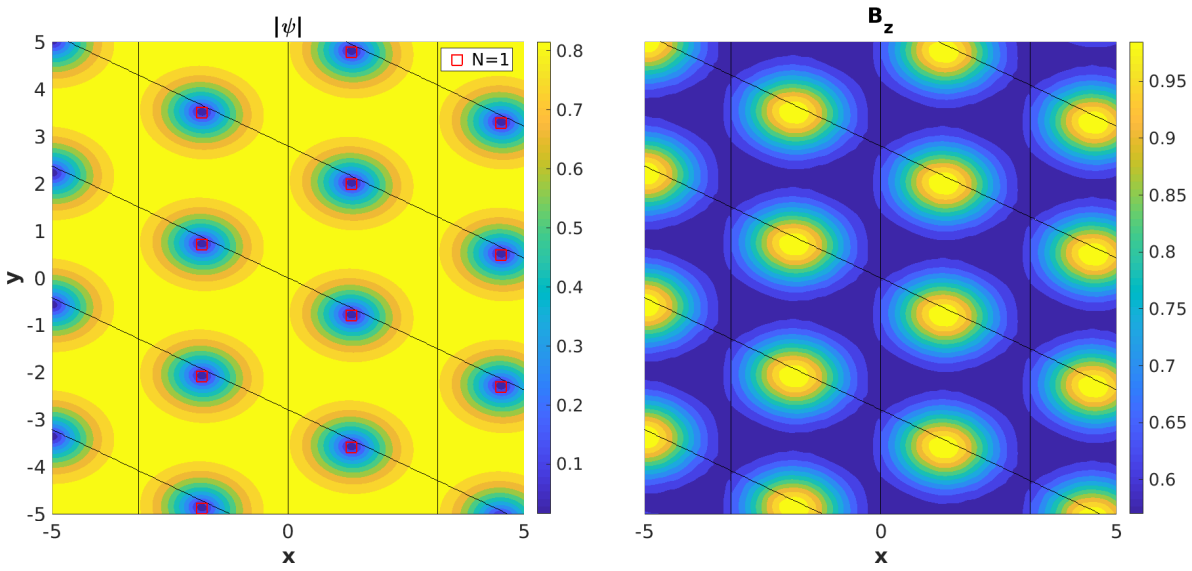

Figure 1.10: *Lattice plots for an $N = 1$ vortex in an isotropic superconductor which shows the Abrikosov lattice with hexagonal unit cells, marked by the black lines. Each vortex is rotationally symmetric in the immediate area of the vortex centre, as expected, and the peaks of B_z correspond to $\psi = 0$, the centre of the vortex. Here the winding number for each unit cell, N, is marked by* □.
Parameters: $\lambda = 4, u = 1, N = 1, H_0 = 1$, where $H = H_0\hat{z}$.

which closely matches the single component free energy in Equation 1.17. We need to introduce two extra parameters for the potential,

$$F_p(\psi_1, \psi_2) = \sum_{\alpha=1}^{2} \left(\alpha_\alpha |\psi|^2 + \frac{\beta_\alpha}{2} |\psi|^4 \right) \ , \tag{1.92}$$

which has general vacuum solutions,

$$\psi_\alpha = u_\alpha e^{i\chi_\alpha} \tag{1.93}$$

$$A = 0 \ , \tag{1.94}$$

with $u_\alpha = \sqrt{\frac{|\alpha_\alpha|}{\beta_\alpha}}$ and $\chi_1, \chi_2 \in [0, 2\pi]$. We note that the vacuum value for each condensate has an independent $U(1)$ choice of values which is parametrised by χ_α.
Then by varying Equation 1.91 with respect to the real fields the multicomponent Ginzburg-Landau equations are given by;

$$\frac{\partial F_p}{\partial (\psi_\alpha)^*} - \frac{1}{2} D \cdot D\psi_\alpha = 0 \tag{1.95}$$

$$\frac{i}{2} \sum_{\alpha=1}^{2} (\psi_\alpha^* D\psi_\alpha - \psi_\alpha (D\psi_\alpha)^*) - \nabla \times B = 0 \ , \tag{1.96}$$

where we have an extra equation of motion for each new condensate. We also have an updated definition for the supercurrent of a multicomponent superconductor,

$$j_s = \frac{i}{2} \sum_{\alpha=1}^{2} (\psi_\alpha^* D\psi_\alpha - \psi_\alpha (D\psi_\alpha)^*) \ . \tag{1.97}$$

1.7.1 Multicomponent Length Scales

Following on from Section 1.3.3 we linearise Equations 1.95 and 1.96 in the small quantities,

$$\hat{\psi}_1 = |\psi_1| - u_1 \tag{1.98}$$

$$\hat{\psi}_2 = |\psi_2| - u_2 \ , \tag{1.99}$$

where, again, we consider the positive half plane, $x > 0$, which yields three length scales,

$$\xi^2_{mcGL1} = \frac{1}{4\alpha_1} \tag{1.100}$$

$$\xi^2_{mcGL2} = \frac{1}{4\alpha_2} \tag{1.101}$$

$$\frac{1}{\lambda^2_{mcGL}} = \left(\frac{|\alpha_1|}{\beta_1} + \frac{|\alpha_2|}{\beta_2} \right) \ , \tag{1.102}$$

which give the behaviour of the fields at long range as,

$$\hat{\psi}_1 = \psi_{1,0} e^{-\frac{x}{\xi_{mcGL1}}} \tag{1.103}$$

$$\hat{\psi}_2 = \psi_{2,0} e^{-\frac{x}{\xi_{mcGL2}}} \tag{1.104}$$

$$B_z = B_0 e^{-\frac{x}{\lambda_{mcGL}}} \ . \tag{1.105}$$

$\psi_{1,0}, \psi_{2,0}$ and B_0 are constants to be determined by the boundary conditions.
Clearly, there are now two Ginzburg-Landau parameters,

$$\kappa_1 = \frac{\lambda_{mcGL}}{\xi_{mcGL1}} \tag{1.106}$$

$$\kappa_2 = \frac{\lambda_{mcGL}}{\xi_{mcGL2}} \ , \tag{1.107}$$

thus determining the type of superconductor is no longer as simple as reading off the value of the single Ginzburg-Landau parameter, κ. We remind the reader that $\kappa = \frac{1}{4}$ is the critical value that determines the type of superconductor. If both κ_1 and κ_2 are above or below $\frac{1}{4}$ then determining the type of superconductivity is trivial. However, if, for example, $\kappa_1 > \frac{1}{4}$ and $\kappa_2 < \frac{1}{4}$ then the type of superconductivity is not obvious. This is known as type 1.5 superconductivity and arises in unconventional superconductors, [23], [24].

1.7.2 Broken Time Reversal Symmetry

Here we explore how changing the potential in Equation 1.91 can give rise to novel vacuum states and new solutions such as domain walls. We begin by defining time reversal symmetry as the following transformation,

$$\psi_\alpha \mapsto \bar{\psi}_\alpha \tag{1.108}$$

$$A_i \mapsto -A_i \ . \tag{1.109}$$

A solution has time reversal symmetry if it is invariant under this transformation. If we have two condensates $\psi_1 = \rho_1 e^{i\theta_1}$ and $\psi_2 = \rho_2 e^{i\theta_2}$, we consider the following gauge invariant quantities,

$$\rho_1 \tag{1.110}$$

$$\rho_2 \tag{1.111}$$

$$\theta_{12} := \theta_1 - \theta_2 \ , \tag{1.112}$$

where, $\theta_{12} \in [-\pi, \pi]$, is the phase difference between the two condensates. As we only consider even powers of $|\psi_\alpha|$ up to quartic order the way to add complexity to the vacuum solutions is by adding terms that fix the phase difference of the vacuum, θ_{12}, to a specific value or by adding terms of the form $\rho_1^2\rho_2^2$. Considering the phase difference we consider two possible terms that could be added to the potential,

$$\frac{\eta_{12}^J}{2}\left(\psi_1\psi_2^* + \psi_1\psi_2^*\right) \equiv \eta_{12}^J\rho_1\rho_2\cos(\theta_{12}) \tag{1.113}$$

$$\frac{\eta_{12}}{2}\left((\psi_1)^2(\psi_2^*)^2 + (\psi_1)^2(\psi_2^*)^2\right) \equiv \eta_{12}\rho_1^2\rho_2^2\cos(2\theta_{12})\ . \tag{1.114}$$

The linear term in both condensates, Equation 1.113, is known as a Josephson term. If $\eta_{12}^J > 0$, then it is minimised by $\theta_{12} = \pm\pi$ which is known as phase anti-locking and if $\eta_{12}^J < 0$ then $\theta_{12} = 0$ minimises the Josephson term which is known as phase locking.
The quadratic term in both condensates, Equation 1.114, is known as a broken time reversal symmetry term (BTRS) and if $\eta_{12} > 0$ has two vacua with $\theta_{12} = \pm\frac{\pi}{2}$ but if $\eta_{12} < 0$ then phase locking, $\theta_{12} = 0$, minimises the BTRS term.
Starting with,

$$V(\rho_1, \rho_2) = \sum_{j=1}^{2}\left(\alpha_j\rho_j^2 + \frac{\beta_j}{2}\rho_j^4 + \gamma_{12}\rho_1^2\rho_2^2\right)\ , \tag{1.115}$$

which already introduces a coupling between the condensates for $\gamma_{12} \neq 0$. We then define two potentials,

$$F_p^J = V(\rho_1, \rho_2) + \eta_{12}^J\rho_1\rho_2\cos(\theta_{12}) \tag{1.116}$$

$$F_p^B = V(\rho_1, \rho_2) + \eta_{12}\rho_1^2\rho_2^2\cos(2\theta_{12})\ , \tag{1.117}$$

with $\eta_{12}^J > 0$ and $\eta_{12} > 0$, and we require that each $\beta_\alpha > \eta_{12}^J - \gamma_{12}$ or $\beta_\alpha > \eta_{12} - \gamma_{12}$ [25]. This is so that the vacuum values of ρ_α are positive. The vacuum for F_p^J is,

$$(\rho_1, \rho_2, \theta_{12}) = \left(u_1^J, u_2^J, 0\right), \tag{1.118}$$

where $u_\alpha^J = \sqrt{\frac{\alpha_\beta d^J - \alpha_\alpha\beta_\beta}{(\beta_\alpha\beta_\beta - (d^J)^2)}}$ with $\alpha \neq \beta$ and $d^J = (\gamma_{12} - \eta_{12}^J)$.
The vacua for F_p^B are,

$$(\rho_1, \rho_2, \theta_{12}) = \left(u_1^B, u_2^B, \pm\frac{\pi}{2}\right), \tag{1.119}$$

where $u_\alpha^B = \sqrt{\frac{\alpha_\beta d^B - \alpha_\alpha\beta_\beta}{(\beta_\alpha\beta_\beta - (d^B)^2)}}$ with $\alpha \neq \beta$ and $d^B = (\gamma_{12} - \eta_{12})$. Critically, for these parameter choices, we see that the BTRS potential, F_p^B, has two gauge inequivalent vacuum states but the Josephson potential, F_p^J, has only one vacuum state.

If we consider the fields, where we perform a gauge transformation so that ψ_2 is purely real, then we have,

$$(\psi_1, \psi_2)^J = \left(u_1 e^{i\pi}, u_2\right) \tag{1.120}$$

$$(\psi_1, \psi_2)^{B1} = \left(u_1 e^{-i\frac{\pi}{2}}, u_2\right) \tag{1.121}$$

$$(\psi_1, \psi_2)^{B2} = \left(u_1 e^{+i\frac{\pi}{2}}, u_2\right)\ . \tag{1.122}$$

We can now see that $(\psi_1, \psi_2)^J = ((\psi_1, \psi_2)^J)^*$ thus the vacuum for the Josephson term potential is invariant under conjugation or that it does not break time reversal symmetry.
However, $(\psi_1, \psi_2)^{B1} \neq ((\psi_1, \psi_2)^{B1})^*$ which shows us how the vacua for the BTRS term breaks time reversal symmetry.

1.8 Anisotropic Multicomponent Ginzburg-Landau Theory

We now seek to introduce anisotropy to the Ginzburg-Landau theory which will allow us to model more unconventional types of superconductivity as well as describe new phenomena. Anisotropic superconductors can now be studied via the introduction of anisotropy matrices, $Q^{\alpha\beta}$, which are a useful way of encoding the anisotropy of the system. Now that we are dealing with anisotropy the choice of basis matters. To highlight this we relabel our coordinates from the crystalline (x, y, z) to (x_1, x_2, x_3) which is for an arbitrary choice of orthonormal basis not necessarily aligned with any of the crystalline axes. Each direction for the crystalline basis denotes a symmetry axis of the superconductor. The two component free energy is given by,

$$F = \int_{\mathbb{R}^3} \left(\frac{1}{2} Q_{ij}^{\alpha\beta} (D_i \psi_\alpha)^* (D_j \psi_\beta) + \frac{B^2}{2} + F_p(\rho_1, \rho_2, \theta_{12}) \right) \, dx_1 dx_2 dx_3 \ , \tag{1.123}$$

with $D_i = \partial_i - iA_i$, $i, j \in \{1, 2, 3\}$, $\alpha, \beta \in \{1, 2\}$ and there is an implied summation over all repeated indices. We note that $Q_{ij}^{\alpha\beta} \equiv Q_{ji}^{\beta\alpha}$ is required for a real energy and the components $Q_{ij}^{\alpha\beta}$ are all real. The Euler-Lagrange equations are similar to before but are now given as,

$$\frac{\partial F_p}{\partial (\psi_\alpha)^*} - \frac{1}{2} Q_{ij}^{\alpha\beta} D_i D_j \psi_\beta = 0 \tag{1.124}$$

$$\mathbb{I}m(Q_{ij}^{\alpha\beta} (\psi_\alpha)^* D_j \psi_\beta) - \partial_j (\partial_j A_i - \partial_i A_j) = 0 \ . \tag{1.125}$$

Note that the supercurrent is given by,

$$(j_s)_i = \mathbb{I}m(Q_{ij}^{\alpha\beta} (\psi_\alpha)^* D_j \psi_\beta) \ , \tag{1.126}$$

as Equation 1.125 is the anisotropic version of Ampere's law.

1.8.1 Superconductor Types

In this thesis we deal with three types of two component superconductors $p + ip$, $s + id$ and $s+is$. These are defined by the choices made for the $Q_{ij}^{\alpha\beta}$ as well as in the $p+ip$ the parameter choices. The exact form of the anisotropy matrices are given in Table 1.1. We note that the matrix, $Q^{11}Q^{22} - (Q^{12})^2$, must be non negative so that the free energy is positive definite and therefore bounded below.

$s + is$	$s + id$	$p + ip$
$Q^{11} = \begin{pmatrix} a_1 & 0 & 0 \\ 0 & a_1 & 0 \\ 0 & 0 & b_1 \end{pmatrix}$	$Q^{11} = \begin{pmatrix} a_1 & 0 & 0 \\ 0 & a_1 & 0 \\ 0 & 0 & b_1 \end{pmatrix}$	$Q^{11} = \begin{pmatrix} a_1 & 0 & 0 \\ 0 & a_2 & 0 \\ 0 & 0 & b_1 \end{pmatrix}$
$Q^{22} = \begin{pmatrix} a_2 & 0 & 0 \\ 0 & a_2 & 0 \\ 0 & 0 & b_2 \end{pmatrix}$	$Q^{22} = \begin{pmatrix} a_2 & 0 & 0 \\ 0 & a_2 & 0 \\ 0 & 0 & b_2 \end{pmatrix}$	$Q^{22} = \begin{pmatrix} a_2 & 0 & 0 \\ 0 & a_1 & 0 \\ 0 & 0 & b_1 \end{pmatrix}$
$Q^{12} = \begin{pmatrix} a_3 & 0 & 0 \\ 0 & a_3 & 0 \\ 0 & 0 & b_3 \end{pmatrix}$	$Q^{12} = \begin{pmatrix} a_3 & 0 & 0 \\ 0 & -a_3 & 0 \\ 0 & 0 & b_3 \end{pmatrix}$	$Q^{12} = \begin{pmatrix} 0 & a_2 & 0 \\ a_2 & 0 & 0 \\ 0 & 0 & 0 \end{pmatrix}$

Table 1.1: The form of the anisotropy matrices for $s + is$ and $s + id$ systems. Note that in [26] $b_1 = 0$ for the $p + ip$ case.

All three types of superconductors ($s+is$, $s+id$ and $p+ip$) are orthorhombic. We consider a superconductor to be composed of repeating patterns of crystalline unit cells. Each crystalline

unit cell, for an orthorhombic superconductor, has three orthogonal sides of lengths, a, b, c, where $c > a, b$. From this we can construct an orthonormal basis where, $\hat{z}$ is aligned with the longest side of length, c. We then have a choice for $\hat{x}$ to be aligned along the side of length a or b. Then after making this choice we will have fixed $\hat{y}$. Thus we have an orthonormal basis, $(\hat{x}, \hat{y}, \hat{z})$, with coordinates (x, y, z), which we call the crystalline, Cartesian or basal plane basis.

1.8.2 Symmetries in Ginzburg-Landau Theory

If we consider the matrix representation of a spatial symmetry as $S \in O(3)$ then the free energy, F, is symmetric with respect to S if and only if,

$$S_{ki} Q_{ij}^{\alpha\beta} S_{lj} \equiv Q_{kl}^{\alpha\beta} \ . \tag{1.127}$$

We can also consider the matrix representation of a condensate symmetry, for a two component model, as $C \in O(2)$ then the free energy is symmetric with respect to C if the following two conditions are satisfied,

1. $C^{\gamma\alpha} Q_{ij}^{\alpha\beta} C^{\delta\beta} \equiv Q_{ij}^{\gamma\delta}$ (1.128) .
2. $F_p(C^{\gamma\alpha}\psi_\alpha) \equiv F_p(\psi_\gamma)$. (1.129)

The models used are described via their symmetries in Table 1.2 and Table 1.3 shows the action of each symmetry on the coordinates, (x, y, z), and condensates, (ψ_1, ψ_2).

Symmetry	**Spatial Symmetries of** (x, y, z)	**Condensate Symmetries of** (ψ_1, ψ_2)
$C_2(z)$	$(-x, -y, z)$	$(-\psi_1, -\psi_2)$
$C_2(x)$	$(x, -y, -z)$	$(\psi_1, -\psi_2)$
$C_2(y)$	$(-x, y, -z)$	$(-\psi_1, \psi_2)$
$C_4(z)$	$(-y, x, z)$	$(-\psi_2, \psi_1)$
$SO(2)(z)$, θ	$(x\cos\theta - y\sin\theta, x\sin\theta + y\cos\theta, z)$	-
Z_2	-	$((\psi_1)^*, (\psi_2)^*)$
$U(1)$, χ	-	$((\psi_1), (\psi_2))e^{i\chi}$
i	$(-x, -y, -z)$	$(-\psi_1, -\psi_2)$
$\sigma_h = i \cdot C_2(z)$	$(x, y, -z)$	(ψ_1, ψ_2)
$\sigma_\nu = i \cdot C_2(y)$	$(x, -y, z)$	$(\psi_1, -\psi_2)$
$\sigma_d = i \cdot C_2(x)$	$(-x, y, z)$	$(-\psi_1, \psi_2)$
$S_4(z) = \sigma_h \cdot C_4(z)$	$(-y, x, -z)$	$(-\psi_2, \psi_1)$

Table 1.2: The action of the symmetries on the condensates, ψ_α and spatial coordinates, (x, y, z).

Model	**Spatial Symmetries**	**Condensate Symmetries**
$s+is$	$SO(2)(z) \times C_2(x) \times C_2(y)$	Z_2
$s+id$	$C_2(z) \times C_2(x) \times C_2(y)$	Z_2
$p+ip$	$E_u \times Z_2$	

Table 1.3: The spatial and condensate symmetries for the $s+is$, $s+id$ and $p+ip$ superconductors, each model also has a $U(1)$ condensate symmetry and the $s+is$ and $s+id$ models also have the simpler spatial symmetries, $\sigma_h \times \sigma_\nu \times \sigma_d \times i$.
$E_u = C_4(z) \times C_2(x) \times C_2(y) \times \sigma_h \times \sigma_\nu \times \sigma_d \times i$ is an irreducible representation of the tetragonal point group D_{4h}. We note that the $p+ip$ model is a special case that is only symmetric when the spatial and condensate symmetries are simultaneously applied.
For the spatial symmetries: $\sigma_h, \sigma_\nu, \sigma_d$ are reflections in the crystalline xy plane, $C_n(x)$ is the n point reflection symmetry about the x axis and $SO(2)(z)$ is the $SO(2)$ symmetry about the crystalline z axis.

Chapter 2

Domain Walls in $p+ip$, $s+is$ and $s+id$ Superconductors

In this chapter we study domain walls, one-dimensional topological solitons that interpolate between two gauge inequivalent vacua and solve the Ginzburg-Landau equations. We start by considering a two component Ginzburg-Landau theory with broken time reversal symmetry (BTRS), a simple model where domain wall solutions can exist [27]. As discussed in Section 1.7.2, BTRS breaks the $U(1) \times \mathbb{Z}_2$ symmetry of the vacuum, or homogenous superconducting state, allowing domain walls to form. The formation of domain walls can result in a spontaneous internal magnetic field, B, arising (as shown in [28]) without the need for an externally applied magnetic field, H. We will then consider domain walls in anisotropic superconductors, exploring how their phenomenological properties depend on the orientation of the domain wall within the three-dimensional superconductor. All types of domain walls studied, for certain orientations, give rise to a spontaneous internal magnetic field, which can be used to distinguish between domain wall types [1]. We study two main model classes; $p+ip$ [29] and $s+is/s+id$ all of which obey different symmetries and give rise to different types of domain walls and spontaneous magnetic fields. Experiments have shown that the $s+is$ model describes the superconducting state in $Ba_{1\text{-}x}K_xFe_2As_2$ [[30],[31],[32]] whilst the $p+ip$ model has been suggested for the unconventional superconductor Sr_2RuO_4 [[33],[34]]. In the case of $p+ip$, through numerically solving the nonlinear Ginzburg-Landau equations, we observe damped oscillatory decay in both the magnetic field and condensates. This was predicted via linearising the Ginzburg-Landau equations. For all three models we consider magnetic field twisting which we observe in the $p+ip$ and $s+id$ models only. Magnetic field twisting is where the direction in which the spontaneous magnetic field points changes moving in the perpendicular direction away from the domain wall. We see that the orientations where the magnetic field twists can often be predicted by studying the solutions of the linearised Ginzburg-Landau equations. We note that the effects of an external magnetic field are not considered in this chapter so the magnetic field always refers to the spontaneous or internal magnetic field. The $s+is$ and $s+id$ part of this thesis, along with the linearisation calculations, is based on work in the joint papers [1] and [2].

2.1 Domain Walls in Isotropic Superconductors

Consider the two component Ginzburg-Landau free energy with BTRS, previously discussed in Sections 1.3 where we first introduced Ginzburg-Landau theory and Section 1.7 which

specifically looked at this model,

$$F = \int_{\mathbb{R}^3} \left(\sum_{\alpha=1}^{2} |(D\psi_\alpha)|^2 + \frac{B^2}{2} + \left(F_p(\rho_1, \rho_2, \theta_{12}) - F_p(u_1, u_2, \pm\frac{\pi}{2}) \right) \right) d^3x \ , \tag{2.1}$$

for the potential given below. This is the simplest free energy that allows us to form domain walls. The free energy, F, is zeroed with respect to the vacuum or superconducting state, $(\rho_1, \rho_2, \theta_{12}) = (u_1, u_2, \pm\frac{\pi}{2})$, and $\rho_\alpha = |\psi_\alpha|, \theta_{12} = \theta_1 - \theta_2$. The vacua are minimising solutions of the potential, F_p, where the values of the condensates must be non zero for the system to be superconducting.
The potential,

$$F_p = \sum_{\alpha=1}^{2} \left(\alpha_\alpha \rho_\alpha^2 + \frac{\beta_\alpha}{2} \rho_\alpha^4 + \gamma_{12} \rho_1^2 \rho_2^2 \right) + \eta_{12} \rho_1^2 \rho_2^2 \cos(2\theta_{12}) \ , \tag{2.2}$$

contains the BTRS term, with coefficient η_{12}, that splits the vacuum into two gauge inequivalent vacua, as described in Section 1.7.2, and it is this term that allows us to form domain walls. A domain wall is a solution of the Ginzburg-Landau equations (1.95 and 1.96) that interpolates between two gauge inequivalent vacuum values, this interpolation happens in one-dimension which we choose as the $\hat{x}$ direction. Also, a domain wall is a one-dimensional topological soliton that is translationally invariant in both the $\hat{y}$ and $\hat{z}$ directions, the directions perpendicular to $\hat{x}$, where (x, y, z) are the standard crystalline or basal plane coordinates. Note that the use of these coordinates, (x, y, z), signifies that the solution does not depend on orientation. Further, we write the orthonormal basis as,

$$(\hat{x}, \hat{y}, \hat{z}) = ((1, 0, 0), (0, 1, 0), (0, 0, 1)) \ , \tag{2.3}$$

which becomes useful when we study superconductors that do depend on orientation. The domain wall will lie in the yz plane, thus we choose to define the perpendicular direction to this, $\hat{x}$, as the orientation.
The condensate vacua are,

$$(\psi_1, \psi_2) = (u_1, u_2 e^{-i\frac{\pi}{2}}) \tag{2.4}$$

$$(\psi_1, \psi_2) = (u_1, u_2 e^{i\frac{\pi}{2}}) \ , \tag{2.5}$$

up to a choice of global gauge, $\psi_\alpha \mapsto e^{i\chi}\psi_\alpha$, see Section 1.3.2 which discusses gauge transformations. Note that, $\psi_\alpha = \rho_\alpha e^{i\theta_\alpha}$.
To produce domain wall solutions, we consider the following ansatz, known as the translationally invariant ansatz,

$$\begin{aligned} &\psi \to \psi(x) \\ &A \to (A_x(x), A_y(x), 0) \ , \end{aligned} \tag{2.6}$$

which enforces the translational invariance in directions perpendicular to $\hat{x}$ and without loss of generality sets the magnetic field within the superconductor to,

$$B = (0, 0, A_y(x)') \equiv (0, 0, B_z(x)) \ . \tag{2.7}$$

Thus the ansatz, for an isotropic superconductor, is consistent with the three-dimensional Ginzburg-Landau equations. This is due to the rotational invariance that the isotropic model contains. This point will be expanded upon in Section 2.2.1.
This ansatz means that we consider the free energy per unit area of Equation 2.1 so that our

energy is finite. Also, it is due to the lack of anisotropy that we can set $A_z(x) = 0$ everywhere and so fix the magnetic field to point only in the z direction. This point will be discussed in more detail in Section 2.2.1.
In order for the condensates to interpolate between the two gauge inequivalent vacua the following fixed boundary conditions are used,

$$\lim_{x\to\pm\infty} \ (\psi_1, \psi_2, A_x, A_y) = (u_1, \pm i u_2, 0, 0) \ . \tag{2.8}$$

Having A_x, A_y vanishing is a gauge choice that requires $\partial_x \psi_\alpha$ as well as B to vanish on the boundary, a requirement for a finite energy. This then gives us the topological requirement that,

$$\int_{\mathbb{R}} B_z \ dx = 0 \ , \tag{2.9}$$

that is B either vanishes everywhere or is an odd function.
The numerical solutions are produced using a gradient descent method (arrested Newton flow) with boundaries fixed to those of Equation 2.8 which forces domain wall solutions. Figure 2.1 shows such a domain wall solution. We see the smooth interpolation between $\theta_{12} = \frac{\pi}{2}$ and $\theta_{12} = -\frac{\pi}{2}$ which characterises a domain wall. Additionally, the ρ_α, diverge from their vacuum values, u_α, in the centre of the domain, $x = 0$, where the domain wall physically lies. Finally, we see that the spontaneous magnetic field in the z direction, B_z, vanishes everywhere. The form of the potential used for this simulation is given below,

$$\begin{aligned} F_p = &-\frac{1}{2}|\psi_1|^2 - \frac{1}{2}|\psi_2|^2 + 2|\psi_1|^4 + 3|\psi_2|^4 + \frac{3}{2}|\psi_1|^2|\psi_2|^2 \\ &+ \frac{1}{8}|\psi_1|^2|\psi_2|^2 \cos 2\theta_{12} \ . \end{aligned} \tag{2.10}$$

In Section 1.5 we discussed kink solutions of the one-dimensional Sine-Gordon model to give a simple example of a topological soliton that is similar to a domain wall. We note that, analogous to the $N = -1$ anti-kink solution, a domain wall that interpolates between $\theta_{12} = -\frac{\pi}{2}$ and $\theta_{12} = \frac{\pi}{2}$ is called an anti domain wall solution. However, the transformation $x \mapsto -x$ converts between these two solutions that are degenerate in energy. Finally, the fixing of the condensate boundary conditions mean that the domain wall cannot be continuously transformed into the lower energy homogenous superconducting state, $\psi_\alpha = u_\alpha, B_z = 0$, thus this excited state is stable.

2.2 Domain Walls in Anisotropic Superconductors

We build upon the previous section by now considering domain wall solutions in an anisotropic superconductor, the free energy of which is given by,

$$F = \int_{\mathbb{R}^3} \left(\frac{1}{2} Q_{ij}^{\alpha\beta} (D_i \psi_\alpha)^* (D_j \psi_\beta) + \frac{B^2}{2} + \left(F_p - F_p(u_1, u_2, \pm\frac{\pi}{2}) \right) \right) dx_1 dx_2 dx_3 \ , \tag{2.11}$$

with $D_i = \partial_i - iA_i$, $i, j \in \{1, 2, 3\}$, $\alpha, \beta \in \{1, 2\}$ and there is an implied summation over all repeated indices. $B = (B_1, B_2, B_3)$ gives the spontaneous magnetic field in the $\hat{x}_1, \hat{x}_2, \hat{x}_3$ directions respectively. We note that we desire a real energy hence, $Q_{ij}^{\alpha\beta} \equiv Q_{ji}^{\beta\alpha}$, and the components of the anisotropy matrices, $Q_{ij}^{\alpha\beta} \in \mathbb{R}$.
We use the excitation plane coordinates, (x_1, x_2, x_3), to indicate that our solutions now depend upon the orientation of a domain wall. The corresponding orthonormal basis, $(\hat{x}_1, \hat{x}_2, \hat{x}_3)$, can

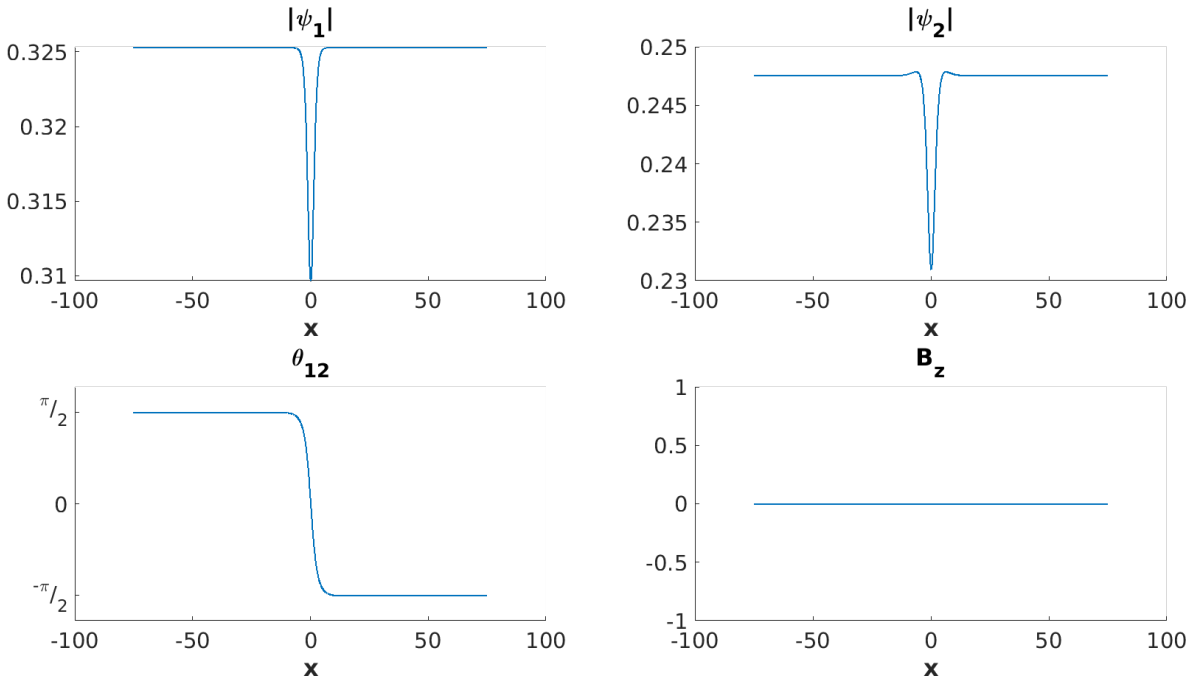

Figure 2.1: *A domain wall solution for an isotropic superconductor with the potential parameters given in the Appendix A.1.* $|\psi_\alpha|$*,* θ_{12} *and* B_z *are the moduli of the condensates, their phase difference and the spontaneous magnetic field in the* $\hat{z}$ *direction respectively.*

be written in terms of the basal plane basis (see Equation 2.3). Now the $\hat{x}_1$ direction defines the orientation of the domain wall and for this model the choice of $\hat{x}_1$ will affect the solutions of the Ginzburg-Landau equations (1.124 and 1.125). The method for changing orientation is discussed in Section 2.2.2 but first we must discuss the choice of ansatz. Note that in the case where $Q_{ij}^{\alpha\beta} = \delta^{\alpha\beta}\delta_{ij}$ we are returned to the isotropic two component Ginzburg-Landau model, Equation 2.1, and our model loses the dependence on orientation. We remind the reader that a domain wall is a solution of the, now anisotropic, Ginzburg-Landau equations with boundary conditions fixed to,

$$\lim_{x_1 \to \pm\infty} (\psi_1, \psi_2, A_1, A_2, A_3) = (u_1, \pm i u_2, 0, 0, 0) \ . \tag{2.12}$$

2.2.1 Translationally Invariant Ansatz

We now revisit the translationally invariant ansatz, Equation 2.6, and see how the introduction of anisotropy requires it to be modified. In order to study domain wall solutions in Equation 2.11 we can consider applying the previous ansatz which we write in terms of our new coordinates,

$$\begin{aligned} \psi &\to \psi(x_1) \\ A &\to (A_1(x_1), A_2(x_1), 0) \ . \end{aligned} \tag{2.13}$$

However, for a given $\hat{x}_1$ direction this ansatz fixes the magnetic field to lie in the $\hat{x}_3$ direction. For a domain wall solution in an isotropic superconductor this choice does not affect the results. However, when anisotropy is introduced there is an S^1 family of directions for $\hat{x}_3$ for each $\hat{x}_1$ that may affect the free energy. Additionally, in order to allow for the possibility of magnetic field twisting, the magnetic field must be allowed to change direction but Ansatz

2.6 forces the magnetic field to lie in a single direction. Both of these issues are solved by introducing a new ansatz where we retain the A_3 component,

$$\begin{aligned} &\psi \to \psi(x_1) \\ &A \to (A_1(x_1), A_2(x_1), A_3(x_1)) \ , \end{aligned} \tag{2.14}$$

which means $B(x_1) = (0, -A_3(x_1)', A_2(x_1)')$. This means that the magnetic field can point in both the $\hat{x}_2$ and $\hat{x}_3$ directions.

This ansatz needs to be consistent with the full three-dimensional Ginzburg-Landau equations. Here, consistency means that the Ginzburg-Landau equations derived by applying Ansatz 2.14 to Equations 1.124 and 1.125 should yield the same equations as when we apply this ansatz to the free energy first, Equation 2.11, and then vary to yield the reduced Ginzburg-Landau equations. This is equivalent to saying that solutions of these reduced Ginzburg-Landau equations are solutions of the full Ginzburg-Landau equations where no ansatz has been applied.

Here we show that, in general, only by keeping $A_3 \neq 0$ are the reduced Ginzburg-Landau equations consistent. That is, in the anisotropic case, Ansatz 2.13 is inconsistent.

Consider,

$$F_{A_3} = \int_{\mathbb{R}^3} \left(\mathrm{Re}\left(\frac{1}{2} Q_{33}^{\alpha\beta} (D_3\psi_\alpha)^* (D_3\psi_\beta) + Q_{23}^{\alpha\beta} (D_2\psi_\alpha)^* (D_3\psi_\beta) + Q_{13}^{\alpha\beta} (D_1\psi_\alpha)^* (D_3\psi_\beta) \right) \right. \tag{2.15}$$

$$\left. + \frac{(\partial_2 A_3 - \partial_3 A_2)^2}{2} + \frac{(\partial_3 A_1 - \partial_1 A_3)^2}{2} + (\text{terms not containing } A_3) \right) dx_1 dx_2 dx_3 \ , \tag{2.16}$$

if we vary F_{A_3} with respect to the real fields then we obtain the corresponding Ginzburg-Landau equations. We focus on the equation arrived at by varying with respect to A_3,

$$\mathbb{I}m \left(Q_{33}^{\alpha\beta} (\psi_\alpha)^* D_3\psi_\beta + Q_{32}^{\alpha\beta} (\psi_\alpha)^* D_2\psi_\beta + Q_{31}^{\alpha\beta} (\psi_\alpha)^* D_1\psi_\beta \right) - A_3'' = 0 \ . \tag{2.17}$$

Note that the $Q_{32}^{\alpha\beta}$ and $Q_{31}^{\alpha\beta}$ terms contain no factors of A_3 but were derived from terms in the free energy that were linear in A_3. If we apply Ansatz 2.13 to Equation 2.17 we see that it does not vanish,

$$\mathbb{I}m \left(-i Q_{32}^{\alpha\beta} (\psi_\alpha)^* A_2\psi_\beta + Q_{31}^{\alpha\beta} (\psi_\alpha)^* D_1\psi_\beta \right) = 0 \ . \tag{2.18}$$

If we consider applying Ansatz 2.13 to F_{A_3} instead we see that the free energy is only dependent on the six real fields,

$$(\mathrm{Re}(\psi_1), \mathrm{Im}(\psi_1), \mathrm{Re}(\psi_2), \mathrm{Im}(\psi_2), A_1, A_2) \ , \tag{2.19}$$

thus there are six Ginzburg-Landau equations so in order for this ansatz to be consistent Equation 2.18 must vanish. However, in general $Q_{32}^{\alpha\beta} \neq 0$ and $Q_{31}^{\alpha\beta} \neq 0$ so Equation 2.18 does not vanish and Ansatz 2.13 is not consistent.

Thus Ansatz 2.13 is always valid for isotropic superconductors, where $Q_{32}^{\alpha\beta} = Q_{31}^{\alpha\beta} = 0$ always but when anisotropy is used we must switch to Ansatz 2.14 which is consistent. We see that the reduced Ginzburg-Landau equations are simply the same as Equations 1.124 and 1.125, the full Ginzburg-Landau equations, except with,

$$D_2\psi_\alpha \mapsto -iA_2\psi_\alpha \tag{2.20}$$

$$D_3\psi_\alpha \mapsto -iA_3\psi_\alpha \ , \tag{2.21}$$

thus we can say that solutions of the reduced Ginzburg-Landau equations are solutions of the full Ginzburg-Landau equations.

2.2.2 Orientation Selection

Here we introduce the coordinate transformation of the free energy from Equation 2.11, we note that this three-dimensional free energy is independent of coordinate choice. However, if after making a coordinate transformation we apply Ansatz 2.14, this dimensionally reduces the free energy, then the resulting free energy will depend upon the orientation of the domain wall. For the excitation plane coordinates, (x_1, x_2, x_3), there is an associated orthonormal basis, $(\hat{x}_1, \hat{x}_2, \hat{x}_3)$, which can be written in terms of the crystalline orthonormal basis, $(\hat{x}, \hat{y}, \hat{z})$. For a one-dimensional topological soliton, $\hat{x}_1 \in S^2$ defines the orientation and can be used to generate the other two basis vectors $\hat{x}_2, \hat{x}_3$ via the Gram-Schmidt process. An orientation in three-dimensions is represented by the following $SO(3)$ matrix,

$$M = \begin{pmatrix} \vdots & \vdots & \vdots \\ \hat{x}_1 & \hat{x}_2 & \hat{x}_1 \times \hat{x}_2 \\ \vdots & \vdots & \vdots \end{pmatrix} , \tag{2.22}$$

where $\hat{x}_1$ is the normal to the plane that defines the orientation and $\hat{x}_1 \cdot \hat{x}_2 = 0$. Figures 2.2a and 2.2b show two orientations of a domain wall, represented by a plane in a three-dimensional sample.

We now consider applying the coordinate transformation,

$$x_i \mapsto M_{ij} x_j \tag{2.23}$$

with $i, j \in \{1, 2, 3\}$, where the new (x_1, x_2, x_3) are coordinates for an arbitrary orientation given by $M \in SO(3)$. The partial derivatives will transform as follows,

$$\begin{aligned} \partial_i &\mapsto \frac{\partial x_j}{\partial x_i} \partial_j && (2.24) \\ &= (M^{-1})_{ji} \partial_j && (2.25) \\ &= M_{ij} \partial_j \ , && (2.26) \end{aligned}$$

where in the last line we used the property that $M^{-1} = M^T$. The vector potential, A_i, is assumed to transform in the same way as ∂_i so that the covariant derivative transforms as $D_i \mapsto M_{ij} D_j$. Substituting these transformations into the free energy, Equation 2.11, gives,

$$F = \int_{\mathbb{R}^3} \left(\frac{1}{2} M_{ik} Q_{ij}^{\alpha\beta} M_{jl} (D_k \psi_\alpha)^* (D_l \psi_\beta) + \frac{B^2}{2} + F_p(\rho_1, \rho_2, \theta_{12}) \right) \, dx_1 dx_2 dx_3 \ . \tag{2.27}$$

Note that this gives the same form of free energy function because $\det M = 1$ and B is unchanged by this coordinate transformation. Additionally, before applying Ansatz 2.14 our energy is unchanged. However, the free energy will depend upon our choice of $\hat{x}_1$ once Ansatz 2.14 is applied.

By defining the transformation,

$$\tilde{Q}_{ij}^{\alpha\beta} \mapsto M_{ik} Q_{ij}^{\alpha\beta} M_{jl} \ , \tag{2.28}$$

we can change coordinates by simply changing the values of the anisotropic matrices, $Q^{\alpha\beta}$, allow the form of the free energy to remain unchanged. This transformation can be rewritten as,

$$Q^{\alpha\beta} \mapsto M^T Q^{\alpha\beta} M \ . \tag{2.29}$$

This method works very well for numerical simulations as a change of coordinates has been made equivalent to a change of parameters.

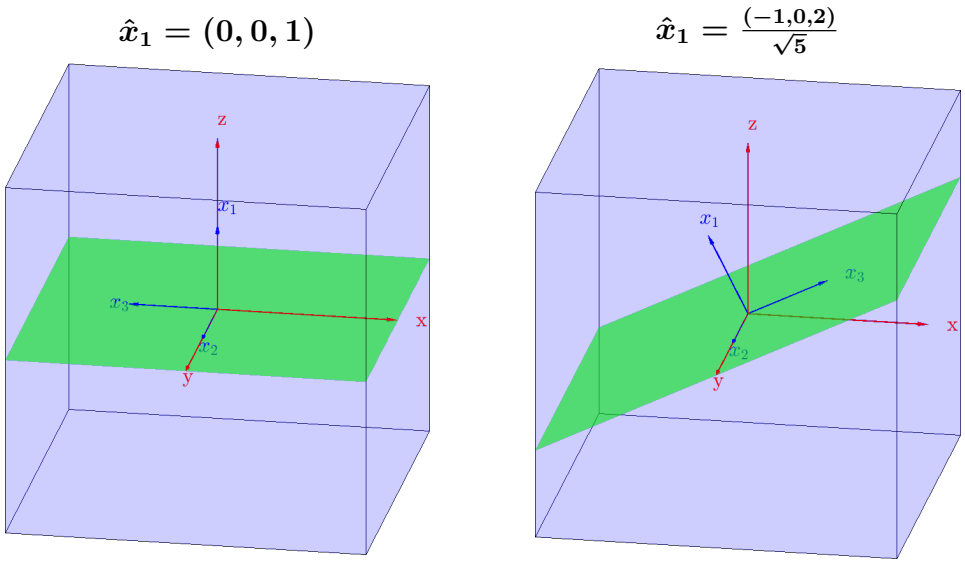

(a) *Plane equation:* $z = const.$ **(b)** *Plane equation:* $\frac{-x+2z}{\sqrt{5}} = const.$

Figure 2.2: *Diagram showing the orientation of two domain walls in a three-dimensional sample, where the orientation is defined by the unit normal to the plane,* $\hat{x}_1$*. The plane in green represents a domain wall dividing the sample into two domains* $x_1 < 0$ *and* $x_1 > 0$*.*

2.2.3 Numerical Method

We produce domain wall solutions by numerically evolving Equations 1.124 and 1.125 (the anisotropic Ginzburg-Landau equations) using arrested Newton flow, a gradient descent method. We discretise our one-dimensional domain with a grid of, $N_x = 900$, evenly spaced points with a lattice spacing of $h_x = 0.05$. The fields ψ_α and A_i are discretised on this grid such that,

$$\psi_\alpha^{(I)} = \psi_\alpha(x_1^{(I)}) \tag{2.30}$$

$$A_i^{(I)} = A_i(x_1^{(I)}) \ , \tag{2.31}$$

denote the values of the discretised ψ_α and A_i at the position, (I), on the one-dimensional grid. The derivatives are approximated by central fourth order finite differences which are given for, $\psi_\alpha^{(I)}$,

$$\frac{d\psi_\alpha^{(I)}}{dx_1} = \frac{-\psi_\alpha^{(I+2)} + 8\psi_\alpha^{(I+1)} - 8\psi_\alpha^{(I-1)} + \psi_\alpha^{(I-2)}}{12h_x} + \mathcal{O}(h^9) \tag{2.32}$$

$$\frac{d^2\psi_\alpha^{(I)}}{dx_1^2} = \frac{-\psi_\alpha^{(I+2)} + 16\psi_\alpha^{(I+1)} - 30\psi_\alpha^{(I)} + 16\psi_\alpha^{(I-1)} - \psi_\alpha^{(I-2)}}{12h_x^2} + \mathcal{O}(h^4) \ , \tag{2.33}$$

which allows us to form a discretised approximation to free energy density,

$$f_{disc}^{(I)}(\Phi) = \frac{1}{2}\tilde{Q}_{ij}^{\alpha\beta}\left(D_k^{(I)}\psi_\alpha^{(I)}\right)^*\left(D_l^{(I)}\psi_\beta^{(I)}\right) + \frac{\left(B^{(I)}\right)^2}{2} + F_p\left(\rho_1^{(I)}, \rho_2^{(I)}, \theta_{12}^{(I)}\right) \ , \tag{2.34}$$

where $\Phi^{(I)} = ((\mathrm{Re}(\psi_1)^{(I)}, \mathrm{Im}(\psi_1)^{(I)}, \mathrm{Re}(\psi_2)^{(I)}, \mathrm{Im}(\psi_2)^{(I)}, A_1^{(I)}, A_2^{(I)}, A_3^{(I)}))$ is a list of all the real fields. Also, as discussed in Section 2.2.2, we modify the values of $\tilde{Q}_{ij}^{\alpha\beta}$ to perform a coordinate transformation of the free energy which when coupled with Ansatz 2.14 changes the orientation of our domain wall.

We can produce local minima of $f^{(I)}_{disc}$ using arrested Newton flow. This is done by solving the equation of motion,

$$\frac{d^2\Phi^{(I)}}{dt^2} = -grad_{(\Phi)} f^{(I)}_{disc}(\Phi), \tag{2.35}$$

for each, (I), in our discretised domain with a smooth initial configuration or condition, $\Phi(t = 0)$, that has the correct domain wall boundary conditions as given in 2.12, and $\frac{d\Phi}{dt}(t = 0) = 0$. We note that the boundary points are those labelled by $I = \{1, 900\}$, that is the two end points on either side of the one-dimensional domain. If we have chosen a large enough value of N_x then $I = 1$ and $I = 900$ approximates the continuous boundaries $x_1 \to \mp\infty$ respectively. The value of the gradient of f_{disc} for each value of ϕ, $grad_{(\Phi)} f_{disc}(\Phi)$, is set to vanish on the boundaries of the one-dimensional domain. This fixes the boundary conditions throughout the evolution of Φ. We calculate the new value of Φ by splitting the second order differential equation into two coupled first order differential equations,

$$\frac{d\Phi^{(I)}}{dt} = \check{\Phi}^{(I)} \tag{2.36}$$

$$\frac{d\check{\Phi}^{(I)}}{dt} = -grad_{(\Phi)} f^{(I)}_{disc}(\Phi) \ , \tag{2.37}$$

where the variable $\check{\Phi}$ is introduced so we can form these differential equations. These equations are then solved, for each time step, $t \to t + \delta t$, via the Runge-Kutta method. However, for simplicity we demonstrate this using the Euler method,

$$\Phi(t + \delta t)^{(I)} = \Phi(t)^{(I)} + \delta t \cdot \check{\Phi}(t)^{(I)} \tag{2.38}$$

$$\check{\Phi}(t + \delta t)^{(I)} = \check{\Phi}(t)^{(I)} - \delta t \cdot grad_{(\Phi)} f^{(I)}_{disc}(\Phi, t) \ . \tag{2.39}$$

For each time step, $t \to t + \delta t$, if,

$$\frac{d^2\Phi}{dt^2} \cdot \frac{d\Phi}{dt} < 0 \ , \tag{2.40}$$

we then set $\frac{d\Phi}{dt} = 0$. This condition indicates that our configuration is moving in a direction that increases energy so we set the velocity of the configuration, $\frac{d\Phi}{dt}$, to vanish. This method is much faster than standard gradient flow.
At sufficiently large values of t and assuming our choice of $\Phi(t = 0)$, h_x and δt was well chosen then Φ should relax towards a local minimum. The algorithm terminates when every component of $grad_{(\Phi)} f_{disc}(\Phi)$ is less than a certain, user set, tolerance,

$$\max\left(\left|grad_{(\Phi)} f_{disc}(\Phi)\right|\right) < tol \ . \tag{2.41}$$

For domain walls a tolerance of, at least, $tol = 10^{-5}$ was used.

2.2.3.1 Orientation Parametrisation

For numerical purposes we want to test a range of orientations so we can see the dependence of our solutions on orientation. To do this we need to parametrise points for our orientation. All of the models that we deal with have a reflection symmetry, $z \mapsto -z$, such that $\hat{x}_1 \in S^2$ can be reduced to the upper hemisphere. If we parametrise it as,

$$\hat{x}_1 = (\cos\phi \sin\theta, \sin\phi \cos\theta, \cos\theta) \ , \tag{2.42}$$

with $\phi \in [0, 2\pi]$ and $\theta \in [0, \frac{\pi}{2}]$. We can generate a given $M \in SO(3)$ matrix for a given $\hat{x}_1$. We note that, with our translationally invariant ansatz which dimensionally reduces the free energy to be one-dimensional, only the value of $\hat{x}_1$ affects the free energy. We then use,

$$\hat{x}_2 = (\pi, -2e, 3\pi) \ , \tag{2.43}$$

as our initial value for $\hat{x}_2$, chosen to ensure it will never be parallel to $\hat{x}_1$, then apply the Gram-Schmidt process to generate an orthonormal basis that makes up the columns of M. It is important to note that because of this method the value of $\hat{x}_3$ will be different for each value of $\hat{x}_1$.

2.3 Linearisation of the Anisotropic Ginzburg-Landau Equations

We now look to linearise the full anisotropic multicomponent model, Equation 2.11, which describes the behaviour of the fields when they are close to their vacuum values. To reiterate, a vacuum is the value of the fields when the superconductor is in the homogenous superconducting state. The linearisation describes the behaviour of the fields as exponential decay, the rate of decay is governed by a so called length scale. For a domain wall this is only valid as, $|x_1|\to\infty$, which is known as the linear region of the model. In terms of the Ginzburg-Landau theory, anisotropy introduces couplings between matter, $|\psi_\alpha|, \theta_{12}$, and magnetic fields, B_i, through the values of $\tilde{Q}_{ij}^{\alpha\beta}$. Additional couplings between the different condensates, ψ_α, can be introduced by terms in the potential, F_p. In Section 1.3.3 we linearised the simpler isotropic model which contains no such couplings. In this case there was a length scale associated with each condensate, the correlation length, and one associated with the magnetic field, the penetration length. However, for the anisotropic case and due to the aforementioned couplings the length scales derived are no longer associated with a single field. Our approach is based upon previous methods: in [35] a multicomponent anisotropic Ginzburg-Landau theory with no BTRS and in the limit where the density, $|\psi_\alpha|$, is assumed to be constant is linearised. This introduces the idea that anisotropy can couple the Leggett mode, which governs the behaviour of the phase difference, θ_{12}, in the linear region of the model, and the magnetic modes. This coupling or hybridisation caused there to be multiple magnetic modes with different penetration length scales. This is expanded upon in [36] which generalised the idea of the Ginzburg-Landau parameter (κ) also introduced in Section 1.3.3, to the multicomponent anisotropic case that has multiple lengths scales that are also directionally dependent. Finally, in [37] the $p+ip$ model was fully linearised for only the basal plane, $\hat{x}_1 = (\cos\theta, \sin\theta, 0), \theta \in [0, 2\pi]$, and predictions from the linearisation were applied to full nonlinear solutions for the Meissner state. In this section we include an improved method that linearises a one-dimensional defect for any arbitrary orientation. We can compare predictions from the linearisation to simulations of the full nonlinear model to test its validity. Starting by introducing a new gauge invariant vector field,

$$p_i := A_i - \partial_i \theta_\Sigma \ , \tag{2.44}$$

where $\theta_\Sigma = \frac{1}{2}(\theta_1 + \theta_2)$, which will allow us to write our free energy in terms of gauge invariant quantities only. As discussed in Section 1.3.2, gauge invariant quantities are unchanged by the transformation,

$$\psi_\alpha \mapsto \psi_\alpha e^{i\chi} \tag{2.45}$$

$$A_i \mapsto A_i + \partial_i \chi \ , \tag{2.46}$$

for the smooth function χ. We note that θ_α and therefore p_i is not well defined if $\psi_\alpha = 0$ thus only in the linear region, where we know $\psi_\alpha \neq 0$, can we write the energy in terms of p_i without issues. The components of the linear magnetic field are written as, $(B_{lin})_i = \epsilon_{ijk}\partial_j p_k$. We also define,

$$\theta_\Delta := \frac{1}{2}\theta_{12} = \frac{1}{2}(\theta_1 - \theta_2) \ . \tag{2.47}$$

We can now write our condensates in terms of these new variables,

$$\psi_\alpha = \rho_\alpha e^{i(\theta_\Sigma + d_\alpha \theta_\Delta)} \ , \tag{2.48}$$

where $d_\alpha = (-1)^{\alpha+1}$.
We assume that away from the defect, for example a domain wall, the fields decay to their vacuum values, $(\rho_\alpha, \theta_\Delta, p_i) \approx (u_\alpha, \theta_0, 0)$. In the BTRS case $\theta_0 = \pm\frac{\pi}{4}$, note the extra factor of $\frac{1}{2}$ which comes from the definition of θ_Δ. We now define the quantities,

$$\epsilon_\alpha = \rho_\alpha - u_\alpha \tag{2.49}$$

$$\vartheta = \theta_\Delta - \theta_0 \ , \tag{2.50}$$

and note that when the system is close to a vacuum value, $\epsilon_\alpha, \vartheta, p_i$ are small. When they are small we can assume that linear terms will dominate the field equations which can be derived by varying a quadratic order version of the free energy. We derive this below.
Focussing first on the gradient energy density term, we write the gauge covariant derivative in terms of $\epsilon_\alpha, \vartheta, p_i$ and then linearise,

$$(D_i\psi_\alpha)^* = (\partial_i + i(p_i + \partial_i\theta_\Sigma))(\epsilon_\alpha + u_\alpha)e^{-i(\theta_\Sigma + d_\alpha(\vartheta+\theta_0))} \tag{2.51}$$

$$\approx (\partial_i\epsilon_\alpha + iu_\alpha\,(p_i - d_\alpha\partial_i\vartheta))e^{-i(\theta_\Sigma + d_\alpha\theta_0)} \ , \tag{2.52}$$

where, to linear order, we can neglect $e^{-id_\alpha\vartheta}$.
We can now write the associated energy density term as,

$$E^{grad}_{quad} = \frac{1}{2}\mathbb{Q}^{\alpha\beta}_{ij}(\partial_i\epsilon_\alpha + iu_\alpha\,(p_i - d_\alpha\partial_i\vartheta))(\partial_j\epsilon_\beta - iu_\beta\,(p_j - d_\beta\partial_j\vartheta)) \ , \tag{2.53}$$

where, for convenience, we have defined $\mathbb{Q}^{\alpha\beta}_{ij} = \mathbb{R}^{\alpha\beta}_{ij} + i\mathbb{I}^{\alpha\beta}_{ij} = e^{i(d_\beta - d_\alpha)\theta_0}Q^{\alpha\beta}_{ij}$, with both $R^{\alpha\beta}_{ij}, \mathbb{I}^{\alpha\beta}_{ij} \in \mathbb{R}$. We note that when $\alpha \neq \beta$ and $\theta_0 \neq 0$, then $\mathbb{Q}^{\alpha\beta}_{ij}$ can be complex even if the original $Q^{\alpha\beta}_{ij}$ is real. Also, $\mathbb{Q}^{\alpha\beta}_{ij} = (\mathbb{Q}^{\beta\alpha}_{ji})^*$. This is the same symmetry that the original $Q^{\alpha\beta}_{ij}$ respect, thus $\mathbb{R}^{\alpha\beta}_{ij} = \mathbb{R}^{\beta\alpha}_{ji}$ and $\mathbb{I}^{\alpha\beta}_{ij} = -\mathbb{I}^{\beta\alpha}_{ji}$.
The magnetic energy density is already quadratic in derivatives of p_i,

$$E^{Mag}_{quad} = \frac{1}{4}(\partial_i p_j - \partial_j p_i)(\partial_i p_j - \partial_j p_i) \ , \tag{2.54}$$

the extra factor of $\frac{1}{2}$ is included to avoid double counting terms. Finally, starting from the 3×3 Hessian matrix of partial derivatives of the potential evaluated at the specified vacuum value,

$$\mathcal{H}_{ab} = \left.\frac{d^2F_p}{dX_a dX_b}\right|_{(u_1,u_2,\theta_0)} \ , \tag{2.55}$$

where $(X_1, X_2, X_3) = (\rho_1, \rho_2, \theta_\Delta)$ and $a, b \in \{1, 2, 3\}$. The potential energy density term is then given by,

$$E^{Pot}_{quad} = \frac{1}{2}\left.\frac{d^2F_p}{dX_a dX_b}\right|_{(u_1,u_2,\theta_0)} X_a X_b \tag{2.56}$$

$$= \frac{1}{2}\left(\mathcal{H}_{\alpha\beta}\epsilon_\alpha\epsilon_\beta + 2\mathcal{H}_{\alpha 3}\epsilon_\alpha\vartheta + \mathcal{H}_{33}\vartheta^2\right) \ . \tag{2.57}$$

Thus the full quadratic energy density is given by,

$$\begin{aligned} E_{quad} =& \frac{1}{2}\mathbb{Q}^{\alpha\beta}_{ij}(\partial_i\epsilon_\alpha + iu_\alpha\,(p_i - d_\alpha\partial_i\vartheta))(\partial_j\epsilon_\beta - iu_\beta\,(p_j - d_\beta\partial_j\vartheta)) \\ &+\frac{1}{4}(\partial_i p_j - \partial_j p_i)(\partial_i p_j - \partial_j p_i) \\ &+\frac{1}{2}\mathcal{H}_{\alpha\beta}\epsilon_\alpha\epsilon_\beta + \mathcal{H}_{\alpha 3}\epsilon_\alpha\vartheta + \frac{1}{2}\mathcal{H}_{33}\vartheta^2 \ . \end{aligned} \tag{2.58}$$

This leads to the linear Ginzburg-Landau equations,

$$\epsilon_\alpha : \ -\mathbb{R}_{ij}^{\alpha\beta}\partial_i\partial_j\epsilon_\beta - \mathbb{I}_{ij}^{\alpha\beta}u_\beta(\partial_i p_j - d_\beta\partial_i\partial_j\vartheta) + \mathcal{H}_{\alpha\beta}\epsilon_\beta + \mathcal{H}_{\alpha 3}\vartheta = 0 \tag{2.59}$$

$$\vartheta : \ \mathbb{R}_{ij}^{\alpha\beta}d_\alpha u_\alpha u_\beta(\partial_i p_j - d_\beta\partial_i\partial_j\vartheta) - \mathbb{I}_{ij}^{\alpha\beta}d_\alpha u_\alpha\partial_i\partial_j\epsilon_\beta + \mathcal{H}_{\alpha 3}\epsilon_\alpha + \mathcal{H}_{33}\vartheta = 0 \tag{2.60}$$

$$p_i : \ \mathbb{R}_{ij}^{\alpha\beta}u_\alpha u_\beta(p_j - d_\beta\partial_j\vartheta) - \mathbb{I}_{ij}^{\alpha\beta}u_\alpha\partial_j\epsilon_\beta + (\partial_j\partial_i p_j - \partial_j^2 p_i) = 0 \ . \tag{2.61}$$

These equations are coupled which means, for example, Equation 2.59 contains a p_j term thus solving it requires you to simultaneously solve Equations 2.60 and 2.61. The source of this coupling is having $\mathbb{I}_{ij}^{\alpha\beta} \neq 0$ as if all of the $\mathbb{I}_{ij}^{\alpha\beta}$ vanish then Equation 2.59 will not depend on p_j, for example. We note that, as we are linearising a general anisotropic system, the direction in which we linearise will affect the above equations through the values of $\mathbb{Q}_{ij}^{\alpha\beta}$. Building upon the orientation selection method, detailed in Section 2.2.2, we only allow the fields to vary in the $\hat{x}_1$ direction through the choice of ansatz (2.14). Equations 2.59, 2.60 and 2.61 are now reduced to a coupled system of ordinary differential equations which will depend upon orientation via the transformation of the anisotropy matrices, $Q^{\alpha\beta} \mapsto M^T Q^{\alpha\beta} M$. Remember that (x_1, x_2, x_3) give the coordinates whilst $(\hat{x}_1, \hat{x}_2, \hat{x}_3)$ is the associated orthonormal basis. We can write them in a combined form using,

$$\vec{w}(x_1) = (\epsilon_1(x_1), \epsilon_2(x_1), \vartheta(x_1), p_1(x_1), p_2(x_1), p_3(x_1))^T \ , \tag{2.62}$$

where the p_i are the components of p in the new basis. The combined form for the coupled linear Ginzburg-Landau equations is,

$$\left(\mathcal{A}\frac{d^2\vec{w}}{dx_1^2} + \mathcal{B}\frac{d\vec{w}}{dx_1} + \mathcal{C}\vec{w}\right) = 0 \ , \tag{2.63}$$

where

$$\mathcal{A} = \begin{pmatrix} a & 0 \\ 0 & a' \end{pmatrix} \tag{2.64}$$

$$a := \begin{pmatrix} -\mathbb{R}_{11}^{11} & -\mathbb{R}_{11}^{12} & \mathbb{I}_{11}^{1\beta}u_\beta d_\beta \\ -\mathbb{R}_{11}^{12} & -\mathbb{R}_{11}^{22} & \mathbb{I}_{11}^{2\beta}u_\beta d_\beta \\ \mathbb{I}_{11}^{1\beta}u_\beta d_\beta & \mathbb{I}_{11}^{2\beta}u_\beta d_\beta & -\mathbb{R}_{11}^{\alpha\beta}u_\alpha u_\beta d_\alpha d_\beta \end{pmatrix} \tag{2.65}$$

$$a' := \mathrm{diag}(0, -1, -1) \tag{2.66}$$

$$\mathcal{B} = \begin{pmatrix} 0 & b_1 \\ -b_1^T & 0 \end{pmatrix} \tag{2.67}$$

$$b_1 := \begin{pmatrix} -\mathbb{I}_{11}^{1\beta}u_\beta & -\mathbb{I}_{12}^{1\beta}u_\beta & -\mathbb{I}_{13}^{1\beta}u_\beta \\ -\mathbb{I}_{11}^{2\beta}u_\beta & -\mathbb{I}_{12}^{2\beta}u_\beta & -\mathbb{I}_{13}^{2\beta}u_\beta \\ \mathbb{R}_{11}^{\alpha\beta}u_\alpha u_\beta d_\alpha & \mathbb{R}_{12}^{\alpha\beta}u_\alpha u_\beta d_\alpha & \mathbb{R}_{13}^{\alpha\beta}u_\alpha u_\beta d_\alpha \end{pmatrix} \tag{2.68}$$

$$\mathcal{C} = \begin{pmatrix} \mathcal{H} & 0 \\ 0 & \langle\mathbb{R}\rangle \end{pmatrix} \tag{2.69}$$

$$\langle\mathbb{R}\rangle_{ij} := u_\alpha\mathbb{R}_{ij}^{\alpha\beta}u_\beta \ . \tag{2.70}$$

Note that $\mathcal{A}$ and $\mathcal{C}$ are symmetric and $\mathcal{B}$ is skew symmetric but all three are real 6×6 matrices. Additionally, all three of these matrices depend implicitly on the choice of orientation, $\hat{x}_1$, through the transformation, Equation 2.29. Equation 2.63 describes how the fields decay away from a defect, such as a domain wall, along the $\hat{x}_1$ direction, with the assumption of translational invariance in the directions perpendicular to $\hat{x}_1$. In order to calculate the length scales for this model we seek exponentially decaying solutions of Equation 2.63 of the form,

$$\vec{w}(x_1) = \vec{v}e^{-\mu x_1} \ , \tag{2.71}$$

where $\mu \in \mathbb{C}$ and we require $\mathrm{Re}(\mu) > 0$ so that we only consider the physically relevant solutions where the fields decay to their vacuum values as $x_1 \to \infty$. The constant vector, $\vec{v}$, is what we call the normal mode and $\lambda = \frac{1}{\mu}$ gives the length scale for that mode. Note that unlike linearising the isotropic case, see Section 1.3.3, the length scales are **not** purely real. Additionally, the components of the normal mode, $\vec{v}$, describes in which fields, see Equation 2.62, the oscillations (and or decay) of $\vec{w}(x_1)$ occur about the ground state, $\vec{0}$.
For $\vec{w}(x_1)$ to be a solution of Equation 2.63 then,

$$\left(\mu^2\mathcal{A} - \mu\mathcal{B} + \mathcal{C}\right)\vec{v} = 0 \ , \tag{2.72}$$

must be true. By defining $\vec{z} = -\mu\vec{v}$, left multiplying by $\mathcal{C}^{-1}$ and then rearranging we obtain the following equation,

$$\left(\mathcal{C}^{-1}\mathcal{A}\vec{z} + \mathcal{C}^{-1}\mathcal{B}\vec{v}\right) = \frac{1}{\mu}\vec{v} \ . \tag{2.73}$$

This equation can be rewritten as follows,

$$\Omega \begin{pmatrix} \vec{v} \\ \vec{z} \end{pmatrix} = \frac{1}{\mu} \begin{pmatrix} \vec{v} \\ \vec{z} \end{pmatrix} \ , \tag{2.74}$$

where $(\vec{v}, \vec{z})^T$ satisfies this linear equation and Ω is the 12×12 matrix,

$$\Omega := \begin{pmatrix} \mathcal{C}^{-1}\mathcal{B} & \mathcal{C}^{-1}\mathcal{A} \\ -I_6 & 0 \end{pmatrix} \ . \tag{2.75}$$

Hence, $\lambda = 1/\mu$ are the eigenvalue of Ω which are found as the solutions of the real, degree 12 polynomial equation,

$$\det\left(\mathcal{A} - \mathcal{B}\lambda + \mathcal{C}\lambda^2\right) = 0 \ . \tag{2.76}$$

However, using the symmetric properties of the real matrices $\mathcal{A}, \mathcal{B}, \mathcal{C}$, the following must also be true,

$$\det\left(\mathcal{A}^T - \mathcal{B}^T\lambda + \mathcal{C}^T\lambda^2\right) \equiv \det\left(\mathcal{A} + \mathcal{B}\lambda + \mathcal{C}\lambda^2\right) = 0 \ , \tag{2.77}$$

thus for a solution λ, $-\lambda$ is also a solution. Additionally, the polynomial is real hence $(\bar{\lambda}, -\bar{\lambda})$ are also solutions of Equation 2.76. Furthermore, $\det(\Omega) \equiv \det(-\mathcal{C}^{-1}\mathcal{A}) = 0$ is the condition required for λ to vanish. From Equation 2.66 and the structure of $\mathcal{A}$ we can see that $\vec{v} = (0,0,0,1,0,0)^T$ is an eigenvector of $\mathcal{A}$ with eigenvalue 0. Therefore, $\lambda = 0$ has the eigenvector $(\vec{v}, \vec{z})^T = (0,0,....,0,1,0,0)^T$. We note that, (again) due to the symmetric properties of $\mathcal{A}, \mathcal{B}, \mathcal{C}$, the $\lambda = 0$ eigenvalue has algebraic multiplicity of at least 2. These should be discarded as they are not a solution of Equation 2.63.
Of the 10 remaining eigenvalues 5 will have the positive real parts that we are interested in for decaying solutions. We choose to order them by decreasing real part, $\lambda_1, \lambda_2, ..., \lambda_5$ with corresponding modes $\vec{v}_1, ..\vec{v}_5$. We call $\vec{v}_1$ the dominant mode, as for large x_1 this mode will dominate the solution to Equation 2.63. However, for some defects the modes, $\vec{v}_2, ..., \vec{v}_5$, may still be relevant phenomenologically. We note that,

$$\vec{w}(x_1) = \sum_{i=1}^{5} c_i \vec{v}_i e^{-\mu_i x_1} \ , \tag{2.78}$$

where the constants c_i are determined from the boundary conditions and nonlinear solutions. If $c_i = 0$ then the mode $\vec{v}_i$ is not excited and therefore does not contribute to the behaviour of the nonlinear solutions in the linear region of the model.

Coupled Modes

Here we present a way of classifying how mixed the modes are between magnetic and matter modes. If we consider each,

$$\vec{v}_i = (v_i^1, v_i^2, v_i^3, v_i^4, v_i^5, v_i^6)^T \ , \tag{2.79}$$

with $i \in \{1, 2, ..., 5\}$ then each of the six components corresponds to a different field, as shown in Equation 2.62. Thus for example the exponential decay of $\vartheta(x_1)$, in the linear region of the model, is,

$$\vartheta(x_1) = \sum_{i=1}^{5} c_i v_i^3 e^{-\mu_i x_1} \ , \tag{2.80}$$

where normally the leading length scale $i = 1$ contributes most significantly to the behaviour of $\vartheta(x_1)$. Thus v_i^5, v_i^6 are the magnetic and then v_i^1, v_i^2, v_i^3 are the matter modes. We note that v_i^4 (which corresponds to the p_1 field) is redundant in that it does not contribute to the magnetic field nor the condensates. If we then consider $\vec{v}_i$ as a vector in $\mathbb{R}^5$, with the v_i^4 dimension removed, we can define the mixing angle for each mode,

$$\cos\theta_m^i = \sqrt{|v_i^1|^2+|v_i^2|^2+|v_i^3|^2} \tag{2.81}$$

$$\sin\theta_m^i = \sqrt{|v_i^5|^2+|v_i^6|^2} \ . \tag{2.82}$$

Note that we choose to normalise the v_i as,

$$|v_i^1|^2+|v_i^2|^2+|v_i^3|^2+|v_i^5|^2+|v_i^6|^2 = 1 \ , \tag{2.83}$$

such that the equality $\left(\cos\theta_m^i\right)^2 + \left(\sin\theta_m^i\right)^2 = 1$ holds for all values of θ_m^i. If $\theta_m^i = 0$ then we classify our mode as purely matter. If $\theta_m^i = \frac{\pi}{2}$ then it is purely magnetic and for $0 < \theta_m^i < \frac{\pi}{2}$ then it is mixed which occurs for some modes and orientations in anisotropic superconductors. Additionally, if θ_m^i is closer to 0 than $\frac{\pi}{2}$ we could describe that mode as a mixed matter mode and if it is closer to $\frac{\pi}{2}$ then it would be a mixed magnetic mode.
Finally, if we set $Q_{ij}^{\alpha\beta} = \delta^{\alpha\beta}\delta_{ij}$ and $\eta_{12} = \gamma_{12} = 0$ in the potential, F_p, then the linearised Equations 2.59, 2.60 and 2.61 will decouple and we get purely matter and magnetic modes. We note that this is identical to recovering the concept of a coherence and penetration length scales, as discussed in Section 1.3.3. Note that the matrix $\mathcal{C}$ is not invertible in this case so the length scales can be found via a different method [38]. However, if our superconductor is anisotropic, $Q_{ij}^{\alpha\beta} \neq \delta^{\alpha\beta}\delta_{ij}$, then at least some of the modes will be coupled. So the modes $\vec{v}_1, ..., \vec{v}_5$ are no longer associated with a specific field and are in fact linear combinations of each field. This is used and expanded upon in Chapter 3.

Magnetic Field Twisting

It is vital to note that the normal ansatz used for a linearisation would be to keep only a single component of p_i, which is equivalent to fixing the direction of the magnetic field. In terms of our modes it means assuming $v_i^4 = v_i^6 = 0$. However, as discussed in Section 2.2.1, this ansatz is inconsistent with the full equations of motion for an anisotropic superconductor. Now when we use Ansatz 2.14 we retain all three components of p_i allowing for the mixing of magnetic field modes. Our choice of ansatz, which keeps $p_3 \neq 0$, means we have a linear magnetic field, $B_{lin} = (0, -p_3', p_2')$, that depends only on p_2 and p_3. Note that p_2 and p_3 may

become undefined away from the linear region where ψ_α can vanish and thus θ_α is undefined. For the linear theory the linear magnetic field direction can be approximated as,

$$B_{lin} \propto \mathrm{Re}(0, -v_1^6, v_1^5) \ , \tag{2.84}$$

where it is the dominant mode, $\vec{v}_1$, that determines the direction of the magnetic field.
If the direction of the spontaneous or internal magnetic field, B, in the nonlinear region differs from the direction in the linear region, B_{lin}, then we can expect the magnetic field to change direction or twist as $x_1 \to \infty$. This, of course, will depend upon whether the dominant mode is excited or not.
This is most pronounced for the Meissner state, which will be explored in Chapter 3, where we can choose the direction of the external magnetic field, H, to be different from B_{lin} and thus force magnetic field twisting into the system. However, we do still see magnetic field twisting in domain walls.

Oscillating Tails

The linearisation predicts that if the dominant mode is complex then it is possible to see the fields, $\epsilon_\alpha, \vartheta, p_i$, oscillate in the linear region, $x_1 \to \infty$, of a defect. The existence of complex length scales, $\lambda_i \in \mathbb{C}$, is down to the coupling of the matter and magnetic fields in Equations 2.59, 2.60 and 2.61. If we consider the isotropic case, $Q_{ij}^{\alpha\beta} = \delta^{\alpha\beta}\delta_{ij}$, then the length scales become real again. Whether the fields oscillate depends upon the dominant mode being complex or not, this can be written as,

$$\vec{w}_1 = \vec{v} e^{-\mathrm{Re}\,(\mu_1)x_1} \cos\left(\mathrm{Im}\,(\mu_1)x_1\right) \tag{2.85}$$

$$= (\epsilon_1(x_1), \epsilon_2(x_1), \vartheta(x_1), p_1(x_1), p_2(x_1), p_3(x_1))^T e^{-\mathrm{Re}\,(\mu_1)x_1} \cos\left(\mathrm{Im}\,(\mu_1)x_1\right) \ , \tag{2.86}$$

we see that if, $\mathrm{Re}\,(\mu_1)$, is small relative to $\mathrm{Im}\,(\mu_1)$ then we can expect oscillations of the fields in the linear regions of a domain wall, for example. Whether we see oscillating tails or not is governed by the ratio,

$$R_{\mu_1} = \frac{\mathrm{Im}\,(\mu_1)}{\mathrm{Re}\,(\mu_1)} \ . \tag{2.87}$$

If $\mathrm{Im}(\mu_1) = 0$ then $R_{\mu_1} = 0$ and there we have no oscillations. However, as $R_{\mu_1} \to 1$ we approach the case where the fields decay slowly enough, relative to the period of the oscillations, such that we see their oscillations in the nonlinear solutions
Section 2.4.3 explores oscillations in $p+ip$ superconductors where, for some orientations, the ratio in Equation 2.87 is large enough that we see oscillations in the nonlinear simulations. For the $s+is$ and $s+id$ domain walls, although we have complex length scales, the oscillations are too heavily damped to be seen in the nonlinear solutions.

2.4 Domain Walls in $p+ip$ Superconductors

The $p+ip$ model allows us to explore the effects of anisotropy on a domain wall. The model is interesting as it has two non-degenerate in energy domain wall solutions depending on the choice of boundary conditions. We build on the work of [26] and [39] by considering orientations away from the basal plane, $\hat{x}_1 = (\cos\chi, \sin\chi, 0), \chi \in [0, 2\pi]$. We produce numerical solutions using the arrested Newton flow method outlined in Section 2.2.3 with the ansatz given in Equation 2.14 where we allow $A_3 \neq 0$. This model also allows us to confirm that the oscillations in the fields, predicted by the linearisation and detailed in Section 2.3, occur when we solve the full non-linear Ginzburg-Landau equations. Thus extending the results of

[37] to domain walls.

A $p+ip$ superconductor is identifiable by the symmetries that the associated free energy obeys. A symmetry is a transformation of the coordinates/condensates that leaves the free energy unchanged. These symmetries are set via the choice of anisotropy matrices, $Q^{\alpha\beta}$, and the choice of potential parameters, all of which can be microscopically (that is not phenomenologically) derived [40]. We present such a microscopically derived three-dimensional free energy functional for a $p+ip$ superconductor [[41],[26]],

$$\begin{aligned} F^b = \int_{\mathbb{R}^3} \Bigg(& K_1 \left(\left| \mathcal{D}_1 \psi_1^b \right|^2 + \left| \mathcal{D}_2 \psi_2^b \right|^2 \right) + K_2 \left(\left| \mathcal{D}_1 \psi_2^b \right|^2 + \left| \mathcal{D}_2 \psi_1^b \right|^2 \right) \\ & + \{ K_3 (\mathcal{D}_1 \psi_1^b)^* (\mathcal{D}_2 \psi_2^b) + K_4 (\mathcal{D}_1 \psi_2^b)^* (\mathcal{D}_2 \psi_1^b) + c.c. \} \\ & + K_5 \left(\left| \mathcal{D}_3 \psi_1^b \right|^2 + \left| \mathcal{D}_3 \psi_2^b \right|^2 \right) + \frac{(B^b)^2}{8\pi} + \left(F_p - F_p(u_1, u_2, \pm\frac{\pi}{2}) \right) \Bigg) \, dx_1^b dx_2^b dx_3^b \end{aligned} \tag{2.88}$$

$$F_p = a_p((\rho_1^b)^2 + (\rho_2^b)^2) + b_1((\rho_1^b)^2 + (\rho_2^b)^2)^2 + b_3(\rho_1^b)^2(\rho_2^b)^2 + b_2(\rho_1^b)^2(\rho_2^b)^2 \cos(2\theta_{12}) \ , \tag{2.89}$$

where $\mathcal{D}_i = \partial_i - ieA_i$ and the u_α are the vacuum values of $|\psi_\alpha| = \rho_\alpha$. This free energy is not of the form of Equation 2.11 so we use the superscript b, $\Box^b$, to highlight that the coordinates and fields differ from those in Equation 2.11.

The potential, F_p, requires $a_p < 0$, $b_2 > 0$, $b_2 > b_3$ and $4b_1 > b_2 - b_3$ for the broken time reversal symmetry (BTRS) vacuum state of $(u_1 \neq 0, u_2 \neq 0, \theta_{12} = \pm\frac{\pi}{2})$ to be energetically stable. The anisotropy matrices, $Q^{\alpha\beta}$, are,

$$Q^{11} = \begin{pmatrix} K_1 & 0 & 0 \\ 0 & K_2 & 0 \\ 0 & 0 & K_5 \end{pmatrix} \tag{2.90}$$

$$Q^{22} = \begin{pmatrix} K_2 & 0 & 0 \\ 0 & K_1 & 0 \\ 0 & 0 & K_5 \end{pmatrix} \tag{2.91}$$

$$Q^{12} \equiv (Q^{21})^T = \begin{pmatrix} 0 & K_3 & 0 \\ K_4 & 0 & 0 \\ 0 & 0 & 0 \end{pmatrix} \ . \tag{2.92}$$

Before analysing the symmetries of this model we re-parametrise and rescale Equation 2.88 so it has fewer parameters and is in the form of Equation 2.27. The reparametrisation is as follows,

$$K_1 = K\frac{3+\nu}{4}, K_2 = K_3 = K_4 = K\frac{1-\nu}{4} \tag{2.93}$$

$$K_5 = \frac{K}{4}k_5 \tag{2.94}$$

$$b_1 = b\frac{3+\nu}{8}, b_2 = b\frac{1-\nu}{4}, b_3 = -b\frac{1+3\nu}{4} \ , \tag{2.95}$$

with $\nu \in [-1, 1]$. This simplifies the parameter space to the material dependent parameters b, K and ν which sets the anisotropy of the model. We note that unlike, [26], we keep $K_5 \neq 0$ so the anisotropy matrices are 3×3 which allows us to investigate orientations away from the basal plane.

We now rescale the condensates and spatial coordinated, adapted from [37], to convert the free energy, F^b, into the more convenient form of Equation 2.11. We start with the following

rescalings;

$$\psi_\alpha = \frac{\psi^b_\alpha}{\lambda},\ \lambda := \sqrt{\frac{-a_p}{b}} \tag{2.96}$$

$$A_i = \frac{A^b_i}{\lambda_A},\ \lambda_A := \lambda\sqrt{4\pi K} \tag{2.97}$$

$$x_i = \frac{x^b_i}{\lambda_x},\ \lambda_x := \frac{1}{e\lambda_A}\ , \tag{2.98}$$

and finally we rescale the free energy, F,

$$F = \frac{F^b}{\lambda_F},\ \lambda_F := \frac{K\lambda^2}{2}\frac{1}{\lambda_A}. \tag{2.99}$$

The extra factor of $\frac{1}{\lambda_A}$ in the free energy rescaling is due to our model being three-dimensional. Finally,

$$V_0 = \frac{b}{2\pi e^2 K^2}\ , \tag{2.100}$$

to give the three-dimensional, orientation dependent, $p + ip$ model,

$$F = \int_{\mathbb{R}^3} \left(\frac{1}{2}\tilde{Q}^{\alpha\beta}_{ij}(D_i\psi_\alpha)^*(D_j\psi_\beta) + \frac{B^2}{2} + V_0 \left(F_p - F_p(u_1, u_2, \pm\frac{\pi}{2}) \right) \right) dx_1 dx_2 dx_3 \tag{2.101}$$

$$Q^{11} = \begin{pmatrix} 3+\nu & 0 & 0 \\ 0 & 1-\nu & 0 \\ 0 & 0 & k_5 \end{pmatrix} \tag{2.102}$$

$$Q^{22} = \begin{pmatrix} 1-\nu & 0 & 0 \\ 0 & 3+\nu & 0 \\ 0 & 0 & k_5 \end{pmatrix} \tag{2.103}$$

$$Q^{12} \equiv (Q^{21})^T = \begin{pmatrix} 0 & 1-\nu & 0 \\ 1-\nu & 0 & 0 \\ 0 & 0 & 0 \end{pmatrix} \tag{2.104}$$

$$F_p = -(\rho_1^2 + \rho_2^2) + \frac{1}{8}(3+\nu)(\rho_1^2 + \rho_2^2)^2 - \frac{1}{4}(1+3\nu)\rho_1^2\rho_2^2 + \frac{1}{4}(1-\nu)\rho_1^2\rho_2^2\cos(2\theta_{12})\ , \tag{2.105}$$

with $D_i = \partial_i - iA_i$. We note that $\tilde{Q}^{\alpha\beta} = M^T Q^{\alpha\beta} M$. Performing a coordinate transformation such that the $\hat{x}_1$ direction is changed and then applying Ansatz 2.14 to fix the dependence of the fields on only that direction is how the orientation of a domain wall solution is changed. This was previously discussed in Section 2.2.1.

We are now left with three parameters, ν, k_5 and $V_0 = \frac{b}{2\pi e^2 K^2}$, along with the orientation, $\hat{x}_1$, the changing of which allows us to explore the possible domain wall solution in our the $p + ip$ model. We note that the introduction of the transformation $Q^{\alpha\beta} \mapsto M^T Q^{\alpha\beta} M$, for $M \in SO(3)$, has no effect on the three-dimensional energy as this is just equivalent to a coordinate transformation. However, if we apply our dimensional reduction Ansatz 2.14, then this coordinate transformation will change the orientation of our domain wall, within this anisotropic superconductor, which **will** affect the now one-dimensional free energy. Thus solving the dimensionally reduced Ginzburg-Landau equations for different, M, yields different field solutions.

The potential, F_p, of Equation 2.101 is invariant under the transformations,

$$(\psi_1, \psi_2) \mapsto (\psi_2, \psi_1) \tag{2.106}$$
$$(\psi_1, \psi_2) \mapsto (-\psi_2, \psi_1) \ , \tag{2.107}$$

but the free energy, F, is not. This is because the free energy is only invariant under the transformation of both the condensates, ψ_α, and the spatial coordinates, (x_1, x_2, x_3) which we call mixed symmetries. The main mixed symmetries of the $p + ip$ model are, $C_4(z) \times C_2(x) \times C_2(y)$. Table 1.2 gives the actions of these symmetries on both the condensates and coordinates. The spatial symmetries are written in terms of the crystalline coordinates, (x, y, z), which are defined relative to the symmetry axes of the superconductor. For example, we see that the transformations for the $C_4(z)$ mixed symmetry,

$$(x, y, z) \mapsto (-y, x, z) \tag{2.108}$$
$$(\psi_1, \psi_2) \mapsto (-\psi_2, \psi_1) \ , \tag{2.109}$$

leave the free energy unchanged. This was previously discussed in 1.8.1 where a mixed symmetry must satisfy the following:

1. $S_{ki} Q_{ij}^{\alpha\beta} S_{lj} \equiv Q_{kl}^{\alpha\beta}$.
2. $C^{\gamma\alpha} Q_{ij}^{\alpha\beta} C^{\delta\beta} \equiv Q_{ij}^{\gamma\delta}$ and $F_p(C^{\alpha\gamma}\psi_\gamma) \equiv F_p(\psi_\alpha)$.

$S \in O(3)$ and $C \in O(2)$ are the matrix representations of the spatial and condensate symmetries respectively. The spatial symmetries require that the orientation transformation, Equation 2.29, has no affect on the anisotropy matrices.
Furthermore, the $C_4(z)$ condensate symmetry of potential, F_p, means that $F_p(\psi_1, \psi_2) \equiv F_p(-\psi_2, \psi_1)$ thus $u_1 = u_2$ and therefore the two gauge inequivalent vacua are given by,

$$(\psi_1, \psi_2) = (1, e^{-i\frac{\pi}{2}}) e^{i\omega_1} \tag{2.110}$$
$$(\psi_1, \psi_2) = (1, e^{i\frac{\pi}{2}}) e^{i\omega_2} \ , \tag{2.111}$$

up to a choice of global gauge, $\omega_1, \omega_2 \in [0, 2\pi]$, and $u_1 = 1$ due to our rescaling. We remind the reader that the general gauge transformation is given by,

$$\psi_\alpha \mapsto e^{i\omega} \psi_\alpha \tag{2.112}$$
$$A_i \mapsto A_i + \partial_i \omega \ . \tag{2.113}$$

For a domain wall solution each boundary has a different choice of global gauge. This is depicted in Figure 2.3. We see that each boundary has a choice of values on the unit circle set by ω_1 and ω_2. However, our system still allows us to make a gauge choice and thus remove ω_1 and ω_2. We can trivially fix one boundary via the following, global, gauge transformation, $\psi_\alpha \mapsto e^{-i\omega_2}$ which leaves the vector potential unchanged. Additionally, we can fix both boundaries, using a local gauge transformation, at the cost of modifying the values of A_i. The necessary gauge would be an ω that has $\omega(-\infty) = -\omega_1, \omega(\infty) = -\omega_2$ and $\partial_1 \omega(x_1 = \pm\infty) = 0$. This would fix $\omega_1 = \omega_2 = 0$ as well as leaving A_i unchanged on the boundary.

2.4.1 Domain Wall Types

The $p + ip$ model allows two special types of domain walls to occur which are identifiable by which condensate vanishes at $x_1 = 0$. If we consider, Figure 2.3, and apply the global gauge

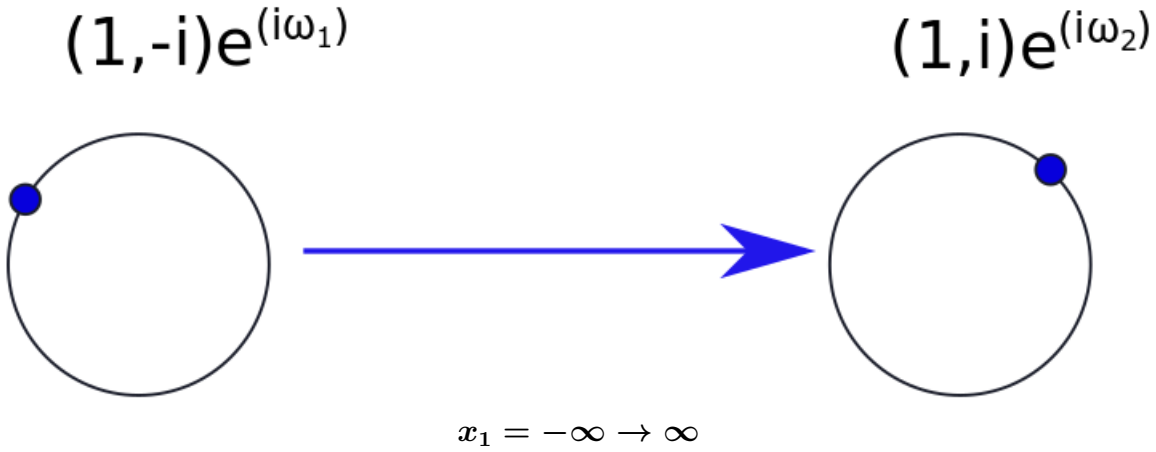

Figure 2.3: *Diagram of the boundary values of* (ψ_1, ψ_2) *for a domain wall,* $x_1 = \pm\infty$*, on the right and left hand side respectively. We see that the gauge choice* $(\omega_1, \omega_2 \in [0, 2\pi])$*, for a given vacuum solution can be expressed as a point on a circle, where the value of* (ψ_1, ψ_2) *is given by the blue dot.*

transformation, $\omega = -\omega_1$, which changes the boundary conditions to,

$$\lim_{x_1 \to -\infty} (\psi_1, \psi_2) = e^{i(\omega_1 - \omega_2)}(1, -i) \tag{2.114}$$

$$\lim_{x_1 \to -\infty} (\psi_1, \psi_2) = (1, i) \ . \tag{2.115}$$

If we choose $(\omega_1 - \omega_2) = 0$ and $(\omega_1 - \omega_2) = \pi$ the left boundary becomes $(1, -i)$ and $(-1, i)$ respectively.
Numerically, we start with an initial condition and then evolve it using arrested Newton flow. This method only finds the local minimum closest in phase space to the initial condition used. If we use a simple initial condition (such as a Sine-Gordon kink with the correct boundary conditions, see Section 1.5) we can, through the choice of boundary conditions, make the desired domain wall type the local minimum. For a $p + ip$ domain wall these two choices, of gauge equivalent boundaries, are,

$$\psi_2 \ DW: \quad \lim_{x_1 \to \pm\infty} (\psi_1, \psi_2) = (1, \pm i) \tag{2.116}$$

$$\psi_1 \ DW: \quad \lim_{x_1 \to \pm\infty} (\psi_1, \psi_2) = (\pm 1, i) \ , \tag{2.117}$$

which we will see are non degenerate in energy. These two boundary conditions are depicted in Figure 2.4. If we consider the ψ_2 *DW* boundary condition we see that it forces $\mathrm{Im}(\psi_2) = 0$ at least once as ψ_2 interpolates from $-i \to i$. In this case having $\mathrm{Re}(\psi_2)$ vanish at the same point that $\mathrm{Im}(\psi_2)$ vanishes is likely to be the local minimum found by the arrested Newton flow method. Therefore, the numerical method with these boundary conditions returns a ψ_2 *DW*. However, we note that this boundary condition does not force a ψ_2 *DW* domain wall to occur. It may be possible, with a very complicated initial condition, to yield at ψ_1 *DW* solution. This does not happen for any of our results as we use a simple initial condition for all solutions.
We remind the reader that numerically we fix the values of the fields on the boundaries, stopping them from evolving. This stops the value of $(\omega_1 - \omega_2)$ from changing and therefore biases the type of domain wall solution that is the local minimum through our choice of $(\omega_1 - \omega_2)$. We label these two domain walls as a ψ_2 and ψ_1 domain wall to denote which condensate

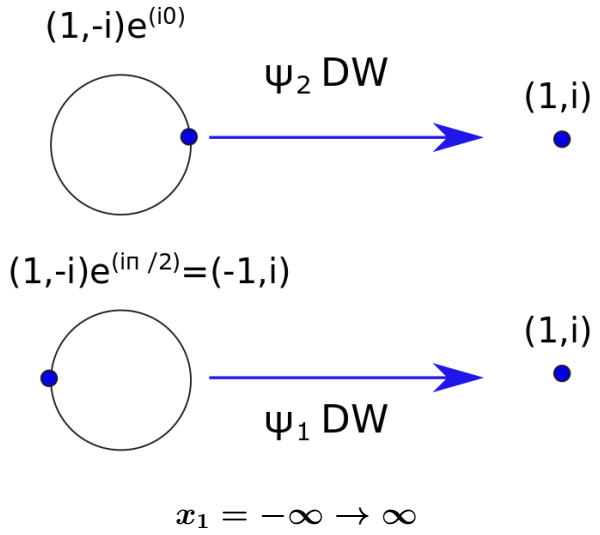

Figure 2.4: *Diagram of the boundary values of* (ψ_1, ψ_2) *for the* ψ_2 *and* ψ_1 *domain wall types in a* $p + ip$ *superconductor, with* $x_1 = \pm\infty$ *on the right and left hand side respectively. We see that the gauge choice for a given vacuum solution can be expressed as a point on a circle, where the value of* (ψ_1, ψ_2) *is given by the blue dot.*

vanishes at the centre of the domain, $x_1 = 0$. Note that the ψ_2 *DW* boundary condition is the version more commonly used for a general domain wall, although it is gauge equivalent to the ψ_1 *DW* boundary condition, which is why we put it first.
Figures 2.5a and 2.5b show plots of these two types of domain walls for two different orientations. We remind the reader that, $B = (B_1, B_2, B_3)$ gives the spontaneous magnetic field in the $\hat{x}_1, \hat{x}_2, \hat{x}_3$ directions respectively. That is the magnetic field that arises inside the superconductor due to the domain wall and the anisotropy of the superconductor. We see that the ψ_2 *DW* has its $|\psi_2|$ condensate vanish at $x_1 = 0$, whereas it is $|\psi_1|$ that vanishes for the ψ_1 *DW*. This is important as the point $\psi_\alpha = 0$ cannot be removed via a gauge transformation thus a ψ_2 *DW* solution is fixed due to the fact that ψ_2 vanishes at one point. The two chosen orientations, $\hat{x}_1 = (1, 0, 0)$ and $\hat{x}_1 = (0, -1, 0)$, are both in the basal plane and a (spatial) $C_4(z)$ rotation away from each other. The free energies (per unit area) for the ψ_2 and ψ_1 domain wall are F_{ψ_2} and F_{ψ_1} respectively. We note that F_{ψ_1}, for $\hat{x}_1 = (1, 0, 0)$, is equal to the value of F_{ψ_2}, for $\hat{x}_1 = (0, -1, 0)$. Due to our choice of Ansatz 2.14, $B_1 = 0$ for every orientation so we do not display it. We note that B_2 vanishes everywhere for these two basal plane orientations where we have fixed $\hat{x}_3 = (0, 0, 1)$, the crystalline z axis.

Finally, we reiterate that it is the choice of boundary condition for the, $x \to -\infty$, or left hand boundary that biases the arrested Newton flow algorithm to produce one domain wall type over the other. Consider the orientation, $\hat{x}_1 = (1, 0, 0)$, where the ψ_2 domain wall has lower energy than the ψ_1 domain wall. If we run a numerical simulation, for that orientation, where we fix the boundary conditions to $\lim_{x_1 \to \pm\infty}(\psi_1, \psi_2) = (\pm 1, i)$, we are in fact making the, higher energy, ψ_1 domain wall the local minimum. If we allow the choice of $\omega_1 - \omega_2$, on the boundary to vary then either domain wall would occur. Numerically we always fix the boundary conditions. However, if we fix the boundaries to the following,

$$\begin{aligned} \text{mixed } DW: \lim_{x_1 \to -\infty}(\psi_1, \psi_2) = e^{i\frac{\pi}{4}}(1, -i) &= \frac{1}{\sqrt{2}}(1 + i, 1 - i) \\ \text{mixed } DW: \lim_{x_1 \to \infty}(\psi_1, \psi_2) &= (1, i)\ , \end{aligned} \tag{2.118}$$

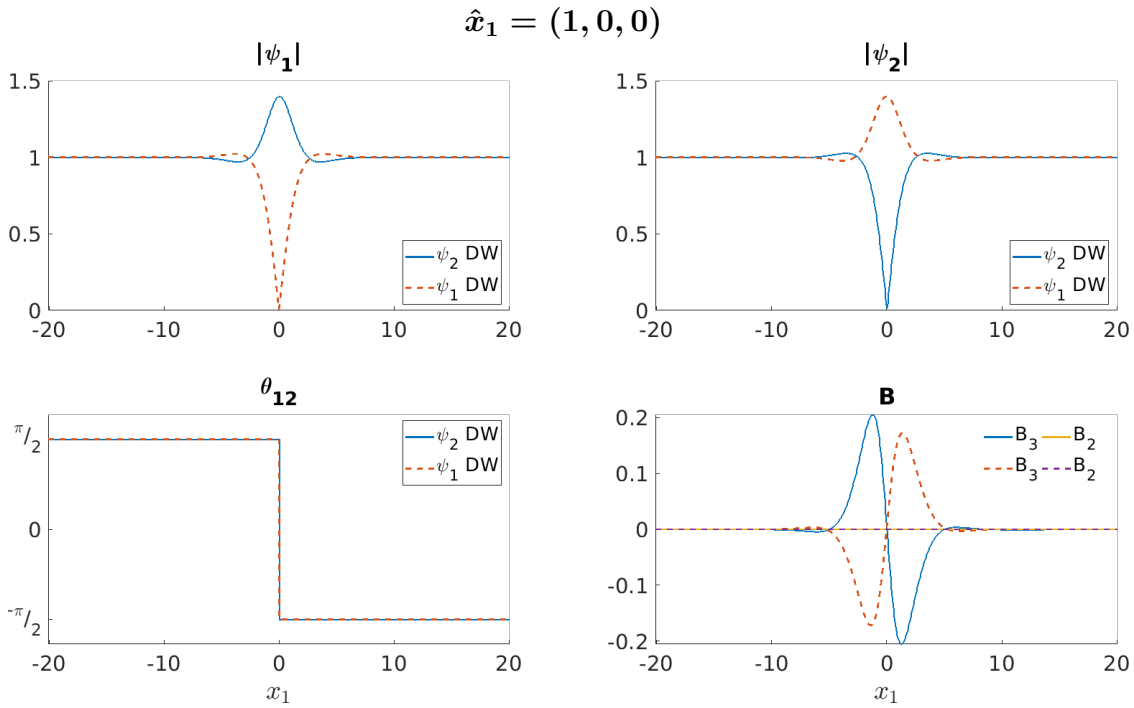

(a) *The free energies of the two domain walls are,* $F_{\psi_2} = 0.35$ *and* $F_{\psi_1} = 0.43$ *respectively.*

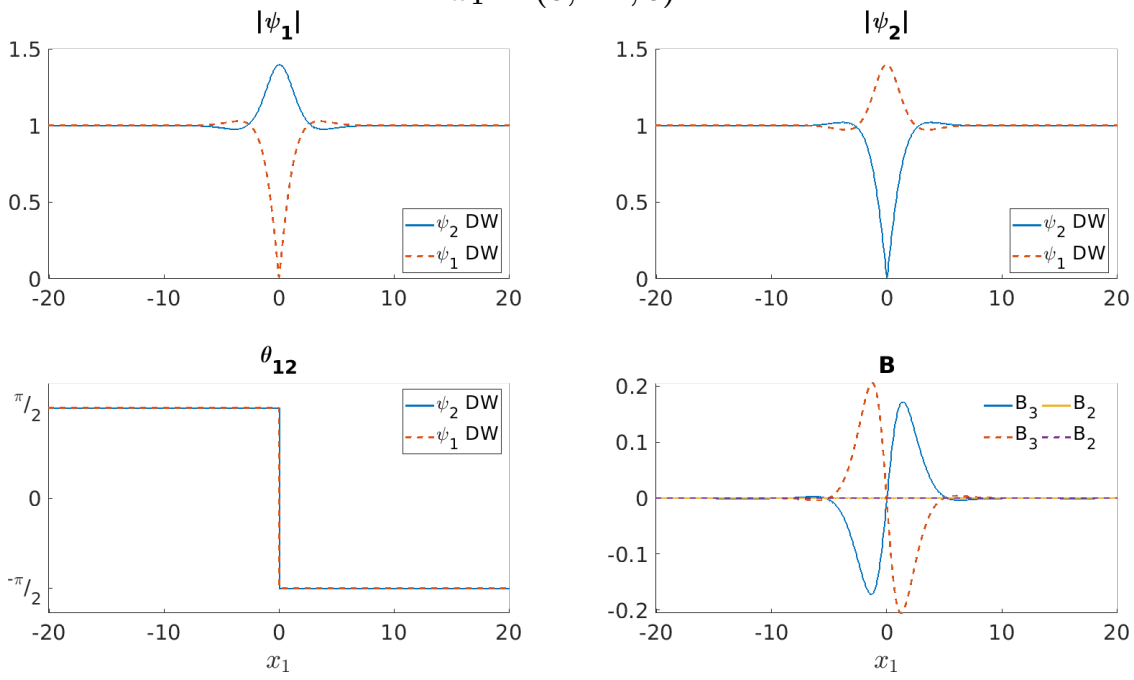

(b) *The free energies of the two domain walls are,* $F_{\psi_2} = 0.43$ *and* $F_{\psi_1} = 0.35$ *respectively.*

Figure 2.5: *Plots of the two domain wall types, for a* $p+ip$ *superconductor, corresponding to the vanishing of the* ψ_2 *or* ψ_1 *condensate at the centre of the domain,* $x_1 = 0$*. We have plotted the key gauge invariant quantities* $|\psi_\alpha|$*,* θ_{12}, B_2, B_3*, where the components of the magnetic field,* B_2 *and* B_3*, are in the* $\hat{x}_2$ *and* $\hat{x}_3$ *directions respectively. The dashed lines represent the* ψ_1 *domain walls and the undashed the* ψ_2 *domain walls. We note that for these two orientations,* $\hat{x}_3 = (0, 0, 1)$*, which is equivalent to the crystalline* z *axis,* $\hat{z}$*. We see that* B_2*, the* $\hat{x}_2$ *component of the magnetic field, vanishes for both orientations.*
The parameters used are; $(\nu, V_0, k_5) = (-0.95, 6, 2.3500)$

we do not favour either type of domain wall so the arrested Newton flow algorithm returns either a ψ_1 domain wall or a ψ_2 domain wall to occur depending on which one has a lower energy. We call this a mixed boundary condition, and they are an efficient way of finding the minimum energy domain wall for a given orientation. Previously we would have had to simulate both domain wall types and then compare their energies to find the globally minimum domain wall type.
This can alternatively be understood by considering the phase, θ_α where $\psi_\alpha = |\psi_\alpha|e^{i\theta_\alpha}$, for each domain wall boundary condition. We see that,

$$\psi_2 \ DW: \quad \lim_{x_1\to\pm\infty}(\theta_1,\theta_2) = (0,\pm\frac{\pi}{2}) \tag{2.119}$$

$$\psi_1 \ DW: \quad \lim_{x_1\to-\infty}(\theta_1,\theta_2) = (-\pi,\frac{\pi}{2}) \tag{2.120}$$

$$\psi_1 \ DW: \quad \lim_{x_1\to+\infty}(\theta_1,\theta_2) = (0,\frac{\pi}{2}) \ , \tag{2.121}$$

there is a π phase change from the left to the right boundary in the θ_α for the associated ψ_α DW but more importantly there is no change in phase in the other condensate. The mixed boundary condition that arises from choosing, $\omega_1 - \omega_2 = \frac{\pi}{4}$, gives the following phase change,

$$\text{mixed } DW: \quad \lim_{x_1\to-\infty}(\theta_1,\theta_2) = (\frac{\pi}{4},-\frac{\pi}{4}) \tag{2.122}$$

$$\text{mixed } DW: \quad \lim_{x_1\to+\infty}(\theta_1,\theta_2) = (0,\frac{\pi}{2}) \ . \tag{2.123}$$

We see it is now non zero in both condensates which we find allows solutions of the Ginzburg-Landau equations, 1.124 and 1.125, to relax to whichever domain wall type has the lower energy.

2.4.2 Solutions in the Basal Plane

In this section we explore the dependence of the free energy and spontaneous magnetic field on the orientation of the domain wall within the basal plane. The basal plane refers to the crystalline $\hat{x},\hat{y}$ plane. The coordinates for the basal plane orientations can be parametrised by, θ_B, and written as follows,

$$(x_1,x_2,x_3) = (x\cos\theta_B - y\sin\theta_B, x\sin\theta_B + y\cos\theta_B, z)^T \ , \tag{2.124}$$

where θ_B is the angle that $\hat{x}_1$ makes with the crystalline $\hat{x}$ axis. We point out that it is the $\hat{x}_1$ direction, the perpendicular direction to the domain wall, that lies in the basal plane not the domain wall itself. With a starting values, θ_S, and an interval, $\delta\theta_B$, we can find numerical solutions to the Ginzburg-Landau equations of motion, for both domain wall types, that will vary with θ_B. This is useful in demonstrating the anisotropy within the basal plane as well as any symmetries of the free energy. Starting at $\theta_S = 0$ the ψ_2 domain wall is of lower energy. The method is as follows:

- We run two simulations each with one of the ψ_2 and ψ_1 DW boundary conditions, given in 2.117, which fixes the domain wall type. This allows us to generate both ψ_1 and ψ_2 domain walls for all orientations.
- We produce a solution for $\theta_B = \theta_S$ using the arrested Newton flow method, see Section 2.2.3.
- Then using this solution as the initial condition for the next simulation, which still fixes the domain wall type and decrease run times, we run solutions for $\theta_B \in [\theta_S, \theta_S + \pi]$

where we change the value of θ_B recursively by adding the interval, $\delta\theta_B$, for each new simulation until we reach $\theta_B = \theta_S + \pi$.

- This method is called using **subsequent initial conditions**.
- If we want the minimising domain wall solution for every θ_B we can compare the energies of these two simulations and select the domain wall type with the lower energy.
- Alternatively, we could use mixed boundary conditions 2.118 and then instead use the same general initial conditions for every value of θ_B. This means we do not bias results to a single domain wall type hence the result would be whatever domain wall type had the lower energy for the current value of θ_B.
- This method is called using **same initial conditions**. This method takes more time than using subsequent initial conditions but for one-dimensional solutions the difference is not that significant.

The spontaneous or internal magnetic field is an odd function, when non zero, due to the topological requirement that, $\int_{\mathbb{R}} B_i(x_1)\, dx_1 = 0$. This can be seen in Figures 2.5a and 2.5b. The maximum spontaneous magnetic field is then given by,

$$B_{max} = \max(|B|)\ , \tag{2.125}$$

which occurs at two points which we call $\pm x_{max}$, where $B(\pm x_{max}) = \pm B_{max}$. Now consider Figures 2.6a and 2.6b which plot how the free energy and maximum magnetic field vary with θ_B. We see how the ψ_2 domain wall has a lower energy in the regions, $\theta_B \in \left[0, \frac{\pi}{4}\right]$ and for $\theta_B \in \left[\frac{3\pi}{4}, \pi\right]$, the free energy, for both domain wall types, is also periodic on π. Most interestingly we have non-zero magnetic field even for $\theta_B = 0$ and match the results of [26]. This is not a trivial result as the spontaneous magnetic field is zero in the isotropic case and even for other anisotropic models it is zero when $\theta_B = 0$.

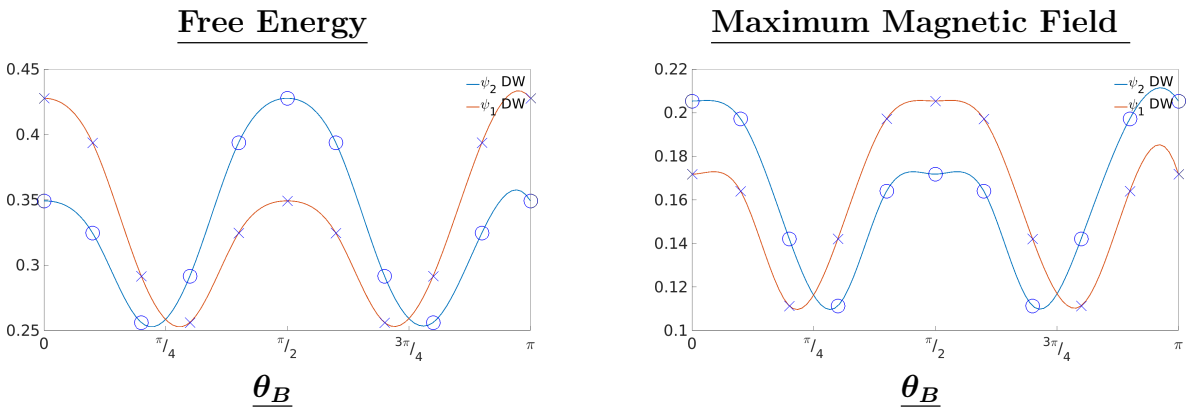

(a) *The free energy (per unit area).*

(b) *The Maximum Magnetic Field,* $B_{max} = \max|B(x_1)|$.

Figure 2.6: *A plot of the free energy per unit area of the domain wall and the associated maximum magnetic field as a function* $\theta_B = \arctan\frac{x_1(2)}{x_1(1)}$ *which parametrises rotation of the domain wall in the basal plane. The energies and maximum magnetic field for the* ψ_2 *and* ψ_1 *domain wall types are shown.*
The parameters used are; $(\nu, V_0, k_5) = (-0.95, 6, 2.35)$ *and interpolation was used to create smooth plots with the simulated points marked by* ○ *and* ×.

Is $A_3 = 0$ a consistent ansatz for the basal plane?

Previous work ([26], [37]) has studied the basal plane using a two-dimensional free energy which is equivalent to applying the ansatz that, $A_3 = 0$ to our three-dimensional free energy. We now include a discussion on why this is valid **but** only in the basal plane. We can show that for any orientation in the basal plane, $A_3 = 0$, is a solution to the equations of motion. In Section 2.2.1, we established that an ansatz needed to be consistent with the three-dimensional Ginzburg-Landau equations to be valid for our domain walls when dealing with anisotropic superconductors.
Consider the general three-dimensional anisotropy matrices for the $p + ip$ model,

$$Q^{11} = \begin{pmatrix} a_1 & 0 & 0 \\ 0 & a_2 & 0 \\ 0 & 0 & b \end{pmatrix} , Q^{22} = \begin{pmatrix} a_2 & 0 & 0 \\ 0 & a_1 & 0 \\ 0 & 0 & b \end{pmatrix} , Q^{12} = \begin{pmatrix} 0 & a_2 & 0 \\ a_2 & 0 & 0 \\ 0 & 0 & 0 \end{pmatrix} , \tag{2.126}$$

where $a_1 = 3 + \nu$ and $a_2 = 1 - \nu$. These are the anisotropy matrices for the orientation, $\hat{x}_1 = (1, 0, 0)$, which corresponds to the crystalline $\hat{x}$ axis. If we rotate the coordinate system and therefore the domain wall orientation by transforming each anisotropy matrix, $\tilde{Q}^{\alpha\beta} \mapsto M^T Q^{\alpha\beta} M$ where,

$$M = \begin{pmatrix} \cos\theta_B & -\sin\theta_B & 0 \\ \sin\theta_B & \cos\theta_B & 0 \\ 0 & 0 & 1 \end{pmatrix} . \tag{2.127}$$

This transforms the orientation of our domain wall to $\hat{x}_1 = (\cos\theta_B, \sin\theta_B, 0)$ which is still in the basal plane. The form of the transformed anisotropy matrices are given as,

$$\tilde{Q}^{11} = \begin{pmatrix} \tilde{a}_1 & \tilde{a}_3 & 0 \\ \tilde{a}_3 & \tilde{a}_2 & 0 \\ 0 & 0 & b \end{pmatrix} , \tilde{Q}^{22} = \begin{pmatrix} \tilde{a}_1 & -\tilde{a}_3 & 0 \\ -\tilde{a}_3 & \tilde{a}_2 & 0 \\ 0 & 0 & b \end{pmatrix} , \tilde{Q}^{12} = a_2 \begin{pmatrix} -\sin 2\theta_B & \cos 2\theta_B & 0 \\ \cos 2\theta_B & \sin 2\theta_B & 0 \\ 0 & 0 & 0 \end{pmatrix} , \tag{2.128}$$

where $\tilde{a}_1 = a_1 \cos^2\theta_B + a_2 \sin^2\theta_B$, $\tilde{a}_2 = a_2 \cos^2\theta_B + a_1 \sin^2\theta_B$, $\tilde{a}_3 = \frac{1}{2}(a_1 \sin 2\theta_B - a_2 \sin 2\theta_B)$. If we focus on $\tilde{Q}^{12}$ and remember from Section 2.2.1 that for the $A_3 = 0$ ansatz to be consistent with the three-dimensional Ginzburg-Landau equations, 1.124 and 1.125, we require all $Q^{12}_{3i}, i \in \{1, 2\}$ to vanish. We can see that, for the basal plane, this is trivially the case. This means, for basal plane orientations of the $p + ip$ model, we can assume $A_3 = 0$ everywhere. This has further implications, the magnetic field will point only in the $\hat{x}_3 = (0, 0, 1) \equiv \hat{z}$ direction. This is because $(B_1, B_2, B_3) = (0, -\partial_1 A_3, \partial_1 A_2)$ and thus, for this ansatz, $B_1 = B_2 = 0$, and so the only non zero component of the magnetic field points in the $\hat{x}_3$ direction. This means that for any orientation in the basal plane, the sensible choice is, $\hat{x}_3 = \hat{z} = (0, 0, 1)$. This analysis is also useful in confirming that the choice of ansatz used in [37] was valid as the authors only considered the basal plane.

Finally, we consider the parameter k_5 which is the coefficient of the following terms in the free energy density,

$$k_5 \frac{1}{2} \left(|D_3\psi_1|^2 + |D_3\psi_2|^2 \right) . \tag{2.129}$$

We have shown that $A_3 = 0$ is a solution of the equations of motion for the basal plane but our choice of ansatz, $A_3 = 0$ implies that $D_3\psi_\alpha = 0$. This means that solutions in the basal plane will not be dependent on the value of k_5 as those terms, in the equations of motion, will vanish. However, we do still need to choose it so that the energy is positive definite.

2.4.3 Oscillatory Decay of Field Solutions

We are now in a position to test one of the predictions of the linearisation, namely, oscillation in the fields as $|x_1|\to\infty$, which we refer to as the linear regions of the fields. The behaviour of the fields in the linear region is governed by the following decay equation,

$$(\epsilon_1,\epsilon_1,\vartheta,p_1,p_2,p_3)=\sum_{i=1}^{5}c_i\vec{v}_i e^{-\mu_i x_1}\ , \tag{2.130}$$

with $\vec{v}_i=(v_i^1,v_i^2,v_i^3,v_i^4,v_i^5,v_i^6)^T$ and the c_i are arbitrary constants that determine if a mode is excited. The length scales, $\lambda_i=\mu_i^{-1}$, are, in general, complex and ordered by the size of their real parts, $\mathrm{Re}(\lambda_i)$. Thus the leading length scale, $\lambda_1=\mu_1^{-1}$, has the smallest value of $\mu_i>0$ and therefore contributes most significantly to the behaviour of the fields, where each field has a different component of the normal mode, $\vec{v}_i$, but they all decay with the same λ_i. If the ratio,

$$R_{\mu_1}=\frac{|\mathrm{Im}\,(\mu_1)|}{|\mathrm{Re}\,(\mu_1)|}>>0\ , \tag{2.131}$$

we should be able to see oscillations in the tails of the gauge invariant quantities, ρ_1,ρ_2,B_2,B_3 but as we focus on the basal plane for this section we do not show B_2 which vanishes there. Figure 2.7 shows the dependence of R_{μ_1} on the model parameters ν,ω,V_0. ν,V_0 are parameters of the free energy, Equation 2.11, and ω selects the orientation, $\hat{x}_1=(\cos\omega,\sin\omega,0)$. We see that for increasing values of V_0 the regions of the parameter space where we expect oscillating tails increases, note that R_{μ_1} is also periodic on $\omega=\frac{\pi}{2}$.

The period of an oscillation, predicted by the linearisation, is,

$$l_p=\frac{\pi}{\mathrm{Im}\,(\mu_1)}\ , \tag{2.132}$$

which we can compare to the period we find from the full non-linear numerical simulations. We use the globally minimum domain wall type, though these particular results do not differ between for the domain wall types.
The first set of results is for $\omega=0,\phi=0$ where $R_{\mu_1}\approx 1$. Figure 2.8a plots numerical solutions of the nonlinear Ginzburg-Landau equations, ϵ_1,ϵ_2 and B, for $x_1>0$. The locations of zeros and extrema for the nonlinear case are marked and the distance between these points is compared to the distance that the linearisation predicts. We can see that there is a close agreement between the two. The associated length scales and normal modes are given by,

$$\begin{aligned}
\mu_1=0,\quad & \vec{v}_1=(0,0,0,0,0,1)^T\ ,\\
\mu_2=0.8199+0.6507i,\quad & \vec{v}_2=\begin{pmatrix}0.5685-i0.0073\\-0.5681+i0.0099\\0\\0\\-0.3543-i0.4779\\0\end{pmatrix},\\
\mu_3=(\mu_2)^*,\quad & \vec{v}_3=(\vec{v}_2)^*\ ,\\
\mu_4=3.4216,\quad & \vec{v}_4=(0,0,-0.9964,0.0852,0,0)^T\ ,\\
\mu_5=3.4648,\quad & \vec{v}_5=(0.6947,0.7190,0,0,-0.0206,0)^T\ .
\end{aligned} \tag{2.133}$$

Discounting the non physical $\mu_1=0$ eigenvalue we see that the next, leading, eigenvalue is complex and R_{μ_2} which we relabel as $R_{\mu_1}\approx 0.8$ thus we predict oscillating tails. However, we

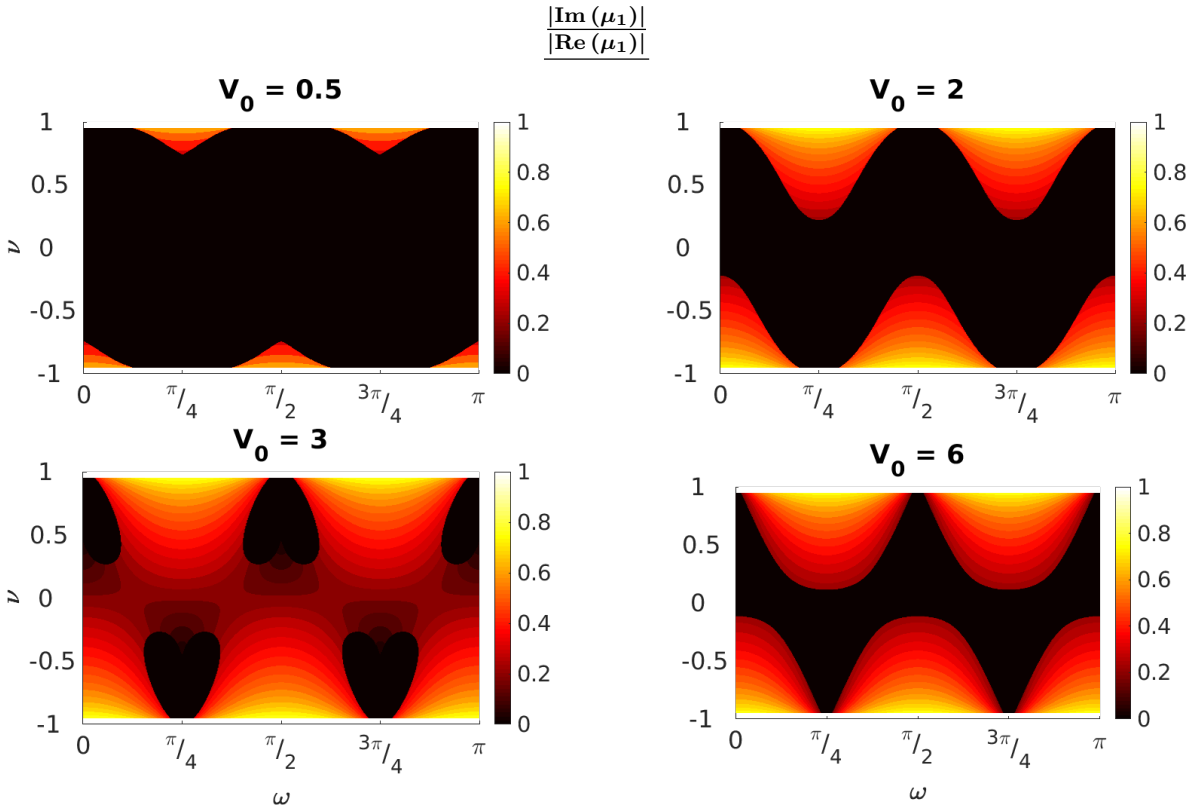

Figure 2.7: *Plot to show the likelihood of oscillations in the fields at longer range for the parameters* (ν, ω)*, where* $\hat{x}_1 = (\cos\omega, \sin\omega, 0)$*. When* $1 > R_{\mu_1} >> 0$ *then oscillating tails are likely as the leading length scale,* $\lambda_1 = \mu_1^{-1}$*, is complex and the imaginary part of,* λ_1 *dominates over the real part. Note that this figure shows only basal plane orientations for a* $p + ip$ *superconductor. We use a value of* $k_5 = 2.35$ *such that our energy is positive definite but as long as that is the case then the value of* k_5 *does not affect these results in the basal plane because* $A_3 = 0$ *in the basal plane.*
This matches [37] which used a two-dimensional ansatz and a different method of linearisation.

can see that $v_2^3 = v_2^4 = v_2^6 = 0$ which means we do not predict oscillations in the $\vartheta(x_1), p_1, p_2$ fields respectively. This leaves $\vec{v}_2^5$ as the only non zero magnetic component. This means that the only direction of the linear magnetic field, $B_{lin} = (0, -p_3', p_2')$, coupled to this mode is, p_2, which corresponds to the $\hat{x}_3$ linear magnetic field direction. If we consider every other mode we note that the v_i^6 component, which corresponds to the value of p_3 for that mode, is only non zero for $\vec{v}_1$ where all the other components vanish. In this case, $\mu_1 = 0$, thus p_3 is constant in the linear region and this constant is zero due to the boundary conditions. This means that B_{lin} vanishes for this mode. In summary, we find that the linearisation predicts that the linear magnetic field for each mode is either zero or pointing only in the $\hat{x}_3$ direction. This matches what we find in the nonlinear simulations, where in the basal plane only B_3, the magnetic field in the $\hat{x}_3$ direction, is non zero.
Due to the form of the quadratic order free energy, E_{quad}, having $p_3 \neq 0$ is only energetically favoured when there are couplings between p_3 and the condensates, introduced by the anisotropy matrices. In terms of the linearisation that would mean any of v_i^1, v_i^2, v_i^3 would need to be non zero. This is why we see the v_i^6 component as equal to zero for every mode bar $\vec{v}_1$.
The next image is for $\omega = \frac{\pi}{3}$ where $R_{\mu_1} \approx 1$. Figure 2.8b shows good agreement between the linear theory prediction and the non-linear solutions. The length scales are similar to those in Equation 2.133.

The next set of results is for $(\nu, \theta, V_0) = (0, 0, 0.5)$ which is a region of the parameter space where we expect no oscillations, $R_{\mu_1} = 0$. In Figure 2.9 we can see that no oscillations occur as the only zeros found are on the edges, $x_1 = 0$ or $x_1 \to \infty$, due to the boundary conditions.

The length scales are,

$$\begin{aligned}
\mu_1 = 0, \quad & \vec{v}_1 = (0,0,0,0,0,1)^T, \\
\mu_2 = 0.7083, \quad & \vec{v}_2 = (0.9840, -0.1373, 0, 0, 0.1135, 0)^T, \\
\mu_3 = 0.7559, \quad & \vec{v}_3 = (0, 0, -0.8669, 0.4932, 0, 0)^T, \\
\mu_4 = 1.8921 \pm 0.3417, \quad & \vec{v}_4 = \begin{pmatrix} 0.0063 \mp 0.0515i \\ 0.8132 \pm 0.1216i \\ 0 \\ 0 \\ 0.019 \pm 0.5667i \\ 0 \end{pmatrix}, \\
\mu_5 = (\mu_4)^*, \quad & \vec{v}_5 = (\vec{v}_4)^*,
\end{aligned} \tag{2.134}$$

where we see the leading length scale, μ_2 is real, (as we ignore the $\mu = 0$ solution) hence we find no oscillations. We note however that there are still complex length scales but they are not in the dominant mode so we do not see spatially oscillating tails in the nonlinear solutions.

Finally, we include Figure 2.10, which depicts the fields for the non basal plane orientation, $\hat{x}_1 = (0, 0, 1)$. As we are no longer in the basal plane we include the value of B_2, which in general is non zero. However, for this orientation the magnetic field vanishes in both components. All length scales are real with the leading length scale, $\lambda_1 = 1.9791$ thus we expect (and find) no oscillations in the fields for the nonlinear solutions. In fact every length scale is real for this orientation, this can be seen from the mixing angle for each mode,

$$(\theta_m^1 \theta_m^2, \theta_m^3, \theta_m^4, \theta_m^5,) = (0, \frac{\pi}{2}, \frac{\pi}{2}, 0, 0) \ , \tag{2.135}$$

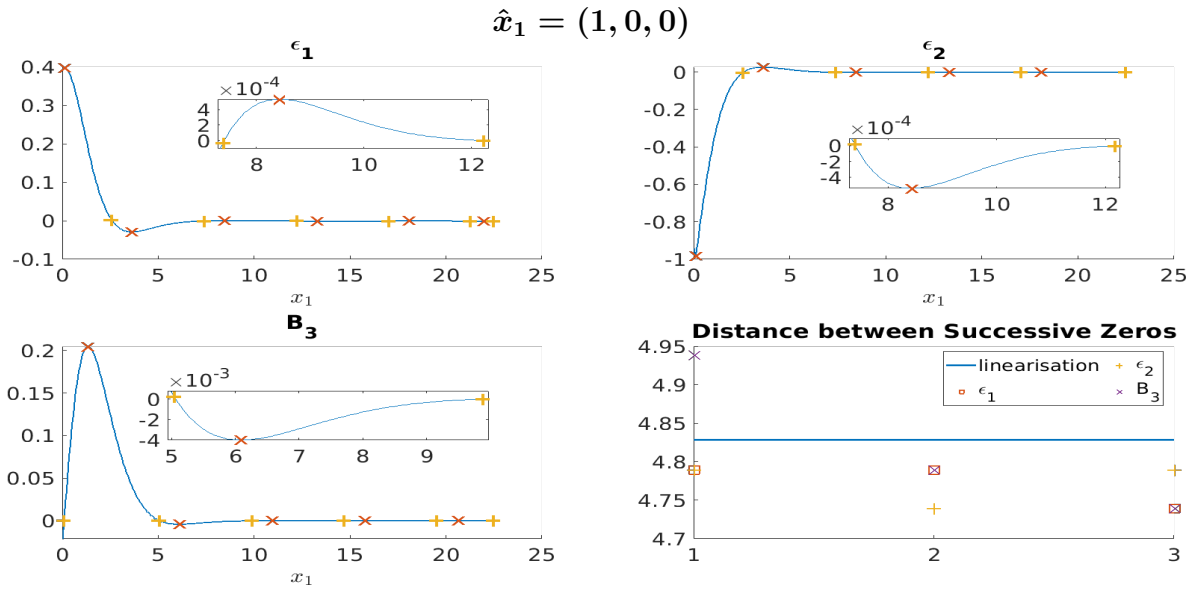

(a) *Plots of the gauge invariant quantities with the zeros marked. The predicted value for the linear period, is* $l_p = 4.8283$ *with* $(\nu, \theta, V_0, k_5) = (-0.95, 0, 6, 0)$.

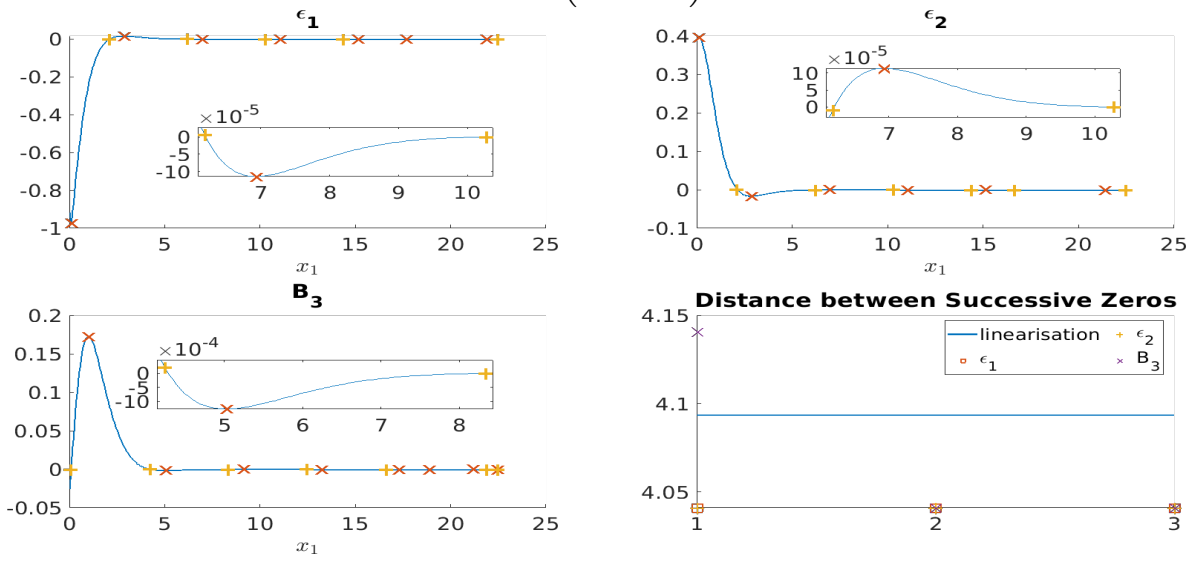

(b) *Plots of the gauge invariant quantities with the zeros marked. The predicted value for the linear period,is* $l_p = 4.0935$ *with* $(\nu, \theta, V_0, k_5) = (-0.95, \frac{\pi}{3}, 6, 0)$.

Figure 2.8: *$p + ip$ domain wall field solutions for, $x_1 > 0$, showing oscillations in the fields, predicted by the linearisation. The extrema are marked by $\times$ and the zeros, or y-intercepts, by $+$ where $\hat{x}_1 = (\cos\omega, \sin\omega, 0)$. Note that the zeros at the end of the solution are due to the fixing of the boundary conditions to the vacua values and thus $\epsilon_1, \epsilon_2, B$ trivially vanish. Note that as $\hat{x}_1$ is in the basal plane the choice of k_5 does not affect the solutions this is because $A_3 = 0$ in the basal plane.*

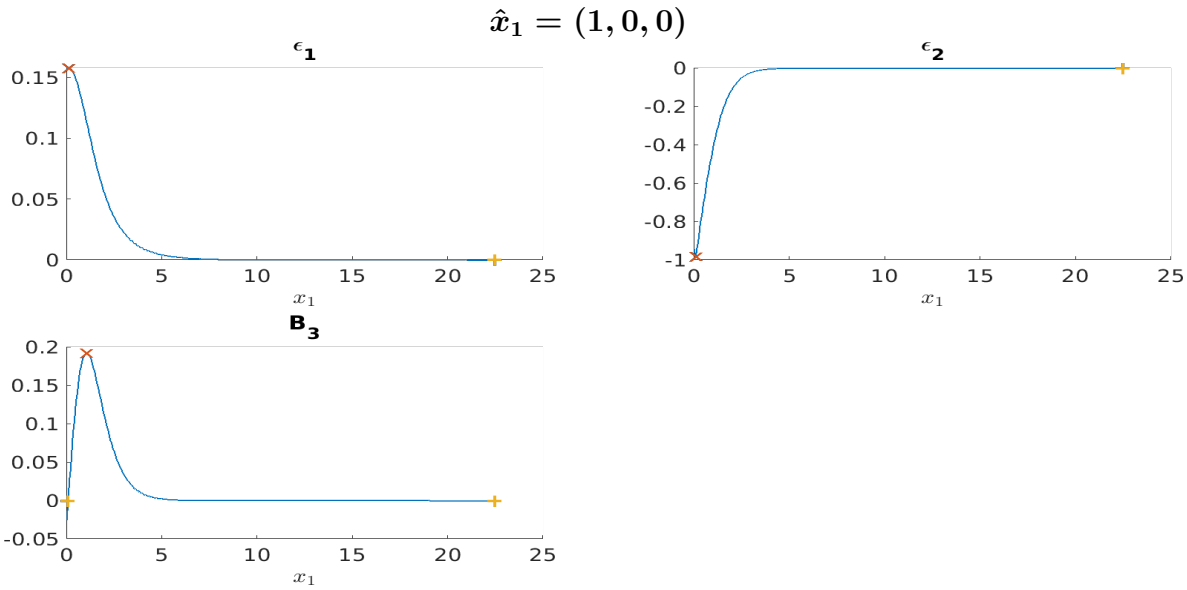

Figure 2.9: *Plots of the gauge invariant quantities with the zeros marked. The predicted value for the linear period, $l_p = 0$ with $(\nu, \theta, V_0, k_5) = (0, 0, 0.5, 0)$. We do not observe oscillations in this part of the parameter space, as expected. As $\hat{x}_1$ is in the basal plane the choice of k_5 does not affect the solutions. This is because $A_3 = 0$ in the basal plane.*
Domain wall field solutions for, $x_1 > 0$, with the extrema marked by $\times$ and the zeros, or y-intercepts, $+$. The zeros at the end of the solution are due to the fixing of the boundary conditions to the vacua values and thus $\epsilon_1, \epsilon_2, B$ trivially vanish.

where we remind the reader that θ_m^i is a measure of how coupled the condensate and magnetic modes are with $\theta_m^i = 0$ and $\theta_m^i = \frac{\pi}{2}$ meaning the mode is purely condensate or magnetic. As there are no modes that have a coupling between condensate and magnetic modes we return to the more standard real length scales.

2.4.4 Visualising the Orientation Dependence of Physical Quantities

In Section 2.4.2 we study the dependence of the free energy and maximum magnetic field on the orientation of a domain wall within the basal plane. We now extend this to orientations out of the basal plane, where $\hat{x}_1 \cdot \hat{z} \neq 0$. For this we introduce a specific, non zero, value of k_5, so that the free energy is positive definite. Additionally, we use the parameters $(\nu, V_0) = (-0.95, 6)$ which for the linearisation, as seen in Figure 2.7, is a point in the parameter space where oscillations, in the basal plane at least, should occur very strongly. In this section we are interested in demonstrating that the linearisation as well as the energy and maximum magnetic field from the nonlinear solutions are orientation dependent. Specifically, we choose $k_5 = 2.35$ so it is larger than the $Q_{11}^{11} = 2.05$ and $Q_{22}^{11} = 1.95$ components of the anisotropy matrices but still of comparable size. Even with our rescaling, the parameter space is quite large hence the need to pick values which we assume should show general behaviour of the $p + ip$ model.

Predicting Oscillatory Decay

Figure 2.11 extends Figure 2.7, which shows how the ratio $R_{\mu_1} = \frac{|\mathrm{Im}\,(\mu_1)|}{|\mathrm{Re}\,(\mu_1)|}$ varies in the basal plane, to all of the possible orientations of the model.
An orientation is defined by our choice of $\hat{x}_1$ which, if we pick a general $\hat{x}_2$ that is perpendicular

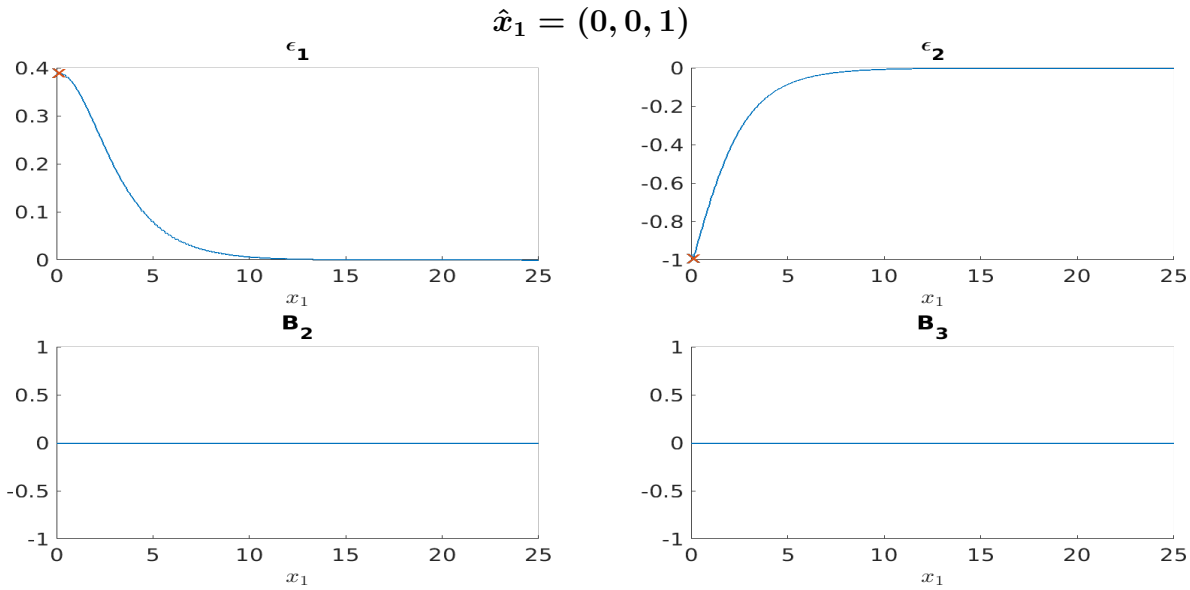

Figure 2.10: *Plots of the gauge invariant quantities with the zeros marked. The predicted value for the linear period is* $l_p = 0$ *with* $(\nu, V_0, k_5) = (-0.95, 6, 2.35)$*. We do not observe oscillations in this part of the parameter space, as expected. This solution is not in the basal plane so we have included the value of* B_2*. However, both* $B_2 = B_3 = 0$ *everywhere for this orientation. Domain wall field solutions for,* $x_1 > 0$*, with the extrema marked by* $\times$ *and the zeros, or y-intercepts,* $+$*.*

to $\hat{x}_1$, gives us the following $SO(3)$ orientation matrix,

$$M = \begin{pmatrix} \vdots & \vdots & \vdots \\ \hat{x}_1 & \hat{x}_2 & \hat{x}_1 \times \hat{x}_2 \\ \vdots & \vdots & \vdots \end{pmatrix} . \tag{2.136}$$

The scheme for generating M is outlined in Section 2.2.3.1.
For domain wall solutions we have made the ansatz choice that the fields only depend upon the x_1 coordinate, Ansatz 2.14, so the choice of $\hat{x}_2$ does not affect the values of the scalar fields, $|\psi_1|, |\psi_2|, \theta_{12}, |B|$. Thus we only need to specify $\hat{x}_1$ to define an orientation of a domain wall. The unit vector, $\hat{x}_1$, that defines the orientation, can be thought of as a point on the unit sphere, that is $\hat{x}_1 \in S^2$. However, the $p + ip$ model obeys the reflection symmetry $z \mapsto -z$ which means we need only consider the upper hemisphere, $z > 0$. If we consider, Figure 2.11, every point on the surface of the hemisphere represents an orientation, $\hat{x}_1$, defined by the unit vector from the origin to that point on the surface of the hemisphere. We can then colour each point to represent the value of, R_{μ_1}, at that point. Any point on the equator of the hemisphere represents the basal plane, whilst the north pole corresponds to $\hat{x}_1 = (0, 0, 1)$ which is the crystalline z axis. The orientation can be written in terms of spherical polar coordinates, $\hat{x}_1 = (\cos\omega\cos\phi, \sin\omega\cos\phi, \cos\phi)$, $\omega \in [0,\ 2\pi)$, $\phi \in [0, \frac{\pi}{2}]$ which helps with interpreting these types of plots.
Returning to Figure 2.11, we see that oscillations occur in the basal plane, the equator in Figure 2.11, and then moving from the equator to the north pole we see R_{μ_1} decreases in value until it vanishes signifying that the dominant length scales, λ_1, are now purely real.

We remind the reader that the free energy of the $p+ip$ model is invariant under the combined spatial and condensate symmetry. For example the action of the two relevant symmetries is

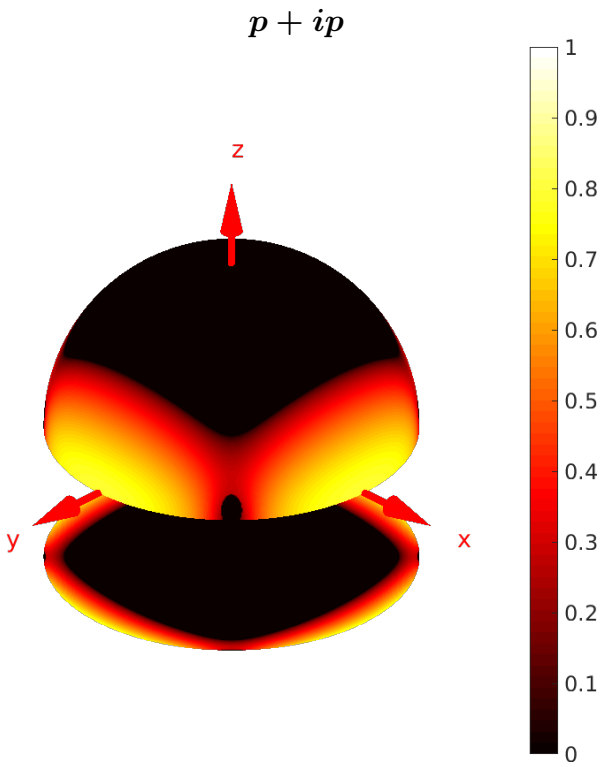

Figure 2.11: *Orientation dependence of* $R_{\mu_1} = \frac{|\mathrm{Im}\,(\mu_1)|}{|\mathrm{Re}\,(\mu_1)|}$*, for a* $p+ip$ *superconductor, with* $\hat{x}_1 = (\cos\omega\cos\phi, \sin\omega\cos\phi, \sin\phi)$*. Each unit vector from the origin to a point on the hemisphere defines a domain wall orientation (in terms of the crystalline basis), with the colour of that point giving the value of* R_{μ_1} *for that orientation. Note that the orientation is given by* $\hat{x}_1 \in S^2$*. However, as the* $p+ip$ *free energy is invariant under the symmetry,* $z \mapsto -z$*, we record only the upper hemisphere.*
$(\nu, V_0, k_5) = (-0.95, 6, 2.35)$

shown below,

$$C_2(z) : (\psi_1, \psi_2, x, y, z) \mapsto (-\psi_1, -\psi_2, -x, -y, z) \tag{2.137}$$
$$C_4(z) : (\psi_1, \psi_2, x, y, z) \mapsto (-\psi_2, -\psi_1, -y, x, z) \ , \tag{2.138}$$

with the full list of the action of the symmetries given in Table 1.2. Figure 2.11 demonstrates the spatial $C_4(z)$ symmetry, and therefore spatial $C_2(z)$, that the model contains but it does not show the $C_4(z)$ condensate symmetry.

Free Energy and Maximum Magnetic Field

We now consider the full orientation dependence of the energy and maximum magnetic field, adding to the results from [26]. For consistency we use the same parameters as we did in Figure 2.11, $(\nu, V_0, k_5) = (-0.95, 6, 2.35)$. We present numerical solutions to the full nonlinear Ginzburg-Landau equations. Figure 2.12a shows the free energy for both domain wall types. We observe that the energies are spatially $C_4(z)$ symmetric as expected but it is difficult to tell the difference between the two domain walls. This difference is made clearer by Figure 2.12b which shows the orientation dependence of the difference between the two energies and two maximum magnetic fields. Near to the equator, or basal plane orientation, this difference is most pronounced and the two domain walls are clearly $C_4(z)$ spatial rotations of each other. This is because the difference in free energy changes sign, but not magnitude, every $\frac{\pi}{4}$ rotation about the z axis. Moving away from the basal plane, along the surface of the hemisphere, towards the north pole, we see the difference become less and less pronounced until it vanishes.

The maximum magnetic field is given by,

$$B_{max} = \max|B(x_1)| \equiv |B(\pm x_1^{max})| \ , \tag{2.139}$$

where $\pm x_1^{max}$ denotes the two coordinates where the magnetic field is extremal, $B(\pm x_1^{max}) = \pm B_{max}$. B_{max} allows us to quickly determine if an orientation has non zero spontaneous magnetic field as well as presenting the spatial symmetries of the magnetic field. Furthermore, for $B_{max} \neq 0$ it also has a direction given by,

$$\hat{B}_{max} = \frac{(B_2(x_1^{max})\hat{x}_2 + B_3(x_1^{max})\hat{x}_3)}{\sqrt{B_2(x_1^{max})^2 + B_3(x_1^{max})^2}} \ . \tag{2.140}$$

We can plot the direction of $\hat{B}_{max}$ as well as the value of B_{max} at each point on the surface of the hemisphere to show the orientation dependence of these two quantities. This is shown in Figure 2.13 where we note that as B is an odd function so the directions $\hat{B}_{max}$ and $-\hat{B}_{max}$ are equivalent and are shown by the double headed arrows at each point. For the two types of domain walls we actually see that the maximum magnetic field is only $C_2(z)$ spatially symmetric. However, when the two energies are combined to produce the globally minimum energy, we see that the maximum magnetic field becomes $C_4(z)$ spatially symmetric again. Furthermore, the included arrows, which show $\hat{B}_{max}$, do not change between the two domain walls. Interestingly, the only point where the maximum magnetic field vanishes, for our chosen parameters, is at the north pole ($\hat{x}_1 = (0, 0, 1)$), but in the basal plane it is non zero at every point. This differs from the model in Section 2.5, where, in addition to the z axis, the spontaneous magnetic field vanishes at the x and y axes.
If we consider $\hat{B}_{max} \in S^2$ then we can assign a winding number, N, to the field cycling around the points where $\hat{B}_{max} = 0$. If $N = 1$ is a clockwise winding and $N = -1$ anticlockwise then $N = -1$ at the north pole. We describe, $\hat{B}_{max}$, as having a vorticity about the points

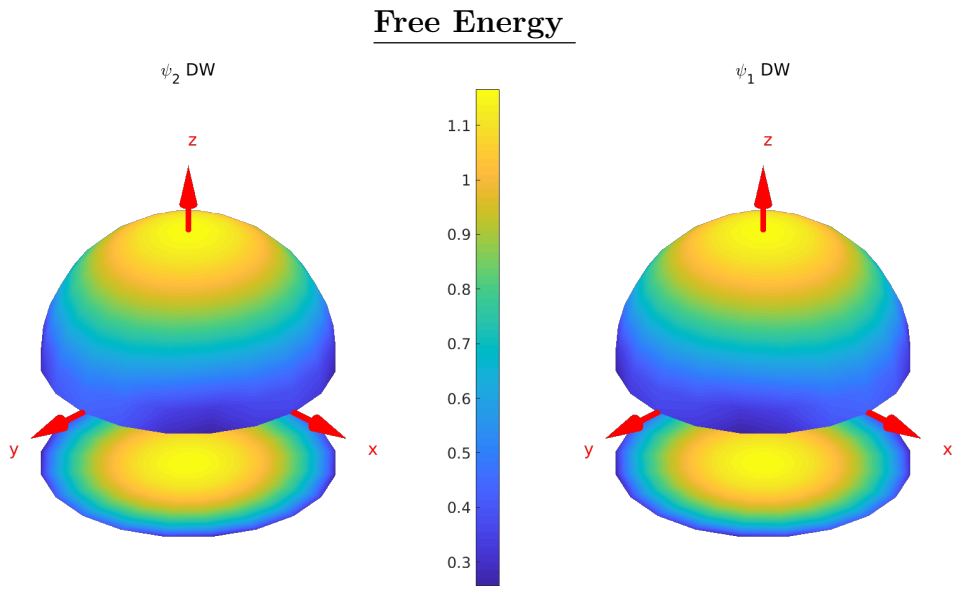

(a)

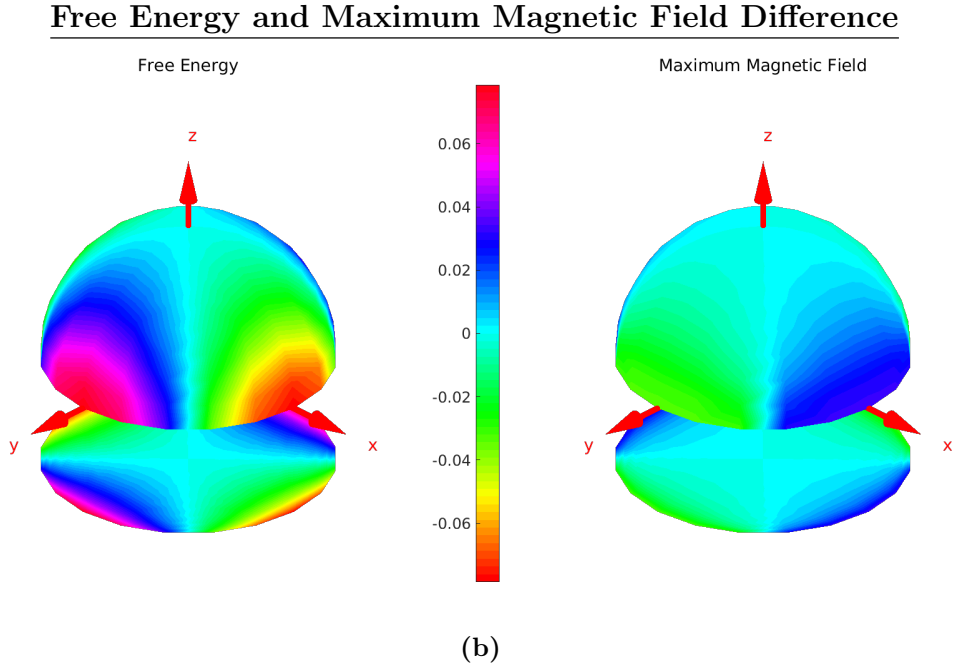

(b)

Figure 2.12: *Figure 2.12a plots the free energy of domain walls in a $p+ip$ superconductor and how this varies with orientation: ψ_2 domain wall (left) and ψ_1 domain wall (right). The free energy appears to be indistinguishable between the two domain wall types.*
Figure 2.12b plots the orientation dependence of the difference between the ψ_2 and ψ_1 domain wall for the free energy (left) and the maximum magnetic field (right). We see that the two free energies are different. The maximum magnetic field is given by $B_{max} = \max|B|$. Here we see that the plots of the two domain wall types are simply $C_4(z)$ rotations of each other, which can be seen by the change of sign in the energy difference every $\frac{\pi}{4}$ rotation about the z axis. We have changed the colormap to one that highlights small differences more effectively. Each unit vector from the origin to a point on the hemisphere defines a domain wall orientation (in terms of the crystalline basis), with the colour, for example, giving the value of the free energy for that orientation.

where $B_{max} = 0$. This is likely to be a result that does not depend on parameter choice and could therefore be another observable experimental signature used to identify a $p + ip$ superconductor. Furthermore, the linearisation predicts, that in the basal plane, $B_{lin} \parallel \hat{z}$. However, this result appears to extend to the the nonlinear region, we see this by looking at the arrows on the equator of Figure 2.13, which are perpendicular to the equator.

2.4.5 Magnetic Field Twisting

Due to our choice of ansatz, for some orientations, we are able to see the magnetic field direction twisting away from the direction of the maximum magnetic field, $\hat{B}_{max}$, as $|x_1| \to \infty$. For domain walls we compare the direction of the magnetic field at each point, $\hat{B}(x_1)$, with the direction of $\hat{B}_{max}$ giving the local twisting angle,

$$\theta_t(x_1) = \arctan\left(\frac{|\hat{B}_{max} \times \hat{B}(x_1)|}{|\hat{B}_{max} \cdot \hat{B}(x_1)|}\right) , \tag{2.141}$$

where $\theta_t(x_1) \in [0, \frac{\pi}{2}]$ and $\theta_t(x_1) = 0$ implies that the magnetic field is either parallel or anti-parallel to $\hat{B}_{max}$ and $\theta_t(x_1) = \frac{\pi}{2}$ is the maximum amount the magnetic field can twist. This occurs when it is orthogonal to $\hat{B}_{max}$.
We note that the magnetic field, $\hat{B}(x_1)$, is an odd function this means there are two $x_1 = \pm x_1^{max}$ which give $\pm\hat{B}_{max} = \hat{B}(\pm x_1^{max})$. We have defined $\theta_t(x_1)$ so that it is an even function so that magnetic fields parallel and anti-parallel to $\hat{B}_{max}$ are treated equivalently. Otherwise, for any non zero magnetic field, we would have a non zero maximum value of $\theta_t(x_1)$ simply due to the odd nature of the maximum magnetic field. We want the twisting angle to only be non zero in cases where $\hat{B}(x_1)$ changes from pointing in either the $\pm\hat{B}_{max}$ directions.
Numerically, we calculate $\theta_t(x_1)$ using the variable, cutoff, to remove non zero values of $\theta_t(x_1)$ close to the boundaries that arise because the magnetic field strength is smaller than the accuracy of the numerics. We check each point in the domain with the condition,

$$\begin{aligned} &\text{if } \Big(|\hat{B}_{max}(x_1)| < \text{cutoff}\Big) \\ &\theta_t(x_1) = 0 \\ &\text{end} , \end{aligned} \tag{2.142}$$

which allows us to remove the erroneous values of $\theta_t(x_1)$.

Consider Figure 2.14 which plots the maximum value of the twisting angle,

$$\theta_t^{max} := \max(\theta_t(x_1)) . \tag{2.143}$$

We see that θ_t^{max} is approximately the same for the ψ_2 and ψ_1 DW types as well as being spatially $C_4(z)$ symmetric. The peaks in the values of, θ_t^{max}, are approximately $\frac{\pi}{2}$. We see that along the great circles that connect the $\pm x$ and $\pm y$ axes with the z axis there is zero twisting as well as along the equator. We know that, in the basal plane, the magnetic field points only in the $\hat{x}_3$ direction, in both the nonlinear and linear regions, and thus we would expect no twisting of the magnetic field to occur there.
Consider Figure 2.15, which plots the twisting angle, for the orientations that give the two largest values of θ_t^{max}. This illustrates how, for $p+ip$, this quantity is not particularly precise; we see oscillations in the twisting angle that peak at similar, but not identical, values. The peaks in the twisting angle occur away from the centre of the domain and are oscillatory with an approximately constant period. In general, these oscillations do not appear to be explained

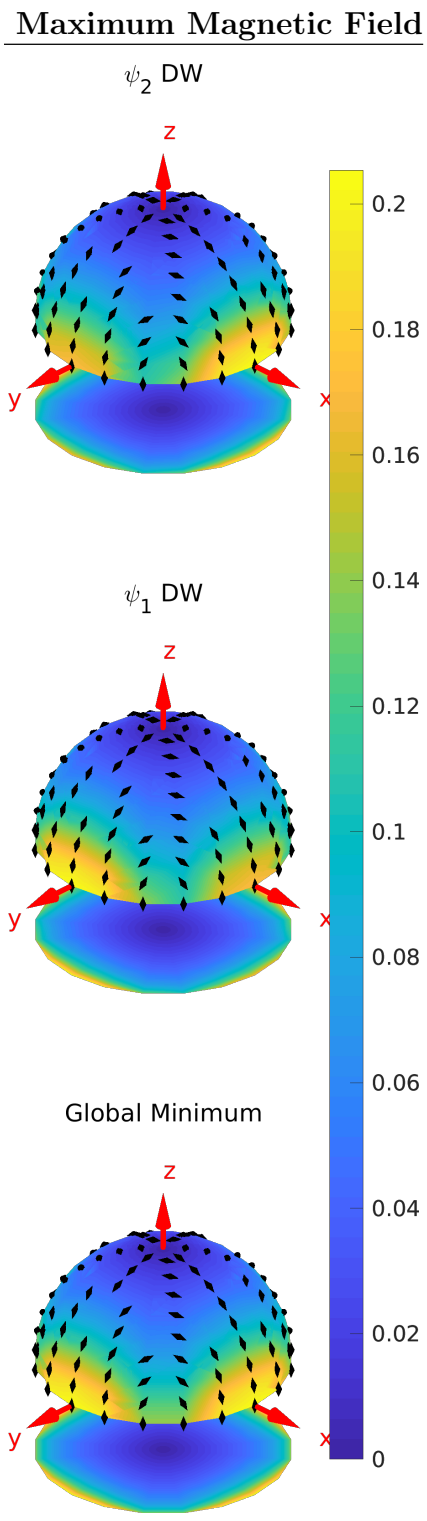

Figure 2.13: *Orientation dependence of the maximum magnetic field, $B_{max} = \max|B|$, for a $p+ip$ superconductor for each domain wall type. We have mapped each orientation, $\hat{x}_1$, to a point on the hemisphere. The hemisphere has then been coloured by the value of B_{max} of the corresponding domain wall solution. In addition, we have plotted the direction of the magnetic field, where $|B| = B_{max}$, as an arrow tangent to the hemisphere. The corresponding direction for $B = -B_{max}$ is also plotted at each point which occurs because B is an odd function. The arrows have all been scaled to have the same length to illustrate the winding of the field around the zeros of the maximum magnetic field.*
We see that the two domain wall types differ by the value of B_{max} but not in the direction that B_{max} points.

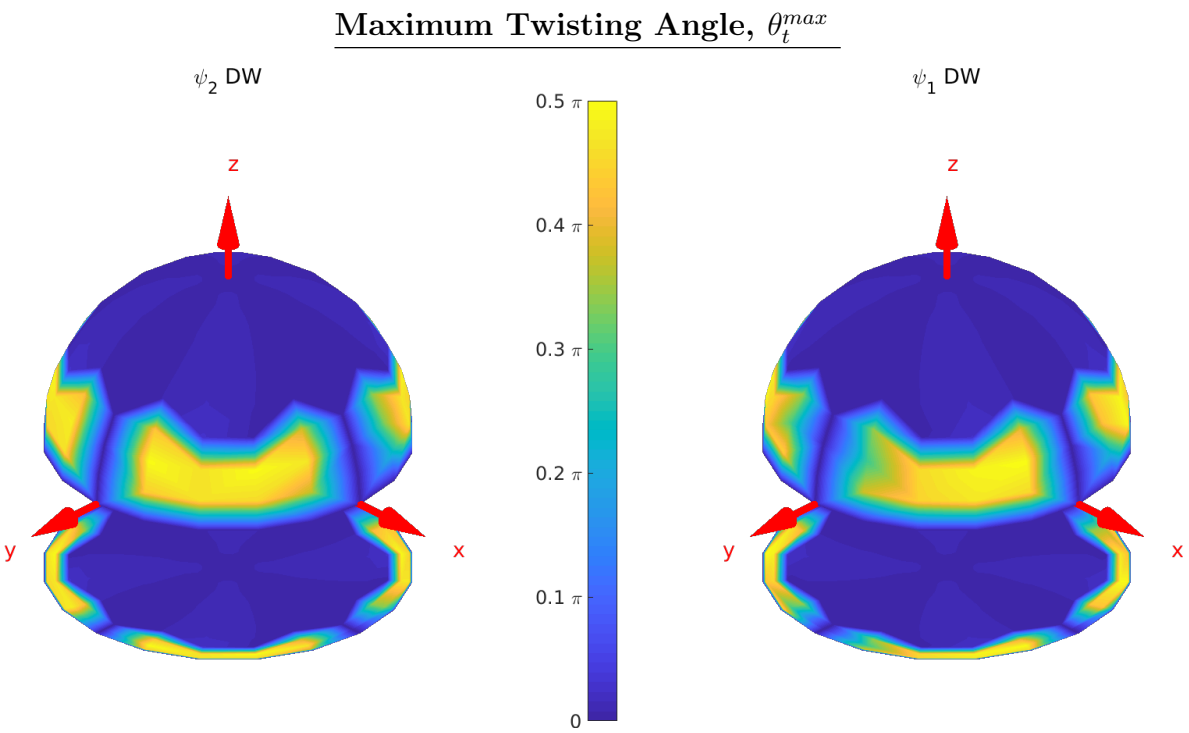

Figure 2.14: *Orientation dependence of the maximum twisting angle of the magnetic field of domain wall in a $p+ip$ superconductor: clockwise phase difference winding (left) and anticlockwise phase difference winding (right). Each unit vector from the origin to a point on the hemisphere defines a domain wall orientation (in terms of the crystalline basis), with the colour giving the value of θ_t^{max} for that orientation. Here we see that θ_t^{max} is approximately the same for both ψ_1 and ψ_2 domain wall types.*
Note we use a value of cutoff $= \frac{tol}{100}$ to remove boundary effects.

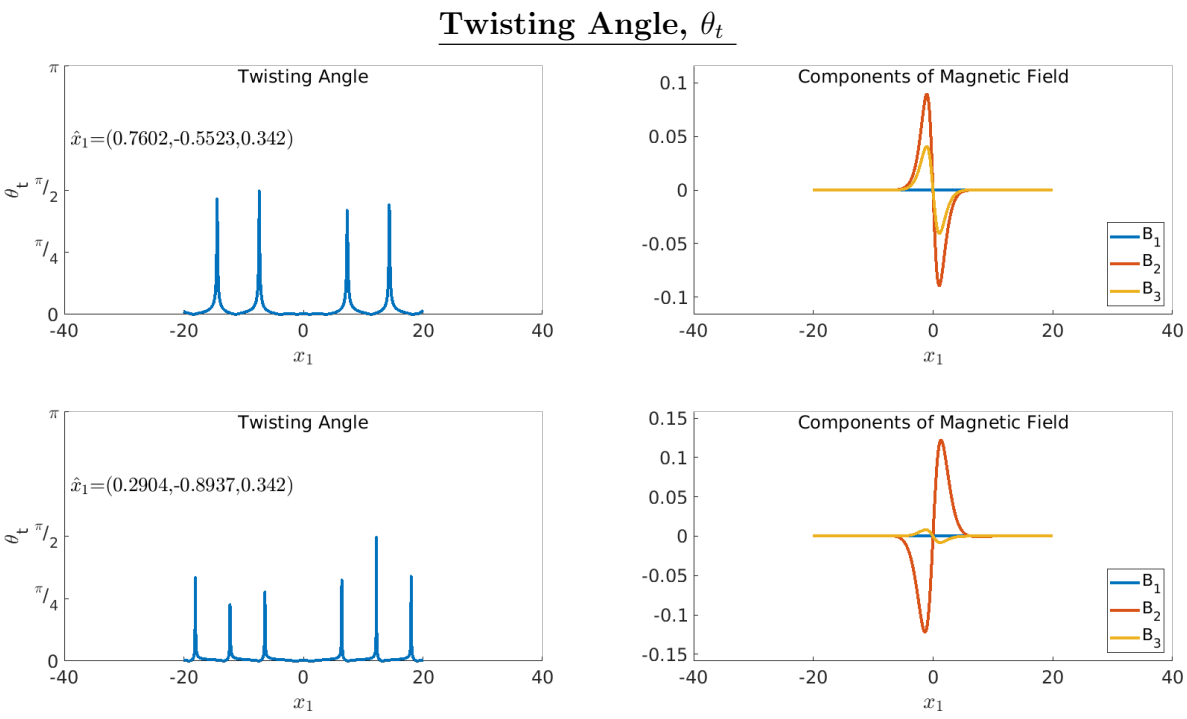

Figure 2.15: *Field plots for the twisting angle, $\theta_t \in [0, \frac{\pi}{2}]$, for two orientations, $\hat{x}_1 = (0.7602, -0.5523, 0.342)$ and $\hat{x}_1 = (0.2904, -0.8937, 0.342)$, that give the largest values of the maximum twisting angle, θ_t^{max}. We observe oscillations in the twisting angle in the linear region of the model.*

by the linearisation as when we compare Figure 2.11, which show the orientations where the linearisation predicts oscillations to occur, to Figure 2.14. We see that, for example, θ_t^{max} vanishes at $\hat{x}_1 = (1, 0, 0)$ but R_{μ_1} vanishes at $\hat{x}_1 = \frac{1}{\sqrt{2}}(1, 1, 0)$.
However, for the two orientations in Figure 2.15 we note that the leading length scales, as predicted by the linearisation, are $\lambda_1 = 0.6888 - 0.2367i$ and $\lambda_1 = 0.7820 - 0.4310i$ with $l_p = 7.1$ and $l_p = 5.8$ respectively, which we see are complex. The values of the period for the peaks of θ_t, $l_p = \frac{\pi}{\text{Im}(\mu_1)}$, calculated directly from the nonlinear solutions are, 6.78 and 5.79 respectively, which fairly closely match the values of l_p predicted by the linearisation. Thus it would appear that the oscillation in the twisting angle, only for some orientations, can be explained by the linearisation.

Finally, it is important to note that having non zero, $\theta_t(x_1)$, confirms that employing Ansatz 2.14, which has $A_3 \neq 0$ and so does not fix the direction of the magnetic field, is required. We see that the basal plane has $\theta_t(x_1) = 0$ which is explained by the fact that setting $A_3 = 0$ is consistent with the equations of motion for these orientations.

2.5 Domain Walls in $s + is$ and $s + id$ Superconductors

We now move to studying domain walls in $s + is$ and $s + id$ superconductors. These models have only spatial symmetries and unlike the $p+ip$ model do not appear to show the ψ_1 and ψ_2 domain wall types. However, we do find two new types of domain walls in this model based on the direction around the unit circle the phase difference, θ_{12}, interpolates from $\theta_{12} = \frac{\pi}{2}$ to $\theta_{12} = -\frac{\pi}{2}$. Additionally, we find magnetic field twisting in the $s + id$ model, something predicted by the linearisation. Magnetic field twisting is where the direction that the magnetic field points in changes as we move away from the domain wall, $|x_1| \to \infty$. We also study the

orientation dependence of the maximum magnetic field and the free energy. This is based on joint work in [1] and [2] .

We now explore the $s+is$ and $s+id$ models. The structure of the anisotropy matrices comes from the requirement that they must be spatially symmetric, that is $Q^{\alpha\beta} = S^T Q^{\alpha\beta} S$ where $S \in O(3)$ is the matrix representation of a spatial symmetry. An $s+is$ superconductor has the $SO(2)(z) \times C_2(x) \times C_2(y)$ spatial symmetries whereas an $s+id$ superconductor has the $C_2(z) \times C_2(x) \times C_2(y)$ spatial symmetries. The actions of these symmetries are,

$$C_2(x) : (x,y,z) \mapsto (x,-y,-z) \tag{2.144}$$
$$C_2(y) : (x,y,z) \mapsto (-x,y,-z) \tag{2.145}$$
$$C_2(z) : (x,y,z) \mapsto (-x,-y,z) \tag{2.146}$$
$$SO(2)(z) : (x,y,z) \mapsto (x\cos\theta - y\sin\theta, x\sin\theta + y\cos\theta, z)\ , \theta \in [0,2\pi]\ , \tag{2.147}$$

and this is described in more detail in Section 1.8.1. With these requirements in mind along with the fact that domain walls require broken time reversal symmetry, the following general anisotropy matrices and potential coefficients are used [25]:

$$Q^{11} = \begin{pmatrix} a_1 & 0 & 0 \\ 0 & a_1 & 0 \\ 0 & 0 & b_1 \end{pmatrix}\ , Q^{22} = \begin{pmatrix} a_2 & 0 & 0 \\ 0 & a_2 & 0 \\ 0 & 0 & b_2 \end{pmatrix}\ , Q^{12} \equiv (Q^{21})^T = \begin{pmatrix} a_3 & 0 & 0 \\ 0 & s\cdot a_3 & 0 \\ 0 & 0 & b_3 \end{pmatrix} \tag{2.148}$$

$$F_p = \alpha_1\rho_1^2 + \alpha_2\rho_2^2 + \frac{\beta_1}{2}\rho_1^4 + \frac{\beta_2}{2}\rho_2^4 + \gamma_{12}\rho_1^2\rho_2^2 + \eta_{12}\rho_1^2\rho_2^2\cos(2\theta_{12})\ , \tag{2.149}$$

where $s=1$ for the $s+is$ superconductor and $s=-1$ for the $s+id$. We can see immediately that, unlike the $p+ip$ potential, this potential no longer has the $C_4(z)$ condensate symmetry as, $F_p(\psi_1,\psi_2) \neq F_p(-\psi_2,\psi_1)$. This is because $\alpha_1 \neq \alpha_2$ and $\beta_1 \neq \beta_2$ in general. This means that, $u_1 \neq u_2$, where the u_α are the vacuum values for $\rho_\alpha \equiv |\psi_\alpha|$. Additionally, these two models have different spatial symmetries about the crystalline z axis where the factor of $s=-1$ in the $s+id$ case breaks the $SO(2)(z)$ (spatial) symmetry leaving the simpler $C_2(z)$ symmetry.

As we can see this model has twelve free parameters so investigating the full parameter space, as we did with the $p+ip$ case, is not realistic. So moving forwards, we choose a particular set of parameters for the whole section,

s+is	s+id
$Q^{11} = \begin{pmatrix} 4 & 0 & 0 \\ 0 & 4 & 0 \\ 0 & 0 & 0.3 \end{pmatrix}$	$Q^{11} = \begin{pmatrix} 4 & 0 & 0 \\ 0 & 4 & 0 \\ 0 & 0 & 0.3 \end{pmatrix}$
$Q^{22} = \begin{pmatrix} 0.5 & 0 & 0 \\ 0 & 0.5 & 0 \\ 0 & 0 & 2 \end{pmatrix}$	$Q^{22} = \begin{pmatrix} 0.5 & 0 & 0 \\ 0 & 0.5 & 0 \\ 0 & 0 & 2 \end{pmatrix}$
$Q^{12} = \begin{pmatrix} 1 & 0 & 0 \\ 0 & 1 & 0 \\ 0 & 0 & 0.2 \end{pmatrix}$	$Q^{12} = \begin{pmatrix} 1 & 0 & 0 \\ 0 & -1 & 0 \\ 0 & 0 & 0.2 \end{pmatrix}$

Table 2.1: Form of the anisotropy matrices for $s+is$ and $s+id$ systems.

with the following potential

$$F_p = -\frac{1}{2}|\psi_1|^2 - \frac{1}{2}|\psi_2|^2 + 2|\psi_1|^4 + 3|\psi_2|^4 + \frac{3}{2}|\psi_1|^2|\psi_2|^2 + \frac{1}{8}|\psi_1|^2|\psi_2|^2\cos 2\theta_{12}\ . \tag{2.150}$$

This set of parameters was chosen, as always, so that the free energy was positively defined. Additionally, it is where the linearisation predicted complex leading length scales for certain orientations. We note that the maximum value of this ratio is still only $\max\left(\frac{|\mathrm{Im}\,(\mu_1)|}{|\mathrm{Re}\,(\mu_1)|}\right) \approx 0.4$, which means although we get complex leading length scales we do not see oscillations in the fields. We expect the features discovered using this set of parameters to remain robust throughout the parameter space.

2.5.1 Domain Wall Types

We detailed in Section 2.4 how the $p+ip$ model exhibited two types of domain walls which were non degenerate in energy, exist for all orientations and each type could be produced numerically if the boundary conditions were fixed to one of the following,

$$\psi_2 \ DW: \quad \lim_{x_1\to\pm\infty}(\psi_1,\psi_2) = (1,\pm i) \tag{2.151}$$

$$\psi_1 \ DW: \quad \lim_{x_1\to\pm\infty}(\psi_1,\psi_2) = (\pm 1, i)\ , \tag{2.152}$$

We also saw, in Section 2.4.2, that the free energy for a ψ_2 domain wall was equivalent to that of a ψ_1 domain wall that had a $C_4(z)$ spatial symmetry applied to it. These two domain wall types were identified by which condensate, ψ_α, vanishes at the centre of the domain, $x_1 = 0$. This occurs because the $p+ip$ model has the main condensate and spatial symmetries $C_4(z)\times C_2(x)\times C_2(y)$. However, the $s+is$ and $s+id$ models have only spatial symmetries and we find that the ψ_1 and ψ_2 domain walls do not occur in the $s+is$ and $s+id$ models. Simulating $s+is$ and $s+id$ solutions with either of the above boundary conditions does not produce a ψ_2 nor a ψ_1 domain wall. So we use the following boundary conditions throughout,

$$\lim_{x_1\to\pm\infty}(\psi_1,\psi_2) \qquad = (1,\pm i) \tag{2.153}$$

$$\lim_{x_1\to\pm\infty}(A_1,A_2,A_3) = (0,0,0)\ , \tag{2.154}$$

having A_i vanish on the boundary is a gauge choice that will require $\partial_1\psi_\alpha = 0$ on the boundary as well. These boundary conditions force a domain wall whose phase difference, θ_{12}, smoothly interpolates between $[\frac{\pi}{2}, -\frac{\pi}{2}]$.
We use the same numerical method as in Section 2.2.3 which allows magnetic field twisting and respects the original equations of motion. To reiterate this key point: the ansatz is,

$$\begin{aligned} \psi_\alpha &= \psi_\alpha(x_1) \\ A &= A_1(x_1)\hat{x}_1 + A_2(x_1)\hat{x}_2 + A_3(x_1)\hat{x}_3\ , \end{aligned} \tag{2.155}$$

where we have $A_3(x_1) \neq 0$ so that our magnetic field, $B = (0, B_2, B_3) = (0, -A_3', A_2')$, can point in both the x_2 and x_3 direction.
Through careful study of the domain wall solutions, we found two non degenerate domain wall solutions identifiable by the direction the phase difference interpolates. The phase difference, $\theta_{12} \in S^1$ interpolates between the two antipodal points, $\{\frac{\pi}{2}, -\frac{\pi}{2}\}$. This is shown in Figure 2.16 which depicts the interpolation of the phase difference as a point on the unit circle.

We have plotted examples of both domain wall solutions with orientations, $\hat{x}_1 = (0.1736, 0, 0.9848)$, in 2.17a and, $\hat{x}_1 = (0.309, -0.9511, 0)$, in 2.17b. Both the clockwise and anticlockwise domain wall solutions exhibit spontaneous magnetic fields for both orientations, however the strengths differ for each solution. This demonstrates that the two domain wall solutions could be experimentally observed through differences in their magnetic fields, though

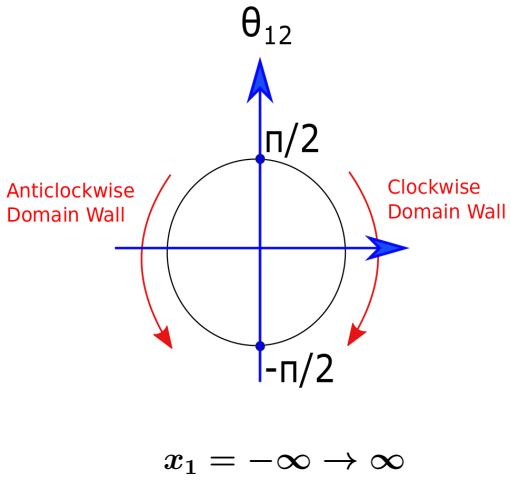

Figure 2.16: *Diagram of the interpolation of the phase difference, θ_{12}, from the left hand boundary, $\lim_{x_1\to-\infty}\theta_{12} = \frac{\pi}{2}$, to the right hand boundary $\lim_{x_1\to\infty}\theta_{12} = -\frac{\pi}{2}$. The direction of travel defines two domain wall types which, for the $s+is$ and $s+id$ models, are not degenerate in energy. The value of θ_{12} is expressed as a point on the unit circle.*

the differences are small. We also see that the only consistent feature of these two domain wall types is the phase difference. We note that the phase different changes smoothly between $\pm\frac{\pi}{2}$ around the centre of the domain. However, in the $p+ip$ case, if we consider the phase difference in Figures 2.5a and 2.5b, we see that the transition from the two boundary values happens very rapidly, in fact both plots look more like step functions than arctangent functions or kinks. It is this discontinuity which means anticlockwise and clockwise domain walls, if they occur, will be degenerate in energy in $p+ip$ superconductors. We note that we saw no evidence of clockwise and anticlockwise domain walls in our $p+ip$ numerical solutions.

Identifying the globally minimum domain wall

For an isotropic BTRS superconductor the direction of the interpolation, clockwise or anticlockwise, does not matter. However, for our anisotropic model the direction of interpolation defines two, non degenerate in energy, domain walls.
This can be seen by considering a simple approximation to an anisotropic domain wall, where we allow θ_{12} to vary with respect to x_1 but fix the other quantities to their vacuum values, $(\rho_\alpha, p_i) = (u_\alpha, 0)$. The free energy (per unit area) for such an approximation is given by,

$$\begin{aligned} F_{reduced} = \int_{-\infty}^{\infty} \Big\{ & \frac{1}{8}(Q_{11}^{11}u_1^2 + Q_{11}^{22}u_2^2)(\theta'_{12}(x_1))^2 \\ & - \frac{1}{4}Q_{11}^{12}u_1u_2\cos\theta_{12}(x_1)(\theta'_{12}(x_1))^2 \\ & + \frac{\eta}{8}u_1^2u_2^2\cos 2\theta_{12}\Big\}\, dx_1. \end{aligned} \tag{2.156}$$

The transformation, $\theta_{12} \to \pi - \theta_{12}$, converts between the two types of domain wall and we see that if $Q_{11}^{12} = 0$ then $F_{reduced}$ is invariant under this transformation. When $Q_{11}^{12} \neq 0$ the second term is either positive or negative definite depending on the sign of Q_{11}^{12} and $\cos\theta_{12}(x_1)$. It is a fact that $\cos\theta_{12}(x_1)$ is positive definite for clockwise interpolation and negative definite for anticlockwise interpolation. Hence if $Q_{11}^{12} > 0$ then the clockwise domain wall has a lower $F_{reduced}$ as the overall sign of that term will be negative. For $Q_{11}^{12} < 0$ it is the anticlockwise domain wall that has a lower $F_{reduced}$. This suggests that the sign of Q_{11}^{12} can be used to

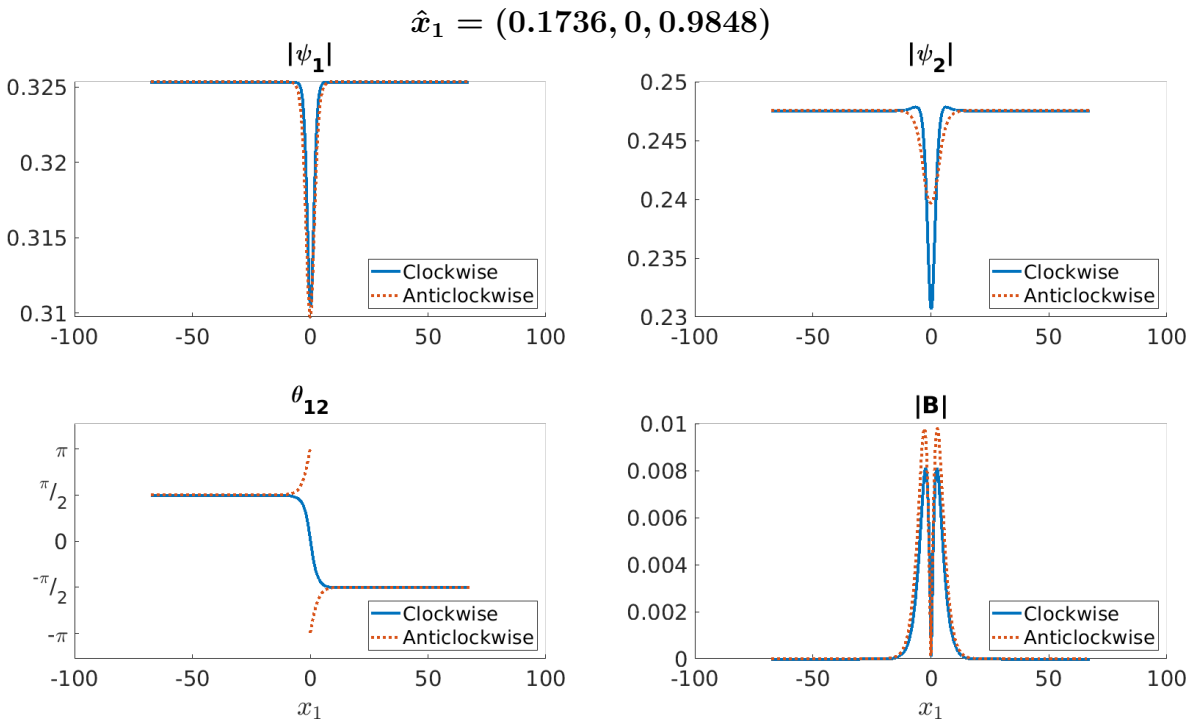

(a)

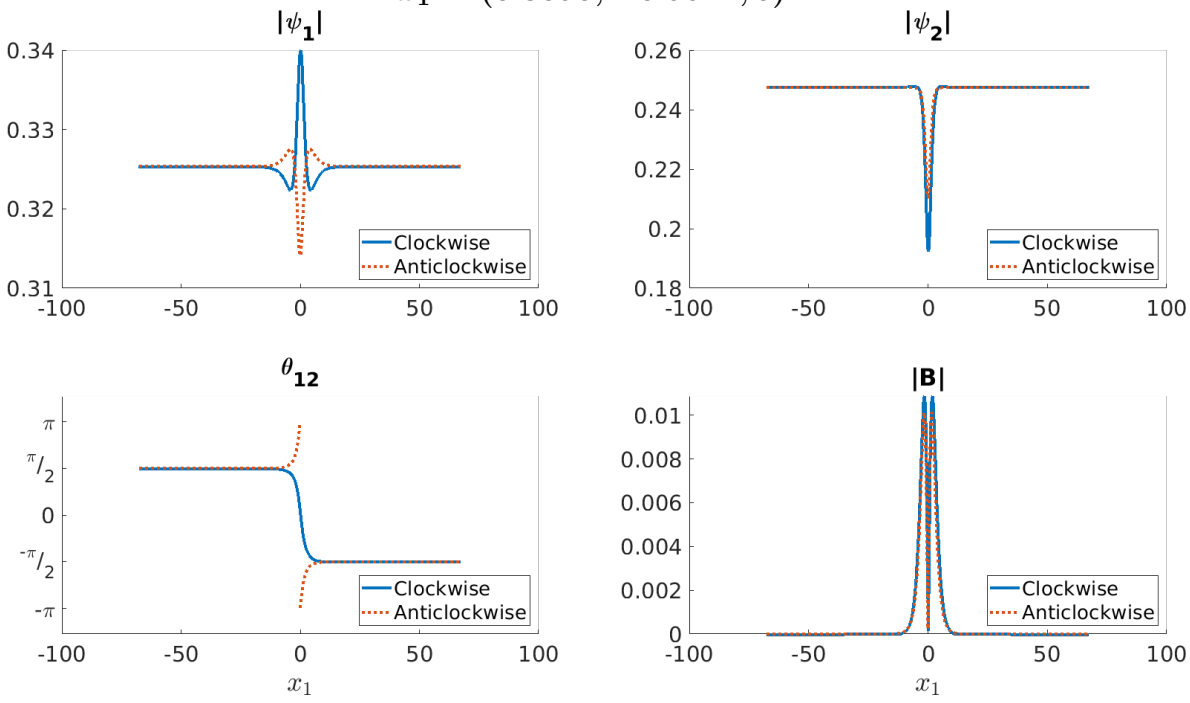

(b)

Figure 2.17: *Plots of two $s+id$ domain wall solutions, for two different orientations, corresponding to the phase difference θ_{12} winding either clockwise (blue) or anticlockwise (orange-dashed). We have plotted the key gauge invariant quantities $|\psi_i|$, θ_{12} and magnetic field strength $|B|$.*

predict the domain wall with the lower energy. This is a very crude approximation but it works for our chosen parameters when the difference in energy between the two domain wall types is not too small, consider Figure 2.18. In the $s + is$ case Q_{11}^{12} is always greater than zero, and correspondingly the free energy of the clockwise domain wall is always lower. In the $s + id$ case changes in the sign of Q_{11}^{12} approximately correspond to the domain wall type that has the lower free energy changing. To reiterate $Q_{11}^{12} < 0$ means the anticlockwise domain wall has the lower free energy and vice versa for the clockwise domain wall.

2.5.2 Orientation Dependence of Physical Quantities

The following solutions were produced by using initial conditions which favoured the domain wall type that we wanted to simulate. We then, as in the $p + ip$ case (Section 2.4), looped through the set of orientations using the solution from the previous run as the initial condition for the next orientation (subsequent initial conditions) which fixes the domain wall type for all orientations.

Free Energy

We plot the total free energy for all possible orientations of the normal $\hat{x}_1$ for the $s+is$ model in 2.19a and the $s + id$ model in 2.19b. These plots display the free energy for all possible orientations for the normal in the crystalline basis, by mapping each orientation to a point on a unit 2-sphere. Due to the symmetry of the free energy, F, under the reflection $z \mapsto -z$, it is sufficient to retain only the upper hemisphere of the resulting plot. So the unit vector from the origin to a point on the upper hemisphere gives an orientation and each point is then coloured by the total (normalised) free energy of the numerical solution. The free energy plots allow us to visualise the spatial symmetries, about the crystalline z axis, of the two models: $SO(2)(z)$ for $s+is$ and $C_2(z)$ for $s+id$ as well as identify which orientations have the lowest free energy. We can see those orientations are $\hat{x}_1 = (1, 0, 0)$, up to $SO(2)(z)$ symmetry, for the $s + is$ case and it is $\hat{x}_1 = (\pm 1, 0, 0)$ or $\hat{x}_1 = (0, \pm 1, 0)$ for the $s + id$ case.

Maximum Magnetic field

We can also visualise the orientation dependence of the maximum magnetic field, $B_{max} = |B(x_1^{max})|$, for the $s + is$ and $s + id$ models given in Figures 2.20a and 2.20b. We include arrows to show the direction of the maximum magnetic field, $\hat{B}_{max}$ defined in Equation 2.140, with the length of the arrow being proportional to the value of B_{max}. For domain walls the topological requirement that, $\int_{\mathbb{R}} B(x_1)dx_1 = 0$, implies that $B(x_1)$ either vanishes or is an odd function about the centre of the domain wall which we set to be $x_1 = 0$. As seen in, Figure 2.21, there are two points, $\pm x_1^{max}$, where we have $B(\pm x_1^{max}) = \pm B_{max}$. This is why the arrows in, Figure 2.20a and 2.20b, point in opposite directions, as discussed previously in Section 2.4.4.

We see that, both models, for $\hat{x}_1$ orientated parallel to the crystalline axes, (x, y, z), have $B_{max} = 0$.

Finally, if we consider the great circles connecting crystalline axes: $(\cos\theta, \sin\theta, 0), (\cos\theta, 0, \sin\theta)$ and $(0, \cos\theta, \sin\theta)$, where $\theta \in [0, 2\pi]$ and $(\cos\theta, \sin\theta, 0)$ denotes the basal plane. We see that, when $B_{max} \neq 0$, the arrows, that give the direction of B_{max}, that lie on great circles are orthogonal to those great circles. Due to the $SO(2)(z)$ symmetry of the $s + is$ model all of the arrows are orthogonal to the single great circle, $(\cos\theta, 0, \sin\theta)$. The linearisation also predicts that along these great circles there is a single direction for the spontaneous magnetic field that is orthogonal to that great circle. We see

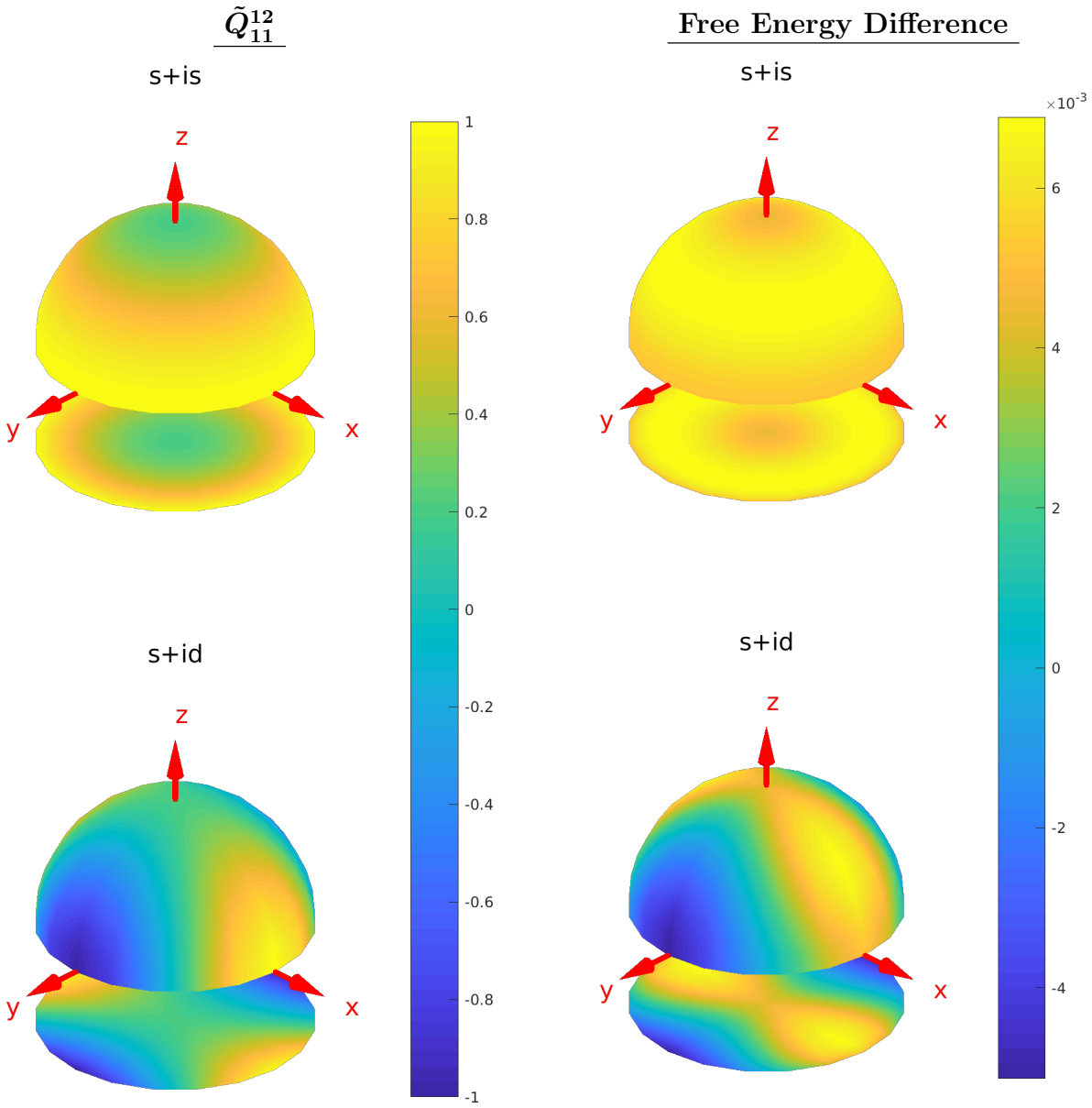

Figure 2.18: *Plots of the value of Q^{12}_{11} and the difference in the free energy (per unit area) between the clockwise and anticlockwise domain wall solutions for both $s+is$ and $s+id$, for all orientations. Each unit vector from the origin to a point on the hemisphere defines a domain wall orientation (in terms of the crystalline basis), with the colour giving the value of $\tilde{Q}^{12}_{11}$ where ($\tilde{Q}^{12} = M^T Q^{12} M$) (left panel) and the energy of an anticlockwise domain wall minus that of a clockwise domain wall (right panel). Note that the orientation is given by $\hat{x}_1 \in S^2$, however as the $s+is$ and $s+id$ free energies are invariant under the symmetry, $z \mapsto -z$, we record only the upper hemisphere.*

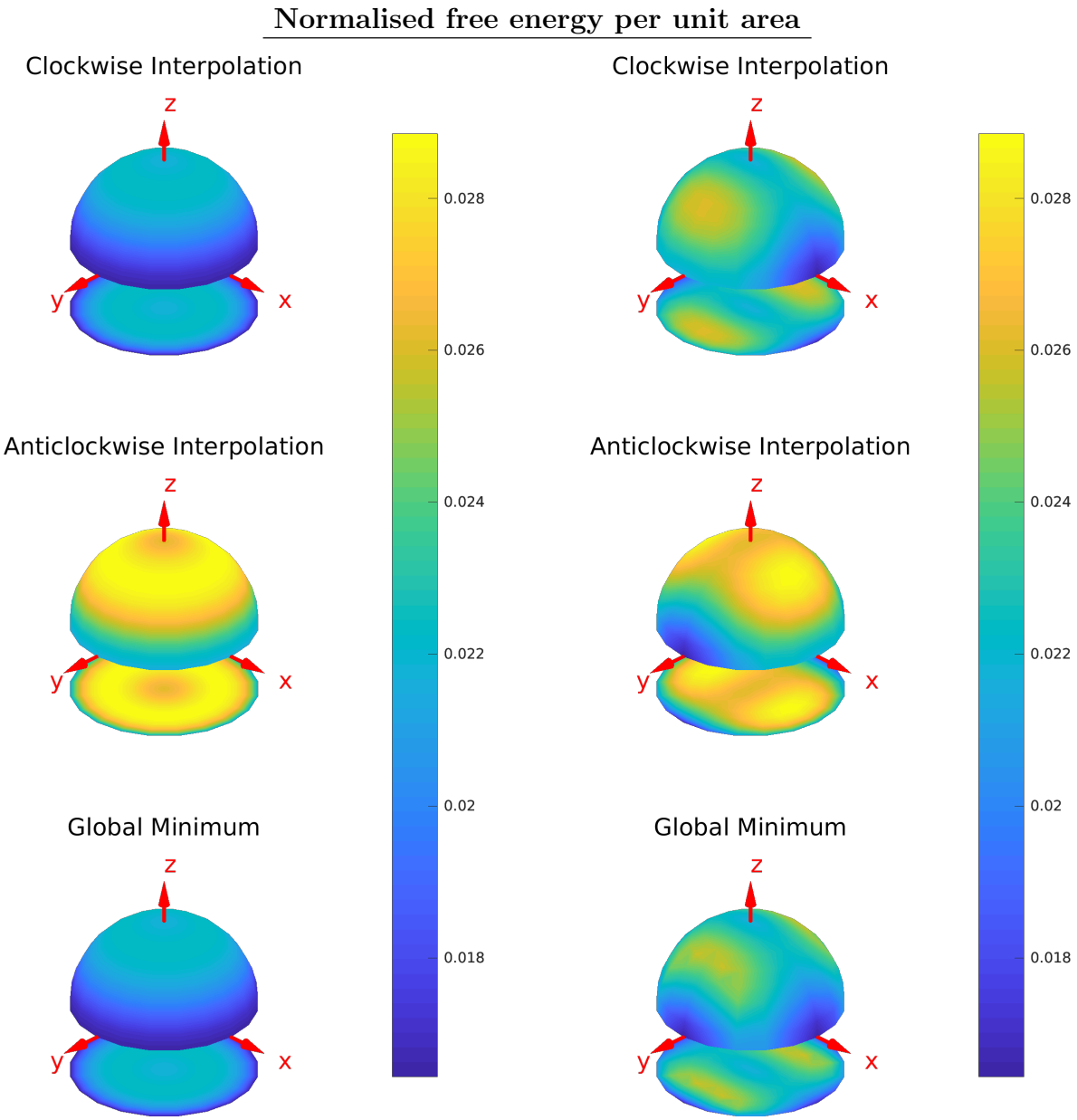

(a) *s+is* **(b)** *s+id*

Figure 2.19: *Plots of the free energy per unit area of each domain wall solution for all possible orientations. Each unit vector from the origin to a point on the hemisphere defines a domain wall orientation (in terms of the crystalline basis), with the colour giving the value of the free energy of the corresponding domain wall solution. There are two non-degenerate domain wall solutions depending on the winding of the phase difference (clockwise and anticlockwise).*

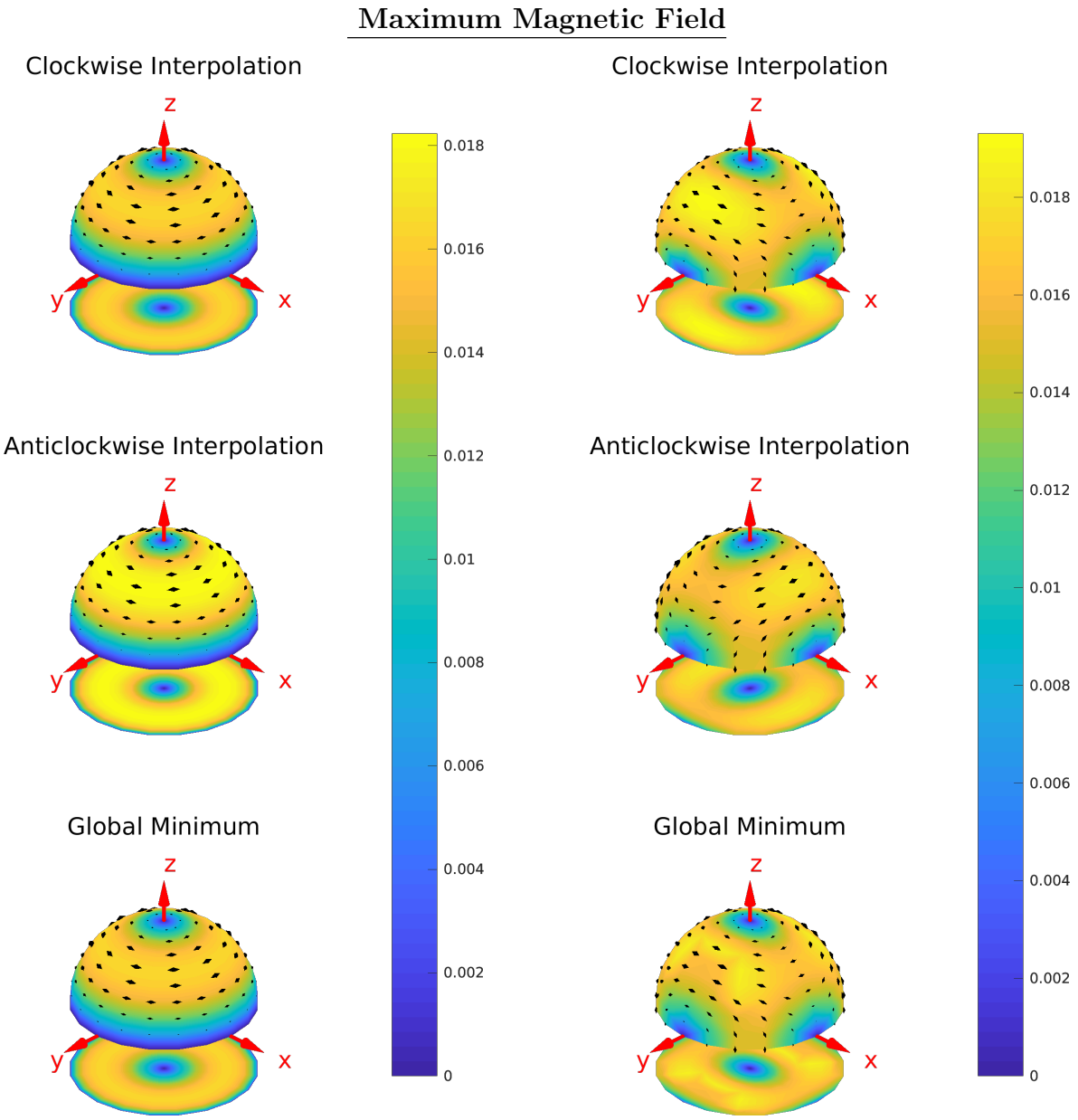

(a) $s + is$ **(b)** $s + id$

Figure 2.20: *Plot of the maximum magnetic field,* $B_{max} = \max|B|$*, of each domain wall solution for all possible orientations. Each unit vector from the origin to a point on the hemisphere defines a domain wall orientation (in terms of the crystalline basis), with the colour giving the value of the maximum magnetic field strength of the corresponding domain wall solution. In addition, we have plotted the direction of the maximum magnetic field as an arrow tangent to the hemisphere. There are two non-degenerate domain wall solutions depending on the winding of the phase difference (clockwise and anticlockwise).*

that for these orientations the direction of the maximum magnetic field in the nonlinear region matches the direction in the linear region. This is a nice result as predicting the direction of the maximum magnetic field, something that occurs in the nonlinear region, should be beyond the linearisation.
If we then visualise $\hat{B}_{max} \in S^2$, for the $s + id$ case, we see that $B_{max} = 0$ at $\hat{x}_1 = \pm x$ and $\hat{x}_1 = \pm \hat{x}$. These four points lie on two great circles each and this causes the winding of $\hat{B}_{max}$ around the x and y axes. We can define a winding number, N, where $N = 1$ is clockwise winding and $N = -1$ is anticlockwise winding. For the clockwise domain wall the winding around x and y is -1 and $+1$ respectively. For the anticlockwise domain wall case it is the reverse, the winding around the x and y axes is 1 and -1 respectively. The winding around the z axis is the same for both domain walls and is $N = 1$. We remind the reader that we found that $N = -1$, about the z axis, in the $p + ip$ case, and there is no winding in the $s + is$ case. This could potentially provide experimentalists with a way of distinguishing between superconductor types.

2.5.3 Magnetic Field Twisting

As we did in Section 2.4.5 we compare the spontaneous magnetic field direction with that of B_{max}, defining the local twisting angle, $\theta_t(x_1)$, in Equation 2.141. We reiterate the fact that there are two values of, $x_1 = \pm x_1^{max}$, that give the same value of $|B_{max}|$ with magnetic field $\pm|B_{max}|$. Our definition of $\theta_t(x_1)$ means that the twisting angle is the same regardless of which value we use. Close to the boundaries the value of the magnetic field is lower than the accuracy of our numerics so we use the condition in Equation 2.142 to set $\theta_t(x_1) = 0$ for such points. We plot the spontaneous field and twisting angle for two different orientations for an anticlockwise $s + id$ domain wall in 2.21, noting that there is no apparent difference in twisting between the two domain wall types.

Twisting is caused by the direction of the magnetic field, B_{max}, changing between the nonlinear and linear regions of the domain wall. The direction for the linearised magnetic field is given by,

$$B_{lin} \propto (0, -v_1^6, v_1^5). \tag{2.157}$$

The $s+is$ model exhibits no twisting, as predicted by the linearisation. This is because, where $B_{max} \neq 0$, both $\hat{B}_{max}$ and $\hat{B}_{lin}$ are orthogonal to the great circle $(\cos\theta, 0, \sin\theta)$ so there is no change in direction moving from the nonlinear to linear region.
For the $s + id$ model we see significant magnetic field twisting, as seen in Figure 2.21. Along the great circles we do still have $\theta_t(x_1) = 0$ as the direction of $\hat{B}_{max}$ matches $\hat{B}_{lin}$. However, away from the great circles they do not match giving non zero twisting. We consider,

$$\theta_t^{max} := \max(\theta_t(x_1)) \ , \tag{2.158}$$

which we plot in Figure 2.22.

We see that $\theta_t(x_1) = 0$ along the great circles which matches the linearisation. Away from these we have non zero twisting which allow differentiation between the $s + is$ and $s + id$ models. We note that compared to the $p + ip$ case, see Figure 2.15, the twisting angle in this model does not oscillate and approaches a constant value away from the centre of the domain wall.

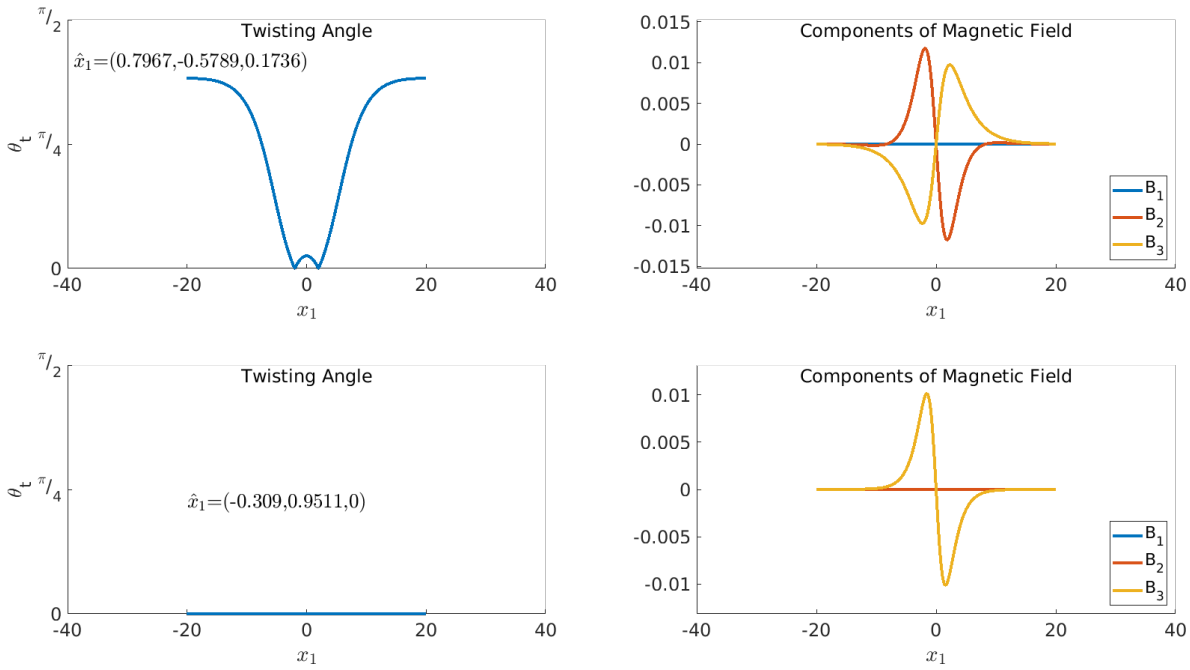

Figure 2.21: *Plots of the maximum value of the twisting angle, $\theta_t(x_1)$, for a clockwise $s+id$ domain wall. We choose an orientation, $\hat{x}_1 = (0.7967, -0.5789, 0.1736)$, where θ_t is close to the maximum value for all orientations and another, $\hat{x}_1 = (-0.309, 0.9511, 0)$, in the basal plane where $\theta_t = 0$. We only include anticlockwise domain walls as there is not an appreciable difference in magnetic response between clockwise and anticlockwise domain walls. Note that we have chosen to set $\hat{x}_3 = (0, 0, 1)$ for the orientation in the basal plane.*

2.5.4 Oscillatory Decay of Field Solutions

Unlike Section 2.4.3 we do not see any evidence of oscillating tails in the non-linear solutions. This is because the real part of the dominant length scale too heavily damps the oscillations for them to be seen in the linear region. This can be seen in Figure 2.23, where we see $R_{\mu_1} = \frac{\mathrm{Im}\,(\mu_1)}{\mathrm{Re}\,(\mu_1)} < 0.4$ for all orientations. This means finding these oscillating tails numerically, for this parameter set, is not possible.

2.6 Summary

We have shown that domain walls provide a good way of analysing the symmetries and solutions of the three different models, $p + ip$, $s + is$ and $s + id$. We have also seen that these domain walls produce a spontaneous magnetic field which can be explained due to the anisotropy which couples the condensates and magnetic fields. In the $p + ip$ case we have extended the results of [26] from orientations in the basal plane to the full, $SO(3)$, set of orientations. Furthermore, we have shown that the linearisation correctly predicts oscillatory decay of fields in the linear region of domain walls. In the $s + is$ and $s + id$ case we have found and analysed a new type of domain wall as well as showing that the linearisation is remarkably accurate in predicting the behaviour of the spontaneous magnetic field, including the existence (or non existence) of magnetic field twisting in $s+id$ and $s+is$ superconductors.

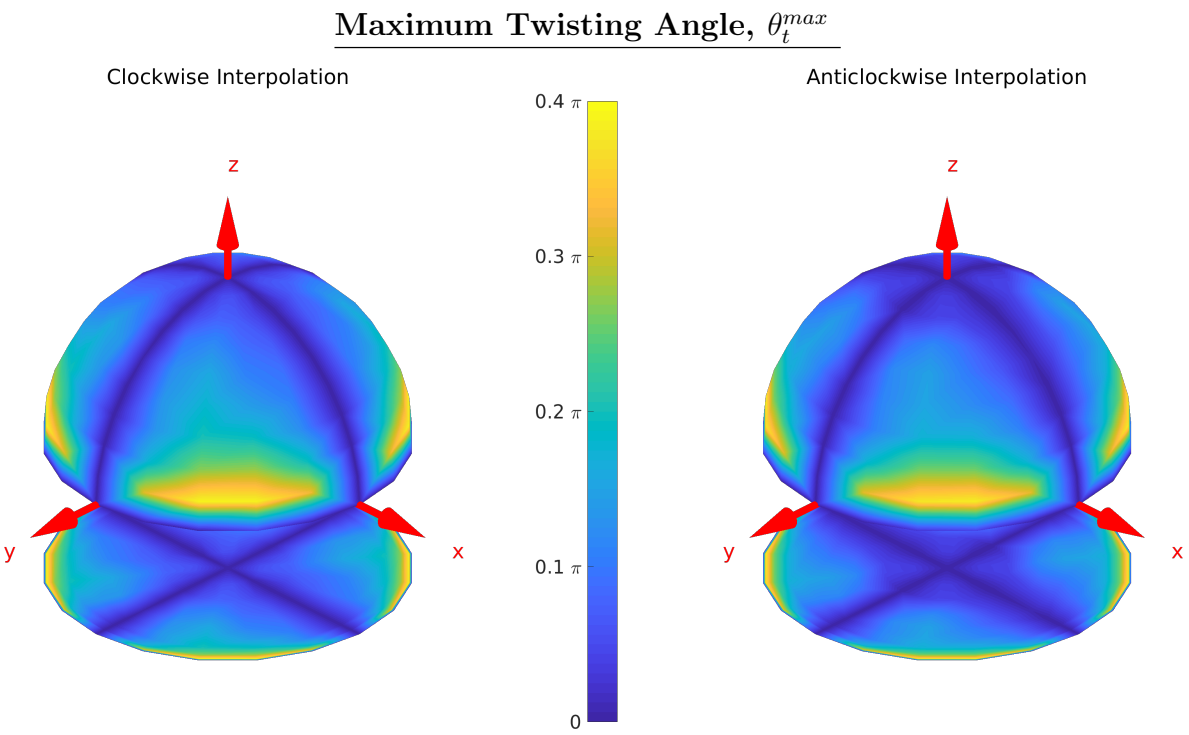

Figure 2.22: *Plots of the maximum twisting angle of the magnetic field of domain wall in an $s + id$ superconductor: clockwise phase difference winding (left) and anticlockwise phase difference winding (right). Each unit vector from the origin to a point on the hemisphere defines a domain wall orientation (in terms of the crystalline basis), with the colour giving the value of θ_{max} for that orientation. Here we see that θ_{max} is essentially the same for both clockwise and anticlockwise domain walls. We use a value of cutoff $= 5e-06$ which matches the numerical tolerance used.*

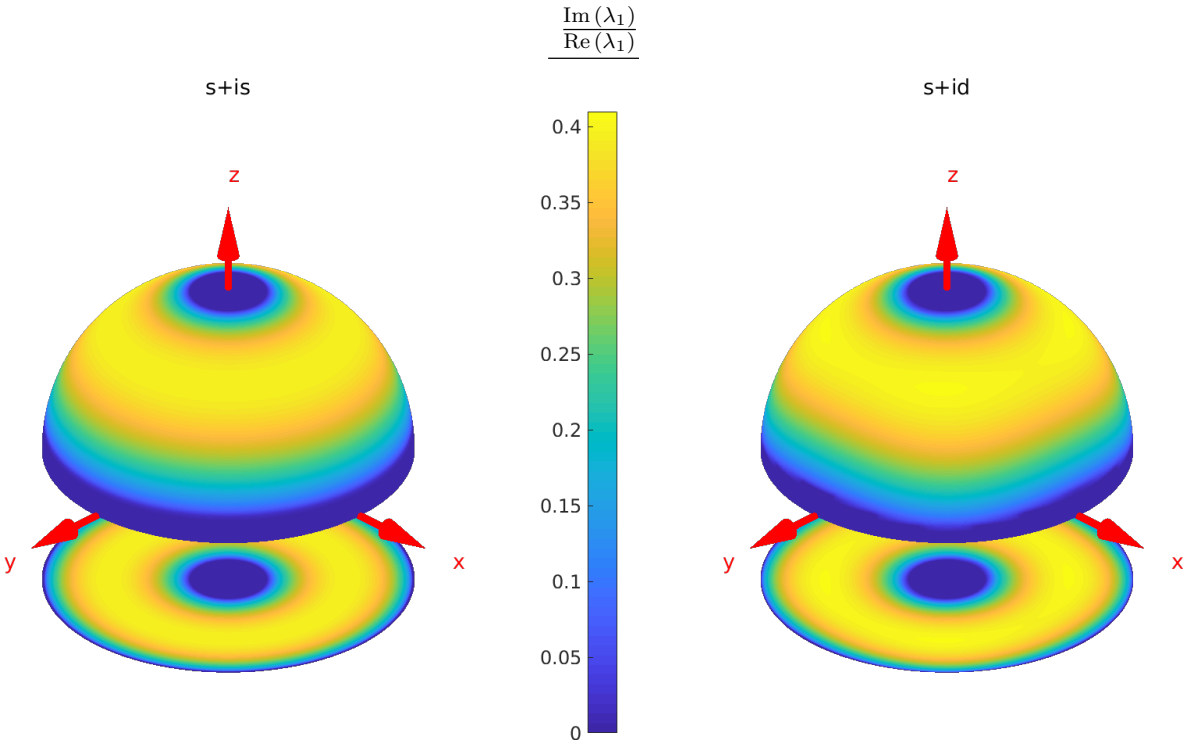

Figure 2.23: *Orientation dependence of* $R_{\mu_1} = \frac{|\mathrm{Im}\,(\mu_1)|}{|\mathrm{Re}\,(\mu_1)|}$ *for* $\hat{x}_1 = (\cos\omega\cos\phi, \sin\omega\cos\phi, \sin\phi)$. *Each unit vector from the origin to a point on the hemisphere defines a domain wall orientation (in terms of the crystalline basis), with the colour giving the value of* R_{μ_1} *for that orientation. The* $s+is$ *plot has* $SO(2)(z)$ *symmetry. The* $s+id$ *is very similar to the* $s+is$ *case (it only differs by* 0.08 *at most). However, it does exhibit the expected* $C_2(z)$ *symmetry. The important thing is that both models have* $\frac{\mathrm{Im}\,(\lambda_1)}{\mathrm{Re}\,(\lambda_1)} < 0.4$ *which means the oscillating tails are likely too heavily damped to be seen in the nonlinear solutions.*
$(\nu, V_0, k_5) = (-0.95, 6, 2.35)$

Chapter 3

Meissner State in $s+is$ and $s+id$ Superconductors

In this chapter we study how an external magnetic field, H, interacts with the boundary of a superconductor and an electrical insulator. This is a three-dimensional effect that can be modelled by a one-dimensional Ginzburg-Landau theory by considering how the fields vary in a given direction, $\hat{x}_1$, perpendicular to the aforementioned boundary. This is known as the Meissner state and was first introduced in Chapter 1 where we studied it in an isotropic superconductor. In the isotropic case we apply a constant external magnetic field, H_0, perpendicular to the normal to the boundary, $\hat{x}_1$. We note that the choice of external magnetic field direction, $\hat{x}_3$, for an isotropic model, does not change the solutions to the Ginzburg-Landau equations, neither does the choice of $\hat{x}_1$. However, when we consider the anisotropic $s+is$ and $s+id$ models we find that both the choice of $\hat{x}_1$ and the choice of $\hat{x}_3$ affects the solutions to the Ginzburg-Landau equations. Varying $\hat{x}_3$ can introduce magnetic field twisting, which is where the direction of the internal magnetic field, B, differs from that of the externally applied magnetic field, H. The twisting can be by as much as $\frac{\pi}{2}$, where B and H are orthogonal, and provides a good opportunity to verify the linear model derived in Section 2.3 by comparing its predictions of magnetic field twisting to those found from solutions to the nonlinear Ginzburg-Landau equations. This chapter is based on work from the joint paper [2].

3.1 Gibbs Free Energy

We build upon Section 1.4 which introduced the Meissner state in a single component isotropic superconductor. For the Meissner state we consider how an applied external magnetic field, H, affects the internal fields of a superconductor, (B, ψ_1, ψ_2). However, doing so means we need to modify the Ginzburg-Landau free energy to include energy contributions from the applied external magnetic field, this is called the Gibbs free energy. The three-dimensional anisotropic multicomponent Gibbs free energy is given below,

$$G = \int_{\mathbb{R}^3} g \; dx_1 dx_2 dx_3 = F - H_i \int_{\mathbb{R}^3} B_i \; dx_1 dx_2 dx_3 \; , \tag{3.1}$$

with the same form of free energy,

$$F = \int_{\mathbb{R}^3} \left(\frac{1}{2} \tilde{Q}_{ij}^{\alpha\beta} (D_i \psi_\alpha)^* (D_j \psi_\beta) + \frac{B^2}{2} + \left(F_P - F_P \left(u_1, u_2, \pm \frac{\pi}{2} \right) \right) \right) dx_1 dx_2 dx_3 \; , \tag{3.2}$$

where the $\tilde{Q}^{\alpha\beta} = M^T Q^{\alpha\beta} M$ are the anisotropy matrices, $Q^{\alpha\beta}$, that have been transformed by a choice of $M \in SO(3)$ which is equivalent to a coordinate transformation. There is an implied summation over repeated indices. Additionally, the external magnetic field is written as $H = H_i \hat{x}_i$, where we assume its components, H_i , are constant.
For an $s + is$ and $s + id$ superconductor the anisotropy matrices and general form of the potential are given by,

$$Q^{11} = \begin{pmatrix} a_1 & 0 & 0 \\ 0 & a_1 & 0 \\ 0 & 0 & b_1 \end{pmatrix} , Q^{22} = \begin{pmatrix} a_2 & 0 & 0 \\ 0 & a_2 & 0 \\ 0 & 0 & b_2 \end{pmatrix} , Q^{12} \equiv (Q^{21})^T = \begin{pmatrix} a_3 & 0 & 0 \\ 0 & s \cdot a_3 & 0 \\ 0 & 0 & b_3 \end{pmatrix} \tag{3.3}$$

$$F_p = \alpha_1 \rho_1^2 + \alpha_2 \rho_2^2 + \frac{\beta_1}{2} \rho_1^4 + \frac{\beta_2}{2} \rho_2^4 + \gamma_{12} \rho_1^2 \rho_2^2 + \eta_{12} \rho_1^2 \rho_2^2 \cos(2\theta_{12}) \ , \tag{3.4}$$

where $s = 1$ gives a $s + is$ and $s = -1$ gives an $s + id$ superconductor. These two models have $SO(2)(z) \times C_2(x) \times C_2(y)$ and $C_2(z) \times C_2(x) \times C_2(y)$ spatial symmetries which was discussed in more detail in Section 2.5. The action of the symmetries is given in Table 1.2. We remind the reader that the η_{12} term introduces broken time reversal symmetry to the model which means we have two gauge inequivalent vacuum solutions given by $(\psi_1, \psi_2) = (u_1, -iu_2)e^{i\omega_1}$ and $(u_1, iu_2)e^{i\omega_2}$.
If we consider varying $H_i \int_{\mathbb{R}^3} B_i \ dx_1 dx_2 dx_3$ with respect to A_i we find that it vanishes as we have assumed H_i is constant. As only this term in the Gibbs free energy contains H_i, this means that the Ginzburg-Landau equations for the bulk of the superconductor, Equations 1.124 and 1.125, are not affected by the value of H_i. Thus the choice of H_i only affect the values of the fields on the boundary which then decay to their vacuum values in bulk of the superconductor.
We use the orthonormal basis $(\hat{x}_1, \hat{x}_3 \times \hat{x}_1, \hat{x}_3)$, which gives us the orientation matrix, M, used to transform the anisotropy matrices. We can now study the Meissner state in the $\hat{x}_1$ direction which we define as the inward pointing normal to the boundary between the superconductor and insulator. We then apply a constant external magnetic field, H_0, in the $\hat{x}_3$ direction, such that $H = H_0 \hat{x}_3$. This introduces a translations invariance, of the fields, in the directions perpendicular to the normal, $\hat{x}_2$ and $\hat{x}_3$, which allows us to dimensionally reduce Equation 3.1 using the ansatz,

$$\begin{aligned} \psi_\alpha &\mapsto \psi_\alpha(x_1) \\ A &\mapsto (A_1(x_1), A_2(x_1), A_3(x_1)) \ . \end{aligned} \tag{3.5}$$

This is the same one-dimensional ansatz that we used for domain walls, described in Section 2.5. We retain A_3 for the one-dimensional Ginzburg-Landau equations to be consistent with the fully three-dimensional versions, as discussed in Section 2.2.1. Thus $x_1 = 0$ is the boundary between an insulator, $x_1 < 0$, and a superconductor $x_1 > 0$. Furthermore, the value of H_0 will affect the values of the fields on the boundary, $x_1 = 0$, but due to the anisotropy the choice we make for the $\hat{x}_3$, the direction for the externally applied magnetic field, also affects the Gibbs free energy through the transformation $\tilde{Q}^{\alpha\beta} \mapsto M^T Q^{\alpha\beta} M$.
As our ansatz allows the magnetic field within the superconductor, B, to point in both the $\hat{x}_2$ and $\hat{x}_3$ directions. For some orientations, $\hat{x}_1$, the internal magnetic field may not point in the $\hat{x}_3$ direction. This is called magnetic field twisting and is best measured by,

$$\cos(\theta_t) = \frac{B_3}{\sqrt{B_2^2 + B_3^2}} \ , \tag{3.6}$$

where θ_t measures the amount the internal magnetic field deviates from the direction of the external magnetic field, $\hat{x}_3$.

3.1.1 Numerical Method

We, as in Chapter 2, use arrested Newton flow to produce local minimum solutions to Equation 3.1. To recap we discretise our one-dimensional domain into $N_x = 1000$ equally spaced points with a spacing of $h_x = 0.05$. We also discretise the fields at each point and calculate their spatial derivatives using fourth order finite differences. We then apply these discretised fields and derivatives to the Ginzburg-Landau equations. We can consider these equations to be gradients, with respect to the fields, of the discretised Gibbs free energy and then use these gradients to evolve the fields towards a local minimum of the Gibbs free energy.
This method is described in more detail in Section 2.2.3, where the key difference is that, for the Meissner state, only the right hand boundary, $\hat{x}_1 \to \infty$, has the fields fixed to their vacuum values,

$$\lim_{x\to\infty} (\psi_1, \psi_2, A_1, A_2, A3) = (u_1, iu_2, 0, 0, 0) \ . \tag{3.7}$$

We have chosen a gauge that requires, $\partial_1 \psi_\alpha = 0$, for the free energy to be finite as well as choosing the value of $\omega_2 = 0$. Numerically we impose this boundary condition at $x_1 = L$, where L is large, to approximately simulate an infinite superconductor. However, similarly to the isotropic Meissner state in Section 1.4, we use natural boundary conditions at $x_1 = 0$. For our dimensionally reduced system this is the requirement that,

$$\left.\frac{\partial g}{\partial\left(\partial_1 \Phi\right)}\right|_{x_1=0} = 0 \ , \tag{3.8}$$

where $\Phi = (\mathrm{Re}(\psi_1), \mathrm{Im}(\psi_1), \mathrm{Re}(\psi_2), \mathrm{Im}(\psi_2), A_1, A_2, A_3)$. Thus the natural boundary conditions can be expressed as,

$$\left.\tilde{Q}^{1\beta}_{1j} D_j \psi_\beta\right|_{x_1=0} = 0 \tag{3.9}$$

$$\left.\tilde{Q}^{2\beta}_{1j} D_j \psi_\beta\right|_{x_1=0} = 0 \tag{3.10}$$

$$\partial_1 A_1 = 0 \tag{3.11}$$

$$B|_{x_1=0} = H \ , \tag{3.12}$$

where numerically, for each step of the Newton flow algorithm, we must solve the above set of simultaneous equations to calculate the value of the fields on the boundary, $x_1 = 0$. However, the values of A_i are easily determined from Equations 3.11 and 3.12. Then, as Equations 3.9 and 3.10 are linear in ψ_β, we can determine all of the values of the fields on the left boundary.

The parameters used are, $H_0 = 0.1$, and the anisotropy matrices are,

s+is	s+id
$Q^{11} = \begin{pmatrix} 4 & 0 & 0 \\ 0 & 4 & 0 \\ 0 & 0 & 0.3 \end{pmatrix}$	$Q^{11} = \begin{pmatrix} 4 & 0 & 0 \\ 0 & 4 & 0 \\ 0 & 0 & 0.3 \end{pmatrix}$
$Q^{22} = \begin{pmatrix} 0.5 & 0 & 0 \\ 0 & 0.5 & 0 \\ 0 & 0 & 2 \end{pmatrix}$	$Q^{22} = \begin{pmatrix} 0.5 & 0 & 0 \\ 0 & 0.5 & 0 \\ 0 & 0 & 2 \end{pmatrix}$
$Q^{12} = \begin{pmatrix} 1 & 0 & 0 \\ 0 & 1 & 0 \\ 0 & 0 & 0.2 \end{pmatrix}$	$Q^{12} = \begin{pmatrix} 1 & 0 & 0 \\ 0 & -1 & 0 \\ 0 & 0 & 0.2 \end{pmatrix}$

Table 3.1: Form of the anisotropy matrices for $s + is$ and $s + id$ systems.

with the potential given by

$$F_p = -\frac{1}{2}|\psi_1|^2 - \frac{1}{2}|\psi_2|^2 + 2|\psi_1|^4 + 3|\psi_2|^4 + \frac{3}{2}|\psi_1|^2|\psi_2|^2 + \frac{1}{8}|\psi_1|^2|\psi_2|^2 \cos 2\theta_{12} \ . \tag{3.13}$$

We note that these are the same parameter sets as we used for the $s + is$ and $s + id$ domain walls results, Section 2.5.

3.2 Magnetic Field Twisting

Here we show how changing the direction of the external magnetic field, $\hat{x}_3$, for a given $\hat{x}_1$ orientation, can cause the component of the magnetic field in the $\hat{x}_2$ direction, B_2, to be non zero. This would mean that the internal magnetic field is pointing in a different direction to that of the externally applied magnetic field. In other words the model can exhibit magnetic field twisting.

We now return to the linearisation, see Section 2.3, as a way of predicting/interpreting which $\hat{x}_3$ causes magnetic field twisting. We remind the reader that the linearisation finds five modes, $\vec{v}_i$, along with the length scales, λ_i. These describe the long range behaviour of the fields, $x_1 \to \infty$, when the fields are close to their vacuum values, as $x_1 \to \infty$, and thus the linearisation is valid. The modes and length scales are ordered by decreasing real part of λ_i. We call λ_1 the leading or dominant length scale and assume that the corresponding mode, $\vec{v}_1$, will dominate the linear solution. In general, the linearisation does not predict if a mode is excited, which means it contributes towards the long range behaviour of the full nonlinear solutions. Thus the non leading modes may also contribute to the behaviour of the linear solutions. However, we can predict all of the possible directions for the linear magnetic field, there will be one associated with each magnetic or mixed mode. Then if our chosen direction for the external magnetic field, $\hat{x}_3$, does not align with any of these direction then we can expect magnetic field twisting.

Consider Figure 3.1a that shows the Meissner state for the $s + is$ model for the orientation, $\hat{x}_1 = (1, 0, 0)$. This is an example of the type of plots we will be using to analyse the relationship between magnetic field twisting and the linearisation. It shows the components of the magnetic field where, $B = (0, B_2, B_3)$. Additionally, we include ρ_α where we have written the condensate in polar coordinates, $\psi_\alpha = \rho_\alpha e^{i\theta_\alpha}$. The phase difference is defined as $\theta_{12} := \theta_1 - \theta_2$ and the magnetic twisting angle, θ_t, from Equation 3.6 .

If we focus only on the fields for the $\chi = \frac{\pi}{2}$ solution which gives $\hat{x}_3 = (0, 0, 1)$. The plots start with $B_3 = H_0$ for $x_1 = 0$ and show it decaying to zero as we move into the superconductor. This shows how an external magnetic field will penetrate the superconductor close to the surface. Correspondingly the values of ρ_1, ρ_2 and θ_{12} approach their vacuum values as B_3 decays to zero. We note that $B_2 = 0$ on the boundary as the applied magnetic field, $H = H_0\hat{x}_3$, is zero in that direction.

$\hat{x}_1 = (1, 0, 0)$

Consider the simplest orientation, $\hat{x}_1 = (1, 0, 0)$. We then define $\hat{x}_3(\chi) = (0, \cos\chi, \sin\chi)$, where $H = H_0\hat{x}_3(\chi)$, which fixes the orthonormal basis, for a given value of χ, as we generate the final basis vector via, $\hat{x}_2 = \hat{x}_3(\chi) \times \hat{x}_1$. In this case the length scales for the $s + is$ and

$s + id$ states are exactly the same and they are all real,

$$\begin{aligned}
\mu_1 = 0.3124, \quad \vec{v}_1 &= (-0.0356, 0.0077, 0.9665, -0.2541, 0, 0)^T , \\
\mu_2 = 0.3874, \quad \vec{v}_2 &= (0, 0, 0, 0, 0, 1)^T , \\
\mu_3 = 0.6694, \quad \vec{v}_3 &= (0, 0, 0, 0, 1, 0)^T , \\
\mu_4 = 0.9332, \quad \vec{v}_4 &= (-0.1553, 0.0585, -0.7053, 0.6892, 0, 0)^T , \\
\mu_5 = 2.4065, \quad \vec{v}_5 &= (-0.0376, -0.8038, -0.4742, -0.3572, 0, 0)^T \ .
\end{aligned} \tag{3.14}$$

This is because the two models differ only by the value of Q_{22}^{12} and for $\hat{x}_1 = (1, 0, 0)$ this term vanishes because none of the fields depend on the value of x_2 due to the dimensionally reduced ansatz that is employed. This can be seen from the structure of the linearised Ginzburg-Landau equations, 2.59, 2.60 and 2.61

If we consider the value of the mixing angles, defined in Equations 2.81 and 2.82,

$$(\theta_m^1, \theta_m^2, \theta_m^3, \theta_m^4, \theta_m^5) = \left(0, \frac{\pi}{2}, \frac{\pi}{2}, 0, 0, 0\right) \ , \tag{3.15}$$

this states that modes $\vec{v}_2$ and $\vec{v}_3$ are purely magnetic, $\theta_m^i = \frac{\pi}{2}$, and the rest are purely condensate, $\theta_m^i = 0$. This means that linear magnetic field, B_{lin}, points in purely the $(0, 0, 1)$ or $(0, 1, 0)$ direction. We remind reader that the simplest choice of $\hat{x}_3 = (0, 0, 1)$ was used for the linearisation. Thus if $\chi = 0$ or $\chi = \frac{\pi}{2}$ then the external magnetic field, H, will point in either the $(0, 1, 0)$ and $(0, 0, 1)$ directions respectively. This results in only the linear modes parallel to the direction of H being excited and thus we see no magnetic field twisting.

However, when $\chi = \frac{\pi}{4}$ we expect to see magnetic field twisting as neither B_{lin}, for the modes $\vec{v}_2$ or $\vec{v}_3$, is parallel to $\hat{x}_3(\chi = \frac{\pi}{4})$. Thus both modes should be excited by the external magnetic field. Observing Figures 3.1a and 3.1b we see that for only $\chi = \frac{\pi}{4}$ do we have non zero B_2 which means the internal magnetic field twists away from the applied magnetic field. Thus predictions made with the linearisation match simulations run using the full nonlinear Ginzburg-Landau equations. If we look at both plots for B_2 we see that it vanishes on the left boundary but then peaks and then decays to zero again at long range. If we consider the plots for B_3 we see that changing χ changes how close to the boundary, $x_1 = 0$, it decays to zero. The fact that changing the direction of applied magnetic field changes how the internal magnetic field decays inside the superconductor is a novel result.

The quantity θ_t can only be calculated when $|B| \neq 0$. Considering Figure 3.1a, θ_t **appears discontinuous** around $x_1 = 10$ but that is merely due to the magnetic field vanishing and so a value for θ_t can no longer be calculated for $x_1 > 10$. For Figure 3.1b, θ_t can no longer be calculated for $x_1 > 20$. This is expected as the magnetic field strength decays to zero as it moves deeper into the superconductor, this is the Meissner effect.

The standard picture for an isotropic superconductor is one where the direction, $\hat{x}_3(\chi)$, can be fixed without any change to the physics. This is clearly not the case for even the simplest possible choice of orientation for an anisotropic superconductor.

$\hat{\boldsymbol{x}}_{\mathbf{1}} = \frac{\mathbf{1}}{\sqrt{\mathbf{2}}}(\mathbf{1}, \mathbf{1}, \mathbf{0})$

We now move to an orientation, still in the basal plane but away from any crystalline axes, x or y. This allows us to differentiate between the $s + is$ and $s + id$ models. If $\hat{x}_1 = \frac{1}{\sqrt{2}}(1, 1, 0)$ then $\hat{x}_3(\chi) = \frac{1}{\sqrt{2}}(-\cos\chi, \cos\chi, \sqrt{2}\sin\chi)$, with $H = H_0\hat{x}_3(\chi)$, will define a unique basis for a given value of χ. Note that, for the linearisation **only**, as we are still in the basal plane we can set $\hat{x}_3 = (0, 0, 1)$ without loss of generality.

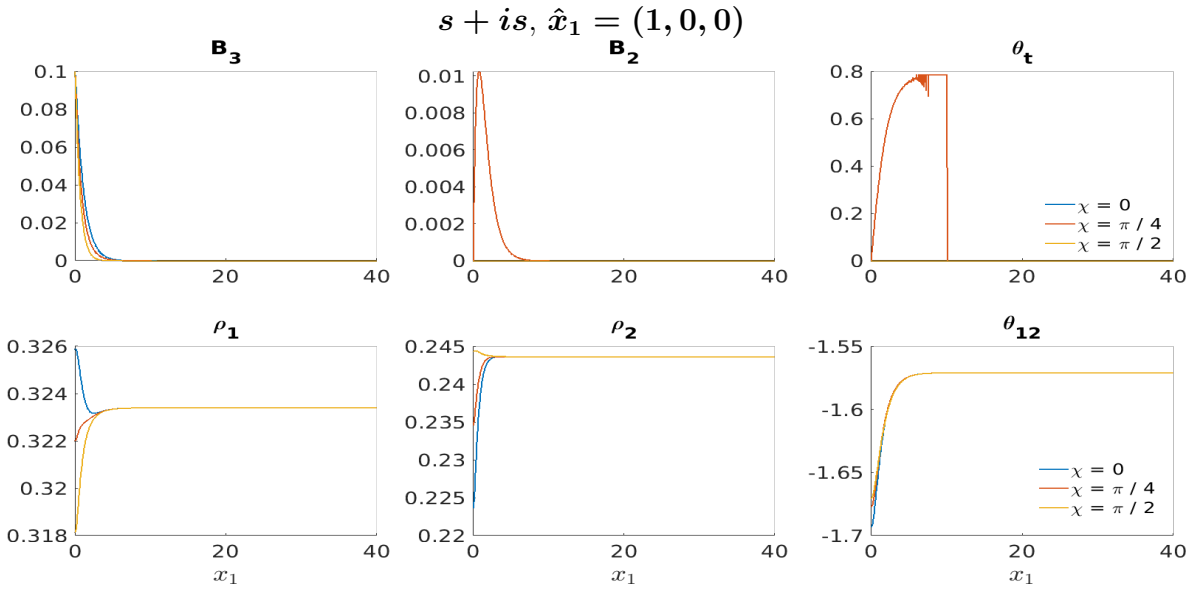

(a) *The Meissner state for an $s + is$ superconductor orientated in the, $\hat{x}_1 = (1, 0, 0)$, direction. We see the only non zero value of B_2, and therefore θ_t, occurs when $\chi = \frac{\pi}{4}$.*

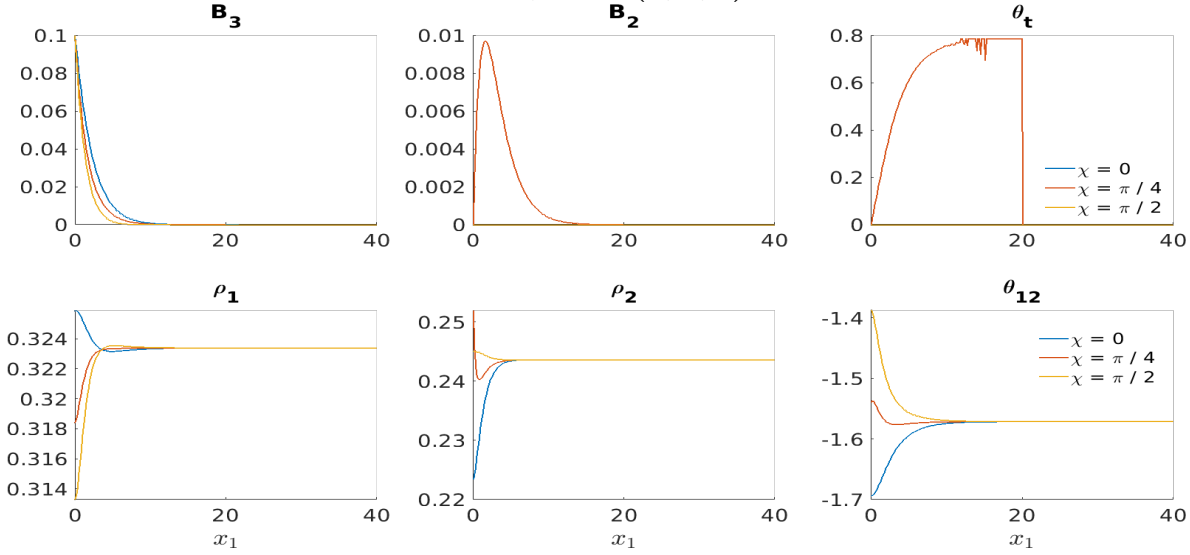

(b) *The Meissner state for an $s + id$ superconductor orientated in the, $\hat{x}_1 = (1, 0, 0)$, direction. Like the $s + is$ case we see that non zero B_2, and therefore θ_t, only occur for $\chi = \frac{\pi}{4}$. We note that in the $s+id$ case the decay to the homogenous superconducting state happens further into the superconductor.*

Figure 3.1: *Field solutions for the Meissner state for $s + is$ and $s + id$ with $\hat{x}_1 = (1, 0, 0)$ and external magnetic field $H = H_0(0, \cos\chi, \sin\chi)$. The fields approach their vacuum values, $(\rho_1, \rho_2, \theta_{12}, B_2, B_3) = (u_1, u_2, -\frac{\pi}{2}, 0, 0)$, as x_1 increases, the external field is given by, $H = H_0(0, \cos\chi, \sin\chi)$, where $H_0 = 0.1$.*

For the $s+is$ model, due to its spatial $SO(2)(z)$ symmetry, the length scales are the same as for Equation 3.14. However, the length scales for the $s+id$ model are,

$$\begin{aligned}
\mu_1 = 0.3347, \quad \vec{v}_1 &= (0, 0, -0.9603, 0.2788, 0, 0)^T, \\
\mu_2 = 0.3874, \quad \vec{v}_2 &= (0, 0, 0, 0, 0, 1)^T, \\
\mu_3 = 0.6505 \pm i0.0837, \quad \vec{v}_3 &= \begin{pmatrix} -0.1992 \pm i0.3962 \\ -0.0733 \mp i0.1650 \\ 0 \\ 0 \\ -0.8779 \mp i0.0061 \\ 0 \end{pmatrix}, \\
\mu_4 = (\mu_3)^*, \quad \vec{v}_4 &= (\vec{v}_3)^*, \\
\mu_5 = 1.6308, \quad \vec{v}_5 &= (0.0569, 0.9734, 0, 0, 0.2219, 0)^T,
\end{aligned} \tag{3.16}$$

which we note that some are now complex. If we consider the mode mixing also we see that,

$$(\theta_m^1, \theta_m^2, \theta_m^3, \theta_m^4, \theta_m^5) = (0, \frac{\pi}{2}, 1.0715, 1.0715, 0.22380), \tag{3.17}$$

and that the leading magnetic mode, $\vec{v}_2$, corresponds to the magnetic field being in the $(0,0,1)$ direction. Thus if H is applied in the $(0,0,1)$ direction, $\hat{x}_3(\chi = \frac{\pi}{2})$, we expect no magnetic field twisting as the applied magnetic field matches the direction of the linear magnetic field. However, for $\chi = 0, \chi = \frac{\pi}{4}$, the external magnetic field does not align with the $(0,0,1)$ direction and so we expect, and do see in Figure 3.2b, magnetic field twisting. However, for the $s+is$ case the results are identical to those given in Figure 3.1a except for the B_2 plot which differs by a factor of -1 which can be accounted for by the different choice of $\hat{x}_2$ and $\hat{x}_3(\chi)$.
The most interesting feature is that for, $\chi = 0$, we see that the $s+is$ case exhibits no magnetic field twisting where as the $s+id$ case does. This would provide an experimentally verifiable signature to distinguish between these two types of superconductors. This is similar to the suggestions in [1]. However, the Meissner state is a more fundamental state of a superconductor and potentially much easier to create in a laboratory than a domain wall. We note that, as with Figures 3.1a and 3.1b, the value of θ_t for Figures 3.2a and 3.2b appears discontinuous at $x_1 > 10$ and $x_1 > 20$ respectively. However, this is merely due to the value of θ_t not being calculated as the magnetic field has vanished past these points.

$\boldsymbol{x_1 = \frac{1}{2}(1, 1, \sqrt{2})}$

As we showed, in Section 2.3, the presence of the BTRS term in the potential means that $\theta_0 = \pm\frac{\pi}{4}$ which means that, $\mathbb{I}_{ij}^{\alpha\beta} \neq 0$, and thus there is coupling of different modes. Therefore for some orientations the internal magnetic field will not solely point in the $\hat{x}_3(\chi = 0)$ or $\hat{x}_3(\chi = \frac{\pi}{2})$ direction and in these cases we expect twisting for all values of χ. We analyse one such orientation here.
If we consider $x_1 = \frac{1}{2}(1, 1, \sqrt{2})$ and then set,

$$\hat{x}_3(\chi) = \left(\cos\chi(1/2, 1/2, -1/\sqrt{2}) + \sin\chi(-\frac{1}{\sqrt{2}}, \frac{1}{\sqrt{2}}, 0) \right), \tag{3.18}$$

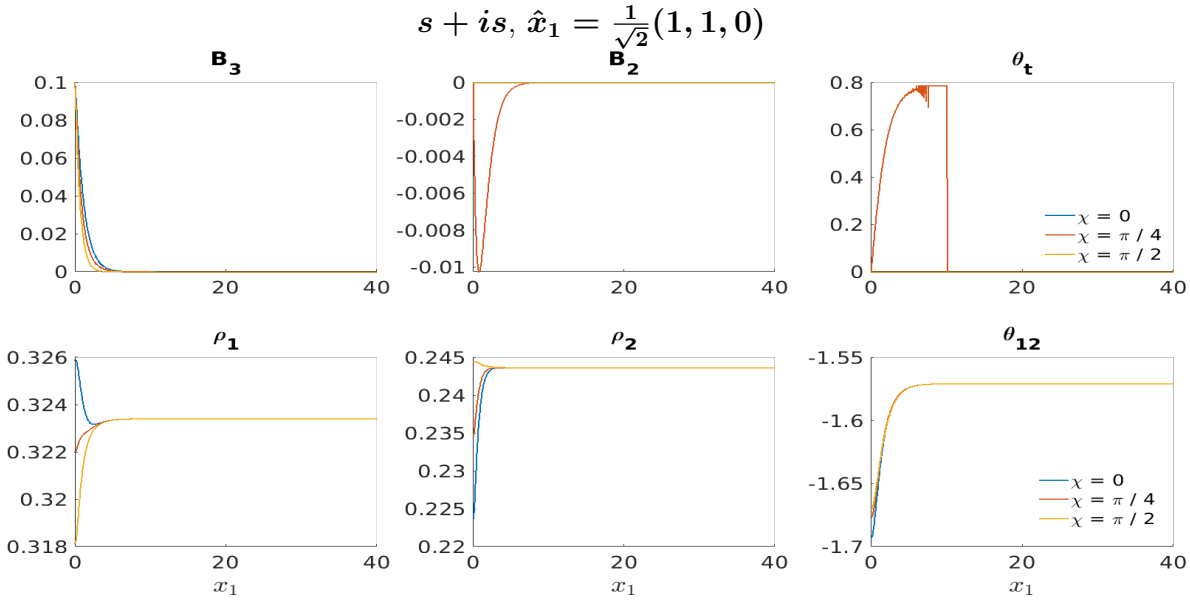

(a) *The Meissner state for an $s+is$ superconductor orientated in the, $\hat{x}_1 = \frac{1}{\sqrt{2}}(1,1,0)$, direction. Due to the $SO(2)(z)$ symmetry of the $s+is$ model these solutions are the same as those for $\hat{x}_1 = (1,0,0)$, Figure 3.1a, up to a sign change for B_2 which is due to $\hat{x}_2 = \hat{x}_3 \times \hat{x}_1$ being different. We see that we still only see magnetic field twisting for $\chi = \frac{\pi}{4}$.*

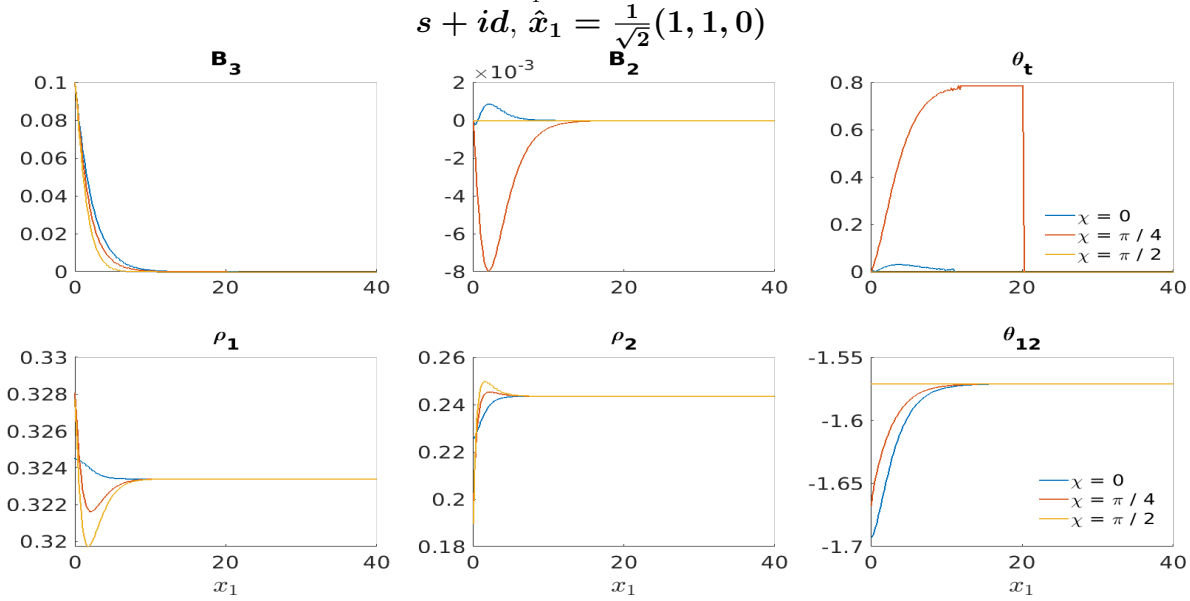

(b) *The Meissner state for an $s+id$ superconductor orientated in the, $\hat{x}_1 = \frac{1}{\sqrt{2}}(1,1,0)$, direction. We see that for $\chi = 0$ and $\chi = \frac{\pi}{4}$ we have magnetic field twisting as predicted by the linearisation.*

Figure 3.2: *Field solutions for the Meissner state for $s+is$ and $s+id$ superconductors with $\hat{x}_1 = \frac{1}{\sqrt{2}}(1,1,0)$ and external magnetic field $H = H_0 \frac{1}{\sqrt{2}}(-\cos\chi, \cos\chi, \sqrt{2}\sin\chi)$. The fields approach their vacuum values, $(\rho_1, \rho_2, \theta_{12}, B_2, B_3) = (u_1, u_2, -\frac{\pi}{2}, 0, 0)$, as x_1 increases, the external field is given by, $H = H_0 \frac{1}{\sqrt{2}}(-\cos\chi, \cos\chi, \sqrt{2}\sin\chi)$, where $H_0 = 0.1$.*

where, $H = H_0\hat{x}_3(\chi)$, we define a unique basis for a given value of χ. For the $s + is$ model, the length scales are given by,

$$\begin{aligned}
\mu_1 = 0.3129 \pm i0.1224, \quad \vec{v}_1 &= \begin{pmatrix} 0.0059 \pm i0.0160 \\ 0.0019 \mp i0.0010 \\ -0.9071 \mp i0.2610 \\ 0.0616 \mp i0.0509 \\ 0.0440 \pm i0.0971 \\ -0.1245 \mp i0.2748 \end{pmatrix}, \\
\mu_2 = (\mu_1)^*, \quad \vec{v}_2 &= (\vec{v}_1)^*, \\
\mu_3 = 0.6694, \quad \vec{v}_3 &= (0, 0, 0, 0, -0.9428, -0.3333)^T, \\
\mu_4 = 0.8523, \quad \vec{v}_4 &= (-0.5696, 0.3828, -0.3078, 0.6460, -0.0435, 0.1229)^T, \\
\mu_5 = 1.2136, \quad \vec{v}_5 &= (0.2941, 0.7487, 0.5889, 0.0168, 0.0255, -0.0722)^T \ .
\end{aligned} \tag{3.19}$$

The mixing angles,

$$(\theta_m^1, \theta_m^2, \theta_m^3, \theta_m^4, \theta_m^5) = (0.3268, 0.3268, \frac{\pi}{2}, 0.1716, 0.0767) \ , \tag{3.20}$$

show us that we have one purely magnetic mode, $\vec{v}_3$, but this mode does not solely point in the $\hat{x}_3(\chi = 0)$ or $\hat{x}_3(\chi = \frac{\pi}{2})$ direction. Additionally, the dominant mode is mixed, has a complex length scale, and also has a B_{lin} that does not solely point in either the $\hat{x}_3(\chi = 0)$ or $\hat{x}_3(\chi = \frac{\pi}{2})$ direction. This means we can expect magnetic field twisting for all values of χ. The $s + id$ tell a similar store, with lengths scales given by,

$$\begin{aligned}
\mu_1 = 0.3106 \pm i0.1247, \quad \vec{v}_1 &= \begin{pmatrix} -0.0009 \pm i0.0020 \\ -0.0012 \mp i0.00540 \\ 0.9444 \pm i0.0512 \\ -0.0502 \pm i0.0582 \\ -0.0637 \mp i0.0830 \\ 0.1782 \pm i0.2384 \end{pmatrix}, \\
\mu_2 = (\mu_1)^*, \quad \vec{v}_2 &= (\vec{v}_1)^*, \\
\mu_3 = 0.7307 \pm i0.0805, \quad \vec{v}_3 &= \begin{pmatrix} 0.2653 \pm i0.3259 \\ -0.2835 \mp i0.2461 \\ 0.0686 \pm i0.0.0598 \\ -0.0393 \mp i0.0561 \\ -0.7800 \pm i0.0489 \\ -0.2386 \pm i0.0423 \end{pmatrix}, \\
\mu_4 = (\mu_3)^*, \quad \vec{v}_4 &= (\vec{v}_3)^*, \\
\mu_5 = 1.1224, \quad \vec{v}_5 &= (-0.4100, -0.8862, -0.1039, 0.0130, -0.1884, -0.0149)^T \ .
\end{aligned} \tag{3.21}$$

In this case all of mixing angles correspond to mixed modes,

$$(\theta_m^1, \theta_m^2, \theta_m^3, \theta_m^4, \theta_m^5) = (0.3220, 0.3220, 0.9617, 0.9617, 0.1901) \ , \tag{3.22}$$

so that B_{lin} will not lie in one direction only. This also means, we cannot predict what direction the linear magnetic field will point in as that will depend upon which modes are excited. However, we do know that any excited mode will not point in the $\hat{x}_3(\chi = 0)$ or $\hat{x}_3(\chi = \frac{\pi}{2})$ directions, so we can expect magnetic field twisting for all of our chosen values of χ.

If we consider Figures 3.3a and 3.3b we see that we have non zero magnetic twisting angles, θ_t, for all three values of χ. We have wildly different internal magnetic fields, that still decay to zero and thus the superconductor will exhibit the Meissner effect, that occur simply by changing the direction of the applied magnetic field whilst still keeping it perpendicular to the boundary normal, $\hat{x}_1$. This orientation shows how different the anisotropic case can be from the isotropic case.

3.3 Summary

We have shown that both the direction of the external magnetic field and the type of superconductivity, through the values of the anisotropy matrices, affect the degree or existence of magnetic field twisting. This twisting can be explained by the competition between the direction of the external magnetic field, and the direction the linearised theory predicts for the magnetic field deep inside the superconductor. This demonstrates another testable prediction of the linearisation which we have confirmed along with the prediction of oscillating tails in $p+ip$ superconductors, see Section 2.4.3. The fact that the magnetic response of the $s+is$ and $s+id$ superconductors differs when the direction of an applied magnetic field changes would provide an experimental method of distinguishing between these types of superconductors.

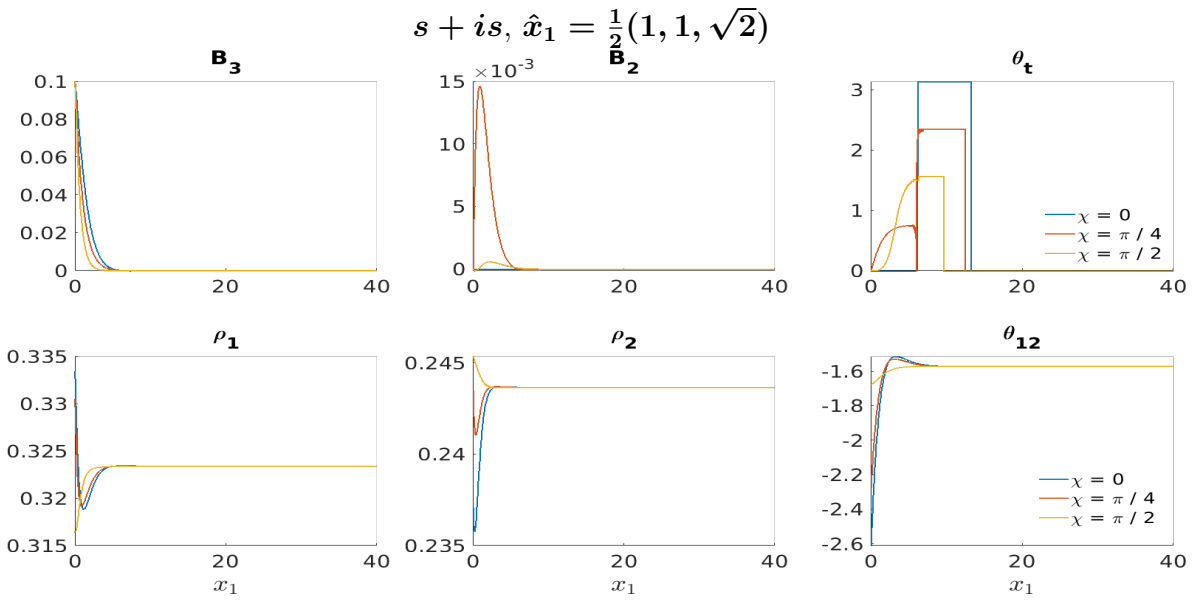

(a) *The Meissner state for an $s + is$ superconductor orientated in the, $\hat{x}_1 = \frac{1}{2}(1, 1, \sqrt{2})$, direction. We see that, for this non basal plane, every orientation of the external magnetic field yields twisting in the magnetic field.*

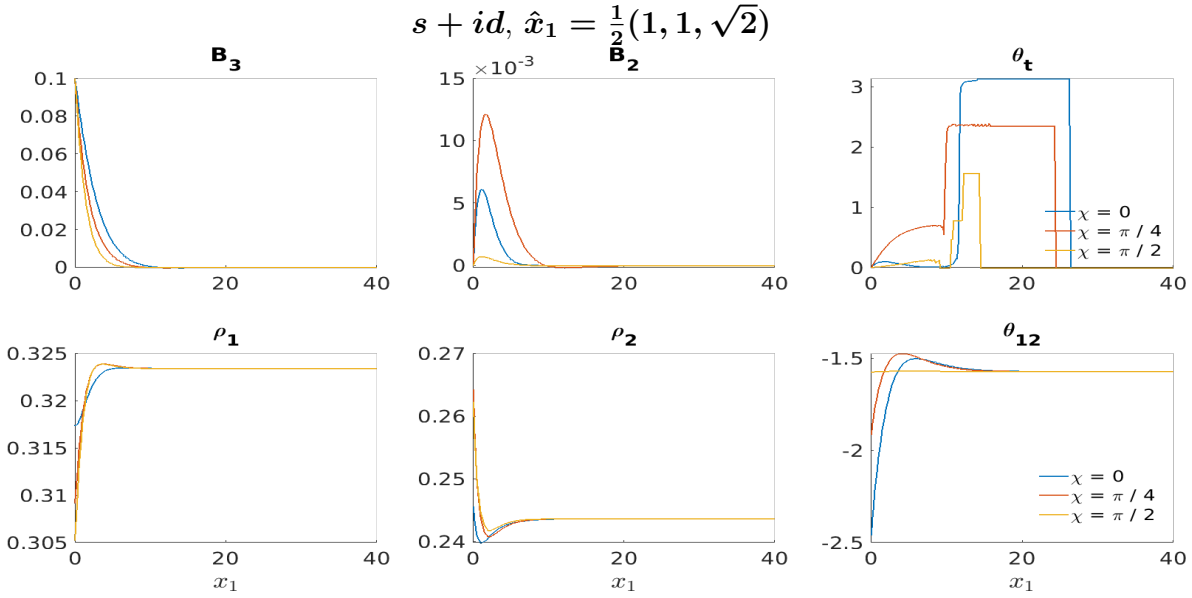

(b) *The Meissner state for an $s + id$ superconductor orientated in the, $\hat{x}_1 = \frac{1}{2}(1, 1, \sqrt{2})$, direction. Like the $s + is$ case we see magnetic field twisting for all directions of the external magnetic field.*

Figure 3.3: *Field solutions for the Meissner state for $s + is$ and $s + id$ with $\hat{x}_1 = \frac{1}{2}(1, 1, \sqrt{2})$ and external magnetic field $H = H_0 \left(\cos\chi(1/2, 1/2, -1/\sqrt{2}) + \sin\chi(-\frac{1}{\sqrt{2}}, \frac{1}{\sqrt{2}}, 0)\right)$. The fields approach their vacuum values, $(\rho_1, \rho_2, \theta_{12}, B_2, B_3) = (u_1, u_2, -\frac{\pi}{2}, 0, 0)$, as x_1 increases, the external field is given by, $H = H_0 \left(\cos\chi(1/2, 1/2, -1/\sqrt{2}) + \sin\chi(-\frac{1}{\sqrt{2}}, \frac{1}{\sqrt{2}}, 0)\right)$, where $H_0 =$ 0.1.*

Chapter 4

Vortices in $s + id$ and $s + is$ Superconductors

In this chapter we explore vortex solutions in multicomponent Ginzburg-Landau theory, [42], which can have sufficient degrees of freedom to allow skyrmion solutions, [43]. Considering these two-dimensional topological solitons in anisotropic $s + id$ superconductors we find two subclasses namely: $\mathbb{C}P^1$ skyrmions and multicomponent vortices. We extend the work of [44] to three-dimensions considering how changing the orientation of our two-dimensional solutions affects the type of vortex solutions we see. Our solutions lie on a plane in a three-dimensional sample and so we can change the orientation of this plane in these anisotropic models. Our solutions are found numerically with fixed boundary conditions that simulate an infinite superconductor allowing us to consider only bulk solutions and thus ignore boundary effects. The effects of changing the orientation on the type of solution as well as the energy and maximum magnetic field are explored. Additionally, we explore how the magnetic field can twist away from the perpendicular direction, $\hat{x}_3$, due to the vortex excitations. When the orientation is not aligned with one of the crystalline axes we see magnetic field twisting. Finally, we show when we consider the $s + is$ model we do not find $\mathbb{C}P^1$ skyrmion solutions, regardless of parameter choice, but do still see twisting in the magnetic field.

4.1 Vortices in Multicomponent Ginzburg-Landau Theory

We have seen in Section 1.6 that by the choice of boundary conditions we can generate two-dimensional topological soliton solutions (vortices), in the isotropic single component Ginzburg-Landau model. We now consider what happens in a two component Ginzburg-Landau model,

$$F = \int_0^\infty \int_0^{2\pi} \left(\frac{1}{2} \sum_{\alpha=1}^{2} \left(|\partial_r \psi_\alpha|^2 + \frac{1}{2r^2} |D_\theta \psi_\alpha|^2 \right) + \frac{(\partial_r a_\theta)^2}{2r^2} + \sum_{\alpha=1}^{2} \left(\frac{\lambda_\alpha}{8} (u_\alpha^2 - |\psi_\alpha|^2)^2 \right) \right) r dr d\theta \tag{4.1}$$

$$F = \int_0^\infty \int_0^{2\pi} f \; r dr d\theta \; , \tag{4.2}$$

written in terms of polar coordinates, $r = \sqrt{x_1^2 + x_2^2}$, $\tan\theta = \frac{x_2}{x_1}$, with $a_r = 0$ through our choice of gauge. The change to polar coordinates does not affect the solutions but allows us to analyse the boundary more easily. For a finite free energy we require the free energy density,

f, to vanish on the boundary, $r \to \infty$. Considering the potential term, we see that for it to vanish we set,

$$\psi_\alpha^\infty = u_\alpha e^{i\chi_\alpha^\infty} \ , \tag{4.3}$$

where ψ_α^∞, denotes the value of the field on the boundary. However, the requirement that $D_\theta \psi_\alpha^\infty = 0$, implies each,

$$\chi_\alpha^\infty = a_\theta \ . \tag{4.4}$$

Therefore a finite energy solution must have, $\chi_1^\infty(\theta) = \chi_2^\infty(\theta) + const$, [45]. This implies that the maps,

$$\psi_1^\infty : S_1^\infty \to S^1 \tag{4.5}$$

$$\psi_2^\infty : S_1^\infty \to S^1 \ , \tag{4.6}$$

have the same integer winding number, which we call N, for a finite energy solution.
Moving our attention to the magnetic field we see that, the magnetic flux is still quantised in units of 2π, as in the single component case.

$$\Phi = \frac{1}{2\pi}\int_{\mathbb{R}^2} B \ dx_1 dx_2 \tag{4.7}$$

$$= \frac{1}{2\pi}\int_0^{2\pi} a_\theta \ d\theta \tag{4.8}$$

$$= \frac{1}{2\pi}\int_0^{2\pi} \chi_\alpha^\infty \ d\theta = N \ , \tag{4.9}$$

where we note that $\Phi = \frac{1}{2\pi}\int_0^{2\pi} \chi_1^\infty \ d\theta \equiv \frac{1}{2\pi}\int_0^{2\pi} \chi_2^\infty \ d\theta$. Furthermore, we remind the reader that a_θ is only equal to χ_α^∞ if $D_\theta \psi_\alpha^\infty$ vanishes which is only required to happen on the boundary. Thus the magnetic flux for the system must be the integer, N, set by the winding of the fields on the boundary.

4.2 Vortices in $s + id$ Superconductors

Vortex solutions in anisotropic $s+id$ superconductors are explored. We use a parametrisation of the $s + id$ model in which, by varying a single parameter, α_s, we can see interesting multi-component vortex solutions that differ from those found in the isotropic multicomponent case such as $\mathbb{C}P^1$ skyrmions, described in Section 4.2.4. We explore how the energetic competition between these solutions changes with the orientation as well as analysing how the magnetic field can twist for certain orientations. In the case of vortices magnetic field twisting is defined as when the magnetic field is no longer parallel to the perpendicular direction, $\hat{x}_3$, which defines the vortex plane.
We consider an alternative parametrisation of the $s+id$ model to that in Section 2.5 which is based on the model in [44] (microscopically derived in [46]) which can be equivalently written as,

$$F_{2D} = \int_{\mathbb{R}^2} (\sum_{i=1}^{2} \left[2(|D_i\psi_1|^2) + (|D_i\psi_2|^2)\right] + \left[(D_1\psi_1)^* D_1\psi_2 - (D_2\psi_1)^* D_2\psi_1 + c.c.\right] + \kappa^2|B|^2 + F_p) \ dx_1 dx_2 \tag{4.10}$$

$$F_p = -2\alpha_s|\psi_1|^2 - |\psi_2|^2 + \frac{4}{3}|\psi_1|^4 + \frac{1}{2}|\psi_2|^4 + \frac{8}{3}|\psi_1|^2|\psi_2|^2 + \frac{4}{3}|\psi_1|^2|\psi_2|^2 \cos(2\theta_{12}) \ . \tag{4.11}$$

We note that the model is formulated for two dimensions only and depends only on the two parameters $\kappa \in [2, 4]$ and $\frac{2}{3} < \alpha_s < 1$. Through our own numerical investigation, which

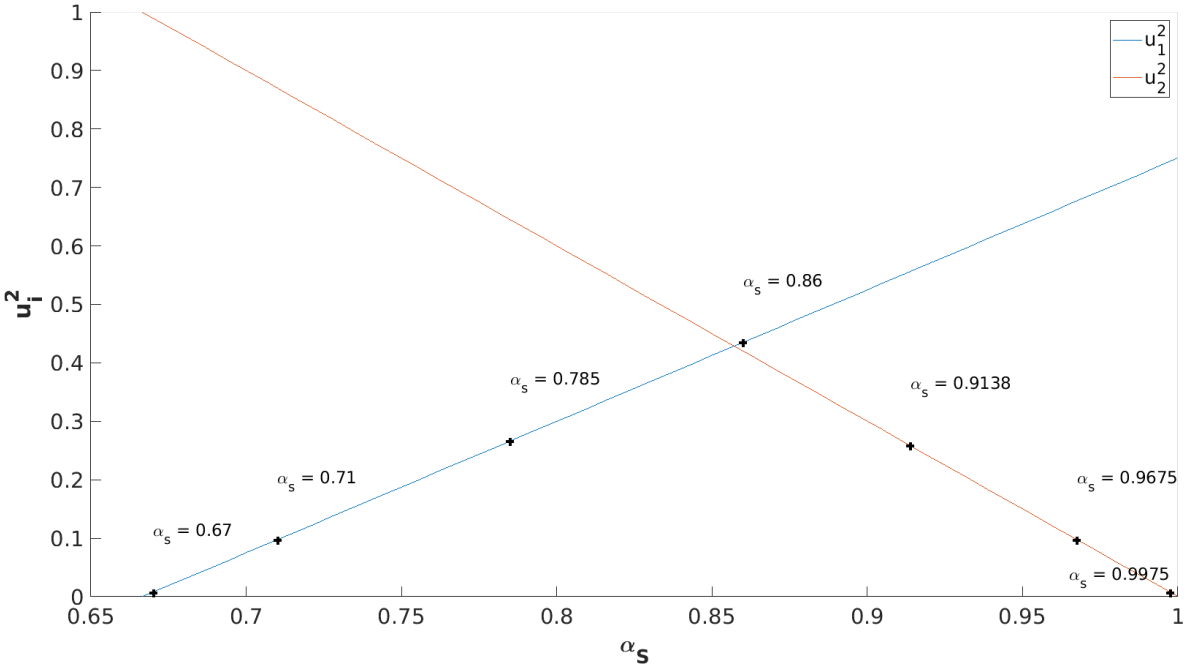

Figure 4.1: *A plot of α_s versus u_i^2 with the data points we have used in later simulations marked, for $\alpha_s \in [\frac{2}{3}, 1]$, the region where both u_1 and u_2 are non zero.*

corroborates [44], we find that, qualitatively, the solutions do not change with the value of κ, in the basal plane, so we choose to set $\kappa = 4$. This now gives us a one-parameter family of solutions to investigate.
If we consider the potential, F_p, we see it depends only on the parameter α_s, and the vacua depend on α_s and are given by,

$$\begin{aligned} u_1^2 &= \frac{9\alpha_s - 6}{4} \\ u_2^2 &= 3(1 - \alpha_S) \\ \theta_{12} &= \pm\frac{\pi}{2} \ , \end{aligned} \tag{4.12}$$

where we find two gauge inequivalent vacua due to the BTRS term $\frac{4}{3}|\psi_1|^2|\psi_2|^2\cos(2\theta_{12})$. We note that the vacuum for, $\alpha_s < \frac{2}{3}$, has $u_1^2 = 0$ and for, $\alpha_s > 1$, it has $u_2^2 = 0$. These two transitions are from the $s+id$ state to the single component isotropic Ginzburg-Landau model discussed in Section 1.3.
If we consider Figure 4.1, which shows the region, $\alpha_s \in [\frac{2}{3}, 1]$, where both condensates are non zero we see for $\alpha_s \in \left[\frac{2}{3}\ ,\ \frac{6}{7}\right)$ $u_1^2 > u_2^2$, whereas at $\alpha_s = \frac{6}{7}$ they equal each other. Then for the region $\alpha_s \in \left(\frac{2}{3}\ ,\ \frac{6}{7}\right]$ the inequality reverses. We find that it is the relative amplitudes of u_1 and u_2 that determines the type of vortex solution that has the lowest energy. We now extend Equation 4.10 to three-dimensions so that we can consider the orientation dependence of the model as well as whether magnetic field twisting occurs. If we consider our three-dimensional version of Equation 4.10,

$$\tilde{F} = \int_{\mathbb{R}^3} \left(P_{ij}^{\alpha\beta} (\tilde{D}_i \psi_\alpha)^* \tilde{D}_j \psi_\beta + \kappa^2 \tilde{B}^2 + (F_p - F_p(u_1, u_2, \pm\frac{\pi}{2})) \right) d\tilde{x_1} d\tilde{x_2} d\tilde{x_3} \ , \tag{4.13}$$

with $i, j \in \{1, 2, 3\}$ and $\alpha, \beta \in \{1, 2\}$. We have normalised the potential relative to the homogenous superconducting state so that the energy is finite. The 3×3 anisotropy matrices

are given as,

$$\hat{P}^{11} = diag([2, 2, 2\mu]) \tag{4.14}$$
$$\hat{P}^{22} = diag([1, 1, \mu]) \tag{4.15}$$
$$\hat{P}^{12} = diag([1, -1, \mu]) \ . \tag{4.16}$$

We already know the form of the anisotropic matrices, in three-dimensions, for the $s + id$ model (see Section 1.8.1). This form gives the model the required $C_2(z) \times C_2(y) \times C_2(x)$ spatial symmetry that defines the $s + id$ model. We have chosen the parameter, μ, such that the matrix $P^{11}P^{22} - (P^{12})^2$ is non-negative. This condition ensures that the energy is positive definite, [25].
We note that Equation 4.13 can be spatially rescaled,

$$\begin{aligned} \tilde{x}_1 &\mapsto \lambda_x x_1 \\ \tilde{A}_i &\mapsto \frac{A_i}{\lambda_x} \\ P^{\alpha\beta} &\mapsto \frac{1}{2}\lambda_x^2 Q^{\alpha\beta} \\ \tilde{F} &\mapsto \frac{F}{\lambda_x^3} \\ \lambda_x &:= (2\kappa^2)^{\frac{1}{4}} \ , \end{aligned} \tag{4.17}$$

giving,

$$F = \int_{\mathbb{R}^3} \left(\frac{1}{2} Q_{ij}^{\alpha\beta} (D_i \psi_\alpha)^* (D_j \psi_\beta) + \frac{B^2}{2} + F_p(\rho_1, \rho_2, \theta_{12}) \right) \ dx_1 dx_2 dx_3 \ , \tag{4.18}$$

the standard form for the free energy that we use throughout this thesis.
As we study vortex solutions, which are translationally invariant in the $\hat{x}_3$ direction, we apply the following ansatz,

$$\psi_\alpha \mapsto \psi_\alpha(x_1, x_2) \tag{4.19}$$
$$A \mapsto A_1(x_1, x_2)dx_1 + A_2(x_1, x_2)dx_2 + A_3(x_1, x_2)dx_3 \ , \tag{4.20}$$

which will allow two-dimensional solution of Equation 1.123 that are translationally invariant in the x_3 direction. Additionally, we retain $A_3 \neq 0$ to allow the magnetic field,

$$B = (B_1, B_2, B_3) = (\partial_2 A_3, -\partial_1 A_3, \partial_1 A_2 - \partial_2 A_1) \ , \tag{4.21}$$

to point in any direction which will allow us to explore magnetic field twisting. This closely mirrors the ansatz choice for domain walls, Section 2.2.1, except we now deal with two-dimensional solutions and the magnetic field can also point in the B_1 direction. Additionally, we define the orientation of the vortex solution by $\hat{x}_3$ not $\hat{x}_1$ as in the domain wall case. This gives us the free energy per unit length,

$$F = \int_{\mathbb{R}^2} \left(\frac{1}{2} Q_{ij}^{\alpha\beta} (D_i \psi_\alpha)^* (D_j \psi_\beta) + \frac{B^2}{2} + F_p(\rho_1, \rho_2, \theta_{12}) \right) \ dx_1 dx_2 \ , \tag{4.22}$$

now written in the above form with the anisotropy matrices given by $Q^{\alpha\beta} = \frac{2}{\lambda_x^2} P^{\alpha\beta}$.

4.2.1 Numerical Method

Here we outline the general numerical method used to generate vortex solutions in the $s+id$ model. We will assume $\kappa = 4$ and $\mu = 0.7$ throughout and refer to the free energy per unit length as simply the energy for the rest of this chapter. The value of $\mu = 0.7$ was chosen to be both non zero and less than one and numerical simulations showed that, like κ, changing μ did **not** change the qualitative behaviour of the solutions.
Similarly, to Section 2.2.3, we discretise our two-dimensional domain as a square grid, $N_x \times N_x$, of evenly spaced points, with spacing $h_x > 0$. Typically we use $N_x = 401$ and $h_x = 0.1$ which we found as the best compromise between numerical accuracy and speed. We label each point with indices, (I, J), such that the field values at that point are labelled,

$$\psi_\alpha^{(I,J)} = \psi_\alpha(x_1^{(I)}, x_2^{(J)}) \tag{4.23}$$

$$A_i^{(I,J)} = A_i(x_1^{(I)}, x_2^{(J)}) \ . \tag{4.24}$$

The now two-dimensional Ginzburg-Landau equations, Equations 1.124 and 1.125, are solved using arrested Newton flow, where again the derivatives are approximated by fourth order central differences.
As we have discretised on a square grid we use boundary conditions in terms of Cartesian (not polar) coordinates where the continuous boundary conditions for vortex solutions in an $s+id$ superconductor (with winding number, N) are,

$$\psi_1 = u_1 \frac{(x_1 + ix_2)^N}{|x_1 + ix_2|^N} \tag{4.25}$$

$$\psi_2 = s \cdot iu_2 \frac{(x_1 + ix_2)^N}{|x_1 + ix_2|^N} \tag{4.26}$$

$$A_1 = N \frac{x_1}{x_1^2 + x_2^2} \tag{4.27}$$

$$A_2 = N \frac{-x_2}{x_1^2 + x_2^2} \tag{4.28}$$

$$A_3 = 0 \ . \tag{4.29}$$

The phase difference, $\theta_{12} = \theta_1 - \theta_2$, on the boundary is $-s\frac{\pi}{2}$ where we choose $s = 1$ so that we have an $s+id$ superconductor. Note that $s = -1$ gives an $s-id$ superconductor which gives the same solutions up to a spatial rotation and conjugation of the solutions in the $\hat{x}_1 \times \hat{x}_2$ plane. Then using arrested Newton flow we generate locally minimising solutions to Equation 4.22. We run all simulations in this chapter for a grid of 401×401 points with a spacing of $h_x = 0.1$ and a numerical tolerance of 0.0075. It should be noted that some of our simulations are limited by available computing power thus we use a larger value of numerical tolerance, see Equation 2.41, and a smaller number of different orientations than are sampled in Chapter 2.
Similarly to Section 2.2.2 we can change the orientation of our solution by transforming the $Q^{\alpha\beta}$ matrices. We note that, as our excitations now occur in both the x_1 and x_2 directions, we now define our orientation by the value of $\hat{x}_3$ rather than $\hat{x}_1$ as we do for one-dimensional solutions. Apart from this the transformation of the anisotropy matrices is still,

$$\tilde{Q}^{\alpha\beta} = M^T Q^{\alpha\beta} M \ , \tag{4.30}$$

where now,

$$M = \begin{pmatrix} \vdots & \vdots & \vdots \\ \hat{x}_1 & \hat{x}_3 \times \hat{x}_1 & \hat{x}_3 \\ \vdots & \vdots & \vdots \end{pmatrix} . \tag{4.31}$$

We can generate a $M \in SO(3)$ matrix for a given value of $\hat{x}_3$ using the Gram-Schmidt method described in Section 2.2.3.1 except we generate M using $\hat{x}_3$ not $\hat{x}_1$.

4.2.2 Vortices

Consider, Figure 4.2a which gives an $N = 2$ two component vortex solution. We see that each condensate vanishes at precisely two points which we call a zero. Each zero has a local winding number of $n_v = 1$. If we draw a closed contour, δC, that contains only an single zero then that region would be considered local and we can calculate its winding number as follows,

$$n_v = \frac{1}{2\pi} \int_{\delta C} \partial_\theta \arg\left(\psi_\alpha(r,\theta)\right) \, d\theta \ . \tag{4.32}$$

If we label the total winding number of the zeros and anti zeros of ψ_1 and ψ_2 as $n_{1v}, n_{1av}, n_{2v}, n_{2av}$ respectively. Then we can choose to name our solutions as a $(n_{1v} + n_{1av}, n_{2v} + n_{2av})$ vortex. We see that Figure 4.2a would be called a $(2+0, 2+0)$ vortex which we shorten to a $(2,2)$ vortex. This naming system may seem excessive for this solution but for some values of α_s we find, for example, both n_{1v} and n_{1av} are non zero. That is solutions occur that contain both zeros and anti zeros in a condensate. The zeros in Figure 4.2a separate into individual $n_v = 1$ zeros. This differs from the single component case, for certain parameter choices, where a single $N = 2$ vortex forms at the centre of the domain. We note that the zeros in the ψ_1 condensate occur at the same spatial points as the zeros in the ψ_2 condensate, thus we call these **coincident** zeros.
To reiterate,

- A zero of ψ_α is a point in the domain where $\psi_\alpha = 0$ and the winding number around that point is **positive**.
- An anti zero of ψ_α is a point in the domain where $\psi_\alpha = 0$ and the winding number around that point is **negative**.

4.2.3 Discretised Zeros of ψ_α

In the continuous case, a zero of a condensate is trivially the point where it vanishes. However, for numerical results we deal with discretised solutions and more thought must be put in to identify such zeros. This is because, in general, we do not find points where the condensates exactly vanish as zeros occur in between lattice sites. Thus the n_v points, marked as □ on Figure 4.2a, are only approximations to the locations of the zeros.
First, we define zeros and coincident zeros on a lattice.

Definition 4.2.1 *Discretised Zero. A condensate $\psi_\alpha^{(I,J)}$, discretised on a square lattice indexed by (I,J), is said to have a zero at the point $(x_1^{(I)}, x_2^{(J)})$ if there is a change of sign in both the real and imaginary part of the condensate that occurs either in the range $[\psi_\alpha^{(I,J)}, \psi_\alpha^{(I+1,J)}]$ or $[\psi_\alpha^{(I,J)}, \psi_\alpha^{(I,J+1)}]$.*

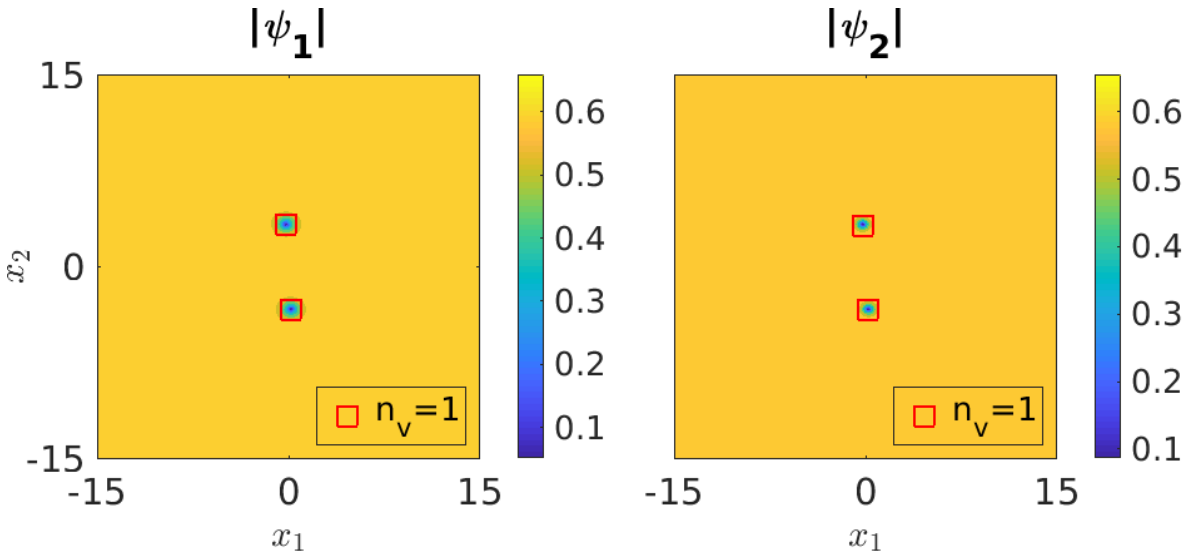

(a) *A* $(2,2)$ *vortex solution showing only the condensates, both* ψ_1 *and* ψ_2 *contain two* $n_v = 1$ *zeros and thus have the same overall winding number* $N = 2$ *and* □ *denotes the winding number of the zero it is identifying.*
We use the same parameter values as Figure 4.8b.

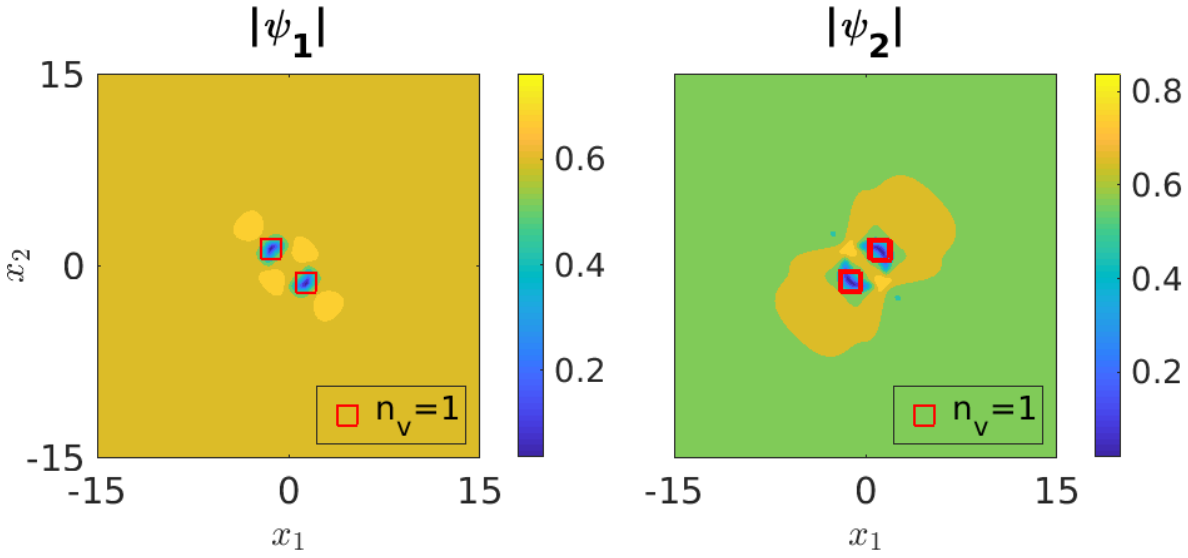

(b) *A* $(2,2)$ $\mathbb{C}P^1$ *skyrmion solution showing only the condensates, which has no coincident zeros,* $\Psi = (\psi_1, \psi_2) \neq \{0\}$. *Note that* □ *denotes the winding number of the zero it is identifying. We use the same parameter values as Figure 4.8a.*

Figure 4.2: *A comparison of the condensates only for a* $(2,2)$ *vortex and a* $(2,2)$ $\mathbb{C}P^1$ *skyrmion solution, where* $\sum n_v = N$ *for each condensate.*

This definition is fairly forgiving as it allows changes of sign of the condensate to occur on different sites but on the same square of the lattice. This square has vertices indexed by, $(I, J), (I+1, J), (I+1, J+1), (I, J+1)$.

Definition 4.2.2 *Discretised Coincident Zero. When there is a discretised zero at both* $\psi_1^{(I,J)}$ *and* $\psi_2^{(I,J)}$ *there is said to be a discretised coincident zero at the point on the lattice* $(x_1^{(I)}, x_2^{(J)})$.

Algorithm 1 details how to calculate the winding number around a point in the lattice. Algorithm 2 details how to find all the discretised zeros of a lattice solution and uses Algorithm 1 to find the winding number for each point as well as listing all of the zeros that are coincident. These algorithms are used to generate the points marked by □ in Figure 4.2a.

4.2.4 $\mathbb{C}P^1$ Skyrmions

We now move onto a special class of vortices, namely $\mathbb{C}P^1$ skyrmions, [47]. They are solutions to the Ginzburg-Landau equations that contains precisely zero coincident zeros. We note that in the isotropic Ginzburg-Landau case a $\mathbb{C}P^1$ skyrmion is not energetically favourable over a vortex solution where the zeros coincide. However, with the introduction of the anisotropic $s + id$ model, they can be energetically favourable.
If we define

$$\Psi = (\psi_1, \psi_2) = (|\psi_1| e^{i\theta_1}, |\psi_2| e^{i\theta_2}) \ , \tag{4.33}$$

then a $\mathbb{C}P^1$ skyrmion has $\Psi \neq \{0\}$. This is equivalent to stating that,

$$\Psi : \mathbb{R}^2 \mapsto \mathbb{C}^2 \setminus \{0\} \ . \tag{4.34}$$

One can define a projection map,

$$\pi : \mathbb{C}^2 \setminus \{0\} \mapsto \mathbb{C}P^1 \ . \tag{4.35}$$

We now define another map,

$$n = \ \pi \circ \Psi \tag{4.36}$$

$$n : \mathbb{R}^2 \mapsto \mathbb{C}P^1 \ . \tag{4.37}$$

We remind the reader of the vortex boundary conditions, which are necessary for a finite free energy, which mean that as $r \to \infty$, $\Psi \to \Psi_0$ where Ψ_0 is a constant (**up to gauge**) determined by the boundary conditions. This means that $\pi \circ \Psi$ tends to a constant as $r \to \infty$. In other words n tends to a constant, which we call n_0, in $\mathbb{C}P^1$ as $r \to \infty$. Thus our function n maps the plane to $\mathbb{C}P^1$ in such a way that all points on the circle at infinity get mapped to a single point in $\mathbb{C}P^1$. By adding a point to $\mathbb{R}^2$, which represents the circle at infinity, and mapping this to n_0 we construct a map,

$$n : S^2 \mapsto \mathbb{C}P^1 \ . \tag{4.38}$$

This is known as one-point compactification. Additionally, as $\mathbb{C}P^1$ is the Riemann sphere, S^2, we now have a map between spheres which is called a skyrmion. We can see that this map only exists when $\Psi \neq 0$ everywhere in the domain. Thus if any zeros in ψ_1 and ψ_2 coincide then we do not have a $\mathbb{C}P^1$ skyrmion.
Figure 4.2b shows a numerical simulation of an, $N = 2$ $\mathbb{C}P^1$, skyrmion solution, which we call a $(2, 2)$ $\mathbb{C}P^1$ skyrmion using our newly defined notation. We see that it is possible to translate the zeros in ψ_1 such that they become coincident with the zeros in ψ_2, converting a $(2, 2)$ $\mathbb{C}P^1$ skyrmion to a $(2, 2)$ vortex.

4.2.5 Classifying Solutions for $N = 2$

Here we study $N = 2$ locally minimising solutions of Equation 4.22, produced numerically using the method detailed in Section 4.2.1. We also consider orientations away from the basal plane to gain a full picture of the possible types of fields solutions for a given value of α_s.
We start with $N = 2$ which is the lowest winding number where we find $\mathbb{C}P^1$ skyrmions, that minimise the free energy. This happens for values of α_s where $u_1 \approx u_2$. However, for such α_s that produces $\mathbb{C}P^1$ skyrmion solution it is generally possible to find an orientation where the more standard $(2, 2)$ vortex solution is energetically favoured. Interestingly, we find a third type of solution namely a vortex solution which contains anti zeros in one condensate that are coincident with the zeros in the other condensate. These occur when either $u_1 >> u_2$ or vice versa. An example being the $(6-4, 2)$ vortex in Figure 4.3a which has six zeros and four anti zeros in the ψ_1 condensate and two zeros and no anti zeros in the ψ_2 condensate.
If we consider Figure 4.1 which shows the relationship between α_s and $|\psi_\alpha|^2$ we can add that for $\alpha_s \leq \frac{2}{3}$ the vacuum is $(u_1, u_2) = (0, 1)$, and for $\alpha_s \geq 1$ we have $(u_1, u_2) = (\frac{3\alpha_s}{4}, 0)$. Thus we no longer have a two component model in those regions and θ_{12} is not defined if either condensate vanishes.
We are interested in multicomponent solutions hence our focus on the region $\alpha_s \in (\frac{2}{3}, 1)$. We also see that for $\alpha_s \in (\frac{2}{3}\ ,\ \frac{6}{7})$ $|\psi_1|^2 < |\psi_2|^2$ however this inequality reverses for the region $\alpha_s \in (\frac{6}{7}, 1)$. From, [44], and studying our own numerical solutions it appears that the ratio of u_1 and u_2 determines which type of solution has the lowest energy. We sample three values of α_s each of which has a different ratio and so favours a different type of solution in the basal plane.
Qualitatively speaking, the possible $N = 2$ solutions to Equation 4.22 for $\alpha_s = (0.67, 0.71, 0.785)$ are similar in type, but not identical, as for $\alpha_s = (0.9138, 0.9675, 0.9975)$, when only considering the basal plane. These values of α_s are all plotted on Figure 4.1. As we want to classify the possible types of solutions for $N = 2$ we focus upon $\alpha_s = (0.67, 0.71)$ as well as the middle value $\alpha_s = 0.86$ which has $|\psi_1|^2 \approx |\psi_2|^2$. We also note that solutions for higher N appear to be made up of combinations of $N = 1$ and $N = 2$ solutions.
We generate an orthonormal basis, $(\hat{x}_1, \hat{x}_2, \hat{x}_3)$, by picking a $\hat{x}_3$ and then using the Gram-Schmidt method to generate all three unit vectors as described in Section 2.2.3.1 but instead we pick $\hat{x}_3$ to generate the basis instead of $\hat{x}_1$. However, this method does not generate the simplest choice of orthonormal basis. For example, for $\hat{x}_3 = (0, 0, 1)$, that basis would be $((1, 0, 0), (0, 1, 0), (0, 0, 1))^T$ and for $\hat{x}_3 = (0, 1, 0)$ it would be $((1, 0, 0), (0, 0, 1), (0, 1, 0))^T$. This can be rectified by rotating solutions about the origin so that the choice of $\hat{x}_1$ and $\hat{x}_2$ generated by the Gram-Schmidt process becomes the desired, simpler choice. This coordinate rotation produces the same solution as if we had re-simulated using the simpler basis as we model an infinite superconductor.
In the following figures we plot the location and winding numbers of the discretised zeros for each condensate, which we label n_v. Noting that as we deal with numerical data finding the exact location is not always possible for the numerical tolerance we used. The reader should consider overlapping □ and ○ as part of the same zero whose location is found imprecisely due to the discretised nature of the solution.

Fields Solutions for $\alpha_s = 0.67$

Here we give numerical solutions to Equation 4.22 for $\alpha_s = 0.67$, where $u_1 << u_2$. This parameter exhibits two types of field solutions which we explore below.
Figure 4.3a shows a $(6 - 4, 2)$ vortex solution for the basal plane orientation, $\hat{x}_3 = (0, 0, 1)$. We see that two of the anti zeros in ψ_1 are coincident with the two zeros in the ψ_2 component.

The remaining zeros and anti zeros in ψ_1 are there to ensure that the overall winding number of ψ_1 is equal to $N = 2$. Additionally, for $|\psi_1|$, we see that we get clusters of overlapping discretised zeros marked by, □. This is due to numerical error, limitations of the zero finding algorithm and the small value of $u_1 \approx 0.087$. The plot of $|\psi_2|$ differs from the isotropic or s wave case, as discussed in Section 1.6, where the zeros do not separate into individual $n_v = 1$ zeros in the type I case and in the type II case the zeros are repulsive [24] so we do not see any sort of bound state.

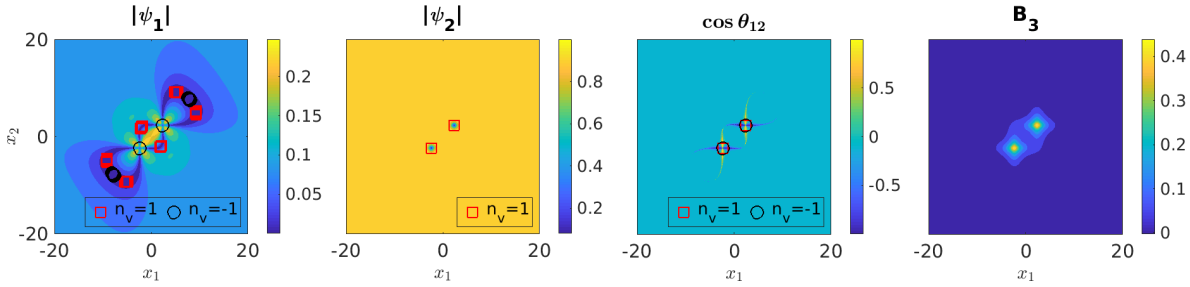

(a) *A* $(6-4,2)$ *vortex, with* $\hat{x}_3 = (0,0,1)$ *and* $\alpha_s = 0.67$.

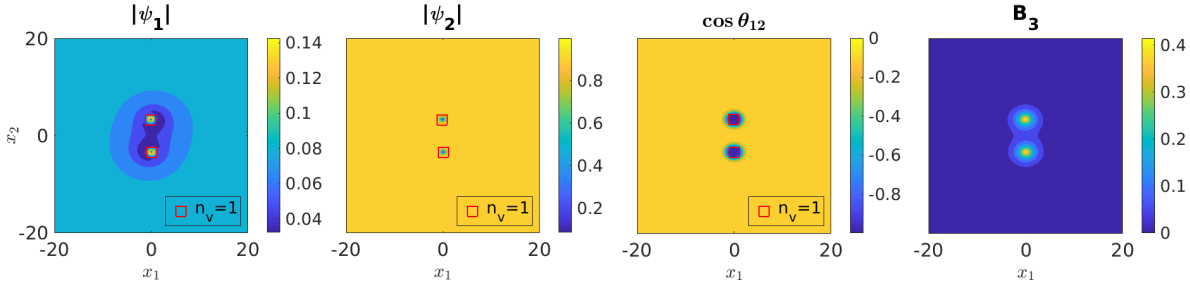

(b) *A* $(2,2)$ *vortex, with* $\hat{x}_3 = (0,1,0)$ *and* $\alpha_s = 0.67$.

Figure 4.3: *Plots of the gauge invariant quantities of the fields,* $N = 2, \alpha_s = 0.67$*, for two different orientations which show the two types of solutions possible for this parameter range. The points,* □ *and* ○*, on* $|\psi_1|, |\psi_2|$ *and* $\cos\theta_{12}$ *show the location and multiplicity of the zeros in the* ψ_1*,* ψ_2 *condensates and the coincident zeros respectively. Note that overlapping points, with the same value of* n_v*, should be considered to represent the same zero and only appear due to numerical error.*
For each condensate $\sum n_v = N$ *and the* B_1 *and* B_2 *components of the magnetic field vanish everywhere.*

The $\cos\theta_{12}$ plots shows us that the coincident zeros and anti zeros are interconnected by domain walls. The rapid change in the value of $\cos\theta_{12}$ corresponds to a domain wall. A domain wall is defined as a minimising solution of the Ginzburg-Landau equations that interpolates from the two boundary values of the phase difference, $\lim_{x\to\pm\infty}\theta_{12} = \mp\frac{\pi}{2}$. However, for our vortex solutions the boundary, $r \to \infty$, fixes the phase difference to $-\frac{\pi}{2}$. If we move in a straight line from one boundary to another a domain wall must occur with a corresponding anti domain wall so that the value of the phase difference on the boundary is correct. Interestingly we see both clockwise and anticlockwise domain walls form. These were first identified in Section 2.5.1 where $\cos\theta_{12}$ becoming positive indicates a clockwise domain wall or equivalently an anticlockwise anti domain wall. A negative value indicates an anticlockwise domain wall or a clockwise anti domain wall. We note that the transformation $\theta_{12} \to -\theta_{12}$ maps a domain wall to an anti domain wall at the cost of reversing the direction that the phase difference

interpolates. However, as $\cos\theta_{12}$ is an even function this change of sign of θ_{12} leaves $\cos\theta_{12}$ unchanged.
If we consider moving along the line $x_2 = 0$ then we find a anticlockwise domain wall (and corresponding anti domain wall). Whereas, if we move along the line $x_1 = 0$ then we find a clockwise domain wall (and corresponding anti domain wall). We demonstrate this in Figures 4.4a and 4.4b which give data for the lines $x_1 = 0$ and $x_2 = 0$ respectively.
In Section 2.5.1 we provided a simple argument as to why these two domain walls occur. We reduced the complexity of the free energy with the assumption that only the phase difference, θ_{12}, is allowed to vary and the other fields are fixed to their vacuum values. The key part of the reduced free energy, Equation 2.156, is the,

$$-\frac{1}{4}\tilde{Q}_{11}^{12}u_1u_2\cos\theta_{12}(x_1)(\theta'_{12}(x_1))^2 \ , \tag{4.39}$$

term. This leads to the prediction that it is the sign of the $\tilde{Q}_{11}^{12}$ component of the anisotropy matrices that determines which domain wall type has the lower energy. If $\tilde{Q}_{11}^{12} > 0$ then the clockwise domain wall has the lower energy and if $\tilde{Q}_{11}^{12} < 0$ then it is the anticlockwise domain wall with the lower energy. In terms of anti domain walls if $\tilde{Q}_{11}^{12} > 0$ then the anticlockwise anti domain wall has the lower energy and if $\tilde{Q}_{11}^{12} < 0$ then it is the clockwise anti domain wall with the lower energy. We remind the reader that $\tilde{Q}^{\alpha\beta} = M^TQ^{\alpha\beta}M$, therefore $\tilde{Q}_{11}^{12} = 1$ for the line $x_2 = 0$ and $\tilde{Q}_{11}^{12} = -1$ for the line $x_1 = 0$. In the first case $M = (\hat{x}, \hat{y}, \hat{z})$ and the second case $M = (-\hat{y}, \hat{x}, \hat{z})$ with $\hat{x} = (1, 0, 0)^T$, $\hat{y} = (0, 1, 0)^T$ and $\hat{z} = (0, 0, 1)^T$. This model predicts, for example, that along the $x_2 = 0$ line a anticlockwise anti domain wall and a clockwise domain wall are energetically favoured and that is what we see in Figure 4.4a.

Considering a different orientation, Figure 4.3b shows the more ordinary $(2, 2)$ vortex which is only a lower energy solution, for $\alpha_s = 0.67$, for $\hat{x}_3 = (0, 1, 0)$. We see that, from $\cos\theta_{12}$, domain walls, connecting zeros, do not occur. Comparing the two orientations we see that both solutions have peaks in the B_3 component of the magnetic field corresponding to the locations of the coincident zeros.
If we consider $\alpha_s = 0.9975$ which according to Figure 4.1 the u_1^2 value for $\alpha_s = 0.67$ is equal to u_2^2 for $\alpha_s = 0.9975$. This change of parameter has the effect of swapping the condensates but we expect the type of solution to remain approximately the same. Figure 4.5 gives a $(2, 6-4)$ vortex solution for $\alpha_s = 0.9975$ and orientation $\hat{x}_1 = (0, 0, 1)$, comparing this to Figure 4.3a we see they are similar with the condensates swapped but the coincident zeros align along the $x_2 = -x_1$ diagonal not the $x_2 = x_1$ diagonal as in the $\alpha_s = 0.67$ case.

We now provide an argument as to why, for $\alpha_s = 0.67$, we see coincident zeros and anti zeros. For $\alpha_s = 0.67$ the vacuum value of $|\psi_1|$, u_1, is much smaller than the vacuum value of $|\psi_2|$, u_2. Thus when considering the free energy, shown in Equation 4.22, the leading term that involves ψ_1 is the term that is linear in ψ_1 which will dominate over the quadratic term. The only such term is,

$$F_{Q12} = \int_{\mathbb{R}^2} \mathrm{Re}\left(Q_{ij}^{12}(D_i\psi_\alpha)^*D_j\psi_\beta\right)\ dx_1dx_2 \ . \tag{4.40}$$

We note that this will also be the leading term that involves ψ_2 in the $\alpha_s = 0.9975$ case where instead we have $u_2 << u_1$. We consider the case where both ψ_1 and ψ_2 vanish at the origin, $x_1 = x_2 = 0$ but have different winding numbers n and m respectively. We can then consider the approximate forms of the condensates close to the origin,

$$\psi_1 \sim C_1re^{i(n\theta+\delta)} \tag{4.41}$$

$$\psi_2 \sim C_2re^{im\theta} \tag{4.42}$$

$$A_i \sim 0 \ , \tag{4.43}$$

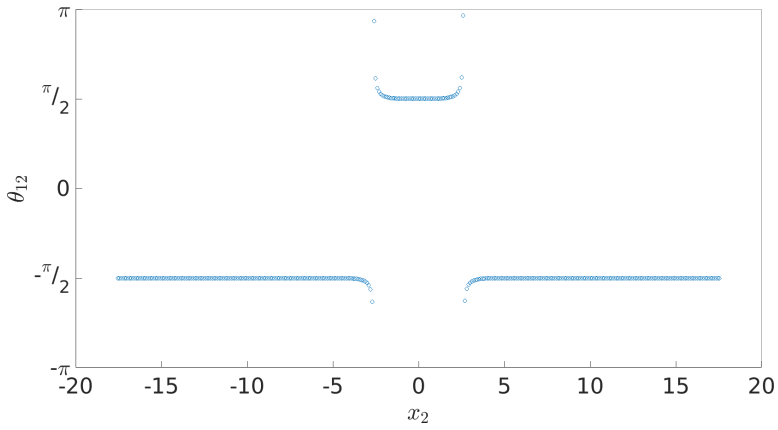

(a) *The phase difference, θ_{12}, along the line $x_1 = 0$ with $\hat{x}_3 = (0, 0, 1)$ and $\alpha_s = 0.67$. Showing a clockwise anti domain wall and an anticlockwise domain wall on the left and right hand sides of $x_2 = 0$ respectively.*

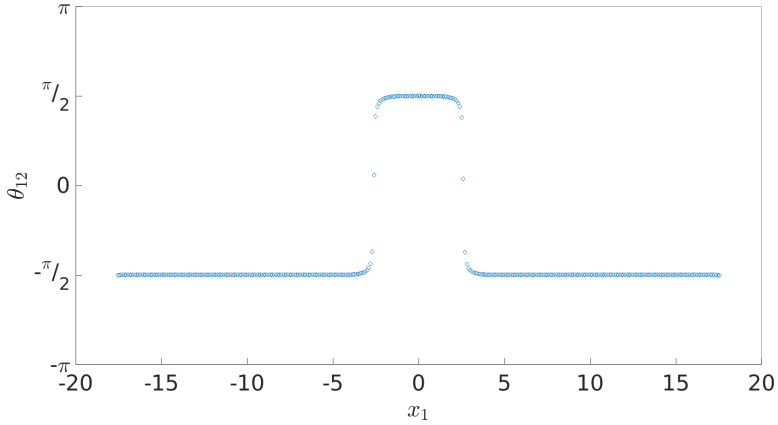

(b) *The phase difference, θ_{12}, along the line $x_2 = 0$ with $\hat{x}_3 = (0, 0, 1)$ and $\alpha_s = 0.67$. Showing an anticlockwise anti domain wall and a clockwise domain wall on the left and right hand sides of $x_1 = 0$ respectively.*

Figure 4.4: *Plots of the phase difference along the lines $x_1 = 0$ and $x_2 = 0$ we see that the phase difference interpolates anticlockwise and clockwise respectively. $\theta_{12} \in [-\pi, \pi]$ and the full dependence of θ_{12} on x_1 and x_2 is shown in Figure 4.3a.*

where $re^{i\theta} = x_1 + ix_2$ and $\delta \in [0, 2\pi]$ is an additional phase factor. The constants C_1 and C_2 either have $C_1 << C_2$ or $C_2 << C_1$ depending on the value of α_s. We note that, for the phase of the condensates, at the boundary we would expect $n = m = N$ and $\delta = -\frac{\pi}{2}$ as specified by the broken time reversal symmetry term, $\frac{4}{3}|\psi_1|^2|\psi_2|^2\cos(2\theta_{12})$, in the potential. However away from the boundary there are no such requirement. Additionally, we are assuming that close to the origin both condensates only differ by their angular not their radial dependence. Finally we assume that, close to the zeros, contributions to the energy from terms involving the vector potential, A_i, are higher order and thus can be ignored.

We can use the above approximate form of the fields to see what values of n, m, δ minimise the energy for the basal plane where $Q^{12} = diag(1, -1, \mu)$, we ignore the constant factor of

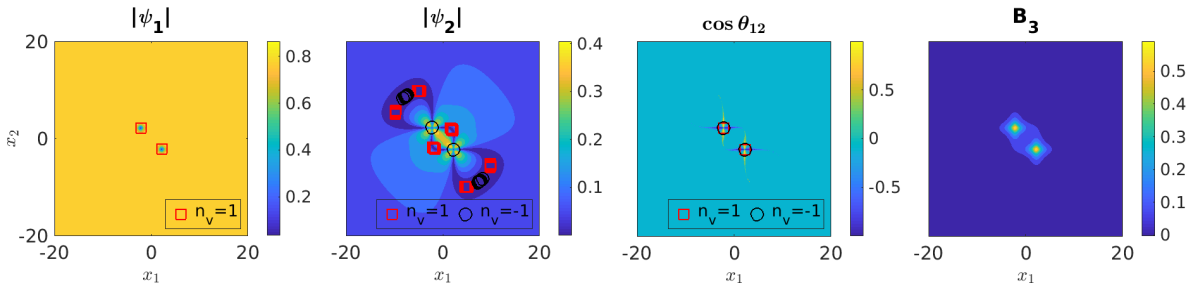

Figure 4.5: *A* $(2, 6-4)$ *vortex, with* $\hat{x}_3 = (0, 0, 1)$ *and* $\alpha_s = 0.9975$*. We note the similarities of this solution with that of Figure 4.3a.*
The points, □ *and* ○*, on* $|\psi_1|, |\psi_2|$ *and* $\cos\theta_{12}$ *show the location and multiplicity of the zeros in the* ψ_1*,* ψ_2 *condensates and the coincident zeros respectively. Note that overlapping points, with the same* n_v*, should be considered to represent the same zero and only appear due to numerical error. We note that* $(u_1, u_2) \approx (0.86, 0.087)$ *and the correspond values for* $\alpha_s = 0.67$ *are* $(u_1, u_2) \approx (0.087, 0.99)$ *so we do not expect these solutions to be identical to those in Figure 4.3a.*
For each condensate $\sum n_v = N$ *and the* B_1 *and* B_2 *components of the magnetic field vanish everywhere.*

$\frac{2}{(2\kappa^2)^{\frac{1}{2}}}$. Substituting them into F_{Q12} gives,

$$F_{Q12} = C_1 C_2 \int_{r<a} \big[\big((\partial_1 r)^2 - (\partial_2 r)^2 + mnr^2((\partial_1\theta)^2 - (\partial_2\theta)^2)\big)\cos((m-n)\theta + \delta) + (n-m)\left(\partial_1 r \partial_1\theta - \partial_2 r \partial_2\theta\right)\sin((m-n)\theta + \delta)\big]\ dx_1 dx_2\ , \tag{4.44}$$

where we only integrate in the region close to the origin where $r < a$ with $0 < a < 1$. We rewrite Equation 4.44 in terms of x_1 and x_2,

$$F_{Q12} = C_1 C_2 \int_{r<a} \frac{1}{x_1^2 + x_2^2}\big[\big(x_1^2 - x_2^2 + mn(x_2^2 - x_1^2)\big)\cos((m-n)\theta + \delta) + 2(n-m)x_1 x_2 \sin((m-n)\theta + \delta)\big]\ dx_1 dx_2\ . \tag{4.45}$$

If we consider $n = m = 1$ then we see that F_{Q12} no longer depends on δ. We then evaluate Equation 4.45 numerically for a given n, m whilst varying δ and we find that F_{Q12} is the lowest when either $n = -1, m = 1$ or $n = 1, m = -1$ both with $\delta = \pi$. Thus the approximate form of the fields that minimise F_{Q12} are,

$$\psi_1 \sim -C_1 r e^{\pm i\theta} \tag{4.46}$$
$$\psi_2 \sim C_2 r e^{\mp i\theta} \tag{4.47}$$
$$A_i \sim 0\ . \tag{4.48}$$

So to summaries when either $u_1 << u_2$ or $u_2 << u_1$ we can assume that F_{Q12} is the dominant term in either ψ_1 or ψ_2. We then show that this term is minimised only when $nm = -1$ and $\delta = \pi$. Thus we provide a rough argument as to why $\alpha = 0.67$ or $\alpha_s = 0.9975$ favour $(6-4, 2)$ or $(2, 6-4)$ vortex solutions.

Fields Solutions for $\alpha_s = 0.71$

Here we give the numerical solutions for $\alpha_s = 0.71$ where $u_1 < u_2$. For this parameter value we no longer find $(6-4, 2)$ vortex solutions (or any other variation) but instead find $\mathbb{C}P^1$

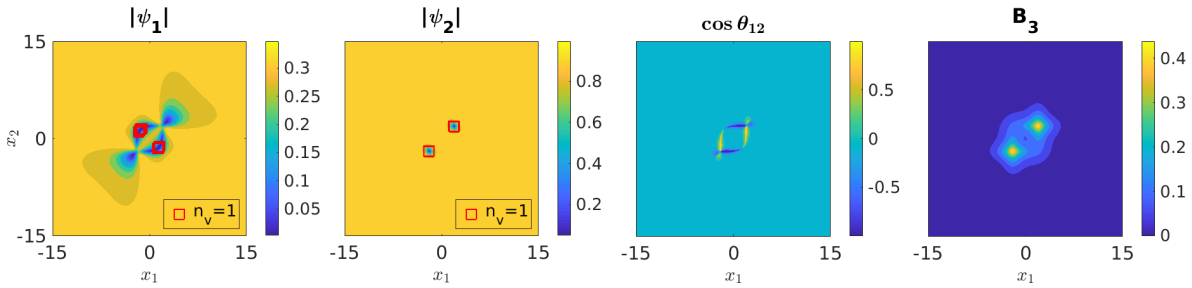

(a) *A* $(2,2)$ $\mathbb{C}P^1$ *skyrmion, with* $\hat{x}_3 = (0,0,1)$ *and* $\alpha_s = 0.71$.

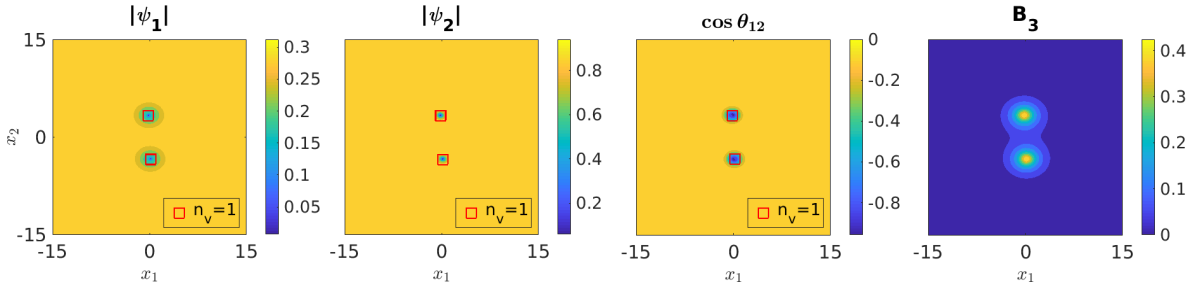

(b) *A* $(2,2)$ *vortex, with* $\hat{x}_3 = (0,1,0)$ *and* $\alpha_s = 0.71$.

Figure 4.6: *Plots of the gauge invariant quantities of the fields,* $N = 2, \alpha_s = 0.71$*, for two different orientations which show the two types of solutions possible for this parameter range. The points,* □*, on* $|\psi_1|, |\psi_2|$ *and* $\cos\theta_{12}$ *show the location and multiplicity of the zeros in the* ψ_1*,* ψ_2 *condensates and the coincident zeros (if they exist) respectively. Note that overlapping points, with the same value of* n_v*, should be considered to represent the same zero and only appear due to numerical error.*
For each condensate $\sum n_v = N$ *and the* B_1 *and* B_2 *components of the magnetic field vanish everywhere. Finally, as the inhomogeneous parts of the solutions are well localised to the centre we only show the central part of the simulated domain.*

skyrmion solutions.
Figure 4.6a shows a $(2,2)$ $\mathbb{C}P^1$ skyrmion for the basal plane orientation, $\hat{x}_3 = (0,0,1)$. Figure 4.6b shows the more ordinary $(2,2)$ vortex which, again, is only a lower energy solution for some non basal plane orientations. Note the observable difference in the B_3 plots between the two figures where the $(2,2)$ $\mathbb{C}P^1$ skyrmion solution has connected B_3 peaks that correspond to the position of the zeros of ψ_2. Furthermore, like Figure 4.3a, we again find domain walls forming as signified by the non zero values of $\cos\theta_{12}$, these only occur for Figure 4.6a.

If we consider $\alpha_s = 0.9675$ where the u_1^2 value for $\alpha_s = 0.71$ is equal to u_2^2 for $\alpha_s = 0.9675$. As shown in Figure 4.1. This change of parameter has the effect of swapping the condensates but additional zeros and anti zeros are added to the solution such that we produce a $(2, 4-2)$ $\mathbb{C}P^1$ skyrmion. Figure 4.7 shows this for the orientation, $\hat{x}_1 = (0,0,1)$. Comparing this to Figure 4.6a we see they are similar solutions with the condensates swapped and the zeros aligned along the $x_2 = -x_1$ diagonal not the $x_2 = x_1$ diagonal as in the $\alpha_s = 0.71$ case. The main difference is the appearance of the additional zeros and anti zeros. Furthermore, we have tested these results for a numerical tolerance, Equation 2.41, ten times smaller than we used for all other solutions and found that we still do not have coincident zeros despite the two anti zeros for $|\psi_2|$ being spatially close to the two zeros in $|\psi_1|$. In fact the positions of the zeros do not change with the numerical tolerance at all. Thus, although a $(2, 4-2)$ $\mathbb{C}P^1$

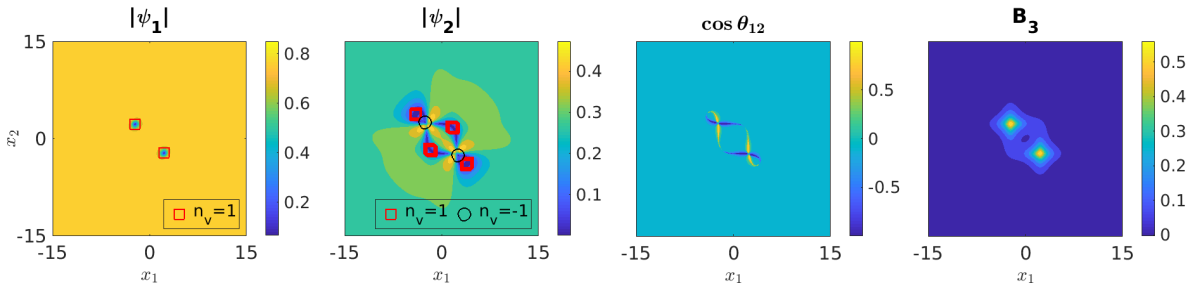

Figure 4.7: *A* $(2, 4-2)$ $\mathbb{C}P^1$ *skyrmion, with* $\hat{x}_3 = (0, 0, 1)$ *and* $\alpha_s = 0.9675$. *We note the similarities of this solution with that of Figure 4.6a. The points,* □, *on* $|\psi_1|, |\psi_2|$ *and* $\cos\theta_{12}$ *show the location and multiplicity of the zeros in the* ψ_1, ψ_2 *condensates and the coincident zeros (if they exist) respectively. Note that overlapping points should be considered to represent the same zero and only appear due to numerical error. We note that* $(u_1, u_2) \approx (0.82, 0.31)$ *and the correspond values for* $\alpha_s = 0.71$ *are* $(u_1, u_2) \approx (0.31, 0.93)$ *so we do not expect these solutions to be identical to those in Figure 4.6a.*
For each condensate $\sum n_v = N$ *and the* B_1 *and* B_2 *components of the magnetic field vanish everywhere. Finally, as the inhomogeneous parts of the solutions are well localised to the centre we only show the central part of the simulated domain.*

skyrmion is novel, it does appear to be a real solution not one that is the result of numerical inaccuracy.

Fields Solutions for $\alpha_s = 0.86$

Finally we study $\alpha_s = 0.86$ where we have $u_1 \approx u_2$ and although, for $N = 2$, we find the same two field solutions as for $\alpha_s = 0.71$ the $N = 2$ $\mathbb{C}P^1$ skyrmion solutions are sufficiently different to warrant attention.
Figure 4.8a shows a $(2, 2)$ $\mathbb{C}P^1$ skyrmion and Figure 4.8b a $(2, 2)$ vortex. If we compare Figure 4.8a with Figure 4.6a we note the difference in magnetic field, B_3, structure. This difference in structure could be down to the relative sizes of u_1 and u_2 as in the $\alpha_s = 0.86$ case they are almost equivalent and so we see similar contributions to B_3 at the zeros of each condensate. Additionally, comparing $\cos\theta_{12}$ we see the domain walls are much more compact in the Figure 4.8a case. We note that we do not find $\mathbb{C}P^1$ skyrmions when $N = 1$. Figure 4.8b is remarkably similar to the result for Figure 4.6b where we again see that the coincident zeros are not connected by domain walls and the magnetic field appears to be relatively well separated.

4.2.6 $N > 2$ Field Solutions

Due to computational limitations investigating results for $N > 2$, for all orientations, was not possible. Thus, we restricted ourselves to a few different orientations (primarily the basal plane) and explored solutions for the values of α_s studied above. We summarise the results as follows:

- $\alpha_s = 0.67$
  - Increasing N does not produce any new types of solutions, we still find the equivalent of the $(n_{1v} - n_{1av}, N)$ vortex and the (N, N) vortex depending on the orientation, n_{1v} and n_{1av} are the total winding number of the zeros and anti zeros of the ψ_1 condensate.

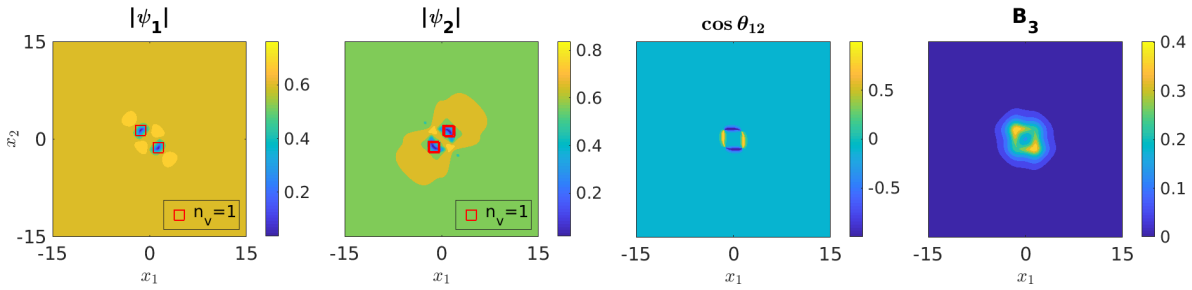

(a) *A* $(2,2)$ $\mathbb{C}P^1$ *skyrmion, with* $\hat{x}_3 = (0,0,1)$ *and* $\alpha_s = 0.86$.

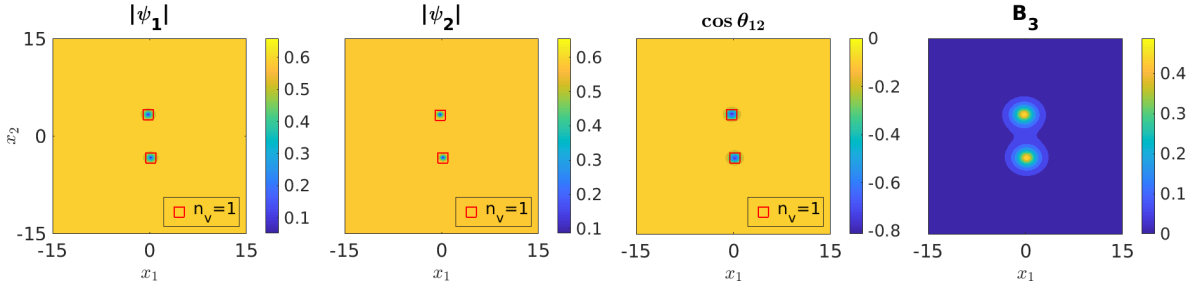

(b) *A* $(2,2)$ *vortex, with* $\hat{x}_3 = (0,1,0)$ *and* $\alpha_s = 0.86$.

Figure 4.8: *Plots of the gauge invariant quantities of the fields,* $N = 2, \alpha_s = 0.86$*, for two different orientations which show the two types of solutions possible for this parameter range. The points,* □*, on* $|\psi_1|, |\psi_2|$ *and* $\cos\theta_{12}$ *show the location and multiplicity of the zeros in the* ψ_1*,* ψ_2 *condensates and the coincident zeros (if they exist) respectively. Note that overlapping points, with the same value of* n_v*, should be considered to represent the same zero and only appear due to numerical error.*
For each condensate $\sum n_v = N$ *and the* B_1 *and* B_2 *components of the magnetic field vanish everywhere. Finally, as the inhomogeneous parts of the solutions are well localised to the centre we only show the central part of the simulated domain.*

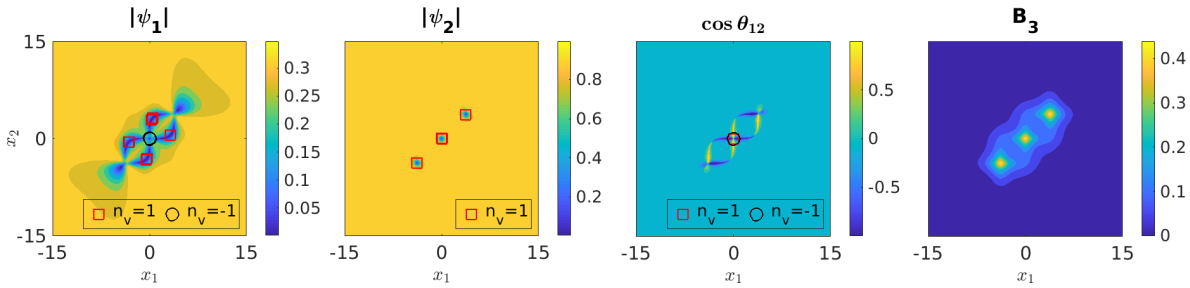

Figure 4.9: *A* $(4-1,3)$ *vortex, with* $\hat{x}_3 = (0,0,1)$ *and* $\alpha_s = 0.71$. *The points,* □ *and* ○, *on* $|\psi_1|, |\psi_2|$ *and* $\cos\theta_{12}$ *show the location and multiplicity of the zeros in the* ψ_1, ψ_2 *condensates and the coincident zeros respectively.*
For each condensate $\sum n_v = N$ *and the* B_1 *and* B_2 *components of the magnetic field vanish everywhere. Finally, as the inhomogeneous parts of the solutions are well localised to the centre we only show the central part of the simulated domain.*

- $\alpha_s = 0.71$
  - We find for $N = 3$ a new bound state that appears to be a combination of a $(2-1,1)$ vortex and a $(2,2)$ $\mathbb{C}P^1$ skyrmion where the numbers of zeros and anti zeros changes so that the total winding number in each condensate is $N = 3$. Figure 4.9 shows this $(4-1,3)$ vortex.
- $\alpha_s = 0.86$
  - We find that, in the basal plane, a N=3 vortex solution is energetically favoured over an N=3 $\mathbb{C}P^1$ skyrmion. However, for $N = 4$ the $N = 4$ $\mathbb{C}P^1$ skyrmion is now favoured leading us to guess that only for even N are $\mathbb{C}P^1$ skyrmion solutions energetically favoured.

4.2.7 Orientation Dependence of Physical Quantities

We now move to considering the complete orientation dependence of relevant physical quantities of the model such as the maximum magnetic field and the twisting angle. Each orientation is defined by a $\hat{x}_3 \in S^2$ which is then reduced to $\hat{x}_3 \in \{S^2 | z > 0\}$, namely the upper hemisphere using the spatial (reflection) symmetry, $z \mapsto -z$, of the model. By symmetry we mean that the free energy is unchanged by this coordinate transformation. We then project $\hat{x}_3$ onto the unit disc. This allows us to show the complete orientation dependence for multiple values of α_s at the same time and so the reader can visualise how changing α_s and $\hat{x}_3$ simultaneously affects these physical quantities. Additionally, we include the values, $\alpha_s = (0.785, 0.9138, 0.9675, 0.9975)$, from Figure 4.1, along with $\alpha_s = (0.67, 0.71, 0.86)$ to attempt to sample the full range of $\alpha_s \in (\frac{2}{3}, 1)$.
For convenience we define the following three types of solution,

- Type A ≡ An $(n_{1v} - n_{1av}, N)$ or $(N, n_{2v} - n_{2av})$ vortex. That is a vortex solution with anti zeros in one condensate. For example Figures 4.3a and 4.5.
- Type B ≡ An (N, N) vortex. For example, Figure 4.3b.
- Type C ≡ An $N = 2$ $\mathbb{C}P^1$ skyrmion. For example, Figures 4.6a, 4.7 and 4.8a.

We give results for $N = 2$ as this is the lowest value of N that we see $\mathbb{C}P^1$ skyrmion solutions and this contributes to more interesting results. Furthermore, we assume that the field solutions given in Section 4.2.5 are exhaustive.
We now seek to find orientation dependence of the type of solution that is globally minimum for $N = 2$ for each α_s. We start by running simulations, for $N = 2$, with initial conditions that favour Type C solutions, if they occur, for the chosen value of α_s. When we simulate multiple orientations, we use these same initial conditions for each which allows us to obtain consistent results that obey the expected spatial symmetries, at the cost of longer computation times. Additionally, we run simulations for $N = 1$ which only ever produces Type A or Type B solutions and allows us to determine which is of lower energy for that orientation. Thus by comparing $N = 1$ and $N = 2$ solutions we can determine which type gives the lowest energy for $N = 2$.
To proceed we introduce,

$$\hat{F}_N = \frac{F_N - F_0}{N} \ , \tag{4.49}$$

where $\hat{F}_N$ is the normalised energy for a winding number of N run using the same initial conditions. The $\hat{F}_1$ solutions tell us if Type A or Type B is energetically favourable and then the $\hat{F}_2$ solution tells us if Type C occurs and is of lower energy than $\hat{F}_1$. Comparing $\hat{F}_1$ and $\hat{F}_2$ means we compare the energy of two unbound or infinitely separated $N = 1$ vortex solutions with the $N = 2$ solution which can be Type A, B or C. This is shown in Table 4.1.

α_S	Type	$\hat{F}_2$	Type	$\hat{F}_1$	$\frac{\hat{F}_2 - \hat{F}_1}{\hat{F}_1}$
0.67	Type A	1.9279	Type A	1.9374	-0.4913 %
0.71	Type C	2.0258	Type A	2.0715	-2.2083 %
0.785	Type C	2.2588	Type B	2.2950	-1.5782 %
0.86	Type C	2.4264	Type B	2.4857	-2.3863 %
0.9138	Type C	2.5184	Type B	2.5980	-3.0640 %
0.9675	Type C	2.6069	Type A	2.6577	-1.9097 %
0.9975	Type A	2.6681	Type A	2.6794	-0.4212 %

Table 4.1: Values of the free energy for an $s+id$ superconductor with orientation $\hat{x}_3 = (0, 0, 1)$, where $\hat{F}_N = \frac{F_N - F_0}{N}$.
Type A $\equiv$ An $(n_{1v} - n_{1av}, n_{2v})$ or $(n_{1v}, n_{2v} - n_{2av})$ vortex ,
Type B $\equiv$ An (N, N) vortex and
Type C $\equiv$ An $N = 2$ $\mathbb{C}P^1$ skyrmion.
We note that even moving from Type B to Type C, in the $\alpha_s = 0.86$ case, the change in energy is still very small $\approx 3\%$.

We see is that for this orientation, $\hat{x}_3 = (0, 0, 1)$, $\hat{F}_2 < \hat{F}_1$ for all values of α_s. Thus the type of solution that is globally minimum is trivially be given by the $N = 2$ solutions. Note that in some cases the percentage difference between $\hat{F}_2$ and $\hat{F}_1$ is very small, $0.5\% <$, and there is no change in the type of superconductor. In this case we can consider the $\hat{F}_2$ solution equivalent to two infinitely separated $\hat{F}_1$ solutions. This is also confirmed by visually inspecting the field solutions.
However, for certain α_s and $\hat{x}_3$ we can have $\hat{F}_2 > \hat{F}_1$ and in this case we would consider the $N = 2$ globally minimum solution to be two infinitely separated $N = 1$ vortex solutions. The corresponding globally minimum free energy will be twice $\hat{F}_1$, the maximum magnetic field the same and the number of coincident zeros will be equal to $N = 2$. This is shown in Table 4.2,

which shows the case where Type C solutions in the $N = 2$ case occur but are energetically unfavourable over the infinitely separated $N = 1$ Type A or B case.

α_S	Type	$\hat{F}_2$	Type	$\hat{F}_1$	$\frac{\hat{F}_2 - \hat{F}_1}{\hat{F}_1}$
0.67	Type B	1.9431	Type B	1.9399	0.1607 %
0.71	Type B	2.034	Type B	2.0227	0.5598 %
0.785	Type C	2.3264	Type B	2.1942	6.0241 %
0.86	Type C	2.4974	Type B	2.3744	5.1805 %
0.9138	Type C	2.5633	Type B	2.5049	2.3314 %
0.9675	Type B	2.6306	Type B	2.6288	0.0686 %
0.9975	Type A	2.6852	Type A	2.6875	-0.086 %

Table 4.2: Values of the free energy for an $s + id$ superconductor with orientation $\hat{x}_3 = (0.7071, -0.7071, 0)$, where $\hat{F}_N = \frac{F_N - F_0}{N}$.
Type A $\equiv$ An $(n_{1v} - n_{1av}, n_{2v})$ or $(n_{1v}, n_{2v} - n_{2av})$ vortex ,
Type B $\equiv$ An (N, N) vortex and
Type C $\equiv$ An $N = 2$ $\mathbb{C}P^1$ skyrmion.
We note that the largest percentage differences come from energetically unfavourable Type C solutions for $\hat{F}_2$ for the $\alpha_s = \{0.785, 0.86, 0.9138\}$. We can see all of the other positive potential differences are very small $< 0.5\%$ so should probably be considered negligible.

Thus if $\hat{F}_2 < \hat{F}_1$ we trivially have found the type of solution that globally minimises for $N = 2$. However, if $\hat{F}_1 > \hat{F}_2$ then we must consider the type of solution found for the $N = 1$ case to be the globally minimum solution in the $N = 2$ case also.

Globally Minimum Free Energy

Figure 4.10 shows the orientation dependence of the presumed globally minimum free energy per unit length. We note that the peak of the energy increases with α_s which is due to our choice of normalisation,

$$F_p(u_1, u_2, \pm\frac{\pi}{2}) = 18\alpha_s^2 + 3\alpha_s - \frac{3}{2} \ . \tag{4.50}$$

In terms of orientation dependence the minimum value of the energy, independent of α_s, occurs at $\hat{x}_3 = \pm\hat{x} = (\pm 1, 0, 0)$ and the energies have the expected C_2 symmetries about the crystalline x and y axes. The action of these spatial symmetries are,

$$C_2(x) : (x, y, z) \mapsto (x, -y, -z) \tag{4.51}$$
$$C_2(y) : (x, y, z) \mapsto (-x, y, -z) \ , \tag{4.52}$$

where, as we are projecting $\hat{x}_3$ onto the unit disc, these two symmetries are equivalent to reflections in the x and y axes respectively.

Coincident Zeros

The orientation dependence of the number of coincident zeros is shown here, where this is calculated using the algorithms described in Appendix B. We note that if this number is zero then we have a $\mathbb{C}P^1$ skyrmion solution otherwise it is either a Type A or B vortex solution. Figure 4.11 gives the orientation dependence of the number of coincident zeros. This plot shows for what orientations and values of α_s that $\mathbb{C}P^1$ skyrmion solutions are energetically

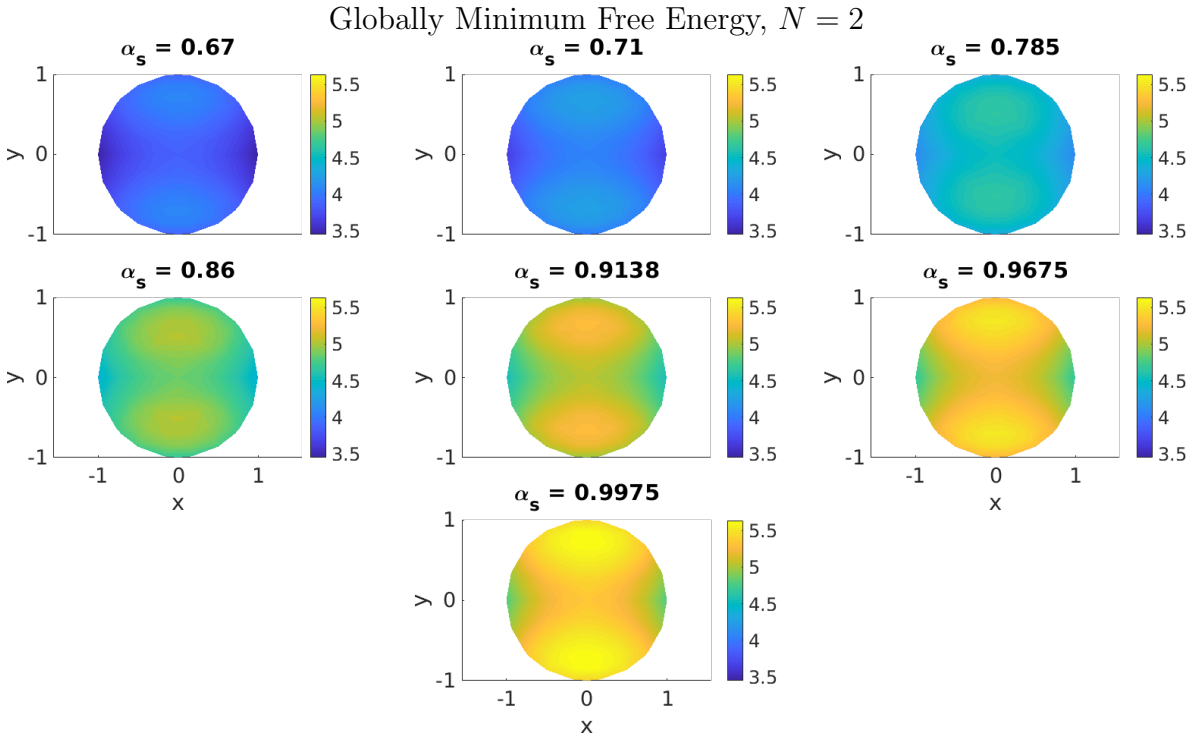

Figure 4.10: *The orientation dependence of the free energy, for $N = 2$.*
Each point gives the (x, y) position of the unit 3-vector, $\hat{x}_3 \in S^2$, which defines the orientation. Due to the free energy being invariant under the transformation, $\hat{z} \mapsto -\hat{z}$, we need only consider the northern hemisphere. Projecting the northern hemisphere onto the disc is done for visual clarity, and the colour at each point on the disc gives the value of the globally minimum free energy for that orientation.

favoured over vortices but does not allow us to distinguish between the vortex solutions. We see initially that no skyrmions occur for $\alpha_s = 0.67$ but for $\alpha_s = \{0.785, 0.86, 0.9138, 0.9675\}$ the region where skyrmions are viably changes shape but $\hat{x}_3 = (\pm 1, 0, 0)$ and $(0, 0, 1)$ (the x and z crystalline axes) always produce skyrmion solutions and in fact $\hat{x}_3 = (\pm 1, 0, 0)$ corresponds to the orientation with the lowest values of the free energy for a given α_s. Then for $\alpha_s = 0.9975$ we return to no $\mathbb{C}P^1$ skyrmion solutions for any orientation.

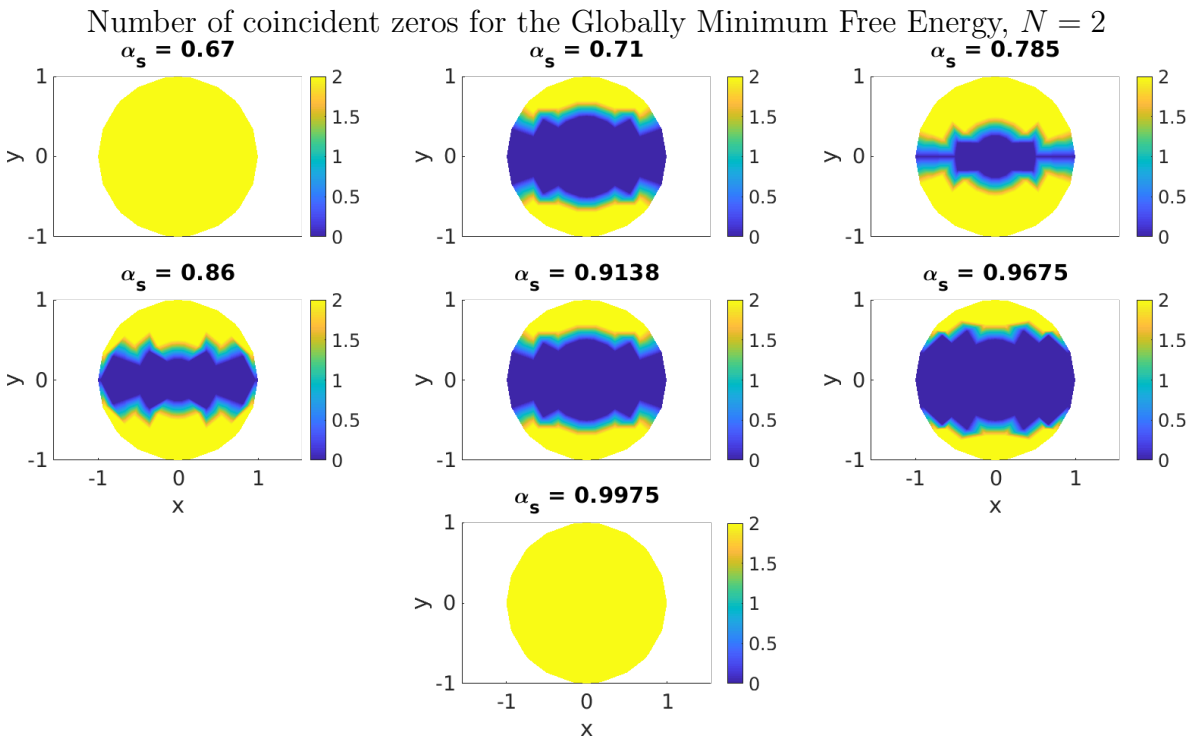

Figure 4.11: *An N=2 plot of the number of coincident zeros calculated on a discrete lattice. Each point gives the (x, y) position of the unit 3-vector, $\hat{x}_3 \in S^2$, which defines the orientation. Due to the free energy being invariant under the transformation, $\hat{z} \mapsto -\hat{z}$, we need only consider the northern hemisphere. Projecting the northern hemisphere onto the disc is done for visual clarity, and the colour at each point on the disc gives the number of coincident zeros for that orientation.*

This only allows us to distinguish between two elements of the previously defined trichotomy, (Type A, Type B, Type C). This trichotomy is better visualised as a scatter plot rather than a heat plot as shown in Figure 4.12. We see how the globally minimising solution moves from a Type A to a Type B solution with orientation when $\alpha_s = \{0.67, 0.9975\}$. The region where this transition occurs is for orientations near to $\hat{x}_3 = (0, \pm 1, 0)$. We also see that Type A only occurs for $\alpha_s = \{0.67, 0.9975\}$. For the remaining values of α_s we see how Type C solutions are energetically favoured near the basal plane but the Type B solutions return close to $\hat{x}_3 = (0, \pm 1, 0)$.

The reader may notice that, in Figure 4.12 for $\alpha_s = 0.9975$, points $(x, y) = (x_a = -0.4330, y_a = 0.7500)$ and $(x, y) = (x_b = -0.4330, y_b = -0.7500)$ are labelled Type B and Type A with free energy per unit length of $F_a = 5.5468$ and $F_b = 5.5488$ respectively. This appears to break the expected x axis reflection symmetry that the other six plots exhibit. However, what this shows is that, as these two points occur close to the boundary between a Type A and Type B solution, the two solutions are (up to numerical error) degenerate in energy. By boundary

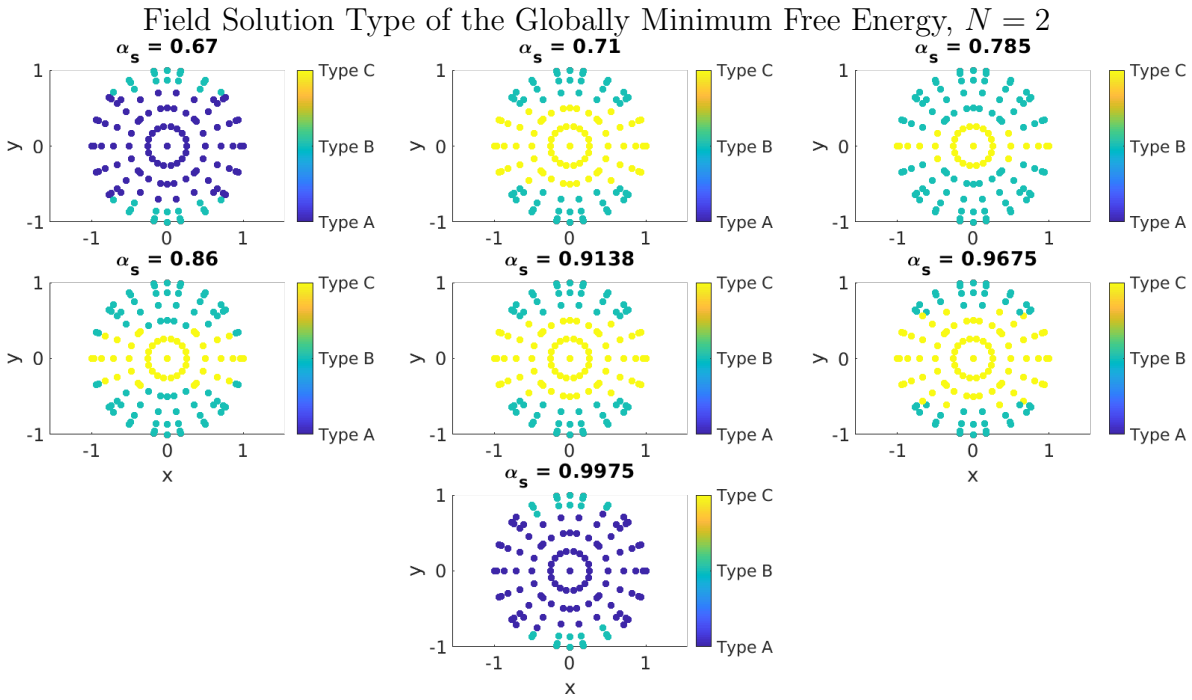

Figure 4.12: *The orientation dependence of the type of solution, for an $N = 2$ vortex in an $s + id$ superconductor.*
Type A $\equiv$ An $(n_{1v} - n_{1av}, N)$ or $(N, n_{2v} - n_{2av})$ vortex. That is a vortex solution with anti zeros in one condensate,
Type B $\equiv$ An (N, N) vortex and
Type C $\equiv$ An $N = 2$ $\mathbb{C}P^1$ skyrmion.
Each point gives the (x, y) position of the unit 3-vector, $\hat{x}_3 \in S^2$, which defines the orientation. Due to the free energy being invariant under the transformation, $\hat{z} \mapsto -\hat{z}$, we need only consider the northern hemisphere. Projecting the northern hemisphere onto the disc is done for visual clarity, and the colour at each point on the disc gives the field solution type for that orientation.

we mean the orientations at which the globally minimum energy type switches from A to B or vice versa.

Maximum Magnetic Field

Here we consider the value of the maximum magnetic field which on a lattice is simply given by the maximum element of,

$$|B^{(I,J)}| = |B(x_1^{(I)}, x_2^{(J)})| \ . \tag{4.53}$$

Figure 4.13 shows this. The feature of interest is the noticeably lower values of the maximum magnetic field which approximately correspond to where the $\mathbb{C}P^1$ skyrmion solutions are energetically favoured. The higher values correspond to where the $N = 2$ vortex solutions are favoured. This can be understood if we consider B_3 in Figures 4.8a and 4.8b where we see peaks in the magnetic field corresponding to the location of zeros. In the case of Figure 4.8b the zeros are coincident which apparently causes the peak to be larger.

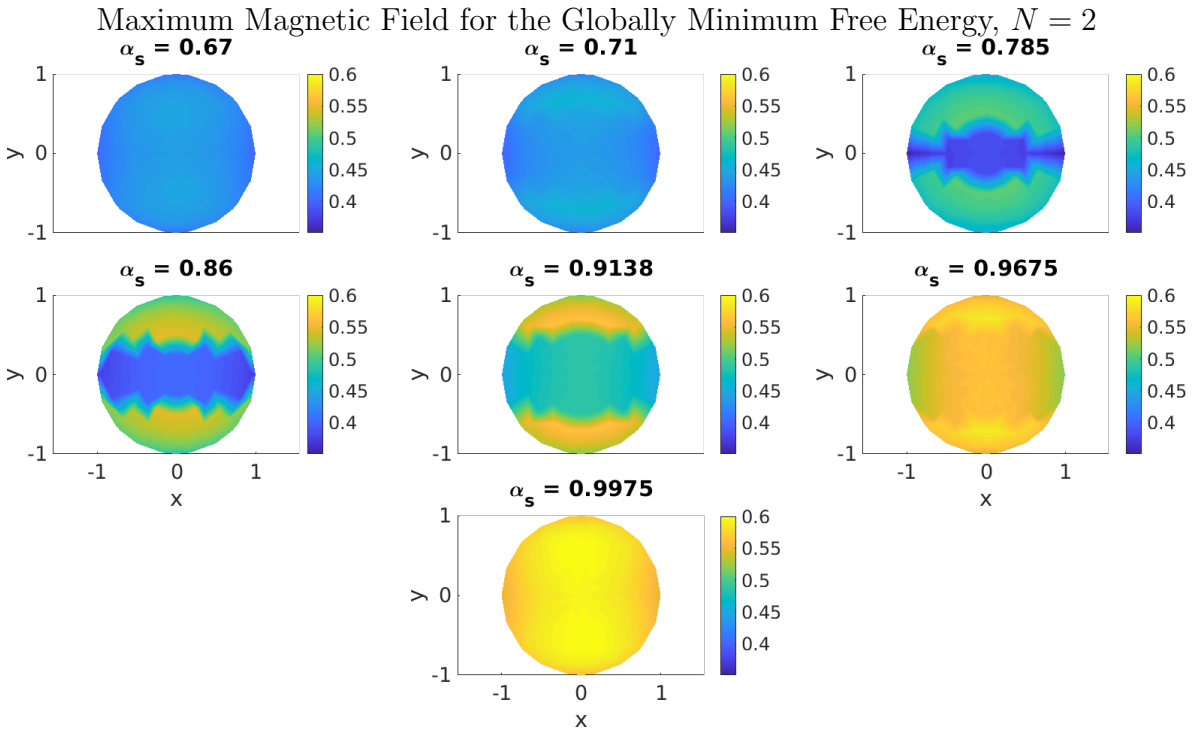

Figure 4.13: *The orientation dependence of the maximum magnetic field, for $N = 2$. Each point gives the (x, y) position of the unit 3-vector, $\hat{x}_3 \in S^2$, which defines the orientation. Due to the free energy being invariant under the transformation, $\hat{z} \mapsto -\hat{z}$, we need only consider the northern hemisphere. Projecting the northern hemisphere onto the disc is done for visual clarity, and the colour at each point on the disc gives the value of the maximum magnetic field for that orientation.*

4.2.8 Magnetic Field Twisting

Here we discuss how changing the orientation of our model can give rise to non zero B_1 and B_2 which can cause the magnetic field direction, $\hat{B}$, to point away from the plane normal $\hat{x}_3$ which we call magnetic field twisting. This is quantified by the local twisting angle given by,

$$\theta_B = \arctan\left(\frac{|\hat{B} \times \hat{x}_3|}{\hat{B} \cdot \hat{x}_3}\right) , \tag{4.54}$$

where $\hat{B} \in S^2$ gives the direction of the magnetic field for each point in space.
Unlike magnetic field twisting in $s + id$ domain walls, see Section 2.5.3, the direction of the magnetic field varies considerably and does not converge to a single value as $r \to \infty$ as it does in the domain wall case when $|x_1| \to \infty$. In the domain wall case we introduce a variable cutoff which if $|B| <$ cutoff we set the twisting angle equal to zero. However, the value of θ_B varies massive depending on the value of cutoff, unlike in the domain wall case. Thus simply selecting the maximum value of θ_B does not give a sensible result. However, consider,

$$B^{max} = B(x_1^{max}, x_2^{max}) , \tag{4.55}$$

which is one of the N points in the domain where the magnetic field, B, reaches its maximum value. Then what we call the vortex twisting angle is given by,

$$\theta_B^{max} = \arctan\left(\frac{|\hat{B}^{max} \times \hat{x}_3|}{\hat{B}^{max} \cdot \hat{x}_3}\right) , \tag{4.56}$$

where $\hat{B}^{max} \in S^2$ is the unit vector giving the direction of the magnetic field at the point (x_1^{max}, x_2^{max}). Here we have decided to take the local twisting angle at this point and use this to measure the overall twisting of the magnetic field.
For our numerical solutions the twisting angle is only calculated at lattice sites so it is possible that our $\theta_B^{max} \neq 0$ occur due to the true value of $|\hat{B}^{(I,J)}|$ being in between lattice sites. However, we investigated the effect that lowering the numerical tolerance had on the value of θ_B for a variety of orientations.
The numerical tolerance is the value that all elements of the gradient of the discretised energy must be lower than for the arrested Newton flow algorithm to terminate, defined in Equation 2.41. We compare two sets of results for $tol1 = 0.0075$ and $tol2 = 0.000625$ where $\frac{tol1}{tol2} = 12$. If we define the ratio,

$$\theta_B^{tol} := \frac{\theta_B^{tol2}}{\theta_B^{tol1}} \ , \tag{4.57}$$

where θ_B^{tol1} and θ_B^{tol2} are the set of values, for different orientations, of θ_B^{max} for $tol1$ and $tol2$ respectively. Any orientations where both θ_B^{tol1} and θ_B^{tol2} vanish we discount. Then Table 4.3 gives various statistical measures of θ_B^{tol}. We note that if this was a numerical artefact we would expect $\theta_B^{tol} \to 0$ as we decrease the value of the numerical tolerance. However, from the mean and standard deviation we see that most values are close to $\theta_B^{tol} = 1$. Thus it would appear that $\theta_B^{max} \neq 0$ does not occur due to numerical error.

$\max \theta_B^{tol}$	$\min \theta_B^{tol}$	Mean θ_B^{tol}	Standard Deviation θ_B^{tol}	Geometric Mean θ_B^{tol}
1.5908	0.7398	0.9593	0.2030	1.0569

Table 4.3: Statistical measures of θ_B^{tol} showing how changing the tolerance affects the value of θ_B, the vortex twisting angle. $\theta_B^{tol} = \frac{\theta_B^{tol2}}{\theta_B^{tol1}}$, is the ratio of the value of the twisting angle for two values numerical tolerance, $tol1 = 0.0075$ and $tol2 = 0.000625$.

Additionally, we investigated halving the space between lattice sites, which is equivalent to quadrupling the computation time, for the orientation where θ_B^{max} is maximum, $\hat{x}_3 = (0.866, 0, 0.5)$, and found no discernable change in the value of θ_B^{max}. Thus we can present, with some confidence, Figure 4.14 which shows how θ_B^{max} changes with the orientation and we see that this angle is not significantly affected by the choice of α_s and the orientations where it is maximal are repeated. We see no twisting for any orientation parallel to a crystalline axes, $(\pm 1, 0, 0)$, $(0, \pm 1, 0)$, $(0, 0, \pm)$.

We can look in more detail at the local twisting angle, θ_B. Figure 4.15a presents field solutions for $\hat{x}_3 = (0.0000, 0.5000, 0.8660)$ where we have a small but non zero $\theta_B^{max} = 0.0065\pi$ as well as larger a non zero θ_B elsewhere. This occurs because we have non zero B_1 and B_2 that are only a power of ten lower in magnitude than the B_3 component. This gives a small, but non zero, value for the magnetic field twisting.

4.3 Vortices in $s + is$ Superconductors

We also investigate two-dimensional vortex solutions in the $s+is$ case. We found only (N, N) vortex solutions but we did still find a non zero vortex twisting angle, θ_B^{max} which may be of interest.
We find minimising solutions of the $s + is$ version of Equation 4.22 with the only difference

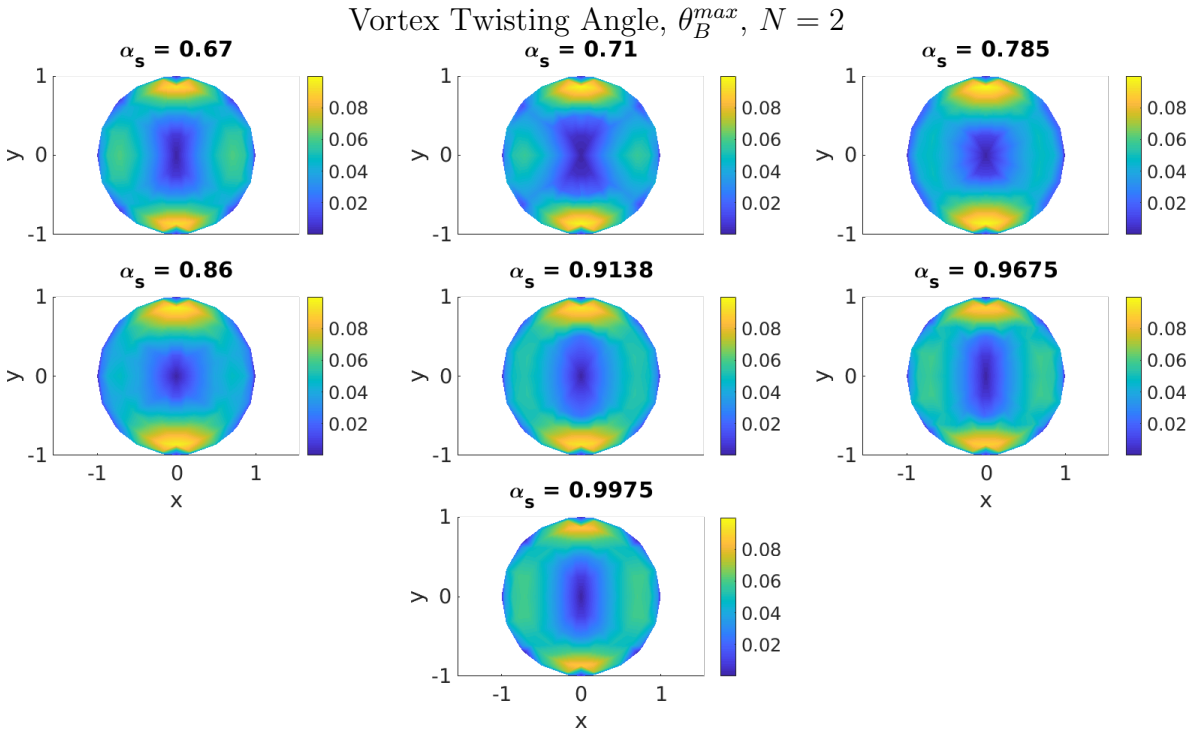

Figure 4.14: *The orientation dependence of the vortex twisting angle, θ_B^{max}, for $N = 2$. Each point gives the (x, y) position of the unit 3-vector, $\hat{x}_3 \in S^2$, which defines the orientation. Due to the free energy being invariant under the transformation, $\hat{z} \mapsto -\hat{z}$, we need only consider the northern hemisphere. Projecting the northern hemisphere onto the disc is done for visual clarity and the colour at each point on the disc gives the vortex twisting angle for that orientation.*

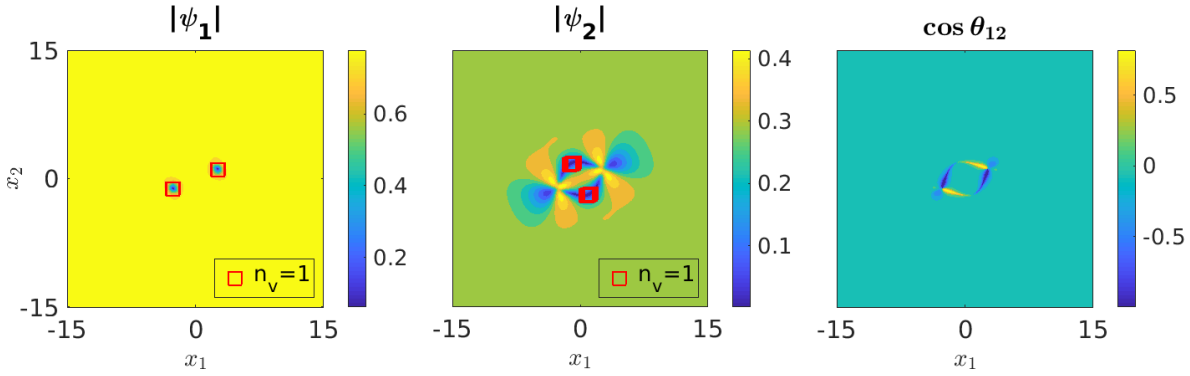

(a) *A* $(2,2)$ $\mathbb{C}P^1$ *for* $\alpha_S = 0.9675$ *for* $\hat{x}_3 = (0.0000, 0.5000, 0.8660)$

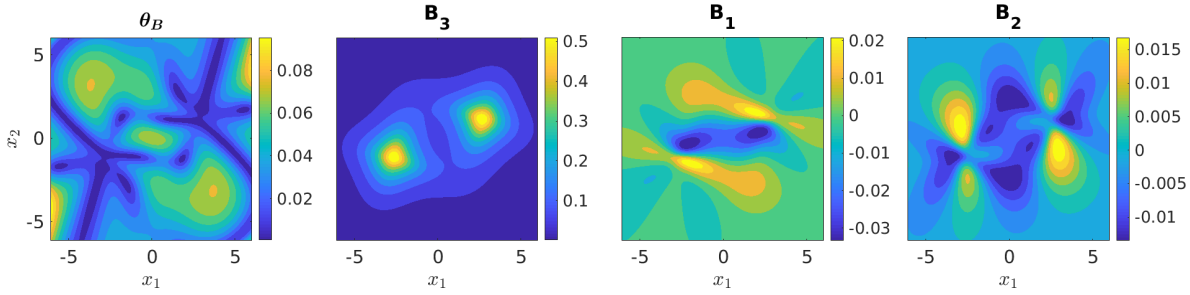

(b) *Visualising magnetic field twisting for an N=2 vortex, with* $\alpha_S = 0.9675$ *for* $\hat{x}_3 = (0.0000, 0.5000, 0.8660)$. *Note that we have zoomed into the region where* B_3 *appears to be non zero in the heat plot.*

Figure 4.15: *Plots of the gauge invariant quantities of the fields,* $N = 2, \alpha_s = 0.9675$, *showing non zero* B_1 *and* B_2 *and how that arises in a non zero twisting angle. The points,* □, *on* $|\psi_1|, |\psi_2|$ *and* $\cos\theta_{12}$ *show the location and multiplicity of the zeros in the* ψ_1, ψ_2 *condensates and the coincident zeros (if they exist) respectively.*

from the $s + id$ case being that $Q_{22}^{12} \to 1$ so we have

$$\hat{Q}^{11} = \frac{2}{\lambda_x^2} diag([2, 2, 2\mu]) \tag{4.58}$$

$$\hat{Q}^{22} = \frac{2}{\lambda_x^2} diag([1, 1, \mu]) \tag{4.59}$$

$$\hat{Q}^{12} = \frac{2}{\lambda_x^2} diag([1, 1, \mu]) \ , \tag{4.60}$$

$\lambda_x = (2\kappa^2)^{\frac{1}{4}}$. As we said above only the (N, N) vortex solutions appear to be local minimisers of the $s + is$ energy functional regardless of the value of α_s. Figures 4.16a and 4.16b show two $(2, 2)$ vortex solutions for $\hat{x}_3 = (0, 0, 1)$ and $\hat{x}_3 = (0.866, 0, 0.5)$. We see that they closely match the equivalent $s + id$ solutions, Figure 4.3b for example. The latter orientation is included because it has non zero values of B_1 and B_2 which lead to a non zero value of the vortex twisting angle.

4.3.1 Orientation Dependence of Physical Quantities

Here we show the full $N = 2$ orientation dependence of the relevant physical quantities in Figure 4.17. We note the expected $SO(2)$ symmetry, as well as the non zero vortex twisting angle, θ_B^{max}.

4.4 Summary

We have shown that by considering vortex solutions in anisotropic multicomponent Ginzburg-Landau theory a variety of novel field solutions occur. Through varying the relative sizes of the vacuum values of $|\psi_1|$ and $|\psi_2|$ we can change the type of field configuration that minimises the Ginzburg-Landau equations. These types are solutions where: the zeros in both condensates are coincident (an (N, N) vortex), none of the zeros are coincident (a $\mathbb{C}P^1$ skyrmion) and a state where zeros in one condensate are coincident with anti zeros in the other (for example a $(6-4, 2)$ vortex). Through the use of our ansatz, that does not fix the direction of the magnetic field, we investigate how changing the orientation of these two-dimensional topological solitons affects the type of solution that minimises the free energy. Finally, we observe magnetic field twisting, where the direction of the magnetic field does not lie perpendicular to the vortex plane, for some orientations.

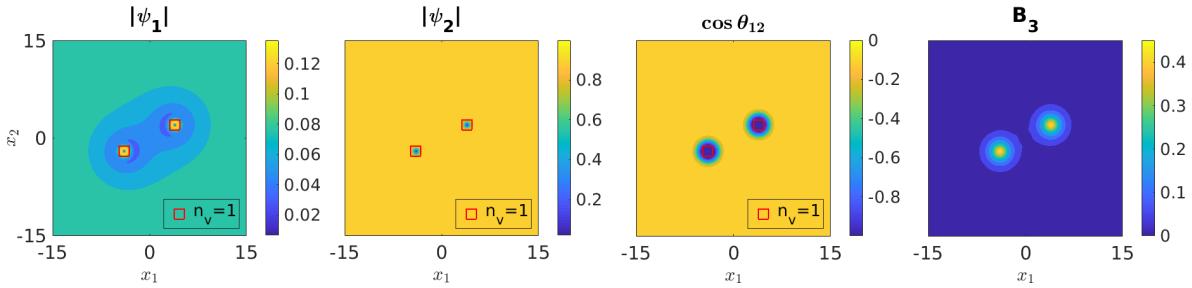

(a) *A* $(2,2)$ *vortex for* $\hat{x}_3 = (0,0,1)$ *and* $\alpha_s = 0.67$.

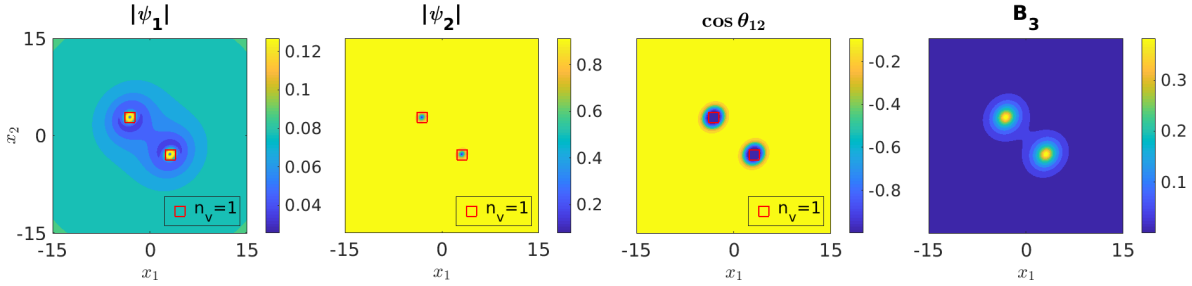

(b) *A* $(2,2)$ *vortex for* $\hat{x}_3 = (0.866,0,0.5)$ *and* $\alpha_s = 0.67$.

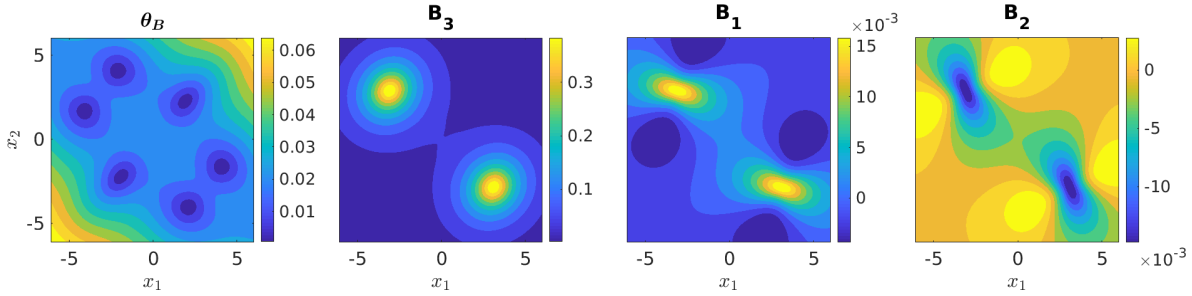

(c) *A* $(2,2)$ *vortex with the local twisting angle,* θ_B*, shown, with* $\hat{x}_3 = (0.866,0,0.5)$ *and* $\alpha_s = 0.67$

Figure 4.16: *$s+is$ plots of the gauge invariant quantities of the fields for $N=2, \alpha_s = 0.67$ vortex solutions, for two different orientations which show the two types of solutions possible for this parameter range. The points, □, on $|\psi_1|, |\psi_2|$ and $\cos\theta_{12}$ show the location and multiplicity of the zeros in the ψ_1, ψ_2 condensates and the coincident zeros (if they exist) respectively.*
For each condensate $\sum n_v = N$.

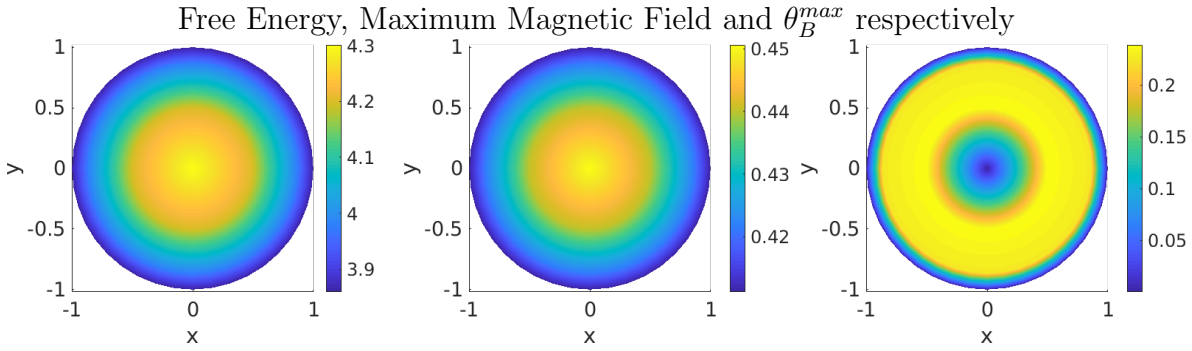

Figure 4.17: *The orientation dependence of the gauge invariant quantities, for* $N = 2$ *and* $\alpha_s = 0.67$.
Each point gives the (x, y) *position of the unit 3-vector,* $\hat{x}_3 \in S^2$*, which defines the orientation. Due to the free energy being invariant under the transformation,* $\hat{z} \mapsto -\hat{z}$*, we need only consider the northern hemisphere. Projecting the northern hemisphere onto the disc is done for visual clarity, and the colour at each point on the disc gives value of the quantity being considered.*

Chapter 5

Vortex Lattices in $s + id$ Superconductors

Here we investigate the $s + id$ model from Chapter 4 (Equation 4.22) on a flat 2-Torus, T^2_Λ, which we can interpret as a solution that is spatially periodic on the x_1, x_2 plane and so forms a vortex lattice. A vortex lattice is composed of repeating parallelograms called unit cells. We apply a constant external magnetic field, $H = H_0\hat{x}_3$, in the perpendicular direction to T^2_Λ. Thus the energy now depends upon H hence we must consider the Gibbs free energy. Focussing on the basal plane, $\hat{x}_3 = \hat{z}$, we investigate how the shape of unit cell that minimises the Gibbs free energy per unit area, G/A, changes with H_0. Unlike [44] we minimise over the area of the unit cell as well as allowing non rectangular units cells to occur.
We introduce a method that, for a given winding number, N, and H_0, produces the locally minimum G/A by minimising the field and unit cell configurations and the unit cell area. This allows us to find the value of N that produces unit cell configurations that minimise G/A for all values of N. For parameter values that energetically favoured $\mathbb{C}P^1$ skyrmion solutions in Chapter 4, where we simulated vortex solutions in an infinite superconductor, we see that $N = 2$ minimises the energy as this is the lowest winding number for which $\mathbb{C}P^1$ skyrmion lattices can occur. We see throughout that the shape of unit cell is not rectangular nor are they hexagonal as they are in the type II isotropic or Abrikosov vortex lattice case [18]. Finally we can calculate the lower, H_{C1}, and upper, H_{C2}, critical fields as well as consider how the vortex lattice solutions change in the range, $H_{C1} < H_0 < H_{C2}$.

5.1 Free Energy on a 2-Torus

Here we consider the free energy on a flat 2-Torus which allows us to investigate vortex lattices. We define the flat 2-Torus, T^2_Λ, as the parallelogram given in Figure 5.1, with opposite sides identified, with lengths $|v_1|, |v_2|$ and smallest internal angle $\alpha \in [0, \frac{\pi}{2}]$. The lattice is composed of these parallelograms and (for a given $v_1, v_2 \in \mathbb{R}^2$) is described by,

$$\Lambda = \{n_1 v_1 + n_2 v_2 |\ n_1, n_2 \in \mathbb{Z}\}\ . \tag{5.1}$$

We note that a square lattice has $|v_1| = |v_2|, \alpha = \frac{\pi}{2}$ and the hexagonal lattice has $|v_1| = |v_2|, \alpha = \frac{\pi}{3}$.

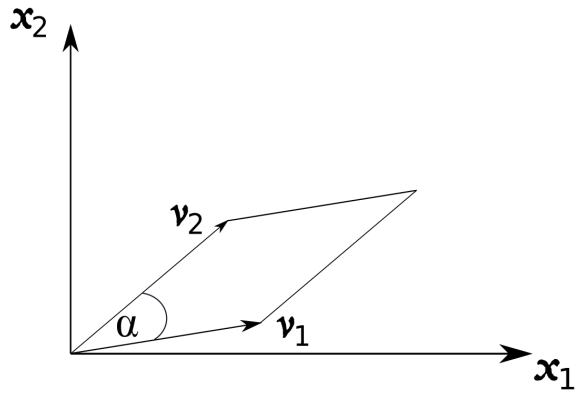

Figure 5.1: *The fundamental parallelogram, or unit cell, of our flat 2-Torus, T^2_Λ. It has internal angle α and side lengths $|v_1|, |v_2|$ where we identify opposite sides to define the flat 2-Torus, where x_1 and x_2 denote the coordinates in the plane of T^2_Λ with normal $\hat{x}_1 \times \hat{x}_2$.*

We can write the free energy (per unit length) for a single unit cell as,

$$F_{T^2_\Lambda} = \int_{T^2_\Lambda} \left(\frac{1}{2} Q^{\alpha\beta}_{ij} (D_i \psi_\alpha)^* (D_j \psi_\beta) + \frac{B^2}{2} + \left(F_p(\rho_1, \rho_2, \theta_{12}) - F_p(u_1, u_2, \pm\frac{\pi}{2}) \right) \right) \, dx_1 dx_2 \tag{5.2}$$

$$F_p(|\psi_1|, |\psi_2|, \theta_{12}) = -2\alpha_s |\psi_1|^2 - |\psi_2|^2 + \frac{4}{3}|\psi_1|^4 + \frac{1}{2}|\psi_2|^4 + \frac{8}{3}|\psi_1|^2|\psi_2|^2 + \frac{4}{3}|\psi_1|^2|\psi_2|^2 \cos(2\theta_{12}) \ , \tag{5.3}$$

with $i, j \in \{1, 2\}$. We use the orthonormal basis, $(\hat{x}_1, \hat{x}_2, \hat{x}_3)$, with the corresponding magnetic field components labelled as (B_1, B_2, B_3). We note it has a similar form and parameter values as Equation 4.22,

$$\begin{aligned} Q^{11} &= \frac{2}{(2\kappa^2)^{\frac{1}{2}}} diag([2, 2]) \\ Q^{22} &= \frac{2}{(2\kappa^2)^{\frac{1}{2}}} diag([1, 1]) \\ Q^{12} &= \frac{2}{(2\kappa^2)^{\frac{1}{2}}} diag([1, -1]) \ , \quad \kappa = 4 \ , \end{aligned} \tag{5.4}$$

except that the anisotropy matrices, $Q^{\alpha\beta}$, are 2×2. This is because, in this chapter, we only consider the basal plane where,

$$(\hat{x}_1, \hat{x}_2, \hat{x}_3) = ((1, 0, 0), (0, 1, 0), (0, 0, 1)) \ . \tag{5.5}$$

This choice of basis is a special case where the free energy on $\mathbb{R}^2$, Equation 4.22, and $F_{T^2_\Lambda}$ can both be reduced in complexity. As similarly discussed in Section 2.2.1, when we study two-dimensional topological solitons in anisotropic superconductors we, in general, need to employ the following ansatz,

$$\psi_\alpha \mapsto \psi_\alpha(x_1, x_2) \tag{5.6}$$

$$A \mapsto A_1(x_1, x_2)\hat{x}_1 + A_2(x_1, x_2)\hat{x}_2 + A_3(x_1, x_2)\hat{x}_3 \ , \tag{5.7}$$

to the three-dimensional Ginzburg-Landau free energy. Despite having dimensionally reduced the system from three to two dimensions, for an anisotropic superconductor, we normally

retain $A_3 \neq 0$. This is because solutions of the dimensionally reduced Ginzburg-Landau equations must be consistent, that is solve, the full three-dimensional Ginzburg-Landau equations. However, in the **basal plane**, we can assume that $A_3 = 0$ and solutions will still be consistent with the full Ginzburg-Landau equations. This means that the covariant derivative, $D_3 = \partial_3 - iA_3$, vanishes. Thus, in the basal plane, both Equation 4.22 and 5.2 are purely two-dimensional. In practice this means that the anisotropy matrices, $Q^{\alpha\beta}$, are 2×2 and that the magnetic field will only point in the $\hat{x}_3$ direction such that,

$$B = (0, 0, B_3) \ . \tag{5.8}$$

We emphasize that our domain is T^2_Λ **not** $\mathbb{R}^2$ as it was in Chapter 4. This point is key as previously we were studying N vortex solutions in an infinite superconductor but now we study vortex lattices which are composed of repeating unit cells. As our domain is now T^2_Λ we use the following (quasi) periodic boundary conditions,

$$\psi_\alpha(\underline{x} + v_1) = \psi_\alpha(\underline{x}) e^{i2\pi N \frac{\underline{x}\cdot v_2}{|v_2|^2}} \tag{5.9}$$

$$\psi_\alpha(\underline{x} + v_2) = \psi_\alpha(\underline{x}) \tag{5.10}$$

$$A_i(\underline{x} + v_1) = A_i(\underline{x}) + \frac{2\pi N}{|v_2|^2} v_2^i \tag{5.11}$$

$$A_i(\underline{x} + v_2) = A_i(\underline{x}) \ , \tag{5.12}$$

where $\underline{x} = (x_1, x_2)^T$ and $v_i = (v_i^1, v_i^2)^T$. The phase factor, $e^{i2\pi N \frac{\underline{x}\cdot v_2}{|v_2|^2}}$, that the condensates gain by moving across the boundary parallel to v_2 ensures that the fields have the correct winding number, N. This, along with the term added to each A_i, means that the magnetic field is quantised such that,

$$\int_{T^2_\Lambda} B_3 \ dx_1 dx_2 = 2\pi N \ . \tag{5.13}$$

This can be derived via Stoke's theorem similarly to Section 4.1 which does this for the magnetic field of an isotropic two component vortex in $\mathbb{R}^2$. These boundary conditions leave the following gauge invariant quantities unchanged,

$$|\psi_\alpha(\underline{x} + v_i)| = |\psi_\alpha(\underline{x})| \tag{5.14}$$

$$\theta_{12}(\underline{x} + v_i) = \theta_{12}(\underline{x}) \tag{5.15}$$

$$B(\underline{x} + v_i) = B(\underline{x}) \ . \tag{5.16}$$

5.1.1 Free Energy on a unit 2-Torus

For numerical purposes it is very useful to make a coordinate change such that our domain becomes the unit 2-Torus, $T^2_\square = [0, 1]^2$. We define the map,

$$L : T^2_\square \mapsto T^2_\Lambda \tag{5.17}$$

$$x_i^\square \mapsto x_i \ , \tag{5.18}$$

where $L \in SL(2, \mathbb{R})$ and has columns v_1, v_2. We note that $|\det L| = \mathcal{A}$, which gives the area of the parallelogram or unit cell depicted in Figure 5.1. Additionally, the $x_i^\square$ (with $i \in \{1, 2\}$) are the coordinates of $T^2_\square$. In order to write the free energy on $T^2_\square$ we define the following transformation matrices,

$$\mathcal{M} \ := \sqrt{\mathcal{A}} L^{-1} \tag{5.19}$$

$$\mathcal{M}^{-1} := \frac{1}{\sqrt{\mathcal{A}}} L \ , \tag{5.20}$$

so that $\mathcal{M} \in SL(2,\mathbb{R})$. Thus we define the following transformations in terms of $\mathcal{M}$,

$$x_i \mapsto \sqrt{\mathcal{A}}(\mathcal{M}^{-1})_{ij} x_j^{\square} \tag{5.21}$$

$$\partial_i \mapsto \frac{1}{\sqrt{\mathcal{A}}} \mathcal{M}_{ji} \partial_j^{\square} \ , \tag{5.22}$$

with $\partial_i^{\square} = \frac{\partial}{\partial x_i^{\square}}$.
In Chapter 4 we were able to transform the coordinates simply by applying the transformation, $Q^{\alpha\beta} \to M^T Q^{\alpha\beta} M$, to the anisotropy matrices thus the form of the free energy remained the same after a coordinate transformation. This worked because our coordinates were orthonormal hence $M \in SO(3)$. However, for T^2_Λ our choice of vectors (v_1, v_2), are in general not orthonormal. This means that the above coordinate transformations adds extra factors of $\sqrt{A}$ to the free energy. This means that the form of the free energy for $F_{T^2_{\square}}$ differs from that of $F_{T^2_\Lambda}$ and is given below,

$$F_{T^2_{\square}} = \int_{[0,1]^2} \left(\frac{1}{2} \tilde{Q}^{\alpha\beta}_{kl} (D_k^{\square} \psi_\alpha^{\square})^* (D_l^{\square} \psi_\beta^{\square}) + \frac{(\partial_1^{\square} A_2^{\square} - \partial_2^{\square} A_1^{\square})^2}{2\mathcal{A}} + \mathcal{A} \left(F_p(\psi_\alpha^{\square}) - F_p(u_1, u_2, \pm\frac{\pi}{2}) \right) \right) \ dx_1^{\square} dx_2^{\square} \ , \tag{5.23}$$

with $k, l \in \{1, 2\}$. The newly introduced coefficients and fields are,

$$\tilde{Q}^{\alpha\beta}_{kl} = \mathcal{M}^{-1}_{ki} Q^{\alpha\beta}_{ij} \mathcal{M}^{-1}_{lj} \tag{5.24}$$

$$\psi_\alpha^{\square} = \psi_\alpha(x_i^{\square}) \tag{5.25}$$

$$A_i^{\square} = A_i(x_i^{\square}) \tag{5.26}$$

$$D_i^{\square} = \partial_i^{\square} - i A_i^{\square} \ . \tag{5.27}$$

Additionally, the unit vectors $(\hat{x}_1^{\square}, \hat{x}_2^{\square}, \hat{x}_3^{\square})$ form an orthonormal basis. The free energy remains the same regardless of the choice of coordinates hence, $F_{T^2_{\square}} \equiv F_{T^2_\Lambda}$.
If we define, $\underline{x}^{\square} := (x_1^{\square}, x_2^{\square})$, then the periodic boundary conditions on $T^2_{\square}$, [38], are now given by,

$$\psi_\alpha(\underline{x}^{\square} + (1,0)) = \psi_\alpha(\underline{x}^{\square}) e^{i 2\pi N x_2^{\square}} \tag{5.28}$$

$$\psi_\alpha(\underline{x}^{\square} + (0,1)) = \psi_\alpha(\underline{x}^{\square}) \tag{5.29}$$

$$A_i(\underline{x}^{\square} + (1,0)) = A_i(\underline{x}^{\square}) + 2\pi N \delta_{i2} \tag{5.30}$$

$$A_i(\underline{x}^{\square} + (0,1)) = A_i(\underline{x}^{\square}) \ . \tag{5.31}$$

Finally, in the special case of the basal plane, the gauge invariant quantity $(\partial_1^{\square} A_2^{\square} - \partial_2^{\square} A_1^{\square})$ is quantised,

$$\int_{[0,1]^2} (\partial_1^{\square} A_2^{\square} - \partial_2^{\square} A_1^{\square}) \ dx_1^{\square} dx_2^{\square} = 2\pi N \ . \tag{5.32}$$

5.1.2 Magnetising the Superconductor

In this chapter we consider the effects of applying a uniform external magnetic field $H = H_0 \hat{x}_3$. This means that there will be extra energy contributions from, H, that we must take into account. Thus we consider the Gibbs free energy of the system which takes into account these extra contributions. This was first introduced in Section 1.3.5 for the simple isotropic Ginzburg-Landau case.

We can construct the anisotropic Gibbs free energy using Equation 5.23 leading to the Gibbs free energy normalised with respect to the normal state,

$$G_{T^2_\square} = \int_{[0,1]^2} \left(\frac{1}{2} \tilde{Q}^{\alpha\beta}_{ij} (D^\square_i \psi^\square_\alpha)^* (D^\square_j \psi^\square_\beta) + \frac{\left((\partial^\square_1 A^\square_2 - \partial^\square_2 A^\square_1) - \mathcal{A} H_0 \right)^2}{2\mathcal{A}} + \mathcal{A} F_p(\psi^\square_\alpha) \right) \, dx^\square_1 dx^\square_2 \ . \tag{5.33}$$

The normal state occurs when the the external magnetic field fully penetrates the superconductor, $(\partial^\square_1 A^\square_2 - \partial^\square_2 A^\square_1) = \mathcal{A} H_0$ and both condensates vanish. In this state the material is no longer superconducting.
As we now consider a lattice, the quantity we are interested in minimising is the Gibbs free energy of the entire periodic lattice,

$$G_{sys} = \mathcal{A}_{sys} \frac{G_{T^2_\square}}{\mathcal{A}} \ , \tag{5.34}$$

where $\mathcal{A}_{sys}$ is the total area of our system. As $\mathcal{A}_{sys}$ is a constant this can be achieved by minimising $\frac{G_{T^2_\square}}{\mathcal{A}}$, the Gibbs free energy per unit area. We note that, as $H = H_0 \hat{x}_3$ is constant throughout the domain, the Gibbs free energy normalised with respect to the homogenous superconducting state is given by,

$$\frac{\hat{G}_{T^2_\square}}{\mathcal{A}} = \frac{G_{T^2_\square}}{\mathcal{A}} - F_p(u_1, u_2, \pm\frac{\pi}{2}) - \frac{H_0^2}{2} \ . \tag{5.35}$$

From this we can see that, for a given H_0, minimising $\frac{\hat{G}_{T^2_\square}}{\mathcal{A}}$ is equivalent to minimising $\frac{G_{T^2_\square}}{\mathcal{A}}$ as they differ by only constants.
We can also calculate approximate values of H_{C1}. This is the lower critical field above which, for a constant temperature, a vortex state is energetically favourable over the homogenous superconducting state. The value of H_0 for which the Gibbs free energy normalised with respect to the homogenous superconducting state, $\frac{1}{\mathcal{A}} \hat{G}_{T^2_\square}$, vanishes will be close to the value of H_{C1}. We note that,

$$\hat{G}_{T^2_\square} = F_{T^2_\square} - H_0 \int_{[0,1]^2} (\partial^\square_1 A^\square_2 - \partial^\square_2 A^\square_1) \, dx^\square_1 dx^\square_2 \ , \tag{5.36}$$

where that $H = H_0 \hat{x}^\square_3$.
We now consider $\hat{G}_{T^2_\square}$ for $H_0 = H_{C1} + \delta$ where $0 < \delta << 1$. In this case $\hat{G}_{T^2_\square} \approx 0$. However, as $H_0 > H_{C1}$ we are in the vortex state where, $\int_{[0,1]^2} (\partial^\square_1 A^\square_2 - \partial^\square_2 A^\square_1) \, dx^\square_1 dx^\square_2 = 2\pi N$. Thus by rearranging Equation 5.36 the lower critical field is approximately given by,

$$H_{C1} \approx \frac{F_{T^2_\square}}{2\pi N} \ . \tag{5.37}$$

Though we do not yet know the value of $F_{T^2_\square}$ for any H_0. However, in Chapter 4 we calculated the free energy on $\mathbb{R}^2$ for a number of different vortex states. In order to accurately estimate H_{C1} we seek the vortex state with the smallest free energy.
If we consider an isotropic superconductor then the lowest energy vortex state is one with a single vortex in the entire superconductor. The free energy of this would be denoted as $\hat{F}_1$ with,

$$\hat{F}_N = \frac{F_N - F_0}{N} \ , \tag{5.38}$$

where F_N denotes the globally minimum free energy vortex solution on $\mathbb{R}^2$ for winding number of N. However, when we consider anisotropy then $\hat{F}_N$ may decrease with N. Thus,

$$H_{C1} \approx \inf_N \frac{\hat{F}_N}{2\pi} \ , \tag{5.39}$$

will allow us to more accurately estimate H_{C1}. However, we cannot check an infinite number of solutions so this must be truncated. It is sufficient for our purposes to truncate at $N = 2$ as we are only looking for a rough estimate as a starting point for our numerics. This is because the method we used returns singular results when $H_0 < H_{C1}$.
In summary, to estimate H_{C1} we find the value of $N \in \{1, 2\}$ that gives the lowest $\hat{F}_N$ to provide an approximate value for H_{C1}. If we consider Table 4.1 which gives the values of the free energy for the $N = 1$ and $N = 2$ solutions ran in Chapter 4. We note that, in the basal plane, solutions for $N > 2$ were found to be combinations of the $N = 1$ and $N = 2$ solutions so only using these two values of the energy should provide a good approximation for H_{C1}. We also include the type of solution as well as the percentage differences of the two energies. As we now consider lattice solutions, Type A,B,C now refers to the number of zeros and anti zeros in a single unit cell.

- Type A $\equiv$ An $(n_{1v} - n_{1av}, N)$ or $(N, n_{2v} - n_{2av})$ vortex. That is a vortex lattice solution with anti zeros in one condensate. For example Figure 5.6a.

- Type B $\equiv$ An (N, N) vortex lattice. For example Figure 5.10.

- Type C $\equiv$ An $N = 2$ $\mathbb{C}P^1$ skyrmion lattice. For example Figure 5.9a.

We note that even in the $N = 2, \alpha_s = 0.86$ case where the Type C solutions are of lower energy the difference is at most $\approx -3\%$. We note that for $\alpha_s = 0.67$ the percentage difference between $\hat{F}_1$ and $\hat{F}_2$ is over four times smaller than for $\alpha_s = 0.86$, we consider this difference to be below the threshold, $\approx 0.5\%$, of numerical error. This can also be seen by the fact that the Type of solution does not change. This intuition is used when we compare the Gibbs free energy for different lattice solutions in Section 5.3.1.

Using Equation 5.39 and the data from Table 4.1 we give the estimated values of H_{C1} in Table 5.1. We note that the data from Table 4.1 was calculated on $\mathbb{R}^2$ with fixed boundary conditions but should serve as an approximate lower bound for H_{C1}.

α_S	H_{C1}
0.67	0.31
0.71	0.32
0.86	0.39

Table 5.1: Here we give the estimated values for H_{C1} using the formula in Equation 5.39 (truncated at $N = 2$) and the data from Table 4.1.

Finally, the value of H_{C2} is best calculated directly from the numerical simulations. Increasing H_0 from H_{C1} we eventually reach H_{C2} which is the first point where $\frac{\hat{G}_{T^2_\square}}{\mathcal{A}}$ first becomes greater than,

$$\frac{\hat{G}_{\text{normal state}}}{\mathcal{A}} = -F_p(u_1, u_2, \pm\frac{\pi}{2}) - \frac{H_0^2}{2} \ . \tag{5.40}$$

This is the point where the normal state becomes the minimum energy state. We reiterate that the normal state occurs when $(\partial_1^{\square} A_2^{\square} - \partial_2^{\square} A_1^{\square}) = \mathcal{A} H_0$ and $\psi_\alpha^{\square} = 0$.

5.2 Numerical Method

If we consider previous work, [44], we see that although they used periodic boundary conditions, they used a large unit cell area which they did not minimise. Additionally, they considered only rectangular unit cells which would be equivalent to fixing $\alpha = \frac{\pi}{2}$ for our general unit cell. The following method improves on this and is based upon, [38].
The method simultaneously minimises the field configuration, $(\psi_\alpha^{\square}, A_i^{\square})$, the shape of the unit cell, $\mathcal{M}$, and its area, $\mathcal{A}$. The field minimisation is performed using the same method as Section 4.2.1 except we use periodic boundary conditions. The domain is discretised as an $N_x \times N_x$ equally spaced grid with spacing, $h_x > 0$. The first and second partial derivatives are approximated by fourth order finite difference operators. We then use arrested Newton flow to move the fields from an initial configuration into a locally minimising configuration. The field minimisation part of the algorithm continues until every component of the gradient of the discretised energy is smaller than the user supplied numerical tolerance, tol. We note that we are minimising Equation 5.36 which differs from the free energy in a term that is only linear in the magnetic field. Thus the Ginzburg-Landau equations are unchanged from those in Equations 1.124 and 1.125. We use $N_x = 101$, $h_x = 0.01$ and $tol = 0.01$.
For every step of field minimisation we perform a step that minimises the lattice configuration and one that minimises the area. Noting that we hold the field configuration constant as well as the area and the lattice configuration for the lattice configuration and area minimisation steps of the algorithm respectively.
If we consider the Gibbs free energy we see that only the gradient term is dependent on $\mathcal{M}$, which gives the configuration of the unit cell. We define,

$$F_{grad} = \frac{1}{2} X^T P^C X \tag{5.41}$$

$$P^C_{ik,jl} := \int_{[0,1]^2} Q_{kl}^{\alpha\beta} (D_i^{\square} \psi_\alpha^{\square})^* (D_j^{\square} \psi_\beta^{\square}) \; dx_1^{\square} dx_2^{\square} \; , \tag{5.42}$$

where $X = (\mathcal{M}_{11}, \mathcal{M}_{12}, \mathcal{M}_{21}, \mathcal{M}_{22})^T$ and the pair of indices $(i,k),(j,l)$ can take any of the values $\{(1,1),(1,2),(2,1),(2,2)\}$. As $Q_{ij}^{\alpha\beta} = Q_{ji}^{\beta\alpha}$ we see that P^C is hermitian. Thus we decompose it into a symmetric and skew-symmetric matrix, $P^C = P + iP^i$, thus the real valued F_{grad} reduces down to,

$$F_{grad} = \frac{1}{2} X^T P X \; , \tag{5.43}$$

the problem can now be expressed as the minimisation of $X^T P X$ subject to the constraint that $\det \mathcal{M} = 1$. This can be written as,

$$\frac{1}{2} X^T J X = 1 \; , \tag{5.44}$$

where,

$$J = \begin{pmatrix} 0 & 0 & 0 & 1 \\ 0 & 0 & -1 & 0 \\ 0 & -1 & 0 & 0 \\ 1 & 0 & 0 & 0 \end{pmatrix} \; . \tag{5.45}$$

We search for critical solutions to F_{grad}, this requires $PX = \lambda JX$ so that $F_{grad} = \lambda$. This is simply the requirement that X is an eigenvector of JP,

$$JPX = \lambda X \ , \tag{5.46}$$

where we have used the fact that $J^2 = \mathrm{I}_4$. Now we can minimise F_{grad} with respect to $\mathcal{M}$ by constructing JP and finding its four eigenvectors, Y, but removing any complex solutions and any with $Y^T JY \leq 0$. The desired solution is $X = Y/\sqrt{Y^T JY}$ such that $F_{grad} = \lambda$. The new lattice configuration is read off as,

$$\mathcal{M} = \begin{pmatrix} X_{11} & X_{12} \\ X_{21} & X_{22} \end{pmatrix} \ . \tag{5.47}$$

Finally, we seek to minimise the unit cell area whilst holding the field and lattice configurations constant. This is done by differentiating the Gibbs free energy per unit area with respect to $\mathcal{A}$. To this purpose we define,

$$E_1 = \int_{[0,1]^2} \frac{1}{2} \tilde{Q}_{ij}^{\alpha\beta} (D_i^{\square} \psi_\alpha^{\square})^* (D_j^{\square} \psi_\beta^{\square}) \ dx_1^{\square} dx_2^{\square} \tag{5.48}$$

$$E_2 = \int_{[0,1]^2} (\partial_1^{\square} A_2^{\square} - \partial_2^{\square} A_1^{\square})^2 \ dx_1^{\square} dx_2^{\square} \tag{5.49}$$

$$E_3 = H_0 \int_{[0,1]^2} (\partial_1^{\square} A_2^{\square} - \partial_2^{\square} A_1^{\square}) \ dx_1^{\square} dx_2^{\square} \ , \tag{5.50}$$

and then solve the following equation,

$$\frac{\partial}{\partial \mathcal{A}} \frac{\hat{G}_{T^2_{\square} 2}}{\mathcal{A}} \bigg|_{\mathcal{A}=\mathcal{A}_{min}} = 0 \tag{5.51}$$

$$\frac{-1}{\mathcal{A}_{min}^2} (E_1 - E_3) + \frac{-1}{\mathcal{A}_{min}^3} E_2 = 0 \ . \tag{5.52}$$

We find the minimum area, for a given field and unit cell configuration as,

$$\mathcal{A}_{min} = \frac{E_2}{E_3 - E_1} \ . \tag{5.53}$$

We then set $\mathcal{A} = \mathcal{A}_{min}$ and the restart the minimisation process.
We note that the area minimisation is only valid in the range $H_{C1} < H_0 < H_{C2}$, where $H = H_0 \hat{x}_3$. For $H_0 < H_{C1}$ the area tends towards infinity as the homogenous superconducting state is the minimising solution in this region of H_0. For $H_0 > H_{C2}$ the area tends towards zero but the numerical algorithm, appears to, return non singular answers.
Thus we estimate the range for $H_{C1} < H_0 < H_{C2}$ and then run the algorithm in this range. We take the estimates of H_{C1} given in Table 4.1 as the lower bound, a and choose the upper bound $b = 6$ based on typical values in other models, [38]. We note that the estimated value of H_{C1} for $\alpha_s = 0.86$ was too low, hence we used $a = 0.45$ for those simulations. We later reran all simulation from $H_0 = [6, 8]$ to allow us to calculate the value of H_{C2}.
We choose a lower and upper bound, $[a, b]$, and number of points that we want to trial. We start at the midpoint, $\frac{a+b}{2}$, then run the ranges $[\frac{a+b}{2}, b]$, $[a, \frac{a+b}{2}]$ independently such that the solutions for H_0 closer to H_{C2} and H_{C1}, which could become singular and therefore the algorithm will not converge, get run last. Further, we choose an initial lattice configuration

that is neither of the standard configurations,

$$\text{square unit cell}: \quad \frac{|v_1|}{|v_2|} = 1, \alpha = \frac{\pi}{2} \tag{5.54}$$

$$\text{hexagonal unit cell}: \quad \frac{|v_1|}{|v_2|} = 1, \alpha = \frac{\pi}{3} \ . \tag{5.55}$$

This should mean that the algorithm is not biased to either of these two special configurations. To summarise the algorithm proceeds as follows,

- For a given $H_0 \in [a, b]$, where $[a, b]$ is chosen in relation to estimated values of the critical fields.
- Choose an initial field and lattice configuration.
- Perform one step of arrested Newton flow, whilst holding the lattice configuration and $\mathcal{A}$ constant.
- Calculate the new value of $\mathcal{M}$ using Equation 5.47. The field configuration is fixed to the newly evolved values and $\mathcal{A}$ is kept constant.
- Calculate the new value of $\mathcal{A}$ using Equation 5.53. The field and lattice configurations are kept constant.

5.3 Numerical Results

Here we analyse how the energy and lattice configuration varies with the applied magnetic field, $H = H_0\hat{x}_3$. Importantly, we see that for all values of α_s and H_0 sampled we do not get the standard hexagonal (Abrikosov) lattice configuration of $\alpha = \frac{\pi}{3}$ but values of $\alpha \in (\frac{\pi}{3}, \frac{\pi}{2})$. Furthermore, we see that for, $\alpha_s = 0.86$, $\mathbb{C}P^1$ skyrmion solutions with a winding number, $N = 2$, give the lowest Gibbs free energy per unit area. However, $\alpha_s = 0.67$ and $\alpha_s = 0.71$, do not give $\mathbb{C}P^1$ skyrmion solutions and have $N = 1$ as the winding number than minimises the energy. For notational simplicity we define,

$$G/A := \frac{\hat{G}_{T^2_\square}}{\mathcal{A}} \ , \tag{5.56}$$

as the Gibbs free energy (normalised with respect to the homogenous superconducting state) per unit area.

5.3.1 Magnetisation

In this section we consider how changing the applied magnetic field, or magnetising our $s+id$ superconductor, affects the Gibbs free energy and lattice configuration. We also calculate values for H_{C1} and H_{C2} where the lower critical field is close to our original estimates given in Table 4.1.
Consider Figure 5.2, for the chosen ranges of H_0 values, which differ slightly as the critical field values depend on α_s and the chosen ranges are inside of $[H_{C1}, H_{C2}]$. We used the estimated values for H_{C1} from Table 5.1 as lower bound of H_0 for our simulations with the exception of $\alpha_s = 0.86$ where the estimation proved less than the true value of H_{C1}. In this case we picked $H_0 = 0.45$ as the starting point. We see that G/A is less than zero meaning all values of $H_0 > H_{C1}$. We note that G_N/A is the value of G/A for the winding number N.

If we consider the nested plot for each value of α_s, we see that in all but the $\alpha_s = 0.86$ case the difference in the values of G/A is very small. This difference is shown in more detail in

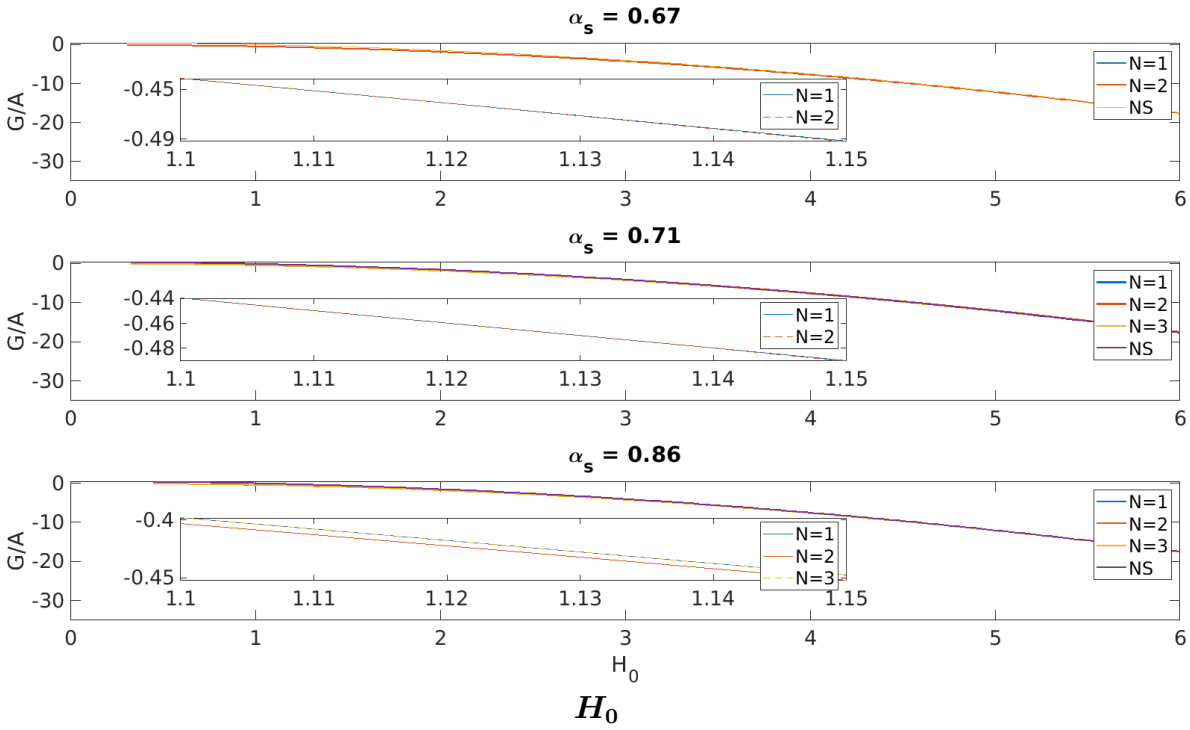

Figure 5.2: *Plots of the Gibbs free energy normalised with respect to the homogenous superconducting state per unit area, G/A, versus the applied magnetic field strength H_0, for different α_s and winding numbers N. $G/A = \frac{\hat{G}_{T^2_\square}}{\mathcal{A}}$ and is normalised with respect to the homogenous superconducting state thus as $G/A < 0$ that means H_0 is always greater than H_{C1}. We compare G/A for different values of N to see if their energies differ and therefore the value of N that gives the lower value of G/A.*

Figure 5.3: only in the $\alpha_s = 0.86$ case does G_2/A differ substantially from G_1/A. Note that the values of G_N/A are the most different for low H_0 and as $H_0 \to 6$ the difference between G_N/A, for different α_s, is negligible. If we consider the values in Table 4.1 we suggest that only when the percentage difference is greater than 0.5% do we consider the energies to be different. The percentage difference is given by,

$$pcd_N = \frac{(G_N/A - G_1/A)}{G_1/A}\% \ . \tag{5.57}$$

Additionally, in Section 5.3.2 we see that the difference in energy does not correspond to a marked difference in the solutions. For example comparing Figures 5.7a and 5.8 which show the fields for $N = 1$ and $N = 2$. From this we can conclude that $N = 1$ is the winding number that gives the minimal value of G/A except in the case of $\alpha_s = 0.86$ where it is $N = 2$. This is due to the existence of $\mathbb{C}P^1$ skyrmions for H_0 close to H_{C1} as we will show in Section 5.3.2. We note that we include $N = 3$ for $\alpha_s = 0.86$ to show that this energy is not lower. Furthermore, as $H_0 \to 6$ we see that $pcd_N \to 0$ showing that the $N = 1$ and $N = 2$ solutions become energetically the same.

We can also look at how the value of α and the values of $|v_1|$ and $|v_2|$ change in relation to H_0. This demonstrates any changes in the configuration of the unit cell that occur. This is depicted in Figures 5.4a5.4b. In the case of α, for all bar $N = 2$, $\alpha_s = 0.86$, it holds at approximately the same value in between $[\frac{\pi}{2}, \frac{\pi}{3}]$. In the case of $\alpha_s = 0.86$ there is a change in

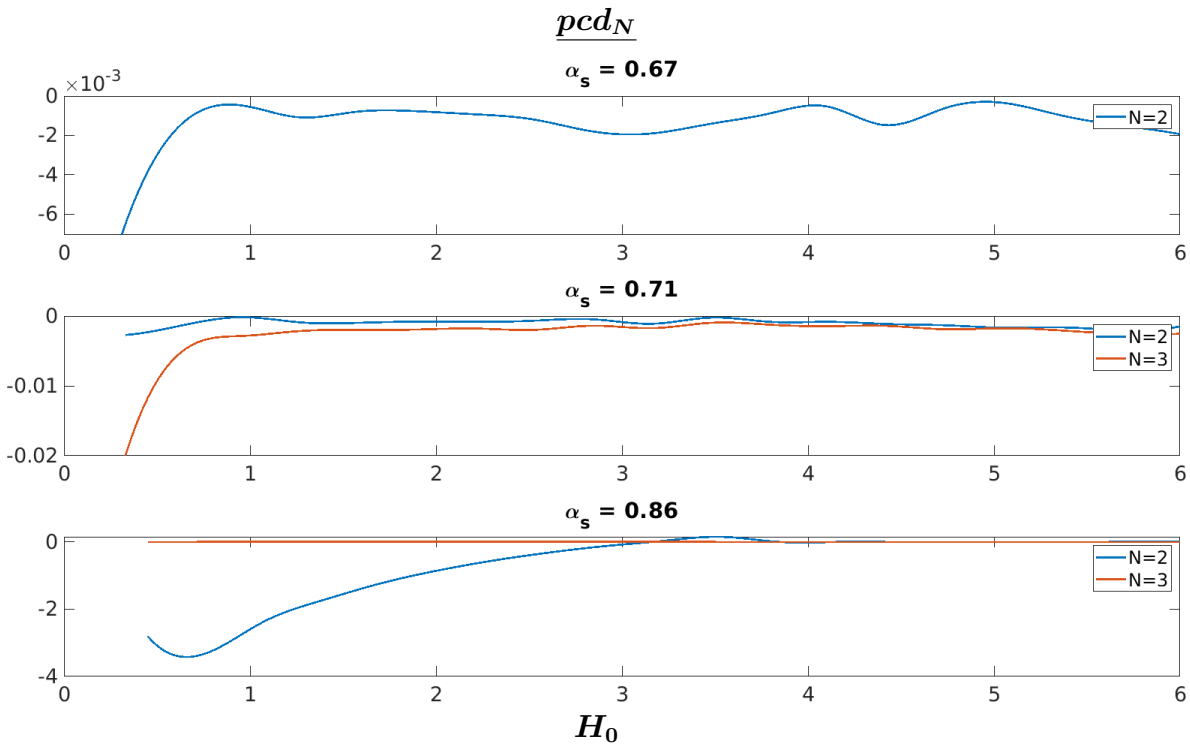

Figure 5.3: *Percentage difference between the values* $G/A = \frac{\hat{G}_{T^2\square}}{\mathcal{A}}$ *for all the simulated values of* N*. The percentage difference is given by,* $pcd_N = \frac{(G_N/A - G_1/A)}{G_1/A}\%$*. We see that apart from, the* $N = 2$ *case for* $\alpha_s = 0.86$*, the percentage difference in energies is less than* 0.5% *and so is considered negligible. We note that* G_N/A *is the value of the Gibbs free energy (normalised with respect to the homogenous superconducting) state per unit area for a winding number of* N*.*

both α and $|v_1|, |v_2|$ that mark the transition from a $(2,2)$ $\mathbb{C}P^1$ skyrmion solution to a $(4-2,2)$ vortex solution. We note that the configuration changes from being nearly rectangular, $\alpha = \frac{\pi}{2}$, to being nearly hexagonal, $\alpha = \frac{\pi}{3}$, as all of the other parameters are. This transition can be seen in Figures 5.9a, 5.9b and 5.9c which is discussed in more detail in Section 5.3.2. We note that $|v_1|, |v_2|$ have been normalised by a factor of $\frac{1}{\sqrt{\mathcal{A}}}$.

Finally, if we consider Figure 5.5, which only shows the plots for the winding numbers that give the minimum G/A. If we consider the nested plots which show the difference between G/A and G_{norm}/A we note that value of H_0 for the x-intercept gives the value of H_{C2} which we can read off. This is because at the point where the vortex state transitions to the normal state the energies of these two states will be equivalent.

We use this data to extrapolate and find the values of the critical fields. In the case of H_{C1} we are so close to the boundary that further simulation runs are likely to run into the issue where the area of the unit cell $\mathcal{A} \to \infty$ as the system seeks to become the homogenous superconducting state everywhere. Hence the need to extrapolate. In the case of H_{C2} we find that the numerical algorithm works on both sides of H_{C2} hence we can find this value to more accuracy using linear interpolation. These values are given in Table 5.2.

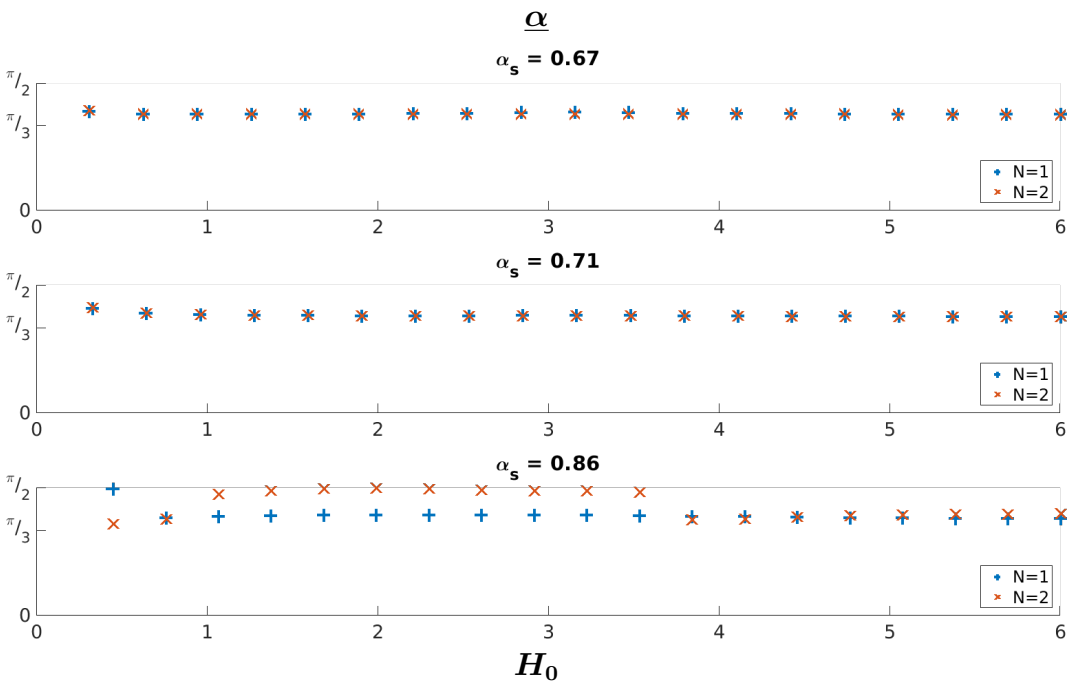

(a) α,*the internal angle of the unit cell, against* H_0.

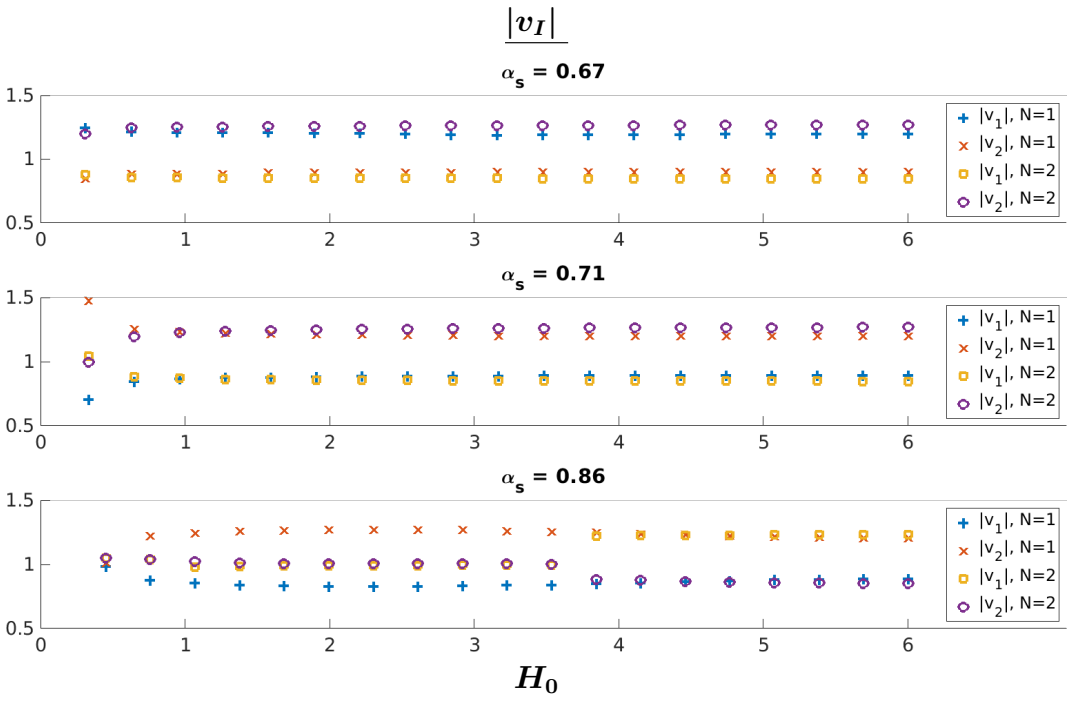

(b) $|v_1|, |v_2|$,*the length of opposite sides of the unit cell, against* H_0. *Note that,* $|v_1|, |v_2|$, *have been scaled by a factor of* $\frac{1}{\sqrt{\mathcal{A}}}$.

Figure 5.4: *Plots of the lattice parameters,* $\alpha, |v_1|, |v_2|$, *versus the external magnetic field,* H_0. *We see that, excepting the value of* H_0 *closest to* H_{C1}, α *takes the same constant value regardless of* H_0 *except in the* $N = 2, \alpha_s = 0.86$ *case. We focus on the region* $H_0 = (H_{C1}, 6]$, *note that the unit cell does not change shape in the region* $H_0 = [6, 8]$.

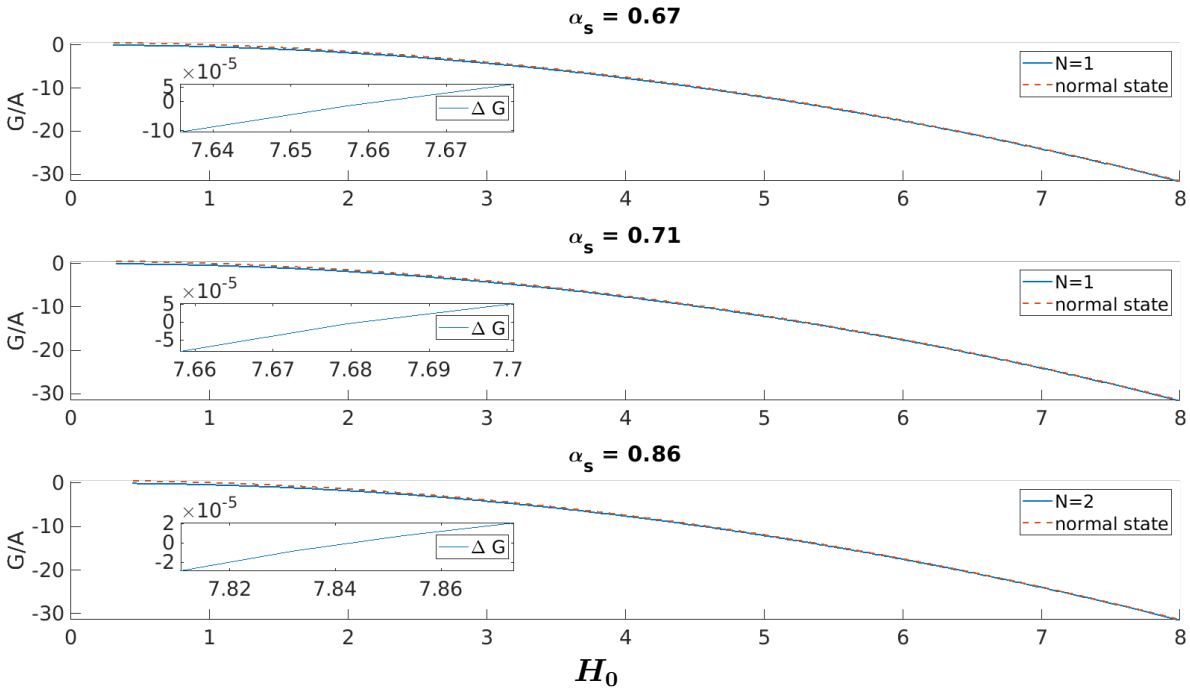

Figure 5.5: *Plots of G/A versus the applied magnetic field strength H_0 for the winding number, N, that gives the lowest value of G/A for a given value of α_s. $G/A = \frac{\hat{G}_{T^2_\square}}{\mathcal{A}}$ and we have added in the range $H_0 \in [6, 8]$, to the results from Figure 5.2. This allows us to find H_{C2} where we note that there is no change in type of solution in range $H_0 \in [6, 8]$, for any α_s. Note that we plot the difference $\Delta G = G/A - G_{norm}/A$ in the zoomed in window where $\Delta G = 0$ denotes the point when $H_0 = H_{C2}$.*

5.3.2 Lattice Solutions

Here we present the visualisation of the lattice solutions for the values of the winding numbers that we have determined do minimise G/A. Note that as the range for H_0 is large, the values of the fields vary hugely as well. This means we use different colour scales throughout which allows us to demonstrate some of the finer details present for the field solution for each value of H_0. Furthermore, we see that for the parameter range $\alpha_s = 0.71$ we do not see $\mathbb{C}P^1$ skyrmion solutions even for H_0 close to H_{C1}, this differs from [44] (and our work in Chapter 4) who find skyrmion solutions in this parameter range of the model. We focus on the three values of $\alpha_s = (0.67, 0.71, 0.86)$, as we did in Chapter 4. Additionally, we use the same naming convention as in Chapter 4, namely for each unit cell we label the total winding number of the zeros and anti zeros of ψ_1 and ψ_2 as $n_{1v}, n_{1av}, n_{2v}, n_{2av}$ respectively. Then we choose to

α_s	H_{C1}	H_{C2}
0.67	0.30	7.66
0.71	0.31	7.68
0.86	0.43	7.83

Table 5.2: The extrapolated values for H_{C1} and H_{C2}, we note the concordance with the values in Table 5.1. We used linear interpolation of the last two data points to $H_0 = 0.2$ to extrapolate a value of H_{C1}. We read off H_{C2} from Figure 5.5.

name our solutions as a $(n_{1v} + n_{1av}, n_{2v} + n_{2av})$ vortex or skyrmion.

$\alpha_s = 0.67$

Figures 5.6a, 5.6b and 5.6c show the lattice solutions for $N = 1$ for $\alpha_s = 0.67$. We see that as expected the area of the unit cell decrease with H_0 and the values of the condensates move towards their vacuum values, whilst the magnetic field approaches H_0. We do not include plots of the $N = 2$ solutions (which have $G_2/A \approx G_1/A$) the unit cell of which is approximately the same as two $N = 1$ unit cells. Although, the unit cell has slightly different values of α, as shown in Figure 5.4a, but this is likely down to numerical error.

$\alpha_s = 0.71$

Here we show lattice solutions for the $N = 1$ case, given in Figures 5.7a, 5.7b and 5.7c.

The $N = 1$ case is very similar to the $\alpha_s = 0.71$ case except with a different unit cell configuration.
We note that the $N = 2$ solution is also a $(2N - N, N)$ vortex except with a different unit cell shape as shown in Figure 5.4a. Interestingly this means that when we allow both the area and the configuration of the unit cell to be minimised $(2, 2)$ $\mathbb{C}P^1$ skyrmion solutions do not appear as they do in [44]. This is shown in Figure 5.8, where even for H_0 close to H_{C1}, we do not find $(2, 2)$ $\mathbb{C}P^1$ skyrmion solutions that are of lower energy than the $(4 - 2, 2)$ vortex solution.

$\alpha_s = 0.86$

Finally, and most interestingly we consider the $N = 2$ case which is the minimum winding number for $\alpha_s = 0.86$. This is because $\mathbb{C}P^1$ skyrmion solutions are present. Figures 5.9a, 5.9b and 5.9a show that for low, $H_0 < 3.5$, $\mathbb{C}P^1$ skyrmions appear with the distinctive pattern of the magnetic field that we recognised from Chapter 4. However, as H_0 increases both $|\psi_\alpha|$ decrease in value and, in keeping with the other two parameters, the value of $|\psi_1|$ decreases faster than $|\psi_2|$ this leads to the more standard $(4 - 2, 2)$ vortex appearing for $H_0 > 3.5$. At this point the solution for $\alpha_s = 0.86$ is barely distinguishable from solutions for the other two values of α_s. We also see a notable change in the phase difference as well as the unit cell shape, which we noted in Figure 5.4a.

We see for $N = 1$, Figure 5.10, we get a $(1, 1)$ vortex solution, this matches the results from Chapter 4. More interestingly this solution is only energetically favourable for low H_0 but as we increase H_0, and we see $|\psi_1|$ decreases relative to $|\psi_2|$, the common solution of a $(2N-N, N)$ vortex solution becomes the minimising solution of the Gibbs free energy per unit area. This becomes a trend where regardless of α_s and N for large H_0 we see a $(2N - N, N)$ vortex solution emerge. This occurs because one of the condensates approaches zero much faster than the other meaning their relatives sizes allow the formation of this solution as H_0 approaches H_{C2}.
Note that the point that H_0 becomes large can be see in Figure 5.4a where there is a change in the value of α for $H_0 \approx 3.5$ for $N = 2, \alpha_s = 0.86$.

Lattice solutions for $\alpha_s = 0.67, N = 1$ for varying values of H_0.

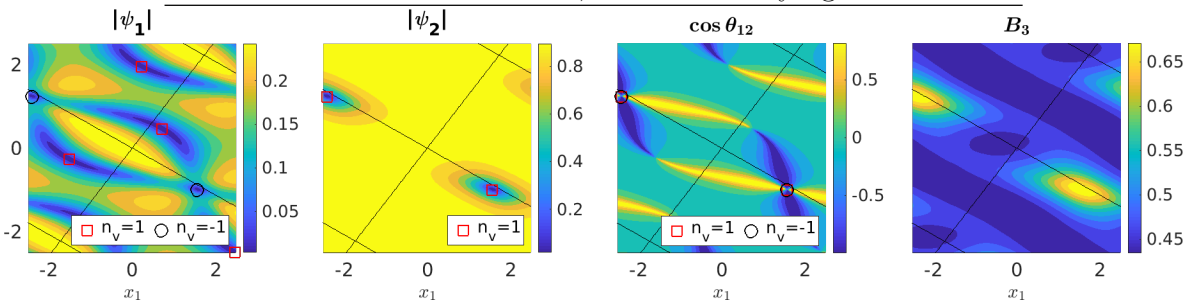

(a) *A* $(2-1,1)$ *vortex with* $\alpha_s = 0.67$, $H_0 = 0.626$ *lattice solution.*

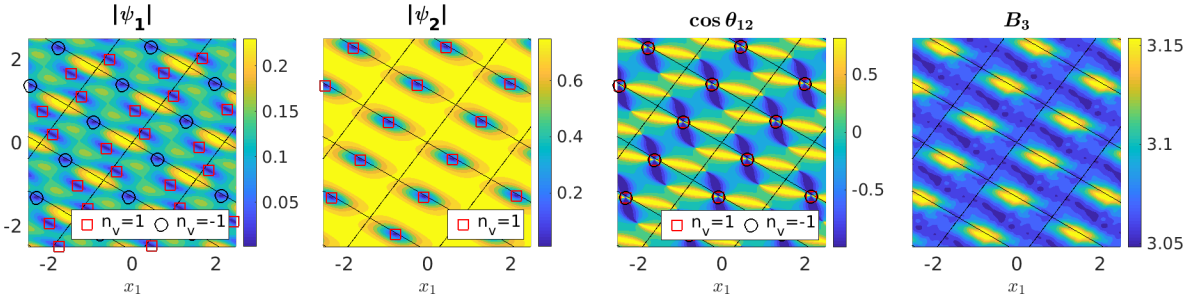

(b) *A* $(2-1,1)$ *vortex with* $\alpha_s = 0.67$, $H_0 = 3.16$ *lattice solution.*

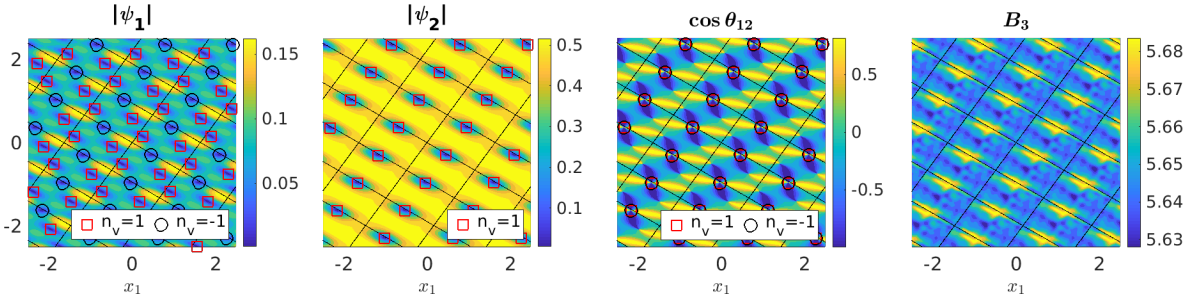

(c) *A* $(2-1,1)$ *vortex with* $\alpha_s = 0.67$, $H_0 = 5.68$ *lattice solution.*

Figure 5.6: *Plots of the gauge invariant quantities of the fields, with* $N = 1, \alpha_s = 0.67$, *for three different values of* H_0. *Figure 5.6a is close to* $H_{C1} = 0.30$ *and Figure 5.6c is closer to* $H_{C2} = 7.66$. *We see that the type of solution, a* $(2-1,1)$ *vortex, does not change with* H_0 *but the values of* $|\psi_\alpha|$ *tend towards zero and the magnetic field approaches* H_0 *everywhere. The points,* □ *and* ○, *on* $|\psi_1|, |\psi_2|$ *and* $\cos\theta_{12}$ *show the location and multiplicity of the zeros in the* ψ_1, ψ_2 *condensates and the coincident zeros respectively.*
For each condensate $\sum n_v = N$ *and* B_1 *and* B_2 *vanish everywhere.*

5.4 Summary

We have shown that when we consider vortex lattice solutions (in the basal plane) for anisotropic multicomponent Ginzburg-Landau theory we still see the novel types of field solutions as we did in Chapter 4. Considering the shape of the unit cell for these lattice solutions, we see that the hexagonal unit cell is no longer the configuration that minimises the Gibbs free energy as it is in an isotropic superconductor. Furthermore, the winding number, N, that produces the unit cell and field configuration that gives the lowest Gibbs free energy is

Lattice solutions for $\alpha_s = 0.71, N = 1$ for varying values of H_0.

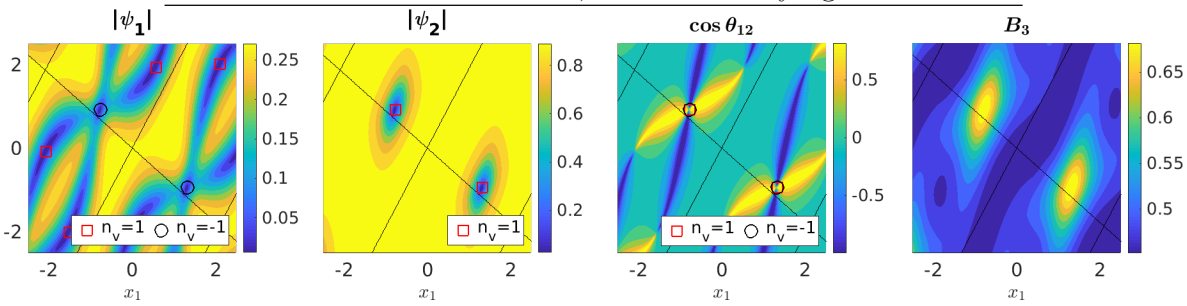

(a) *A* $(2-1,1)$ *vortex with* $\alpha_s = 0.71$, $H_0 = 0.645$ *lattice solution.*

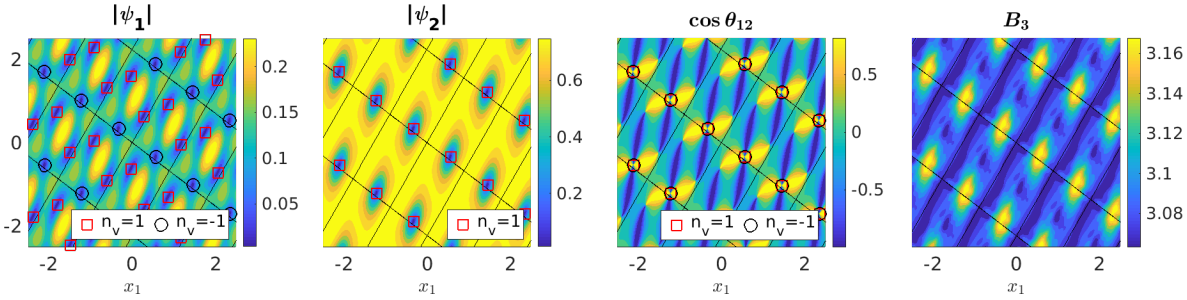

(b) *A* $(2-1,1)$ *vortex with* $\alpha_s = 0.71$, $H_0 = 3.17$ *lattice solution.*

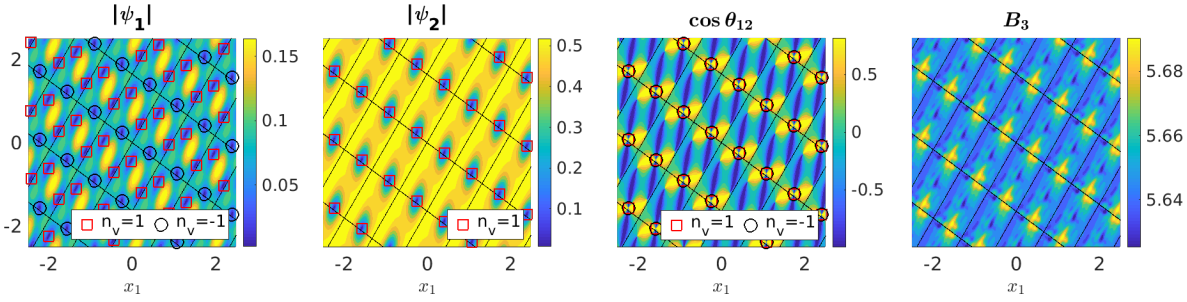

(c) *A* $(2-1,1)$ *vortex with* $\alpha_s = 0.71$, $H_0 = 5.69$ *lattice solution.*

Figure 5.7: *Plots of the gauge invariant quantities of the fields,* $N = 1, \alpha_s = 0.71$*, for three different values of* H_0*. Figure 5.7a is close to* $H_{C1} = 0.31$ *and Figure 5.7c is closer to* $H_{C2} = 7.68$*. We see that the type of solution, a* $(2-1,1)$ *vortex, does not change with* H_0 *but the values of* $|\psi_\alpha|$ *tend towards zero and the magnetic field approaches* H_0 *everywhere. The points,* □ *and* ○*, on* $|\psi_1|, |\psi_2|$ *and* $\cos\theta_{12}$ *show the location and multiplicity of the zeros in the* ψ_1*,* ψ_2 *condensates and the coincident zeros respectively.*
For each condensate $\sum n_v = N$ *and* B_1 *and* B_2 *vanish everywhere.*

usually $N = 1$. The exception is for parameters where $\mathbb{C}P^1$ skyrmions form for $N = 2$ and in this case the Gibbs free energy is lowest for $N = 2$. These skyrmions are only solutions of the Gibbs free energy for an external magnetic field strength, H_0, close to the lower critical field. As H_0 increases we no longer see $\mathbb{C}P^1$ skyrmions as the minimising field configurations. However, field configurations become very similar, regardless of the value of α_s, as H_0 approaches H_{C2}. Finally, we calculate the values of the lower and upper critical fields for the basal plane orientation.

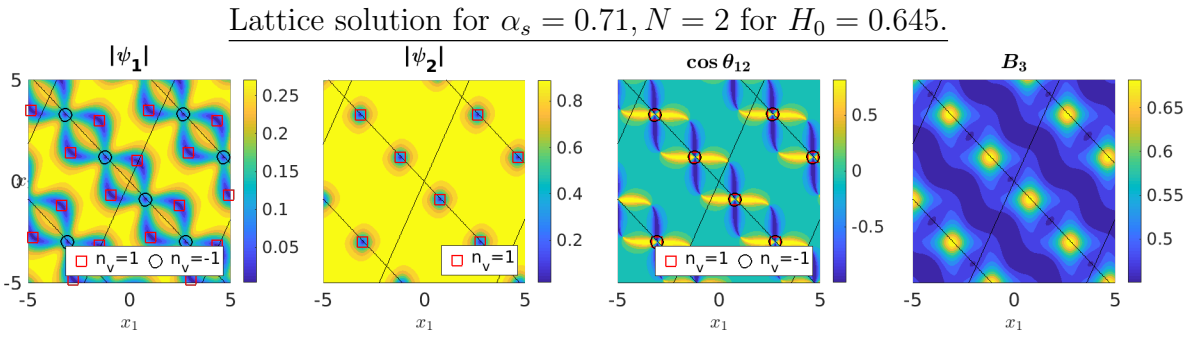

Figure 5.8: *Plots of the gauge invariant quantities of the fields, $N = 2$ $\alpha_s = 0.71$, for $H_0 = 0.645$. We see that it is not a $\mathbb{C}P^1$ skyrmion but a $(4-2,2)$ vortex solution as we would expect from the results of Chapter 4. We have doubled the range, $x_1, x_2 \in [-5,5]$, so this lattice solution can be properly seen. The points, □ and ○, on $|\psi_1|, |\psi_2|$ and $\cos\theta_{12}$ show the location and multiplicity of the zeros in the ψ_1, ψ_2 condensates and the coincident zeros respectively.*
For each condensate $\sum n_v = N$ and B_1 and B_2 vanish everywhere.

Lattice solution for $\alpha_s = 0.86, N = 2$ for varying values of H_0.

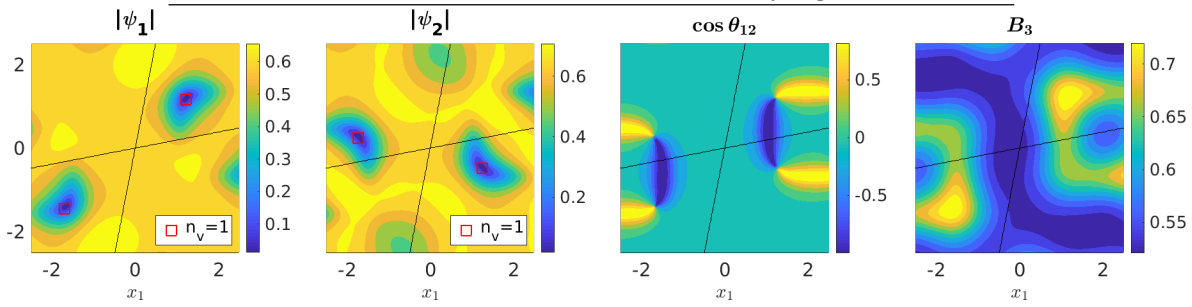

(a) *A* $(2,2)$ $\mathbb{C}P^1$ *skyrmion with* $\alpha_s = 0.86$, $H_0 = 0.758$ *lattice solution.*

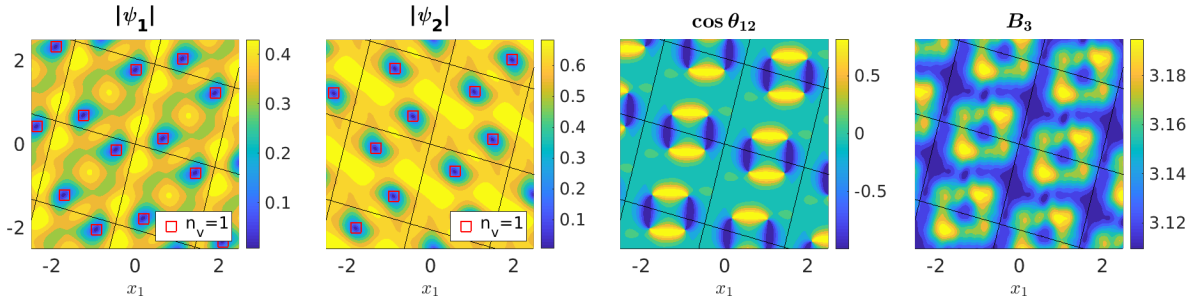

(b) *A* $(2,2)$ $\mathbb{C}P^1$ *skyrmion with* $\alpha_s = 0.86$, $H_0 = 3.23$ *lattice solution.*

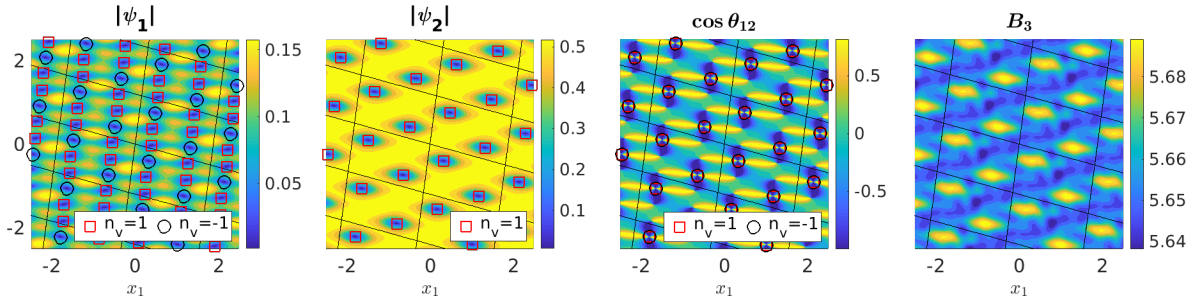

(c) *A* $(4-2,2)$ *vortex with* $\alpha_s = 0.86$, $H_0 = 5.69$ *lattice solution.*

Figure 5.9: *Plots of the gauge invariant quantities of the fields,* $N = 2, \alpha_s = 0.86$, *for three different values of* H_0. *Figure 5.7a is close to* $H_{C1} = 0.43$ *and Figure 5.7c is closer to* $H_{C2} = 7.83$. *We see that the type of solution changes with* H_0, *moving from a* $(2,2)$ $\mathbb{C}P^1$ *skyrmion to a* $(4-2,2)$ *vortex. Additionally, the values of* $|\psi_\alpha|$ *tend towards zero and the magnetic field approaches* H_0 *everywhere. The points,* □ *and* ○, *on* $|\psi_1|, |\psi_2|$ *and* $\cos\theta_{12}$ *show the location and multiplicity of the zeros in the* ψ_1, ψ_2 *condensates and the coincident zeros respectively.*
For each condensate $\sum n_v = N$ *and* B_1 *and* B_2 *vanish everywhere.*

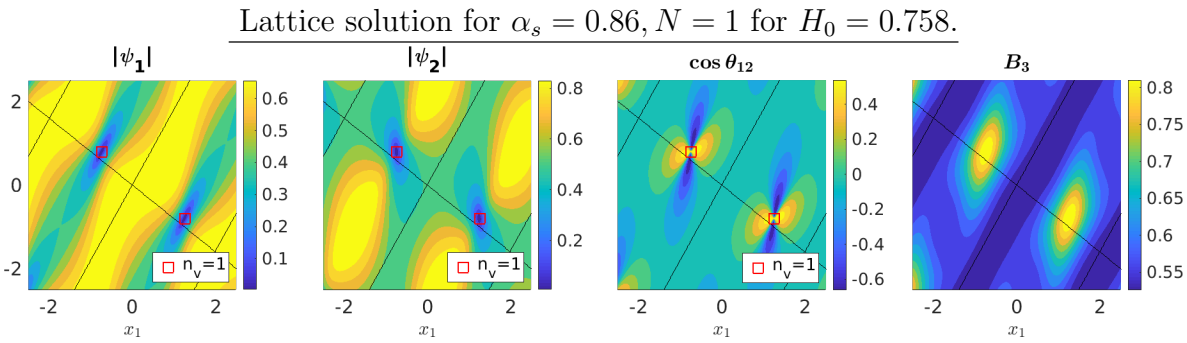

Figure 5.10: *Plots of the gauge invariant quantities of the fields, for a* $(1,1)$ *vortex with* $N = 1, \alpha_s = 0.86$*, for* $H_0 = 0.758$*. We see that unlike the* $N = 2$ *we have only a vortex lattice state not a* $\mathbb{C}P^1$ *skyrmion. The points,* □ *and* ○*, on* $|\psi_1|, |\psi_2|$ *and* $\cos\theta_{12}$ *show the location and multiplicity of the zeros in the* ψ_1*,* ψ_2 *condensates and the coincident zeros respectively. For each condensate* $\sum n_v = N$ *and* B_1 *and* B_2 *vanish everywhere.*

Chapter 6

Conclusions and Key Results

In this thesis, we consider one and two-dimensional topological soliton solutions in three-dimensional multicomponent anisotropic superconductors. For conventional isotropic superconductors an ansatz where the magnetic field direction is fixed is used. However, when anisotropy is considered this ansatz is no longer valid as solutions of the resulting Ginzburg-Landau equations are not, in general, solutions of the full three-dimensional Ginzburg-Landau equations. Thus we would describe the ansatz as inconsistent. We use an ansatz that does not fix the direction of the magnetic field and is therefore consistent with the full Ginzburg-Landau equations. Furthermore, changing the orientation of the one and two dimensional solitons within the anisotropic three-dimensional superconductor can change the physical properties of the superconductor such as the magnetic field. Finally, this ansatz introduces the possibility of magnetic field twisting. This is where the direction of the magnetic field changes moving away from the centre of the soliton.

Key Result: By using an ansatz that does not fix the direction of the magnetic field we can study magnetic field twisting in anisotropic superconductors as well as how solutions of the Ginzburg-Landau equations depend on orientation.

In Chapter 2 we explored domain wall solutions in anisotropic superconductors. We linearised the Ginzburg-Landau equations and found solutions of the form, $c_i\vec{v}_i e^{-\mu_i x_1}$. The key difference in the anisotropic case is that the length scales, $\lambda_i = \frac{1}{\mu_i}$, are complex in general. Thus for some orientations and anisotropies we expect oscillatory decaying field solutions. Additionally, domain walls in anisotropic superconductors can produce a spontaneous magnetic field for some orientations. This could potentially provide experimentalists with a way to distinguish between superconductor types. We study $p+ip$, $s+is$ and $s+id$ superconductors and their magnetic properties using our revised ansatz.

Key Result: Oscillatory decay can occur in the fields of domain wall solutions in the $p+ip$ model but not in the $s+is$ and $s+id$, as predicted by solutions to the linearised Ginzburg-Landau equations.

Key Result: We demonstrate the dependence of the spontaneous magnetic field on the full set of orientations, $\hat{x}_1 \in S^2$, for the $p+ip$, $s+is$ and $s+id$ models. There exist orientations where only one model has a non zero spontaneous magnetic field, from this it is theoretically

possible for experimentalists to determine what type of superconductor a given material is.

Key Result: Magnetic field twisting occurs in $p + ip$ superconductors. The magnetic field is not constant but oscillates between a maximum value and no magnetic field twisting.

In the, more general, $s+is$ and $s+id$ models we found a new type of domain wall that is non degenerate in energy and is determined from the direction the phase difference interpolates between antipodal points, clockwise or anticlockwise, [2]. We found magnetic field twisting occurs only in the $s + id$ model.

Key Result: $s+is$ and $s+id$ superconductors exhibit two types of non degenerate in energy domain walls solutions distinguished by the phase difference between the two condensates.

Key Result: Magnetic field twisting occurs in $s+id$ but not $s+is$ superconductors. Unlike the $p + ip$ case it does not oscillate.

In Chapter 3 we explored the Meissner state in $s + is$ and $s + id$ superconductors. In the isotropic case it is only the strength of the external magnetic field, H, that will affect the field configurations that solve the Ginzburg-Landau equations. However, in $s + is$ and $s + id$ superconductors the direction of the externally applied magnetic field will affect the field configurations. This can lead to the magnetic field twisting away from the direction of the applied magnetic field. Furthermore, by considering the linearisation it is possible to predict in what direction H must point in order to cause magnetic field twisting.

Key Result: Magnetic field twisting occurs in the Meissner state for $s + is$ and $s + id$ superconductors, depending on the direction of the externally applied magnetic field.

In Chapter 4 we studied two-dimensional topological solitons, namely vortices. We extended previous results, [44], to all possible orientations, $\hat{x}_3 \in S^2$. We also observed a small, but non negligible, twisting of the magnetic field for both $s+id$ and $s+is$ vortex solutions that occurs away from the basal plane and regardless of parameter choice. Finally, we have classified the solutions of this model up to a winding number of $N = 2$. Though we note that for $N > 2$ the solutions studied appeared to be combinations of $N = 1$ and $N = 2$ solutions.

Key Result: Vortex solutions in $s+id$ and $s+is$ superconductors are studied and classified.

Key Result: Magnetic field twisting occurs, away from the basal plane orientation, for vortices in both $s + is$ and $s + id$ superconductors contrasting the results in domain walls.

In Chapter 5 we studied vortex lattice solutions in the $s + id$ case for the basal plane only. By applying a constant external magnetic field we saw how varying the field strength affected vortex lattice unit cell and field configurations. We improved upon previous methods by considering non rectangular unit cells and allowing the area of the unit cell to be minimised, using the procedure from [38]. We found the values of the lower and upper critical fields.

Key Result: The upper and lower critical field values for lattice solutions in the basal plane of an $s + id$ superconductor were determined.

Key Result: The shape of unit cell and how it changes with the strength of the applied magnetic field are calculated.

6.1 Future Work

In summary much of the work we have done is the qualitative classification of properties of unconventional superconductors. This is theoretically useful and, especially when comparing maximum magnetic fields, could provide a useful way for experimentalists to identify the type of unconventional superconductivity that a given sample exhibits. Below we explore natural extensions to the thesis.

- Microscopically deriving three-dimensional versions of $s + is, s + id, p + ip$ in order to obtain bounds on the values of the $Q_{3j}^{\alpha\beta}$ components in order to more closely match experimental results, similarly to [28] where the relative sizes of the 3 band anisotropy coefficients are calculated. We note that the $Q_{3j}^{\alpha\beta}$ parameter values used throughout this thesis, k_5 in Chapter 2 and μ in Chapter 4, were chosen so that the model displayed the correct symmetries and that the energy was positive definite.
- Chapter 3 can be extended to consider the $p + ip$ case adding to the work of [37] but using Ansatz 2.14 to allow us to explore orientations that are not in the basal plane. This should allow us to see magnetic field twisting, which does not occur in the basal plane, as well as oscillatory decay most likely in a similar manner to that in Section 2.4.5.
- A larger extension to Chapter 4 would be to consider how the choice of α_s and the values of $Q_{ij}^{\alpha\beta}$ affect the intervortex forces and at what point they are repulsive or attractive. We can already see that, by changing the parameter α_s, a vortex solution can become energetically favourable over a $\mathbb{C}P^1$ skyrmion solution. Moving from a field configuration where we have coincident zeros to one where no zeros coincide is likely to depend on intervortex forces between condensates. A way to understand this is to consider the binding energy of solutions for varying winding numbers, N, then exploring how changing parameters and orientation affects the binding energy would be a good starting point.
- We note that the concept of an intervortex force is not obviously defined even in the isotropic multicomponent case. In the single component case you would fix the position of two zeros in the condensate and then solve the corresponding constrained minimisation problem in order to calculate the intervortex forces. However, when we have multiple condensates the zeros do **not** have to coincide. In this case we can consider the force between zeros in the same and in different condensates.

- Previously the intervortex forces have been calculated, in the single component isotropic case, by approximating the asymptotic behaviour of a vortex by linearising the Ginzburg-Landau equations in the radial direction. Then by calculating the interaction potential between two well separated vortices the intervortex forces can be calculated [48]. As anisotropy breaks the rotational invariance of the problem a linearisation that includes the radial and angular dependence of the fields would be needed. This is a very difficult theoretical problem. One such way of proceeding might be to write the fields as a radial and spherical harmonic part and then to try to linearise the Ginzburg-Landau equations about the vacuum values of the fields.

- For Chapter 5 an obvious extension is to consider the $s+id$ case not in the basal plane in the same manner as Chapter 4. We could then consider the twisting of the magnetic field away from the direction of applied external magnetic field. Additionally, the dependence of H_{C1} and H_{C2} on orientation could be found. Furthermore, studying the $s+is$ case can be done, though when considering the results of Chapter 4 it is unlikely that anything other than (N, N) vortex solutions will appear. However, looking at unit cell shape and critical magnetic field might be of interest.

- Furthermore, using the method of Chapters 4 and 5 for the $p + ip$ case for non basal plane orientations can be done. Similarly to above, classifying the types of solutions, determining the critical field, studying magnetic field twisting as well as unit cell shape could also be of interest.

- Finally, for all of the types of superconductors studied we can look at the so called isoperimetric problem. We consider embedding a plane in $\mathbb{R}^3$ with the plane's boundaries fixed to one vacuum. We start with a circular domain wall (or bubble) at the centre of the plane which separates the vacuum on the boundary from the other (gauge inequivalent) vacuum at the centre of the plane. We note that the solution of the Ginzburg-Landau equations would simply be the homogenous superconducting state. That is this bubble would collapse. However, if we use the area preserving gradient flow method, as detailed in [49]. This allows us to minimise the free energy whilst keeping the area of the bubble constant. We can then explore the shape of the domain wall bubble that minimises the free energy for all three models, $s + is, s + id, p + ip$, and how this changes with orientation. In general we do not know what shape the bubble will take. Additionally, the magnetic response would differ with orientation and superconductor type. This could be extended to a three-dimensional bubble embedded in $\mathbb{R}^3$.

Appendices

Appendix A

Parameters Used

A.1 Parameters used for an Isotropic Superconductor

For the following potential,

$$F_p = -\frac{1}{2}|\psi_1|^2 - \frac{1}{2}|\psi_2|^2 + 2|\psi_1|^4 + 3|\psi_2|^4 + \frac{3}{2}|\psi_1|^2|\psi_2|^2 + \frac{1}{8}|\psi_1|^2|\psi_2|^2 \cos 2\theta_{12} \ . \tag{A.1}$$

Note that the isotropy means that $Q_{ij}^{\alpha\beta} = \delta^{\alpha\beta}\delta_{ij}$.

A.2 Parameters used for $s + is$ and $s + id$ Superconductors

The following parameter set is used in Chapters 2 and 3.

s+is	s+id
$Q^{11} = \begin{pmatrix} 4 & 0 & 0 \\ 0 & 4 & 0 \\ 0 & 0 & 0.3 \end{pmatrix}$	$Q^{11} = \begin{pmatrix} 4 & 0 & 0 \\ 0 & 4 & 0 \\ 0 & 0 & 0.3 \end{pmatrix}$
$Q^{22} = \begin{pmatrix} 0.5 & 0 & 0 \\ 0 & 0.5 & 0 \\ 0 & 0 & 2 \end{pmatrix}$	$Q^{22} = \begin{pmatrix} 0.5 & 0 & 0 \\ 0 & 0.5 & 0 \\ 0 & 0 & 2 \end{pmatrix}$
$Q^{12} = \begin{pmatrix} 1 & 0 & 0 \\ 0 & 1 & 0 \\ 0 & 0 & 0.2 \end{pmatrix}$	$Q^{12} = \begin{pmatrix} 1 & 0 & 0 \\ 0 & -1 & 0 \\ 0 & 0 & 0.2 \end{pmatrix}$

Table A.1: Form of the anisotropy matrices for $s + is$ and $s + id$ systems.

For the following potential,

$$F_p = -\frac{1}{2}|\psi_1|^2 - \frac{1}{2}|\psi_2|^2 + 2|\psi_1|^4 + 3|\psi_2|^4 + \frac{3}{2}|\psi_1|^2|\psi_2|^2 + \frac{1}{8}|\psi_1|^2|\psi_2|^2 \cos 2\theta_{12} \ . \tag{A.2}$$

Appendix B

Numerical Algorithms

B.1 Discrete Winding Number

This algorithm is used to find the winding number around a point on a discretised lattice, where we input both of the discretised condensates, $\psi_\alpha^{(I,J)}$, the lattice position around which we calculate the winding number, (I_Z, J_Z), and L is a parameter determining the size of the square contour surrounding point I_Z, J_Z, depicted in Figure B.1.

Algorithm 1: Discrete Winding Number of a Zero

Input: $(\psi_1^{(I,J)}, \psi_2^{(I,J)}, I_Z, J_Z, \mathrm{L})$

Output: N - the winding number around $\psi_\alpha^{(I_Z,J_Z)}$

Define $\{K = (K_1, K_2)|\ 0 < (I_Z - K_1)^2 + (J_Z - K_2)^2 < (L+1)^2\}$. This gives us the square contour, of length $2L$, surrounding the point (I_Z, J_Z). Figure B.1 shows this for $L = 1$.

// K is ordered so we traverse the square contour anticlockwise from the point $K = (I_Z + L, J_Z)$ and finish at $K = (I_Z + L, J_Z - L)$.

$\mathrm{k} = 1$ // Note that our indexing of K starts at 1 not 0

$L_k = length(K_1) \equiv length(K_2)$ // Note that K_1 and K_2 will have the same number of elements.

while $k < L_k$ **do**

  $V = \left(\mathbb{R}(\psi_\alpha^{K(k)}), \mathbb{I}(\psi_\alpha^{K(k)})\right) / |\psi_\alpha^{K(k)}|$

  $W = \left(\mathbb{R}(\psi_\alpha^{K(k+1)}), \mathbb{I}(\psi_\alpha^{K(k+1)})\right) / |\psi_\alpha^{K(k+1)}|$ // Note that $V, W \in S^1$ and they are the normalised values of ψ_α at the points $(K_1(k), K_2(k))$ and $(K_1(k+1), K_2(k+1))$ respectively.

  $\theta(k) = \arctan\left(\frac{|V \times W|}{V \cdot W}\right)$ // This gives the relative angle between point $K(k)$ and $K(k+1)$

  $k = k + 1$

$N = \frac{1}{2\pi} \sum_k^{L_k - 1} \theta(k)$

B.2 Finding Discretised Zeros

This algorithm is used to find the positions of all zeros, for a two component order parameter on a lattice. It then determines their winding numbers via Algorithm 1 and records which

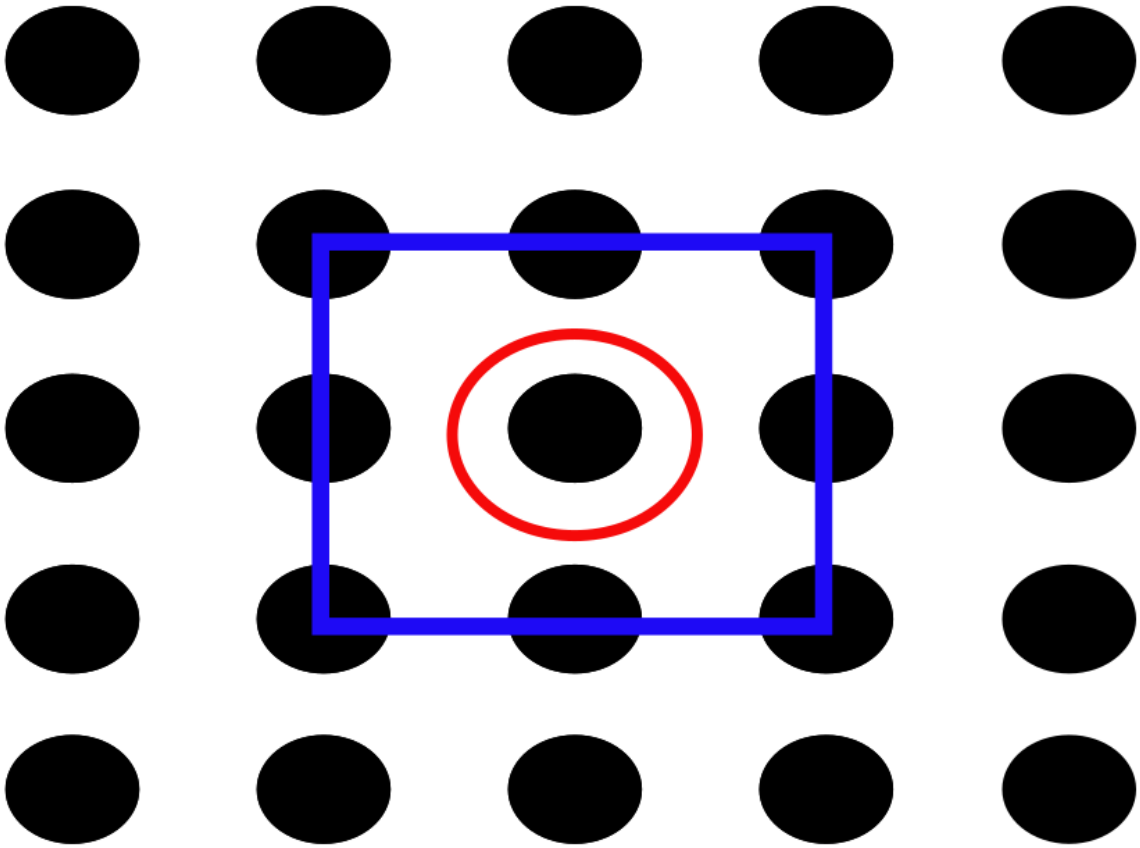

Figure B.1: *A diagram of the square contour which Algorithm 1 uses to find the discrete winding number about a point on a square lattice. Lattice sites are the black points and the point* (I_Z, J_Z) *is circled in red with the winding square for,* $L = 1$*, drawn in blue.*

zeros are coincident. The inputs are both discretised condensates, $\psi_\alpha^{(I,J)}$, and L a parameter determining the size of the square contour surrounding the point I_Z, J_Z, depicted in Figure B.1. Finally, || means or and && means and.

Algorithm 2: Discretised Zeros Finding Algorithm

Begin

Input: $\psi_1^{(I,J)}, \psi_2^{(I,J)}, L$

Output: Z_1, Z_2, Z_0 store the locations and winding numbers of the zeros of ψ_1, ψ_2 and the coincident zeros respectively.

Define $Cond(x_a, x_b) := sign(x_a)sign(y_b)$ // $Cond : \mathbb{R}^2 \to \{-1, 0, 1\}$, this function will tell us when there is a change of sign moving from x_a to x_b and thus a zero lies in $[x_a, x_b]$.

Define $\psi_1^{(I,J)} = R_1^{(I,J)} + iI_1^{(I,J)}$ and $\psi_2^{(I,J)} = R_2^{(I,J)} + iI_2^{(I,J)}$ // According to Definition 4.2.1 a change of sign in both real and imaginary components defines a zero.

Define $(I_M, J_M) = length(R_1^{(I,J)})$ // Note that the lengths of the four field R_1, I_1, R_2, I_2 are all the same and will be equal to (N_x, N_x), where N_x is the number of lattice sites in one dimension.

Define $z_1 = False$, $z_2 = False$ // These two variables will allow us to identify coincident zeros.

// || means or and && means and.

for $I = \{1 + L, ..., I_M - L\}$ **do**

  for $J = \{1 + L, ..., J_M - L\}$ **do**

    // Note that we remove $L \in \mathbb{Z}$ points from either end, this is to avoid complications with changes of sign occurring on the boundaries and therefore giving misleading answers.

    Define $HR_1 = Cond(R_1^{(I,J)}, R_1^{(I+1,J)})$, $HI_1 = Cond(I_1^{(I,J)}, I_1^{(I+1,J)})$, $HR_2 = Cond(R_2^{(I,J)}, R_2^{(I+1,J)})$ and $HI_2 = Cond(I_2^{(I,J)}, I_2^{(I+1,J)})$

    // These quantities allows us to see if a change of sign occurs in any of our four fields between lattice points (I, J) and $(I + 1, J)$, that is horizontally.

    Define $VR_1 = Cond(R_1^{(I,J)}, R_1^{(I,J+1)})$, $VI_1 = Cond(I_1^{(I,J)}, I_1^{(I,J+1)})$, $VR_2 = Cond(R_2^{(I,J)}, R_2^{(I,J+1)})$ and $VI_2 = Cond(I_2^{(I,J)}, I_2^{(I,J+1)})$

    // These quantities allows us to see if a change of sign occurs in any of our four fields between lattice points (I, J) and $(I, J + 1)$, that is vertically.

    Define $C_1 = (HR_1 \equiv -1 || VR_1 \equiv -1) \&\& (HI_1 \equiv -1 || VI_1 \equiv -1)$ and $C_{1,0} = (HR_1 \equiv 0 || VR_1 \equiv 0) \&\& (HI_1 \equiv 0 || VI_1 \equiv 0)$

    // Where C_1 gives the condition for a zero in the ψ_1 condensate at lattice site (I, J). $C_{1,0}$ is there to catch the rare case when $\psi_1^{(I,J)} \equiv 0$ which is very unlikely for discrete solutions.

    if $(C_1 \equiv True) || (C_{1,0} \equiv True)$ **then**

      Store (I, J) in Z_1 as the location of a zero for ψ_1

      Calculate and store the winding number using Algorithm 1 with inputs $(\psi_1^{(I,J)}, I_Z, J_Z, \mathrm{L})$

      Set $z_1 = True$

Algorithm 2: Continued

```
18
19  for I = {1 + L, ..., I_M − L} do
20      for J = {1 + L, ..., J_M − L} do
21          Define C_2 = (HR_2 ≡ −1||VR_2 ≡ −1)&&(HI_2 ≡ −1||VI_2 ≡ −1) and
            C_{2,0} = (HR_2 ≡ 0||VR_2 ≡ 0)&&(HI_2 ≡ 0||VI_2 ≡ 0)
              // Where C_2 gives the condition for a zero in the ψ_2 condensate at lattice
              site (I, J). C_{2,0} is there to catch the rare case when ψ_1^{(I,J)} ≡ 0 which is very
              unlikely for discrete solutions.
22          if (C_2 ≡ True)||(C_{2,0} ≡ True) then
23              Store (I, J) in Z_2 as the location of a zero for ψ_1
24              Calculate and store the winding number using Algorithm 1 with inputs
                (ψ_2^{(I,J)}, I_Z, J_Z,L) Set z_2 = True
25          if (z_1 ≡ True)&&(z_2 ≡ True) then
26              Store (I, J) in Z_0 as the location of a coincident zero of ψ_1 and ψ_2
27              Store the winding numbers for ψ_1^{(I,J)} and ψ_2^{(I,J)}.
                 // Note that as long as L ≥ 2, that is the square contour encompasses the
                 points (I, J), (I + 1, J), (I + 1, J + 1), (I, J + 1), we can be confident that the
                 winding numbers calculated are accurate
28          Re-set z_1 = False, z_2 = False
```

Bibliography

[1] A. Benfenati, M. Barkman, T. Winyard, A. Wormald, M. Speight, and E. Babaev, "Magnetic signatures of domain walls in $s + is$ and $s + id$ superconductors: Observability and what that can tell us about the superconducting order parameter," *Physical Review B*, vol. 101, no. 5, p. 054507, 2020. [Online]. Available: https://journals.aps.org/prb/abstract/10.1103/PhysRevB.101.054507 (pages i, 26, 26, 62, 80).

[2] M. Speight, T. Winyard, A. Wormald, and E. Babaev, "Magnetic field behaviour in $s + is$ and $s + id$ superconductors: twisting of applied and spontaneous fields," *arXiv preprint arXiv:2106.00475*, 2021. [Online]. Available: https://arxiv.org/abs/2106.00475 (pages i, i, 26, 62, 74, 134).

[3] H. K. Onnes, "Further experiments with liquid helium. c. on the change of electric resistance of pure metals at very low temperatures, etc. iv. the resistance of pure mercury at helium temperatures." *Comm. Phys. Lab. Univ. Leiden; No. 120b*, 1911. (page 1).

[4] ——, "Further experiments with liquid helium. d. on the change of electric resistance of pure metals at very low temperatures, etc. v. the disappearance of the resistance of mercury." *Comm. Phys. Lab. Univ. Leiden; No. 122b*, 1911. (page 1).

[5] ——, "Further experiments with liquid helium. g. on the electrical resistance of pure metals, etc. vi. on the sudden change in the rate at which the resistance of mercury disappears." *Comm. Phys. Lab. Univ. Leiden; No. 124c*, 1911. (page 1).

[6] W. Meissner and R. Ochsenfeld, "Ein neuer effekt bei eintritt der supraleiter higkeit," *Naturwissenschaften 21, 787*, 1933. (page 1).

[7] F. London and H. London, "The electromagnetic equations of the supraconductor,," *Proc. Roy. Soc. (Lond.) A149, 71*, 1935. (page 1).

[8] V. L. Ginzburg and L. D. Landau, "To the theory of superconductivity," *Zh. Eksp. Teor. Fiz. 20, 1064*, 1950. (page 1).

[9] J. Bardeen, L. N. Cooper, and J. R. Schrieffer, "Microscopic theory of superconductivity," *Phys. Rev. 106, 162*, 1957. [Online]. Available: https://journals.aps.org/pr/abstract/10.1103/PhysRev.106.162 (page 1).

[10] ——, "Theory of superconductivity," *Phys. Rev. 108, 1175*, 1957. (page 1).

[11] A. I. Larkin and Y. N. Ovchinnikov, "Nonuniform state of superconductors," *Zh. Eksp. Teor. Fiz. 47 [Sov. Phys. JETP 20, 762 (1965)]*, 1964. [Online]. Available: https://elibrary.ru/item.asp?id=21823687 (page 2).

[12] P. Fulde and R. A. Ferrell, "Superconductivity in a strong spin-exchange field," *Phys. Rev.*, vol. 135, pp. A550–A563, Aug 1964. [Online]. Available: https://link.aps.org/doi/10.1103/PhysRev.135.A550 (page 2).

[13] T. K. Ng and N. Nagaosa, "Broken time-reversal symmetry in josephson junction involving two-band superconductors," *EPL (Europhysics Letters)*, vol. 87, no. 1, p. 17003, jul 2009. [Online]. Available: https://doi.org/10.1209/0295-5075/87/17003 (page 2).

[14] V. Stanev and Z. Tešanović, "Three-band superconductivity and the order parameter that breaks time-reversal symmetry," *Phys. Rev. B*, vol. 81, p. 134522, Apr 2010. [Online]. Available: https://link.aps.org/doi/10.1103/PhysRevB.81.134522 (page 2).

[15] J. Carlström, J. Garaud, and E. Babaev, "Length scales, collective modes, and type-1.5 regimes in three-band superconductors," *Phys. Rev. B*, vol. 84, p. 134518, Oct 2011. [Online]. Available: https://link.aps.org/doi/10.1103/PhysRevB.84.134518 (page 2).

[16] S. Maiti and A. V. Chubukov, "$s + is$ state with broken time-reversal symmetry in fe-based superconductors," *Phys. Rev. B*, vol. 87, p. 144511, Apr 2013. [Online]. Available: https://link.aps.org/doi/10.1103/PhysRevB.87.144511 (page 2).

[17] Y. Kamihara, T. Watanabe, M. Hirano, and H. Hosono, "Iron-based layered superconductor La[$O_{(1-x)}F_x$]FeAs (x= 0.05-0.12) with tc= 26 k," *Journal of the American Chemical Society*, vol. 130, no. 11, pp. 3296–3297, 2008, pMID: 18293989. [Online]. Available: https://doi.org/10.1021/ja800073m (page 2).

[18] A. A. Abrikosov, "The magnetic properties of superconducting alloys," *Journal of Physics and Chemistry of Solids*, vol. 2, no. 3, pp. 199–208, 1957. (pages 4, 114).

[19] L. Schubnikow, W. Chotkewitsch, J. Schepelew, and J. Rjabinin, "Magnetische eigenschaften supraleitender metalle und legierungen," *Phys. Z. Sowiet*, vol. 10, no. 2, pp. 165–192, 1936. (page 2).

[20] M. Tinkham, *Introduction to Superconductivity*, ser. Dover Books on Physics Series. Dover Publications, 2004. [Online]. Available: https://books.google.co.uk/books?id=VpUk3NfwDIkC (page 3).

[21] N. Manton and P. Sutcliffe, *Topological Solitons*, ser. Cambridge Monographs on Mathematical Physics. Cambridge University Press, 2004. [Online]. Available: https://books.google.co.uk/books?id=e2tPhFdSUf8C (pages 11, 16).

[22] T. Skyrme, "Particle states of a quantized meson field," *Proceedings of the Royal Society of London. Series A. Mathematical and Physical Sciences*, vol. 262, no. 1309, pp. 237–245, 1961. (page 14).

[23] E. Babaev and M. Speight, "Semi-meissner state and neither type-i nor type-ii superconductivity in multicomponent superconductors," *Phys. Rev. B*, vol. 72, p. 180502, Nov 2005. [Online]. Available: https://link.aps.org/doi/10.1103/PhysRevB.72.180502 (page 21).

[24] J. Carlström, E. Babaev, and M. Speight, "Type-1.5 superconductivity in multiband systems: Effects of interband couplings," *Phys. Rev. B*, vol. 83, p. 174509, May 2011. [Online]. Available: https://link.aps.org/doi/10.1103/PhysRevB.83.174509 (pages 21, 94).

[25] J. Garaud, M. Silaev, and E. Babaev, "Microscopically derived multi-component ginzburglandau theories for $s + is$ superconducting state," *Physica C: Superconductivity and its Applications*, vol. 533, pp. 63 – 73, 2017, ninth international conference on Vortex Matter in nanostructured Superconductors. [Online]. Available: http://www.sciencedirect.com/science/article/pii/S0921453416300983 (pages 22, 62, 88).

[26] A. Bouhon and M. Sigrist, "Influence of the domain walls on the Josephson effect in Sr_2RuO_4," *New Journal of Physics*, vol. 12, no. 4, p. 043031, 2010. [Online]. Available: http://stacks.iop.org/1367-2630/12/i=4/a=043031 (pages 23, 39, 40, 40, 47, 48, 56, 71).

[27] J. Garaud and E. Babaev, "Domain walls and their experimental signatures in $s + is$ superconductors," *Phys. Rev. Lett.*, vol. 112, p. 017003, Jan 2014. [Online]. Available: https://link.aps.org/doi/10.1103/PhysRevLett.112.017003 (page 26).

[28] V. L. Vadimov and M. A. Silaev, "Polarization of the spontaneous magnetic field and magnetic fluctuations in $s + is$ anisotropic multiband superconductors," *Phys. Rev. B*, vol. 98, p. 104504, Sep 2018. [Online]. Available: https://link.aps.org/doi/10.1103/PhysRevB.98.104504 (pages 26, 135).

[29] A. Mackenzie and Y. Maeno, "p-wave superconductivity," *Physica B: Condensed Matter*, vol. 280, no. 1, pp. 148 – 153, 2000. [Online]. Available: http://www.sciencedirect.com/science/article/pii/S092145269901546X (page 26).

[30] V. Grinenko, P. Materne, R. Sarkar, H. Luetkens, K. Kihou, C. Lee, S. Akhmadaliev, D. Efremov, S.-L. Drechsler, and H.-H. Klauss, "Superconductivity with broken time-reversal symmetry in ion-irradiated $Ba_{0.27}K_{0.73}Fe_2As_2$ single crystals," *Physical Review B*, vol. 95, no. 21, p. 214511, 2017. [Online]. Available: https://journals.aps.org/prb/abstract/10.1103/PhysRevB.95.214511 (page 26).

[31] V. Grinenko, R. Sarkar, K. Kihou, C. Lee, I. Morozov, S. Aswartham, B. Büchner, P. Chekhonin, W. Skrotzki, K. Nenkov *et al.*, "Emerging superconductivity with broken time reversal symmetry inside a superconducting s-wave state," *arXiv preprint arXiv:1809.03610*, 2018. [Online]. Available: https://ui.adsabs.harvard.edu/abs/2018arXiv180903610G/abstract (page 26).

[32] Y. N. Ovchinnikov and D. Efremov, "Singular ground state of multiband inhomogeneous superconductors," *Physical Review B*, vol. 99, no. 22, p. 224508, 2019. [Online]. Available: https://journals.aps.org/prb/abstract/10.1103/PhysRevB.99.224508 (page 26).

[33] A. P. Mackenzie and Y. Maeno, "The superconductivity of Sr_2RuO_4 and the physics of spin-triplet pairing," *Rev. Mod. Phys.*, vol. 75, pp. 657–712, May 2003. [Online]. Available: https://link.aps.org/doi/10.1103/RevModPhys.75.657 (page 26).

[34] C. Kallin, "Chiral p-wave order in Sr_2RuO_4," *Reports on Progress in Physics*, vol. 75, no. 4, p. 042501, mar 2012. [Online]. Available: https://doi.org/10.1088/0034-4885/75/4/042501 (page 26).

[35] M. Silaev, T. Winyard, and E. Babaev, "Non-london electrodynamics in a multiband london model: Anisotropy-induced nonlocalities and multiple magnetic field penetration lengths," *Phys. Rev. B*, vol. 97, p. 174504, May 2018. [Online]. Available: https://link.aps.org/doi/10.1103/PhysRevB.97.174504 (page 34).

[36] T. Winyard, M. Silaev, and E. Babaev, "Hierarchies of length-scale based typology in anisotropic $u(1)$ s-wave multiband superconductors," *Phys. Rev. B*, vol. 99, p. 064509, Feb 2019. [Online]. Available: https://link.aps.org/doi/10.1103/PhysRevB.99.064509 (page 34).

[37] M. Speight, T. Winyard, and E. Babaev, "Chiral p-wave superconductors have complex coherence and magnetic field penetration lengths," *Physical Review B*, vol. 100, no. 17, p. 174514, 2019. [Online]. Available: https://journals.aps.org/prb/abstract/10.1103/PhysRevB.100.174514 (pages 34, 40, 40, 48, 48, 50, 135).

[38] ——, "Symmetries, length scales and lattices in nematic superconductors," *Upcoming paper*, 2021. [Online]. Available: https://scholar.google.co.uk/citations?user=nWOv95wAAAAJ&hl=en&oi=ao (pages 38, 117, 120, 121, 135).

[39] A. Bouhon, "Electronic properties of domain walls in sr_2ruo_4," Ph.D. dissertation, ETH-Zrich, 2014. [Online]. Available: https://www.research-collection.ethz.ch/bitstream/handle/20.500.11850/154686/1/eth-14463-01.pdf (page 39).

[40] M. Sigrist and K. Ueda, "Phenomenological theory of unconventional superconductivity," *Rev. Mod. Phys.*, vol. 63, pp. 239–311, Apr 1991. [Online]. Available: https://link.aps.org/doi/10.1103/RevModPhys.63.239 (page 40).

[41] M. Sigrist, T. M. Rice, and K. Ueda, "Low-field magnetic response of complex superconductors," *Phys. Rev. Lett.*, vol. 63, pp. 1727–1730, Oct 1989. [Online]. Available: https://link.aps.org/doi/10.1103/PhysRevLett.63.1727 (page 40).

[42] E. Babaev, "Vortices with fractional flux in two-gap superconductors and in extended faddeev model," *Phys. Rev. Lett.*, vol. 89, p. 067001, Jul 2002. [Online]. Available: https://link.aps.org/doi/10.1103/PhysRevLett.89.067001 (page 85).

[43] T. Winyard, M. Silaev, and E. Babaev, "Skyrmion formation due to unconventional magnetic modes in anisotropic multiband superconductors," *Physical Review B*, vol. 99, no. 2, Jan 2019. [Online]. Available: http://dx.doi.org/10.1103/PhysRevB.99.024501 (page 85).

[44] L.-F. Zhang, Y.-Y. Zhang, G.-Q. Zha, M. V. Milošević, and S.-P. Zhou, "Skyrmionic chains and lattices in $s + id$ superconductors," *Phys. Rev. B*, vol. 101, p. 064501, Feb 2020. [Online]. Available: https://link.aps.org/doi/10.1103/PhysRevB.101.064501 (pages 85, 86, 87, 93, 114, 120, 126, 127, 134).

[45] B. V. Svistunov, E. S. Babaev, and N. V. Prokof'ev, *Superfluid states of matter*. Crc Press, 2015. [Online]. Available: https://dlib.scu.ac.ir/bitstream/Hannan/388036/2/1439802769.pdf (page 86).

[46] Y. Ren, J.-H. Xu, and C. S. Ting, "Ginzburg-landau equations and vortex structure of a $d_{x^2-y^2}$ superconductor," *Phys. Rev. Lett.*, vol. 74, pp. 3680–3683, May 1995. [Online]. Available: https://link.aps.org/doi/10.1103/PhysRevLett.74.3680 (page 86).

[47] J. Garaud, J. Carlström, E. Babaev, and M. Speight, "Chiral CP^2 skyrmions in three-band superconductors," *Physical Review B*, vol. 87, no. 1, Jan 2013. [Online]. Available: http://dx.doi.org/10.1103/PhysRevB.87.014507 (page 92).

[48] J. M. Speight, "Static intervortex forces," *Phys. Rev. D*, vol. 55, pp. 3830–3835, Mar 1997. [Online]. Available: https://link.aps.org/doi/10.1103/PhysRevD.55.3830 (page 136).

[49] M. Gillard and P. Sutcliffe, "Domain walls and double bubbles," *Proceedings of the Royal Society A: Mathematical, Physical and Engineering Sciences*, vol. 465, no. 2109, pp. 2911–2925, 2009. [Online]. Available: https://royalsocietypublishing.org/doi/abs/10.1098/rspa.2009.0227 (page 136).